# New applications of wavefront shaping – from taming dynamic scattering media to precision optical tweezing

Submitted by Christina Sharp to the University of Exeter
as a thesis for the degree of
Doctor of Philosophy in Physics

November 2023

I certify that all material in this thesis which is not my own work has been identified and that any material that has previously been submitted and approved for the award of a degree by this or any other University has been acknowledged.

*Picture a man*
*Seen like a speck out from the shore*
*Swimming out beyond the breakers like he's done his life before*
*He feels the coming of a squall will drag him out a greater length*
*But knows his strength*
*Tries to gather it*

Andrew John Hozier-Byrne

UNIVERSITY OF EXETER

## ABSTRACT

# New applications of wavefront shaping – from taming dynamic scattering media to precision optical tweezing

by Christina SHARP

Over the last 15 years, wavefront shaping has emerged as a powerful technique to control the propagation of light within scattering media by precisely sculpting the spatial distribution of an electromagnetic field. Today, wavefront shaping is a cornerstone approach to solving many light scattering problems in optics. This technique is being used to see and probe deep into tissue, replace traditional optical components like lenses, and render opaque objects transparent. Here we explore applications of wavefront shaping to two new problems.

The first of these is wavefront shaping in the face of dynamic media that results in light scattering that fluctuates in time. Existing wavefront shaping applications rely on light scattering from static scattering media – imagine the constant distortions of sunlight through a frosted glass window. We envisage a scattering scenario wherein some parts of the medium are static, while others are moving – like trying to image inside of a living organism with blood vessels flowing through largely static tissue. We demonstrate, numerically and experimentally, a new suite of wavefront shaping tools that determine paths for the light that carefully navigate through static and around dynamic scattering areas. These tools include an assortment of matrices and optimisation algorithms that use information about the time fluctuations of a light field to find such paths. This research opens the door to combining our new techniques with the plethora of existing methods such as the transmission matrix, phase conjugation, and iterative wavefront optimisation to offer expanded applications in the field of wavefront shaping.

The second problem we investigate is in the field of optical tweezing. Optical tweezers, which use the transfer of momentum from a focused laser beam to a micro-scale object, to trap the object and control its motion, have allowed researchers to gain unrivaled access to and control over the mesoscale world. We aim to trap micro-spheres immersed in water more tightly by moulding the spatial distribution of an optical trap. The interaction between the light and the trapped particle is changed by manipulating the incident optical field. We develop new ways to optimise the optical trap shape, both numerically and experimentally, such that our final optimised traps reduce the 3D motion of trapped micro-scale particles in water by orders of magnitude compared to conventional Gaussian traps. These enhanced optical traps hold promise for many applications in the field of micro-manipulation, including trapping of previously un-trappable particles.

Our work demonstrates that wavefront shaping can be applied to dynamic scattering media and optical tweezers, opening avenues to new applications in imaging, optical communications, and optical micro-manipulation.

# *Acknowledgements*

First and foremost, I want to thank my supervisors: David B. Phillips and Fabrice Gielen. This thesis would not have happened without their supportive guidance. The inception of the ideas herein is entirely due to Dave's unfailing enthusiasm for the research and creative intuition. No matter how many times I pestered him, Dave was always available to advise me. Fabrice's insight and feedback throughout the course of this research were invaluable, even though the projects ended up taking a course far from the originally planned one. For these reasons and many more, I extend a heartfelt thank you to both.

I would not have survived the labyrinth of LabVIEW or the endless hours of experimentation without the assistance and company of Unė G. Būtaitė. I'll never forget the time that Unė and I were stuck on a train halfway to a research conference in London for several hours when a freight train broke down on the tracks. I couldn't have asked for more pleasant company, during that long journey and throughout my PhD.

Furthermore I'd like to thank the rest of the Structured Light Lab – without the whole team's supportive and friendly demeanor, work would have been terribly dreary in our windowless optics laboratory. Thank you Chai, Rachel, John, Hlib, and José, for all of the help, support, and companionship these last few years. Your memes and jokes provided much needed comic relief, and I will treasure our friendship through whatever the future holds.

And finally, I want to thank Rithvik Gutha. You are my rock, and without you none of this would mean anything.

# Contents

# List of Figures

# List of Tables

# List of Abbreviations

| | |
|---|---|
| **SLM** | **S**patial **L**ight **M**odulator |
| **DMD** | **D**igital **M**icro-mirror **D**evice |
| **DDA** | **D**iscrete **D**ipole **A**pproximation |
| **DOPC** | **D**igital **O**ptical **P**hase **C**onjugation |
| **TM** | **T**ransmission **M**atrix |
| **GWS** | **G**eneralized **W**igner **S**mith |
| **FOM** | **F**igure **O**f **M**erit |
| **CoM** | **C**entre **o**f **M**ass |
| **VSWF** | **V**ector **S**pherical **W**ave**f**unction |
| **BSC** | **B**eam **S**hape **C**oefficient |
| **OTT** | **O**ptical **T**weezers **T**oolbox |
| **NA** | **N**umerical **A**perture |
| **GS** | **G**erchberg-**S**axton |
| **FFT** | **F**ast **F**ourier **T**ransform |
| **RMSE** | **R**oot-**M**ean-**S**quare **E**rror |
| **HOT** | **H**olographic **O**ptical **T**weezers |
| **OAM** | **O**rbital **A**ngular **M**omentum |
| **CV** | **C**oefficient of **V**ariance |

*Dedicated to Rithvik & Ciri.*

# Chapter 1

# The scattering of light

LIGHT travels in straight lines, unless it interacts with obstacles in its path. Examples of interactions that redirect the path of light include shadows behind illuminated objects, the perceived bending of an object halfway submerged in water, and the reduction of visibility in fog. Light scattering encompasses all such interactions between optical fields and their environment. Light scattering can be classed as either *elastic*, such that energy of scattered light is conserved, or *inelastic*, such that the scattered light experiences a shift in energy (shift in wavelength). In many situations, such as inside biological tissue, elastic optical scattering – refraction, reflection, diffraction – dominates. For the applications discussed here, elastic scattering fully characterises the light scattering effects.

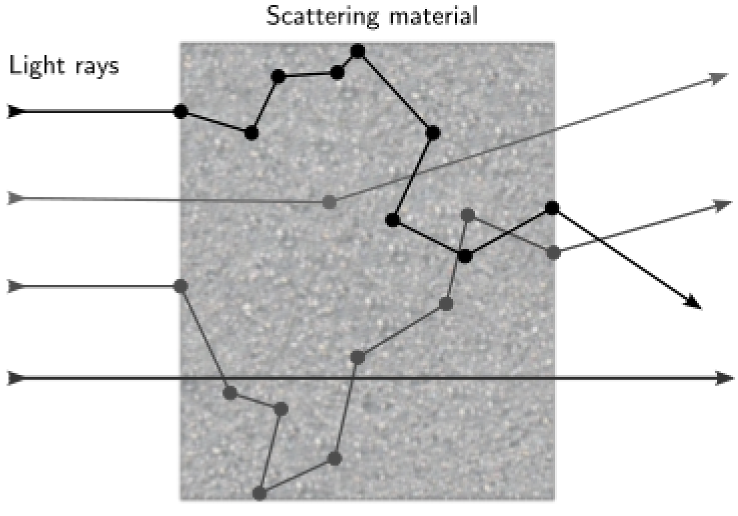

FIGURE 1.1: **Scattering of light rays due to a scattering material.**

The term *scattering material*, as it will be used here, means any material which scatters light. Fig. 1.1 shows an example of such a material, where four incident light rays are scattered within the medium. Here such a scattering material will be imagined as a discrete collection of points in space (circles that the light rays encounter in Fig. 1.1) whose collective action mimics a continuous scattering medium. A few things can happen to light rays within such a scattering material, as illustrated in the figure: single scattering (ray 2), multiple scattering (rays 1 and 3), or no scattering (ray 4).

Such optical scattering can be quantified by several commonly used parameters. The first of these, the scattering coefficient $\mu_s$, is the total scattering cross-sectional area in a scattering medium per unit volume. The higher the scattering coefficient, the more light rays are multiply scattered. The *reduced scattering coefficient* $\mu_s'$ is also used to describe the scattering of photons. It is commonly determined experimentally and given mathematically by

$$\mu_s' = \mu_s(1-g) \tag{1.1}$$

where $g$ is called the anisotropy factor which ranges between -1 (backward scattering) and 1 (forward scattering). A value of $g = 0$ corresponds to isotropic scattering.

Given the scattering coefficient, the *scattering mean free path* $l$ (the average distance between scattering events) and the *transport mean free path* $l_t$ (the average distance before the direction of the incident light is randomised) can be used to describe the behavior of light scattering within a medium. These two quantities are given by

$$l = \frac{1}{\mu_s} \tag{1.2}$$

$$l_t = \frac{1}{\mu_s(1-g)} = \frac{1}{\mu_s'}. \tag{1.3}$$

If the thickness of a scattering material is much larger than the transport mean free path $l_t$, the material is said to be diffusive. In the diffusive regime, the incident light is so strongly scattered that the direction of the light has become randomised and only a small amount of the incident light arrives at the far side of the scattering material.

Scattering impedes the ability of light to transmit information from one point to another in space, for example in an image. Here, an image refers to a specific spatial distribution of an electromagnetic field's intensity; generally, an image can include all of light's degrees of freedom in phase, polarisation, and intensity. The scrambling of such an image due to the scattering of light caused by a scattering medium between the source and receiver is a difficult phenomenon to undo, but has nevertheless been extensively studied [1]. Everyday examples of light scattering distorting spatial intensity information include scenes blurred by frosted glass, the distortion of the light from distant stars by the Earth's atmosphere, and loss of visibility due to fog. However, because elastic scattering is deterministic, the spatial intensity information is merely scrambled, not lost as long as all scattered light is collected. In recent years, significant progress has been made in 'unscrambling' scattered light. Recent advances in counteracting scattering have opened the doors to many exciting new applications in optics, biophysics, and communications technologies [2, 3].

For some applications, however, the scattering of light is beneficial, even essential. Optical tweezers is one such area, completely reliant on the momentum transferred through the scattering action between an incident light field and mesoscale matter. Optical tweezers are created by highly focused laser light and are capable of exerting spatial control over micro-particles.

This thesis explores these two sides of the topic of light scattering. Part I focuses on exploring approaches to undoing the scrambling of information due to scattering, while Part II focuses on harnessing the scattering to maximise momentum transfer between the light and a targeted microscopic object. In the former, scattering is seen as a problem that needs to be addressed or prevented; in the latter, scattering is a powerful tool that is maximised to precisely manipulate the objects light encounters.

## 1.1 Light scattering - an obstacle to overcome

Approaches to imaging when faced with light scattering are many and varied, and have been and continue to be vigorously researched [4, 5]. Perhaps the simplest technique is to ignore light scattering effects by using methods that remove multiply scattered waves. These include optical coherence tomography [6] and multiphoton microscopy [7]. These approaches that throw away the scattered light however become unusable when light diffusion begins to dominate through strongly scattering media larger than a few scattering mean free paths (the average propagation distance between scattering events).

In recent years, another route has emerged that offers a solution to the problem of optical scattering – *wavefront shaping*. Wavefront shaping changes the spatial distribution of a light field's complex amplitude (amplitude and phase) to counteract the scattering effects of a material. This method, in contrast to those mentioned above, aims to use as much light as possible.

This solution has birthed a rich and varied field in modern optics [5, 8], developing out of the use of adaptive optics in astronomy to correct images of far-away galaxies distorted by the Earth's atmosphere [9, 10]. Wavefront shaping in wave physics harnesses the deterministic nature of scattering to undo or counteract the scattering action. Advances in technology have allowed modern wavefront shaping devices to manipulate orders of magnitude more modes than the low dimensional aberrations corrected by deformable mirrors in adaptive optics for astronomy, allowing this technique originally designed for lower scattering levels due to the atmosphere to be used in the diffusive regime in highly scattering media. Wavefront shaping has been used to focus several hundred microns inside biological tissue [11], enhance focusing and fluorescence imaging in combination with meta-surfaces [12], and increase the amount of diffuse light transmitted through a scattering sample [13], to name only a few examples.

Approaches to manipulating the scattering of light using wavefront shaping can be broadly categorised into three techniques: iterative wavefront optimisation [14–18], optical phase conjugation [19–24], and transmission matrix measurement [25–29].

The field of wavefront shaping was pioneered in 2007 by Vellekop and Mosk, who showed how to focus light through strongly scattering and diffuse media [14]. Using a spatial light modulator (SLM) and an iterative wavefront optimisation technique, Vellekoop and Mosk iteratively adjusted the phase and thereby structured the optical field incident on a visibly opaque scattering sample (a ∼10 µm layer of TiO2 particles). This optimisation determined how the relative spatially varying phase of the incident beam needed to be adjusted to promote constructive interference to create a diffraction limited focus through the rutile sample. The publication of this work marked the beginning of a plethora of studies into the control of light propagation in scattering media using wavefront shaping.

The second wavefront shaping technique, optical phase conjugation, relies on the principle of time-reversal [30] which states than an electric field is unchanged if the spatially separated source and detector are interchanged. Over half a century ago, Leith and Upatnieks demonstrated optical phase conjugation using a hologram to undo the scattering effects of a ground glass diffuser [31]. More recently, in 2008, Yaqoob et al. demonstrated optical phase conjugation to suppress the scattering effects through 0.69 mm thick chicken breast tissue [19]. Using a photorefractive crystal to record and generate the phase conjugated field, it was shown that a focus could be reconstructed through the chicken breast tissue even at thicknesses well into the diffusive scattering regime.

The third approach to wavefront shaping, the measurement of the transmission matrix, provides information on how an incident field is transmitted through a scattering material. The first experimental implementation of this method at optical frequencies was performed by Popoff et al. in 2010 [25], who used a spatial light modulator and a full-field interferometric measurement to capture the transmission matrix of an opaque ∼80 µm thick deposit of ZnO on a microscope slide. The transmission matrix is obtained by sending a set of probing fields through the medium, and then measuring and storing the corresponding output fields in the columns of the matrix. In this work it was also shown that the measured transmission matrix can be applied to generate a desired field at the detectors (here, a focus) by wavefront shaping the field incident on the scattering sample.

Many variants of wavefront shaping have been developed, incorporating different aspects of these three approaches. This is also the case for the research presented in this thesis. In this work we build on ideas from these methods and apply them in new ways.

Overall, the field of optical wavefront shaping continues to be an area of active research, with new developments and applications emerging all of the time. By improving the ability to manipulate light waves, this technology has the potential to unlock new capabilities in many scientific fields, ranging from medicine and biology to telecommunications and materials science.

### 1.1.1 Dynamic scattering media

The vast majority of wavefront shaping methods introduced above rely on the medium in question remaining static for the duration of the wavefront shaping process. Overcoming the effects of time-varying scattering media, in which the media changes on time scales shorter than those needed for wavefront shaping techniques, is a much more challenging problem that remains largely unsolved. The first part of this thesis focuses on the development of new wavefront shaping techniques that are compatible with dynamic scattering media. Chapter 2 investigates existing methods and their applicability to dynamic scattering media. Chapter 3 develops several new approaches to wavefront shaping tailored to the problem of time-varying scattering materials.

The process of wavefront shaping can be time-intensive, and often this is the bottleneck in applications. Typically this process takes minutes to hours depending on the spatial light modulator speed, numbers of iterations used, and the number of measurements required to characterise the scattering material. To speed up this process, work has been done primarily in two areas: speeding up the wavefront shaping, and reducing the number of measurements needed e.g. for transmission matrix measurements. These approaches however still require that the medium in question remains static throughout the wavefront shaping process.

Current approaches to overcoming the effects of dynamic scattering media rely largely on decreasing the time needed for applications such that wavefront shaping is performed at a rate greater or equal to the rate of movement of the scattering material [23, 32–35]. To perform this ultra-fast wavefront shaping, spatial light modulators (SLMs) operating at hundreds of kHz [36, 37] or fast digital micro-mirror devices (DMDs) operating at kHz [21, 38, 39] have been used. Faster SLMs, operating at megaHertz to gigaHertz, hold promise as future advances to wavefront shaping technologies [40, 41].

To reduce the number of measurements required to construct a usable transmission matrix, prior knowledge about the scattering medium can be exploited. Such knowledge includes correlations between elements of the transmission matrix known as memory effects, predictions about how the power is distributed over the transmission matrix elements, or a recent but slightly degraded measurement of the transmission matrix [26, 42–48].

Here we take a different approach. We consider an edge case of partially dynamic material, where localised pockets within a largely static scattering material vary on timescales shorter than the wavefront shaping process. Examples of applications in such edge cases are imaging through a living biological system with blood flowing through capillaries within relatively static tissue, improving internet signals in an office building of moving humans, or counteracting the effect of hot air escaping chimneys into colder, more static air above houses to improve telecommunication signals. The goal of this approach is to develop new wavefront shaping approaches to guide light around localised dynamic regions within scattering media. We hope to achieve this without any prior knowledge of the number or location of these regions.

## 1.2 Light scattering - a highly customisable tool

Fundamentally, in addition to scrambling the spatial information carried by an optical field, light scattering causes an exchange of momentum between the light and matter it is interacting with. This occurs anytime a ray of light experiences an inhomogeneity in its path, such as a change in the refractive index, where the ray changes direction. When this occurs, then by conservation of momentum, the ray must have exerted a force on the inhomogeneity. This force is called the *radiation pressure.* Although predicted by Maxwell, the concept of light carrying momentum and imparting force onto massive objects was not experimentally proven until 1901 [49, 50]. Since the advent of the laser, radiation pressure has been harnessed to all-optically reconfigure the operation of integrated photonic circuits [51], damp mechanical oscillations [52], and power solar sails in outer space [53, 54].

Under the right conditions, the light of a focused laser beam scattering from a microscopic particle transfers momentum such that an *optical trap* is formed. This can be understood to be due to the combined change in momentum of the light rays as they strike the interface between media of two different refractive indices (in this case the particle and the media that surrounds it). This change in momentum induces a net backwards force on the particle which counteracts the forward pointing radiation pressure. These two forces balance each other at the *equilibrium* position of the optical trap, where the net force felt by the particle is zero.

In contrast to Part I of this thesis, where the aim of the research is to create lights fields that minimally interact with a region of scattering material via wavefront shaping, in Part II the goal is to maximise the interaction between the incident light and the optically trapped particle, thereby increasing the momentum transfer to create better optical tweezers by wavefront shaping.

Optical tweezers can be used to trap and manipulate microscopic objects. The technology was first demonstrated in the 1970s by Arthur Ashkin [55], who shared the 2018 Nobel Prize in Physics for his work on optical tweezers. Since then, optical tweezers have been used to trap myriad particles from simple spheres [56] to cells [57–59]. Optical tweezers have become a powerful tool in biology and physics research, allowing scientists to study the bio-mechanics of molecular motors and protein-DNA interactions [60, 61] and power artificial micro-machines [62, 63].

Recent developments in optical tweezers technology have focused on increasing their capabilities from simply holding a micro-particle. It is now also possible to create arrays of multiple stable traps [64], create a “tractor beam” that pulls particles back towards the laser beam source [65], rotate particles [66], image surfaces using trapped particles [67, 68], and even cool a single atom to its quantum ground state [69–71], all using optical tweezers. These improvements have opened up new avenues for research in biophysics, nanotechnology, and materials science, and continue to push the boundaries of what is possible with this versatile technology.

### 1.2.1 Enhancing optical tweezing

For some applications, such as the experiments and simulations presented here, the micro-particles are submerged in water, meaning the micro-particles undergo Brownian motion due to the thermal motion of the water molecules. This results in even optically trapped particles exhibiting some degree of motion within the trap. The gradient force on an optically trapped micro-sphere acts as a restoring force that responds to displacements of the micro-sphere from the trap's equilibrium position, such as the displacements due to the collisions with water molecules.

The force felt by an optically trapped micro-particle is given by a Hookean force: $F_x = -\kappa_x x$, and similar equations for $y$ and $z$ directions. This is an approximation of the force which only holds for small $x$ displacements from equilibrium. The *stiffness* $\kappa_x$ is a common measure of the strength of an optical trap, which describes the magnitude of the force felt by an optically trapped particle for a small displacement $x$ from equilibrium. The most straightforward way to more stiffly trap a given particle is to increase the laser power in the optical trap. This, however, can lead to issues in experiments such as increasing the temperature of the particle and its surroundings [72], damaging photosensitive biological systems [73], and increasing decoherence effects in quantum ground state experiments [70]. To avoid such situations, here an alternate paradigm is considered. Namely, is it possible to use wavefront shaping to enhance optical trap stiffness without increasing the amount of laser power used?

This question opens the door to two ways of thinking about enhancing optical trapping: increase the optical trap stiffness using the same total laser power, or decrease the total laser power to achieve the same optical trap stiffness. These are two sides of the same coin.

To utilise the full potential of a focused laser beam, Chapters 4, 5, and 6 approach this problem from the point of view of wavefront shaping. Past work in optical tweezers with wavefront shaping has shown that it is possible to tailor traps to increase trapping stiffness for just some dimensions of motion. This includes increasing trapping stiffness using doughnut modes [74, 75], multiple carefully spaced conventional Gaussian optical traps [76, 77], and super-oscillating Hermite–Gauss, Laguerre–Gauss, and Airy function beams [78]. This thesis delves into the depths of a yet unexplored cave of wonders – three dimensional (3D) enhancement of holographic optical tweezers. It is not straightforward to extend the methods used to increase trapping stiffness in 1D and 2D to 3D. Inspired by existing mathematical techniques, both numerical and experimental implementations are developed and their results presented in this thesis, showing for the first time that it is possible to improve existing optical trap performance by one-to-two orders of magnitude.

# Part I

# Investigating dynamic scattering media

*Faithless is he that says farewell when the road darkens.*

J. R. R. Tolkien

In this part, various existing (Chapter 2) and novel (Chapter 3) applications of wavefront shaping techniques are applied to the problem of unscrambling light scattered by dynamic media. The research presented in this part was conducted by Dr. Chaitanya Mididoddi (CKM), Prof. Simon A. R. Horsley (SARH), Dr. Philipp del Hougne (PdH), Prof. David B. Phillips (DBP), and me. The contributions of each person were as follows: DBP conceived the idea for the project and developed it with all other contributors. CKM performed all experiments and data analysis, with support from DBP. SARH derived the physical adjoint optimisation method and the objective functions investigated here. DBP and PdH conceived the time-averaged TM method. I performed simulations of the various iterative wavefront optimisation approaches, with guidance from DBP and SARH. The numerical results presented in the coming chapter were generated using code written by me, and compared with results from a code provided by SARH to ensure validity of the results. Special thanks to SARH and Dr. James Capers, for their help in the derivations of the discrete dipole approximation and the constraints on dipole polarizability.

## Chapter 2

# Dynamic scattering media and existing wavefront shaping methods

MUCH research has been done in the field of wavefront shaping, specifically with the aim of unscrambling scattered light. A challenging, yet mostly unaddressed problem, is that of moving scattering media. Existing methods begin to fail once the scattering material changes its properties at a rate faster than those changes can be characterised. This is because these existing methods were designed to control light propagation within static scattering media.

Here, an edge case between fully dynamic media and fully static media is considered. What if, embedded within a largely static scattering medium, there existed a pocket of dynamic material? In this chapter, existing methods are explored for this edge case of partially dynamic scattering material.

## 2.1 Background information

### 2.1.1 Discrete dipole approximation

Many methods exist to simulate the phenomenon of scattering. The work for this chapter was simulated using the *discrete dipole approximation* (DDA) [79, 80] in two dimensions. This approach turns the problem of multiple scattering and absorption of electromagnetic waves by particles of arbitrary geometry and composition into a system of linear equations. This approach can be used to model much larger objects by considering them to be periodic arrangements of individual dipoles. In the simulations presented here, the scattering of light by random configurations of dipoles is considered to investigate how light can be manipulated in such general multiply scattering systems.

To derive the equations used to apply the DDA to such configurations of dipoles, we follow the derivation provided by SARH.

First, we consider the Helmholtz equation, which can be derived from Maxwell's equations (see Appendix A), assuming that we are in a uniform and static material in time and space. The incident electric field $\phi$ at every point can be written as the the sum of a scattered field (the field scattered by the combination of dipoles) and an applied field (the field as if no dipoles existed in the space) at each of those points, yielding

$$\left[\nabla^2 + k_0^2\right]\phi = \left[\nabla^2 + k_0^2\right](\phi_\mathrm{s} + \phi_0) \tag{2.1}$$

where $\nabla^2$ denotes the Laplacian, $k_0$ is the wavevector, and the incident electric field $\phi$ is separated into the scattered field $\phi_s$ and the applied field $\phi_0$.

Recognizing that $\left[\nabla^2 + k_0^2\right]\phi_0 = 0$ to satisfy the free space Helmholtz equation, this can be simplified to

$$\left[\nabla^2 + k_0^2\right]\phi = \left[\nabla^2 + k_0^2\right]\phi_\mathrm{s}. \tag{2.2}$$

Treating each of the $n$ dipoles as a source, the inhomogeneous Helmholtz equation (see Appendix A) for an assortment of $n$ dipoles can also be written as

$$\left[\nabla^2 + k_0^2\right]\phi = -k_0^2 \sum_{n=1}^{N} \alpha_n \delta(x - x_n)\phi_\mathrm{inc}(x_n) \tag{2.3}$$

where $\phi_\mathrm{inc}$ is the field incident on each dipole, $\alpha_n$ and $x_n$ are the polarizability and location of the $n^\mathrm{th}$ dipole, respectively, and $\delta(x - x_n)$ is a Dirac delta function centred at the $n^\mathrm{th}$ dipole location $x_n$. Therefore, comparing Equations 2.2 and 2.3,

$$\left[\nabla^2 + k_0^2\right]\phi_\mathrm{s} = -k_0^2 \sum_{n=1}^{N} \alpha_n \delta(x - x_n)\phi_\mathrm{inc}(x_n). \tag{2.4}$$

The Green's function as a solution to the Helmholtz equation is described by

$$\left[\nabla^2 + k_0^2\right]G(x, x_n) = \delta(x - x_n). \tag{2.5}$$

$G(x, x_n)$ is described in 2D by

$$G(x, x_n) = \frac{1}{4i}\mathrm{H}_0^{(1)}(k_0|x - x_n|) \tag{2.6}$$

where $\mathrm{H}_0^{(1)}(k_0|x - x_n|)$ is the Hankel function of zeroth order and first kind. This Green's function describes circular waves emanating from a point. This is exactly what we need here to describe the source field from point sources and the multiply scattered field by arrangements of scattering dipole.

From Equations 2.4 and 2.5, the field scattered by the combination of dipoles $\phi_s$ is given by

$$\phi_s = -k_0^2 \sum_{n=1}^{N} \alpha_n G(x, x_n)\phi_\mathrm{inc}(x_n) \tag{2.7}$$

where $G(x, x_n)$ is the Green's function describing the field at point $x$ due to the $n^\mathrm{th}$ dipole located at $x_n$.

To account for multiple scattering, the applied field on the $m^{\text{th}}$ dipole is the sum of the incident field and the field scattered by each of the other dipoles, giving

$$\phi_{\text{inc}}(x_m) + k_0^2 \sum_{n\neq m} \alpha_n G(x_m, x_n)\phi_{\text{inc}}(x_n) = \phi_0(x_m). \tag{2.8}$$

The polarisability $\alpha$ of a dipole is found using

$$p = \alpha\phi \tag{2.9}$$

describing the relation between the dipole moment $p$ and the electric field $\phi$. This equation can be extended to the $n^{\text{th}}$ dipole in a system and written as

$$p_n = \alpha_n \phi_{\text{inc}}(x_n). \tag{2.10}$$

This equation allows the polarisability of all dipoles to be solved for, and subsequently the applied field everywhere can be found.

$$\phi_0(x_m) = \frac{p_m}{\alpha_m} + k_0^2 \sum_{n\neq m} G(x_m, x_n) p_n \tag{2.11}$$

Equations 2.7 and 2.11 can then be used to calculate the total electric field everywhere, incorporating the multiple scattering from each of the dipoles.

### Constraints on the dipoles' polarisability

The acceptable values of polarisability of the dipoles are dictated by conservation of energy. To derive the constraints for these values, start from Poynting's theorem, which describes the electromagnetic power flow into a differential volume:

$$-\nabla \cdot \mathbf{S} = \mathbf{J} \cdot \mathbf{E} + \mathbf{J}_h \cdot \mathbf{H} \tag{2.12}$$

where $\mathbf{S}$ is the Poynting vector, $\mathbf{J}$ is the electric current, $\mathbf{E}$ is the electric field, $\mathbf{J}_h$ is the magnetic current, and $\mathbf{H}$ is the magnetic field.

Alternatively,

$$-\nabla \cdot \mathbf{S} = \frac{\partial}{\partial t}(u_e + u_h) + (w_e + w_h) \tag{2.13}$$

where $u_e$ and $u_h$ are the energy stored in the electric and magnetic fields, respectively, and $w_e$ and $w_h$ are the energy dissipated by those same fields. Time averaging Equations 2.12 and 2.13 yields an equation for the time-averaged dissipation of energy by a material [81]:

$$\langle w_e \rangle = \langle \mathbf{J} \cdot \mathbf{E} \rangle = \frac{\omega}{2}\epsilon_0 \ \text{Im}\left[\epsilon\right] \ \text{Im}\left[E\right]^2 \tag{2.14}$$

where $\omega$ is the frequency, $\epsilon_0$ is the vacuum permittivity, and $\epsilon$ is the relative permittivity. Recalling that

$$\epsilon = 1 + \chi \tag{2.15}$$

where $\chi$ is the susceptibility, it is clear that the power dissipated by the dipoles must be proportional to $\mathrm{Im}[\chi]$.

To obtain an expression for $\mathrm{Im}[\chi]$, first consider the Helmholtz equation for a system with relative permittivity $\epsilon_r = \epsilon/\epsilon_0$:

$$\left(\nabla^2 + \epsilon k^2\right)\phi = 0, \tag{2.16}$$

and substituting the susceptibility such that

$$\left(\nabla^2 + k^2\right)\phi = -k^2\chi\phi. \tag{2.17}$$

Multiplying both sides by $\phi^*$ and taking the imaginary part,

$$\mathrm{Im}\left[\phi^*\nabla^2\phi\right] + \mathrm{Im}\left[k^2|\phi|^2\right] = -k^2|\phi|^2\mathrm{Im}\left[\chi\right]. \tag{2.18}$$

The second term is purely real, so the imaginary part vanishes. The first term can be expanded using a vector calculus identity:

$$\begin{aligned}\nabla\cdot\left(\phi^*\nabla\phi\right) &= \phi^*\nabla^2\phi + \left(\nabla\phi^*\right)\cdot\left(\nabla\phi\right) && (2.19)\\ &= \phi^*\nabla^2\phi + |\nabla\phi|^2. && (2.20)\end{aligned}$$

The final term here is real, and the imaginary part vanishes. With this,

$$-\nabla\cdot\mathrm{Im}\left[\phi^*\nabla\phi\right] = k^2|\phi|^2\mathrm{Im}\left[\chi\right], \tag{2.21}$$

which can be rearranged to find an equation for $\mathrm{Im}[\chi]$.

To go further, note that the incident and scattered fields obey the free-space and inhomogeneous Helmholtz equations respectively:

$$\begin{aligned}\left(\nabla^2 + k^2\right)\phi_0 &= 0 && (2.22)\\ \left(\nabla^2 + k^2\right)\phi_s &= -\delta(x)k^2\alpha\phi_0(0). && (2.23)\end{aligned}$$

Adding these gives

$$\left(\nabla^2 + k^2\right)\phi = -\delta(x)k^2\alpha\phi_0(0), \tag{2.24}$$

where $\phi = \phi_0 + \phi_s$. The total field from a single dipole scatterer is

$$\phi = \phi_0 - k^2\alpha G(x)\phi_0. \tag{2.25}$$

Multiplying Equation 2.24 by $\phi^*$:

$$\phi^* \nabla^2 \phi + k^2 |\phi|^2 = -\delta(x) k^2 \alpha \phi_0(0) \phi^*. \tag{2.26}$$

Now Equation 2.25 can be used to write

$$\phi^* = \phi_0^* \left(1 - \alpha^* k^2 G^*(0)\right). \tag{2.27}$$

Taking the imaginary part of Equation 2.26 and substituting Equation 2.27 into the right hand side (RHS) yields

$$-\mathrm{Im}\left[\phi^* \nabla \phi\right] = \delta(x) k^2 |\phi_0|^2 \mathrm{Im}\left[\alpha + |\alpha|^2 k^2 G(0)\right], \tag{2.28}$$

where $\mathrm{Im}[G^*(0)] = -\mathrm{Im}[G(0)]$ was used.

Assuming the power flow into the scatterer is positive (at best the flow in equals the flow out, at worst much less comes out), the following equation constrains the imaginary part of the polarizability, $\alpha$, of a dipole:

$$\mathrm{Im}[\alpha] > -|\alpha|^2 k_0^2 \mathrm{Im}[G(0)] \tag{2.29}$$

The simulations in this thesis are for 2D propagation, such that

$$\mathrm{Im}[G(0)] = \mathrm{Im}\left[\frac{1}{4i} \mathrm{H}_0^{(1)}(0)\right] = -\frac{1}{4} \tag{2.30}$$

and so

$$\mathrm{Im}[\alpha] > \frac{1}{4} |\alpha|^2 k_0^2 \tag{2.31}$$

For lossless particles, the inequality is saturated, and writing $\alpha = |\alpha| \exp(\mathrm{i}\theta)$ results in

$$\sin\theta = \frac{1}{4} |\alpha| k_0^2. \tag{2.32}$$

In practice, if the maximum physically allowable polarisability is to be used, this would result in the following equations:

$$|\alpha| = \frac{4}{k_0^2} \tag{2.33}$$

$$\mathrm{Im}(\alpha) = \arcsin\left(\frac{|\alpha|\, k_0^2}{4}\right) \tag{2.34}$$

$$\alpha = |\alpha| \exp\left[i\ \mathrm{Im}(\alpha)\right]. \tag{2.35}$$

For the numerical results presented in this chapter, the maximum physically allowable polarisability of each dipole is used to simulate the most extreme cases of scattering. To investigate a lower scattering scenario, $|\alpha|$ will be set to $0.4k_0^{-2}$, i.e. 10% of this maximum value.

### Example implementation of the discrete dipole approximation

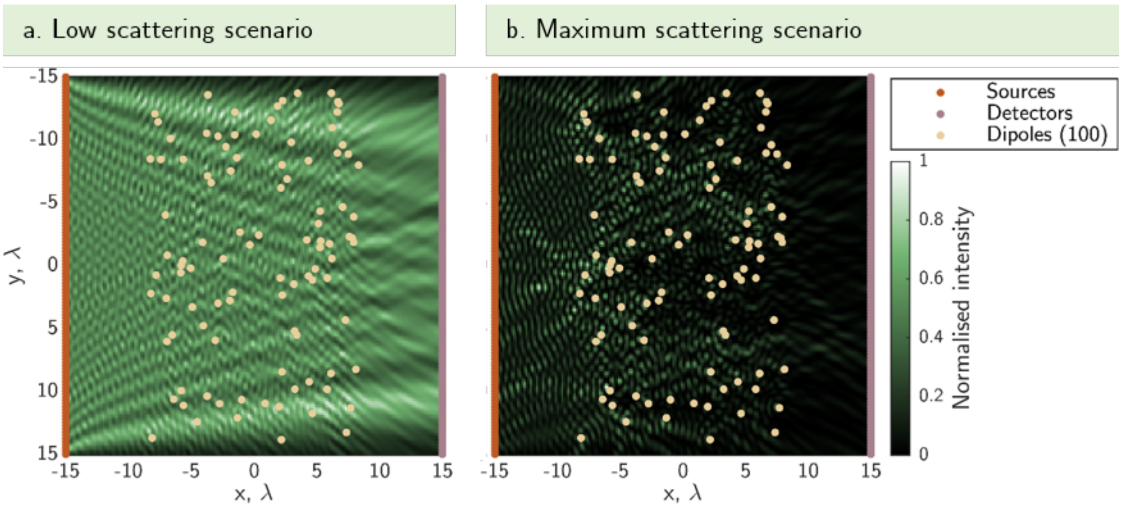

Figure 2.1: **Example results of applying the discrete dipole approximation to a randomly configured scattering region of 100 dipoles.** The sources emit circular waves, and are all in phase with each other; the source field is effectively a plane wave incident from the left. (a) Low scattering scenario where $|\alpha| = 0.4k_0^{-2}$. (b) High scattering limit where $|\alpha| = 4k_0^{-2}$.

An example of the scattering of an incident plane wave induced by a random configuration of 100 dipoles is shown below in Figure 2.1 for low and high scattering scenarios. The wavelength of the simulations is set to $\lambda = 1$ for simplicity, and the size dimensions normalised to wavelengths for ease of interpretation. The size of the simulations shown in Fig. 2.1 are $30 \times 30$ wavelengths, sampled at 6 points per wavelength for a total simulation grid size of $180 \times 180$ pixels at which the field needs to be calculated. At minimum 4 points per wavelength are required to accurately sample the area.

The sources act as individual circular wave point sources – such an array of sources can approximate a plane wave – in fact represent a truncated plane-wave (i.e. one with edges where diffraction takes place) – if all sources emit a circular wave with the same initial phase and amplitude. The detectors are located on the opposite side of the scattering region from the sources, and, as with the sources, separated by a distance of $\lambda/4$ to ensure accurate sampling of the field.

The dipoles are randomly located within the simulation area, and the sources and detectors are separated by a distance of $\lambda/4$ to ensure accurate sampling of the field. The locations of the dipoles are determined using MATLAB's *rand()* function and normalising the outputs, which by default are numbers between 0 and 1, to values determined by the simulation area. The simulation results in the subsequent sections of this chapter will be presented in the same layout: a line of sources on the left incident on some scattering region and a line of detectors on the right.

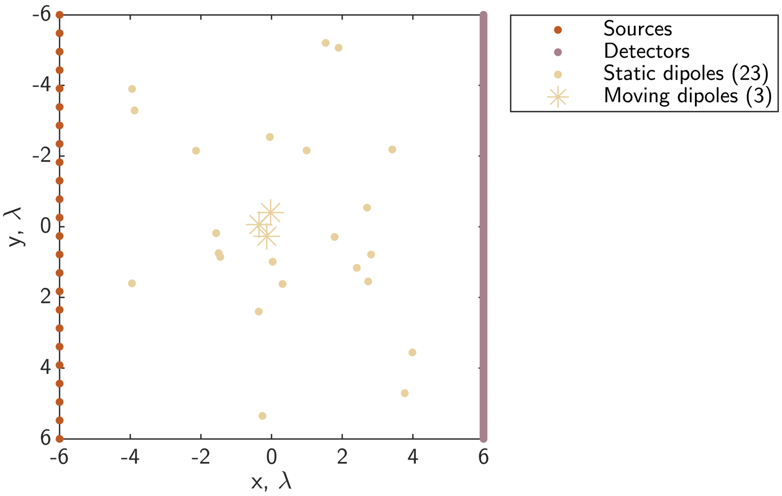

FIGURE 2.2: **Example of a randomly configured scattering region with a pocket of moving dipoles.**

The low scattering and high scattering scenarios shown in Fig. 2.1 will be used in the next chapter to investigate how different methods of finding wavefronts that navigate around moving scatterers perform in these two scenarios.

Additionally, to investigate the novel area of partially moving scattering media, some of the dipoles are allowed to move. For example, a pocket of scatterers within a given region of the medium can be allowed to randomly move, such as those indicated by yellow asterisk markers in Fig. 2.2. The movement of these dipoles is generated using a normal distribution of random $xy$-positions, centred on the initial positions, and with an adjustable standard deviation which limits the total area explored by the dipoles. Fig. 2.3

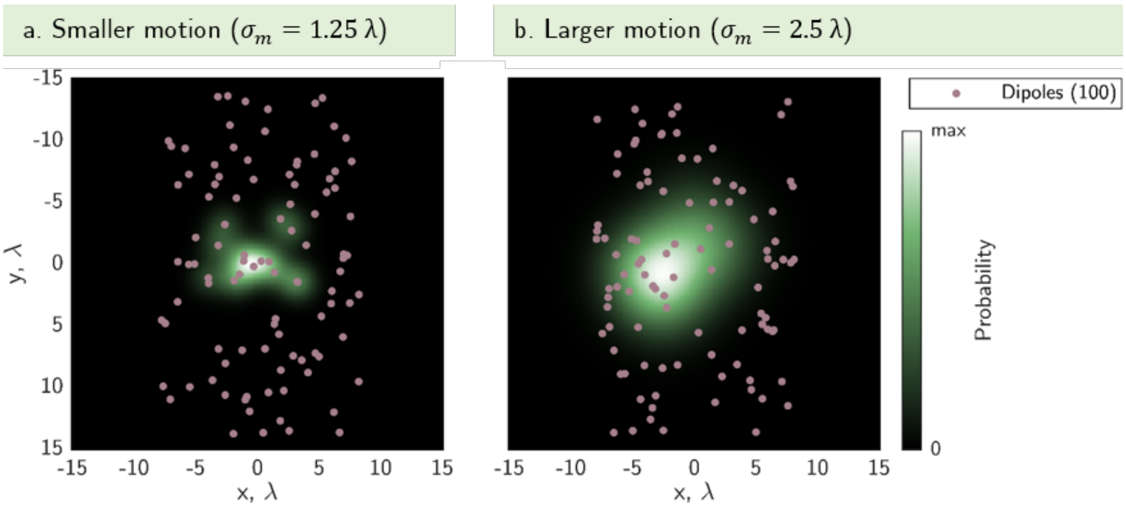

FIGURE 2.3: **Example of position probabilities for a pocket of 15 randomly moving dipoles inside a dynamic pocket within a static configuration of 100 total dipoles** (a) with a standard deviation of motion $\sigma_m = 1.25\lambda$ and (b) $\sigma_m = 2.5\lambda$.

shows an example of the probability heatmap of the positions of example moving scatterers for the two levels of movement considered later on with standard deviations $\sigma_m = 1.25\lambda$ and $\sigma_m = 2.5\lambda$. Different snapshots in time of the dipole locations are referred to as dipole configurations in the coming sections.

### 2.1.2 Quantifying intensity fluctuations

The movement of a scattering material changes the path that incident light fields travel through the medium. This results in fluctuations of the transmitted intensity, which is used in this work to provide feedback on how an electromagnetic field interacts with a partially dynamic scattering medium.

To quantify the level of fluctuation due to the motion of a scattering medium, the ratio $\xi$ is introduced:

$$\xi = \frac{\overline{\sigma_{\sqrt{I}}}}{\bar{I}} \ . \tag{2.36}$$

This is the ratio of $\overline{\sigma_{\sqrt{I}}}$, the mean standard deviation of the field amplitude at the detectors over time, over $\bar{I}$, the mean total intensity at the detectors over time. In the simulations presented here, $\overline{\sigma_{\sqrt{I}}}$ is calculated by calculating the standard deviation of the field amplitude at each detector location over time and then averaging this result over all detector locations. $\bar{I}$ is calculated by averaging the intensity at the detectors over all time and detector locations.

Initially, the ratio of the mean standard deviation of the intensity at the detectors over the mean intensity at the detectors was suggested to quantify fluctuations. However, due to a happy accident in forgetting to raise the amplitude of the field to the power of two, I discovered that the above ratio was a better objective function in the novel methods presented in a Chapter 3. The level of fluctuations $\xi$ is minimised in less time and the resulting wavefront shaped fields transmit more average intensity than if the ratio of the standard deviation of the intensity over time and the average intensity is used to quantify the fluctuations. We believe that the reason for this can be illustrated by rewriting Eqn. 2.36 as

$$\xi = \frac{\overline{\sigma_{\sqrt{I}}}}{\overline{\sqrt{I}}} \frac{1}{\overline{\sqrt{I}}} \tag{2.37}$$

where it becomes clear that this objective function is weighted towards the denominator, so it will more favorably find fields that increase the average transmitted intensity that reaches the detectors.

The goal of the coming sections is to minimise $\xi$, thereby minimising the fluctuations of the intensity of the field at the detector locations due to the motion of pockets of dipoles in a region of scattering dipoles.

## 2.2 Existing approaches to wavefront shaping applied to dynamic scattering media

Scattered light can be unscrambled. Information can be recovered from scattered light in many different ways. Here, existing techniques are applied to the previously unaddressed problem of partially dynamic scattering media.

### 2.2.1 Phase conjugation

It has been shown experimentally that digital optical phase conjugation (DOPC) can be used to create an arbitrary field [19–24, 82], such as a focus, through a strongly scattering material. DOPC relies on the principle of the reciprocity of light propagation [30], meaning that light is transmitted from point A to point B in the same way as the reverse path from point B to point A. Because of this principle, a known limit of the technique of DOPC is that it doesn't perform as well for high and multiple scattering scenarios where good amounts of the light emanating from the sources do not reach the detectors.

In practice, DOPC involves the creation of an exact copy of a detected field, but travelling in the opposite direction back to the initial source location. Mathematically two plane waves $\psi_a$ and $\psi_b$, propagating in opposite directions, can be written as

$$\psi_a = A\exp\left(-i\mathbf{k}\cdot\mathbf{x}\right) \tag{2.38}$$

$$\psi_b = A\exp\left(i\mathbf{k}\cdot\mathbf{x}\right) \tag{2.39}$$

where $A$ is the amplitude of the waves, $\mathbf{k}$ is the wave vector, and $\mathbf{x}$ is the position. These two plane waves are simply the phase conjugate of one another. This is the basis of DOPC.

In 2D simulation, the DOPC process involves generating the desired field distribution (such as a focus) on the line of detectors, and propagating this field through the scattering region backwards (from right to left). The scattered field reaching the line of sources is calculated, phase conjugated, and then propagated through the scattering region forwards (from left to right). In the results presented here, the desired field distribution on the line of detectors are three foci at different locations.

To illustrate the effect of partially dynamic scattering media on an existing wavefront shaping technique, phase conjugation was combined with the above described DDA simulations to model the propagation of light through a region of randomly configured scattering dipoles containing a dynamic pocket.

Fig. 2.4 shows three such light fields forming foci at three distinct locations in the low scattering scenario, where the polarisability $\alpha$ is low (10% the physically allowable maximum value). For all three foci, optical phase conjugation successfully reconstructed the desired intensity distribution at the line of detectors. In this limit, movement inside the dynamic pocket (indicated by the circled dipoles) does not have a significant impact on the formed field.

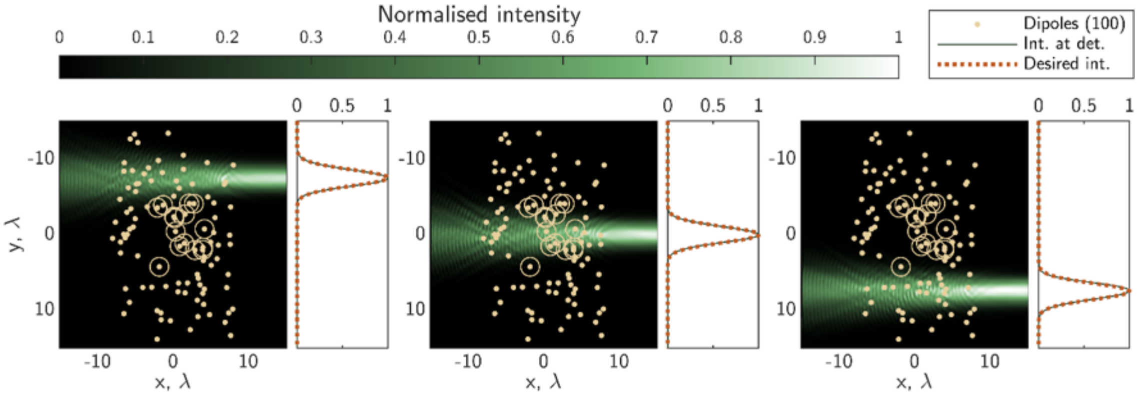

FIGURE 2.4: **Optical phase conjugation in the low scattering scenario.** Three foci are formed at different locations on the detector side (right) of the simulation. Here, the polarisability of the dipoles is $|\alpha| = 0.4k_0^{-2}$, which is 10% of the maximum physically allowable value. The circled dipoles are allowed to randomly move.

Fig. 2.5 shows the results for applying optical phase conjugation to create the same three foci as above in Fig. 2.4 in the limit of high scattering. In this case, unlike above, the fields fail to form a clean focus that is stable with the motion of the dynamic dipoles. The proportion of intensity that is transmitted through the scattering region is much lower, and it is necessary to saturate the heatmap (see Fig. 2.5b) to identify the focus.

Fig. 2.5c shows the fluctuations of the intensity of the field at the line of detectors as the pocket of dynamic dipoles moves in time. The movements of the dipoles are described by normal distributions centred on their initial location, with a standard deviation of $2.5\lambda$. The $x$ axis of the heatmaps corresponds to a different configuration of the dipoles (i.e. different snapshots in time), and the $y$ axis corresponds to the line of detectors. The focus created in the middle of the line of detectors is most heavily impacted by the movements. Intuitively, the simplest path for the light to take to form a focus in the middle of the line of detectors is through the centre of the simulated area, which is also where the dynamic dipole pocket is located in this scenario.

This approach to wavefront shaping does not use any information to selectively navigate light through a scattering region. This method presents an example of existing techniques failing to address the problem of partially dynamic scattering media. If scattering is weak, then the contribution from the scattered light is low and in in this case digital phase conjugation is mainly accounting for free-space diffraction. If scattering is strong, then the dipole positions become important because the contribution from the scattered light is high. To counteract the motion of the dynamic dipoles, phase conjugation would need to be performed at the rate of the motion of the dipoles to form a stable output field. In terms of experimental implementation, this approach typically requires access to and control over the wavefront on both sides of the scattering region. This isn't feasible for applications such as imaging inside biological tissue, where one only has access to one side of the scattering material.

a. Creating foci using optical phase conjugation

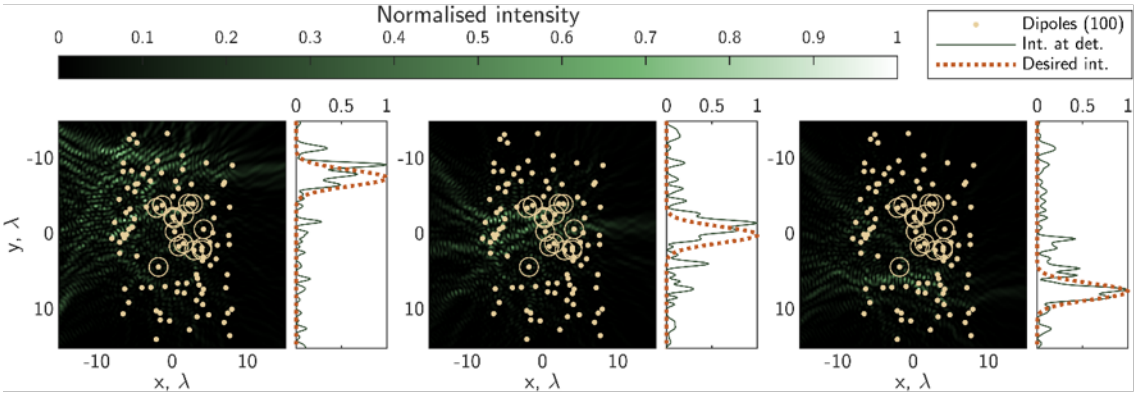

b. Saturated intensity heatmaps showing foci created using optical phase conjugation

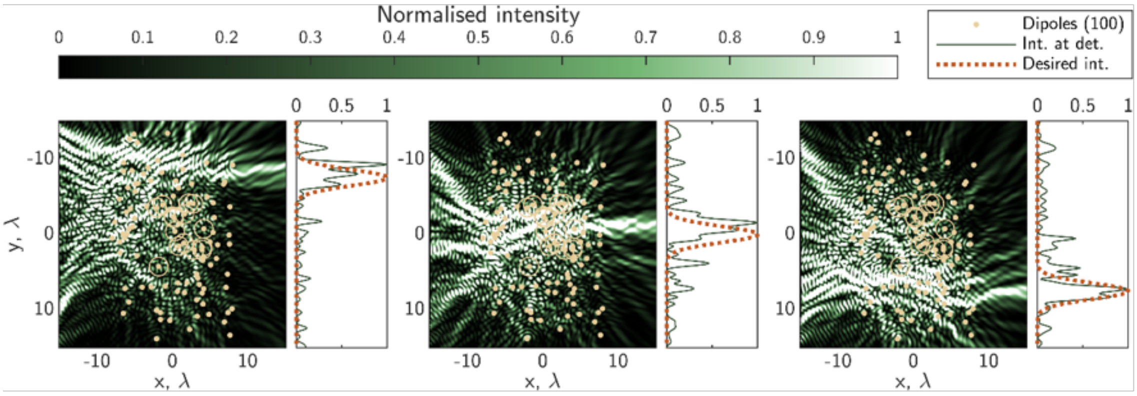

c. Effect of pocket of moving dipoles on created foci

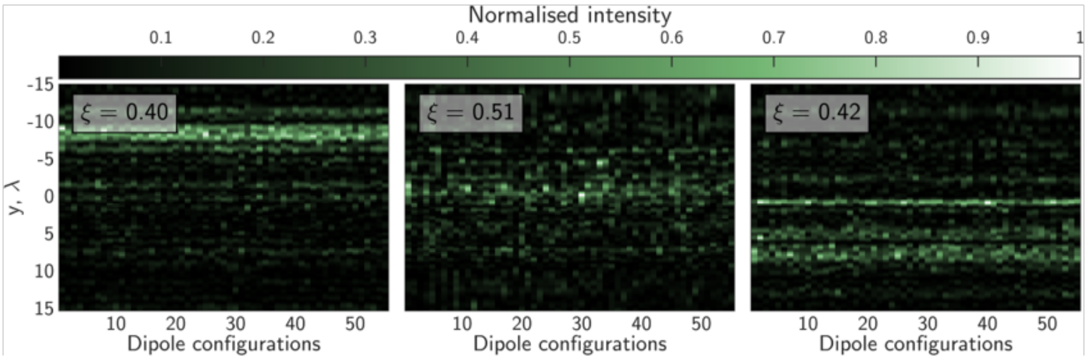

FIGURE 2.5: **Optical phase conjugation through a partially dynamic scattering region in the high scattering limit.** (a) Three foci are formed at different locations on the detector side (right) of the simulation. Here, the polarisability of the dipoles is $|\alpha| = 4k_0^{-2}$, the maximum physically allowable value. (b) Saturated plots from (a), showing the focus. (c) Fluctuations of the intensity at the detectors as the dynamic dipoles (circled) move. Dipole configurations here are equivalent to time (variations in the locations of the dipoles).

### 2.2.2 The transmission matrix

Elastic scattering is a deterministic and linear process. It can be described using the language of linear algebra, such that the entire scattering process is encapsulated in a matrix. Several such matrices exist - they are discussed in this and coming sections. These matrix formulations are helpful tools across many applications, enabling researchers to gain insight into the scattering process.

One such matrix is the *transmission matrix* (TM), $\mathcal{T}$, which provides information about how an incident field is transmitted through a scattering medium. It is a subset of the full scattering matrix, $S$, which is discussed in the next section. $\mathcal{T}$ can be defined as

$$\mathbf{u} = \mathcal{T}\mathbf{v} \ . \tag{2.40}$$

Here $\mathbf{v}$ is the incident field and $\mathbf{u}$ is the transmitted field that has interacted with the medium. This matrix was first measured in coherent optics by Popoff et al. in 2010 [25], and has since been used to characterize multimode fibres [26], determine the multispectral transmission matrix [83], or demonstrate endoscopic imaging through a single multimode optical fibre [84].

Following from Eqn. 2.40, the input field $\mathbf{v}$ needed to form a desired transmitted field $\mathbf{u}$ can be determined mathematically by inverting $\mathcal{T}$:

$$\mathbf{v} = \mathcal{T}^{-1}\mathbf{u} \ . \tag{2.41}$$

To illustrate the limitations of this approach, we simulate the performance of the TM under partially dynamic scattering conditions. The input wavefront is expressed in the pixel basis (though, in principle, any orthogonal complete set of modes would work). A vector of length $n_s$ containing complex numbers defining the amplitude and phase of each of the $n_s$ sources becomes the incident field $\mathbf{v}$. To build the TM, each source is turned on individually, and the resulting transmitted field on all of the $n_d$ detectors is recorded as vector $\mathbf{v}$ of length $n_d$. Each one of these individual vectors becomes one column of the $n_d \times n_s$ transmission matrix.

Once $\mathcal{T}$ has been calculated, Eqn. 2.41 can be used to determine the input field $\mathbf{u}$ needed to form a focus (or other arbitrary field) through the scattering material. Because the matrix is not necessarily square or unitary ($n_d$ need not equal $n_s$), $\mathcal{T}^{-1}$ can be found using the pseudo-inverse. In MATLAB, the pseudo-inverse of a matrix can be calculated in several different ways including performing a singular value decomposition, or approximated with the conjugate transpose of the TM (*ctranspose()* in MATLAB) assuming $\mathcal{T}$ is close to unitary. This assumption holds if most of the light reaches the detectors (i.e. the light is not lost/scattered away).

The choice of inverse impacts the performance of this method. Choosing the conjugate transpose for the inverse of the TM is suitable in the low scattering scenario. Indeed, this is identical to the method of optical phase conjugation described in the previous section. Here, the singular value decomposition is used instead of calculating the inverse.

### Singular value decomposition to find the inverse transmission matrix

A matrix can be factorized into the product of three matrices:

$$A = U\Sigma V^* \tag{2.42}$$

where matrices $U$ and $V$ act as basis transformation matrices from a given coordinate system to singular vector coordinates, and $\Sigma$ is a diagonal matrix with the singular values $\sigma_i$ on its diagonal. The asterisk indicates the conjugate transpose.

To then find the inverse of $A$, calculate

$$A^{-1} = V\Sigma^{-1}U^* \tag{2.43}$$

where $\Sigma^{-1}$ is found by taking the reciprocal of all non-zero elements of $\Sigma$.

An important detail with this method of calculating the inverse in the case of the TM is how low-valued singular values are dealt with. If all singular values of the TM are used to construct the inverse TM, a desired field can be formed optimally at the cost of low total power in the desired field. The trade-off between the quality of the transmitted field and the total power in the field must be considered whenever this approach is used.

One way to adjust this balance between field quality and power is included in MATLAB's *pinv()* pseudo-inverse function, which allows the inclusion of a tolerance. This sets all singular values below the tolerance to zero – effectively ignoring the contributions of the corresponding singular vectors. Another similar way to adjust this balance is to manually determine how many singular values are to be included in calculating the inverse TM, which is done in the next section to illustrate this method's application.

### Using the inverse transmission matrix

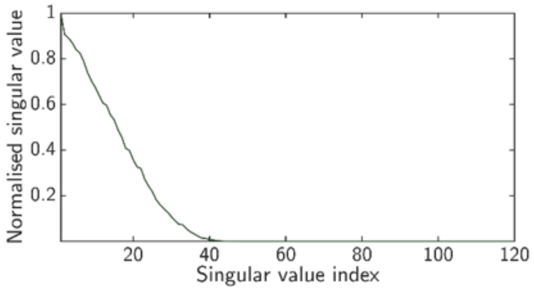

FIGURE 2.6: **Normalised singular values of a transmission matrix.** Higher singular values correspond to singular vectors which are transmitted through the scattering region with more power.

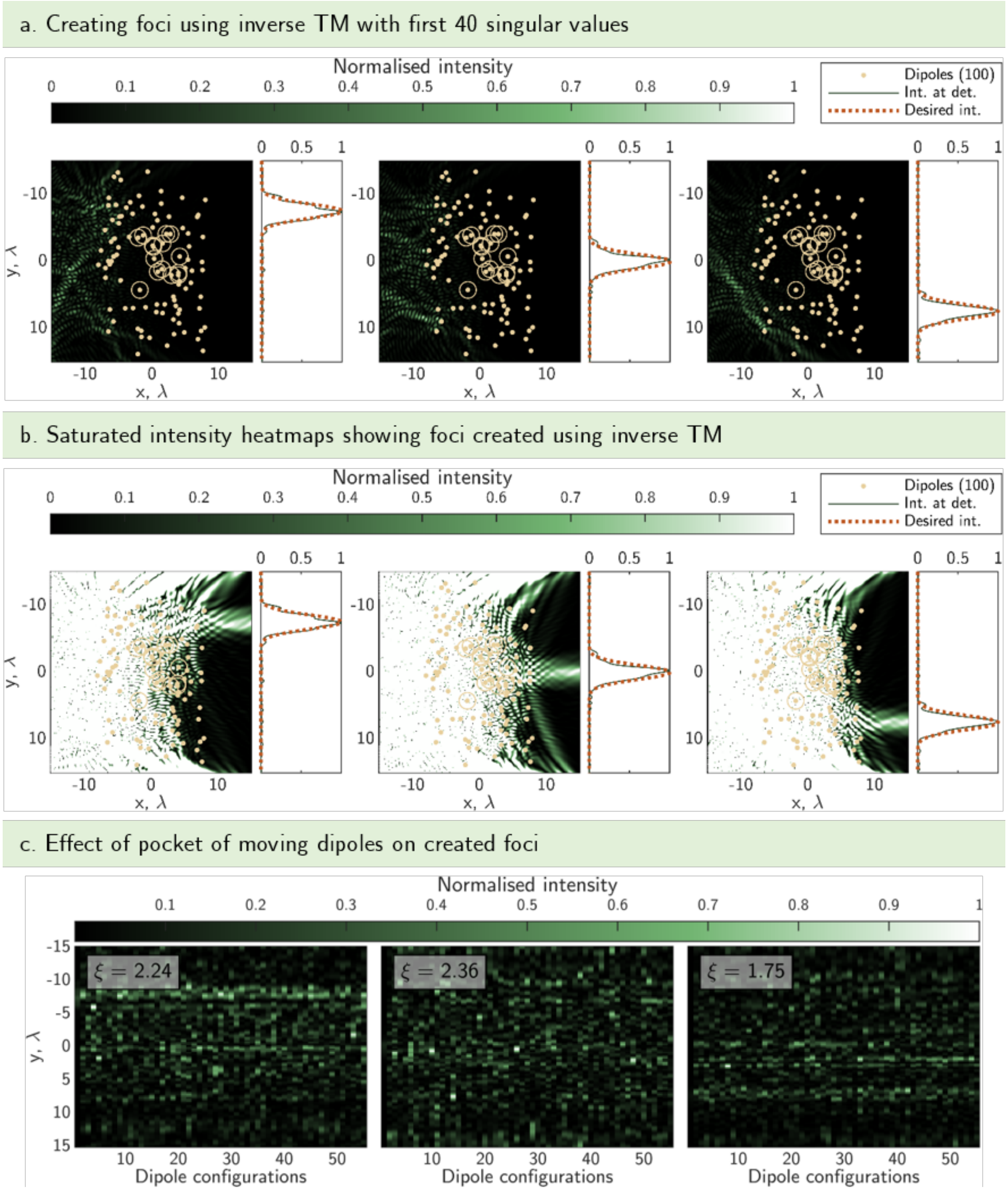

FIGURE 2.7: **Applying the inverse transmission matrix constructed with the first 40 singular values for focusing through a partially dynamic scattering region in the high scattering limit.** (a) Heatmaps of the intensity through the scattering dipole region, and lineplots showing the desired intensity (dashed red line) and the achieved intensity (solid dark green line) at the detectors. (b) Saturated heatmaps from (a). (c) Fluctuations of intensity at detectors for movement of pocket of dipoles. Dipole configurations here are equivalent to time (variations in the locations of the dipoles).

Fig. 2.6 shows an example of sorted normalised singular values of a simulated TM for a specific configuration of 100 dipoles. The largest values indicate the singular vectors with the largest transmitted power through the scattering dipole region.

To investigate the application of the transmission matrix method to the problem of partially dynamic scattering media, the transmission matrix whose singular values are shown in Fig. 2.6 and its corresponding dipole configuration were probed in more detail.

Fig. 2.7 shows the results of using the first 40 singular values to construct the inverse TM, which is in turn used to focus onto three locations on the line of detectors, as was done in the previous section by applying the technique of optical phase conjugation. The intensity heatmaps and line plots in Fig. 2.7a show the creation of precisely the desired field on the detectors. Fig. 2.7b show the same results, this time normalised to the maximum intensity at the detectors, such that the focus is easily visible. If the dipoles in the dynamic pocket move, the focus disappears into fluctuating noise over time, as seen in Fig. 2.7c. The movements of the dipoles are described by normal distributions centred on their initial location, with a standard deviation of $2.5\lambda$. With this it is clear that the wavefront found using the inverse transmission is extremely sensitive to the precise configuration of a scattering system.

Fig. 2.8 shows the same results, this time using the first 20 singular values to construct the inverse TM. Here, the resulting intensity distributions resemble those found using optical phase conjugation in the high scattering limit in Fig. 2.5. The quality of the focus is lower, with increased noise, when compared to the case of the inverse TM constructed from the first 40 singular values in Fig. 2.7.

As discussed above, although the TM can be successfully used in experiment to both create and practically use light that has propagated through static scattering media, its performance decreases if the medium is no longer completely static. As above with optical phase conjugation, this approach does not enforce that the generated wavefront should avoid dynamic pockets within the scattering material. Therefore, as expected this existing tool does not provide a good solution to the problem of finding light fields that navigate through partially moving scattering systems.

### 2.2.3 The scattering matrix

The *scattering matrix*, $S$, provides all of the information needed to determine how an incident field will interact with a given scattering medium, detailed in [85]. $S$ can be described mathematically as

$$\mathbf{u} = S\mathbf{v} \tag{2.44}$$

where $\mathbf{u}$ is the scattered field (reflected and transmitted parts) and $\mathbf{v}$ is the field incident on the scatterer.

Although this is not experimentally measurable in many scenarios – especially those in which the light is not purely forward scattered – $S$ is a powerful mathematical tool.

a. Creating foci using inverse TM with first 20 singular values

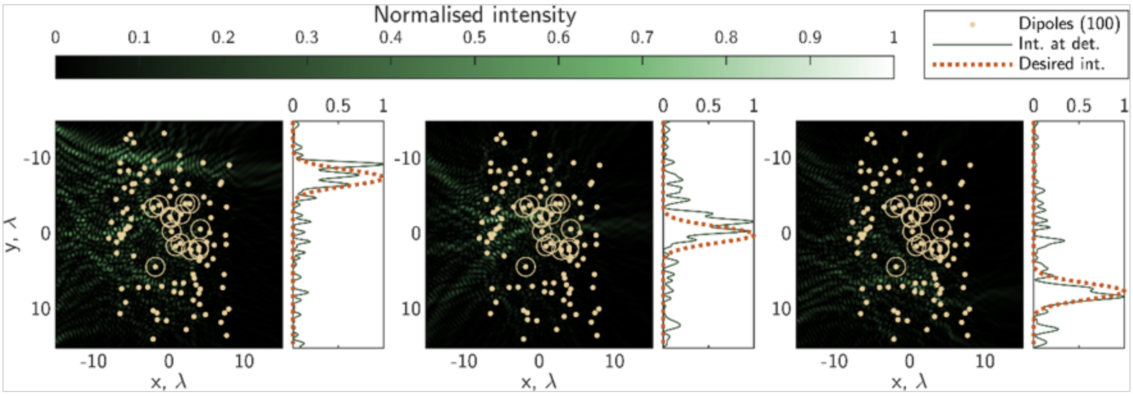

b. Saturated intensity heatmaps showing foci created using inverse TM

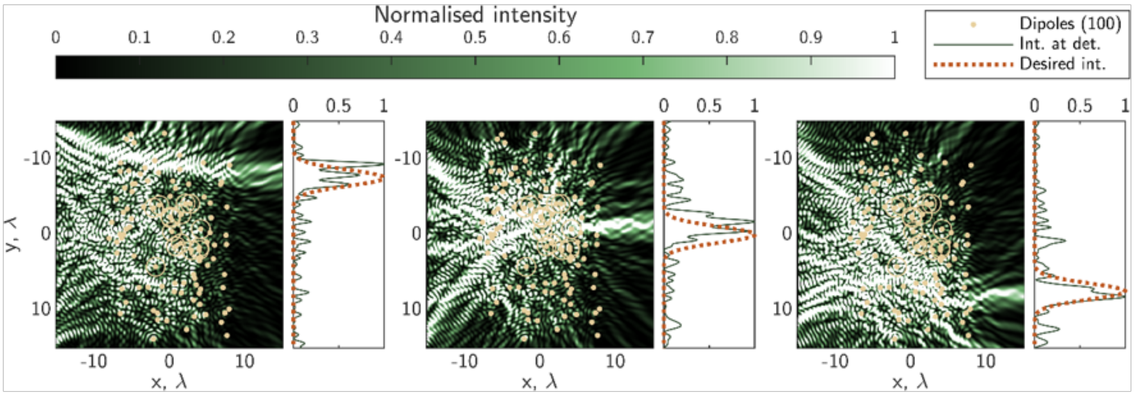

c. Effect of pocket of moving dipoles on created foci

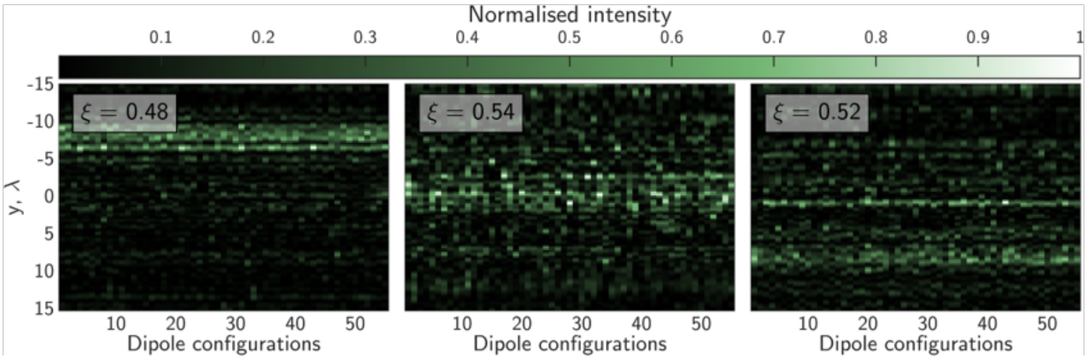

FIGURE 2.8: **Applying the inverse transmission matrix constructed with the first 20 singular values for focusing through a partially dynamic scattering region in the high scattering limit.** (a) Heatmaps of the intensity through the scattering dipole region, and lineplots showing the desired intensity (dashed red line) and the achieved intensity (solid dark green line) at the detectors. (b) Saturated heatmaps from (a). (c) Fluctuations of intensity at detectors for movement of pocket of dipoles. Dipole configurations here are equivalent to time (variations in the locations of the dipoles).

In the next section, it is used to find light fields that specifically focus onto or avoid a specific location within a scattering medium.

### 2.2.4 Generalized Wigner-Smith Operator

The Generalized Wigner-Smith (GWS) operator provides an existing approach to manipulating incident wavefronts specifically to target certain points within scattering environments [86]. In this section, we investigate a new approach using the GWS operator. Previous work on applications of GWS operator only moved a single degree of freedom of a single particle. Therefore the behavior of the operator in scenarios where multiple particles are moved simultaneously is not yet well understood, and we explore how well the GWS operator would work if we randomly move multiple particles as in a dynamic pocket of dipoles. Although it was not specifically designed for this situation, the GWS operator's application to partially dynamic scattering systems is investigated and offers a promising route to investigating these types of systems.

The GWS operator, $Q_\alpha$ is defined as

$$Q_\alpha = -iS^{-1}\frac{dS}{d\alpha}, \tag{2.45}$$

where $S$ is the scattering matrix and $\alpha$ is a configurational degree of freedom of the system of interest. For the work presented here, $\alpha$ will be a spatial degree of freedom (e.g. $x$, $y$, or $z$). This operator has its roots in the quantum mechanics time-delay operator by Wigner and Smith [87, 88], where $\alpha = \omega$ (the frequency), such that the eigenvalues of $Q_\omega$ provide the so-called "proper time delays" – the time delay between a mode entering and exiting a system. Ambichl et al. generalised the operator in [89] to that shown above in Eqn. 2.45.

In the same way that the eigenvalues of the time-delay operator $Q_\omega$ provide information about the time delays experienced by the corresponding eigenstates, the eigenvalues of the generalised operator $Q_\alpha$ provide information about the conjugate variable of $\alpha$ in the system described by the matrix $S$ due to a given eigenstate. For example, $Q_x$ provides information about the fields which impart momentum $p_x$ (and consequently force $F_x = dp_x/dt$) on the system, and the eigenstate corresponding to the largest eigenvalue of $Q_x$ imparts the most momentum (and force).

Intuitively, the field that imparts the most momentum $p_x$, given by the eigenstate of $Q_x$ with the largest eigenvalue, will also focus the most light into the system. Alternatively, the field that imparts the least momentum will focus the least light into the system. Our hope in applying the GWS to an arrangement of dipoles such as that shown in Fig. 2.2 is that eigenstates will be found that focus the least light into the dynamic pocket, thereby minimising the interaction of the incident wavefront with the moving dipoles, and subsequently minimising the fluctuations of the intensity at the detectors.

For a system such as those considered in this chapter, calculating $Q_\alpha$ involves replacing the derivative in Eqn. 2.45 with a finite difference:

$$Q_\alpha = -iS^{-1}\frac{\Delta S}{\Delta \alpha}. \tag{2.46}$$

This is necessary because no analytical derivative of the scattering matrix with respect to $\alpha$ is readily available in experiment. Because the aim of the analysis here is to investigate the practical (experimental) applications of existing methods, including the GWS operator, this is important.

Furthermore, to calculate this difference, three measurements of $S$ are needed:

$$Q_\alpha = -iS_0^{-1}\frac{S_{\Delta\alpha/2} - S_{-\Delta\alpha/2}}{\Delta \alpha}. \tag{2.47}$$

Here $S_0$ is the scattering matrix with the moving dipoles in their initial position, and $S_{\pm\Delta\alpha/2}$ are the scattering matrices with the dipoles displaced from these initial positions by $\pm\Delta\alpha/2$.

Implementing this expression with the DDA simulations used in this chapter involves approximating the scattering matrix to be the transmission matrix, such that the expression used here to determine the GWS operator in simulation is given by

$$Q_\alpha = -i\mathcal{T}_0^{-1}\frac{\mathcal{T}_{\Delta\alpha/2} - \mathcal{T}_{-\Delta\alpha/2}}{\Delta \alpha}. \tag{2.48}$$

In contrast to existing investigations of the GWS operator, here a new situation is explored. To determine how the random motions of dipoles influence the behavior of the GWS operator, $\alpha$ becomes $r$ here, which describes the individual random motions of each single dipole within the dynamic pocket. Each dipole is allowed to make 3 random movements as described above, and the transmission matrix for each of these three configurations is calculated. These three matrices are then used to calculate $Q_r$.

Decomposing $Q_r$ into its eigenvectors and eigenvalues reveals information about the force in the $r$ direction, $F_r$, exerted by the field onto the moving dipoles. Intuitively this does not have a clear meaning because $r$ is random movement of multiple dipoles, but it is expected that the lowest value eigenvalues still correspond to fields that interact least with the dynamic pocket.

Each of the eigenvectors of $Q_r$ contain the amplitude and phase of the individual sources, which is propagated through the entire scattering region. A propagated eigenvector field will be called an eigenfield in this thesis for brevity. The eigenfields are ordered from largest eigenvalue magnitude to smallest.

For the low scattering scenario, where the polarisability of the dipoles used is $|\alpha| = 0.4k_0^{-2}$ (10% of the maximum allowable value), approximating the scattering matrix with the transmission matrix works well. Fig. 2.9 shows intensity heatmaps for 8 of the 120

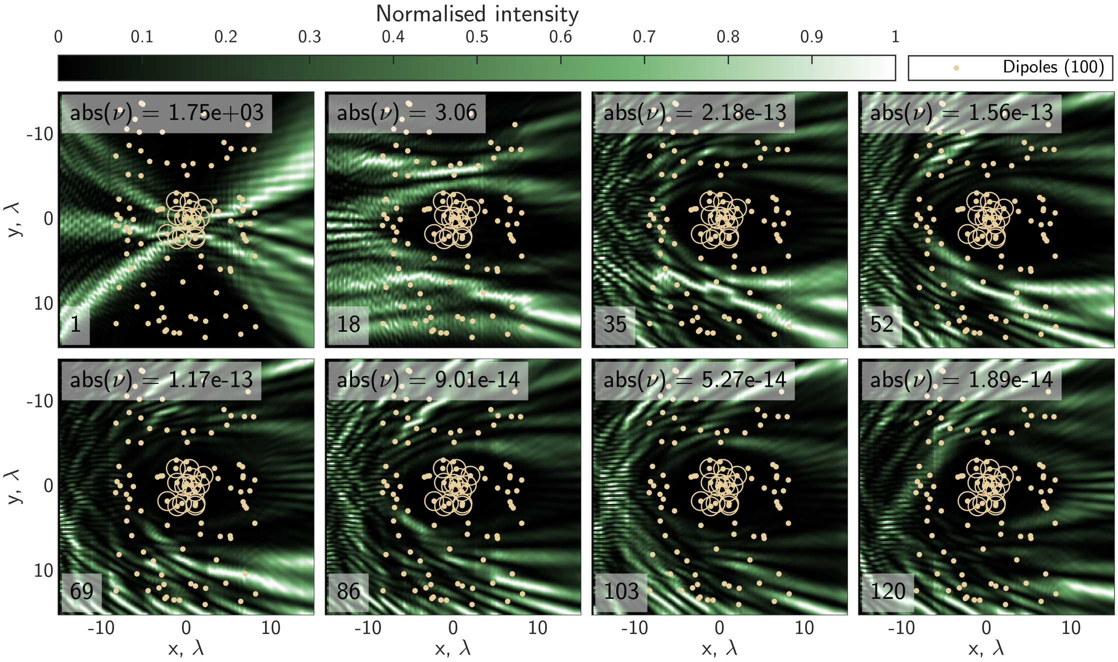

FIGURE 2.9: **Intensity heatmaps showing eigenfields of $Q_r$ for 100 randomly configured scattering dipoles in the low scattering scenario** where $|\alpha| = 0.4k_0^{-2}$ (10% of maximum value). The moving dipoles are circled. The magnitude of each eigenvalue is included in the top left of each heatmap. The indices of the eigenvalues are included in the bottom left of each heatmap.

eigenfields of $Q_r$ for this configuration of 100 dipoles. These plots are roughly representative of the trends seen in all 120 eigenfields. The index of the eigenvalue is included in the bottom left corner of each heatmap. The magnitude of the eigenvalue, abs($\nu$), is included in the top left corner. As before, the yellow dots indicate dipole locations, and the circled yellow dots are the moving dipoles. The same information is replotted on a log scale to emphasize the regions of the eigenfield with the lowest intensity in Fig. 2.10.

For eigenvalue 1 of $Q_r$, which is the largest magnitude eigenvalue, the corresponding eigenfield forms a focus onto the region containing the majority of the moving dipoles. Intuitively, this agrees with the fact that this field will impart the largest force $F_x$ on the pocket of moving dipoles. For all other eigenvalue indices (8-120), the field dances around the pocket of moving dipoles. These eigenfields impart less and less force on the moving scatterers for decreasing eigenvalue magnitude (increasing eigenvalue index).

In addition to finding fields that navigate around pockets of moving dipoles, it is useful for the transmitted intensity to be as high as possible – this is useful for potential future applications, such as imaging. Fig. 2.11 investigates the intensity transmitted to the detectors, as well as the levels of fluctuations quantified by the standard deviation and the ratio $\xi$, for all eigenfields of $Q_r$. The solid light red line shows that for increasing eigenvalue index, the mean intensity reaching the detectors decreases dramatically. The solid light green line shows the mean of the standard deviation of the intensity at the detectors

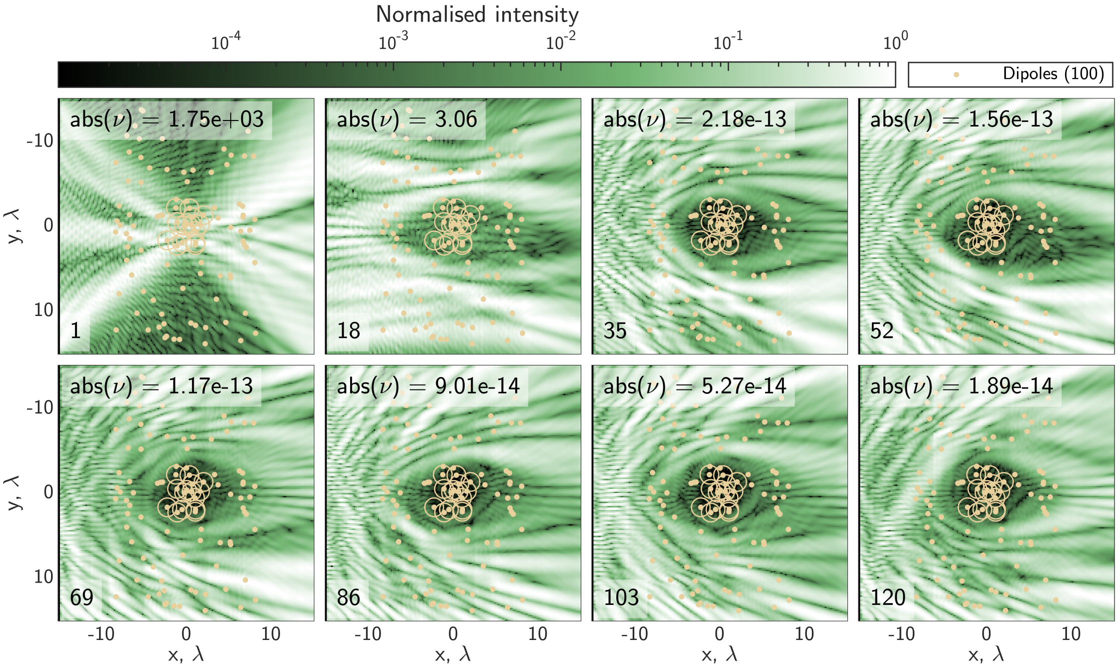

FIGURE 2.10: **Log scale intensity heatmaps showing eigenfields of $Q_r$ for 100 randomly configured scattering dipoles in the low scattering scenario** where $|\alpha| = 0.4k_0^{-2}$ (10% of maximum value). The moving dipoles are circled. The magnitude of each eigenvalue is included in the top left of each heatmap. The indices of the eigenvalues are included in the bottom left of each heatmap.

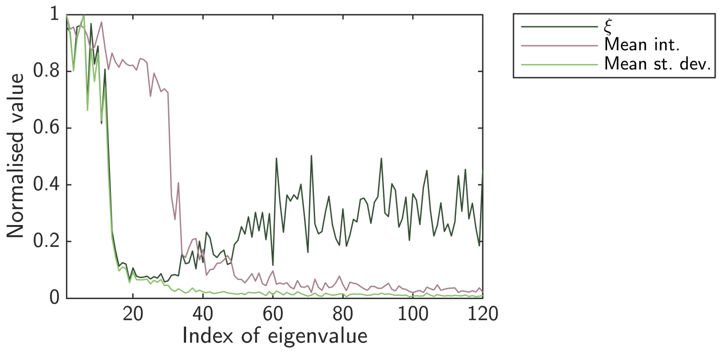

FIGURE 2.11: **Performance of the eigenfields of $Q_r$ for 100 dipoles in the low scattering scenario.** Here $\alpha = 0.4k_0^{-2}$ (10% of maximum). The normalised lines indicate $\xi$ (dark green), mean intensity (light red), and mean standard deviation (light green) of the intensity at the detectors.

over 55 time steps/configurations of the moving pocket of dipoles. The solid dark green line plotting $\xi$ for all eigenvalues, which clearly shows the trade-off occurring between the intensity and the standard deviation. This plot is normalised to show the relative differences in the values plotted. Only ~15 out of the 120 total eigenfields (roughly, indices 20-35) decrease the mean standard deviation of the intensity over time while simultaneously transmitting approximately the same amount of intensity to the detectors.

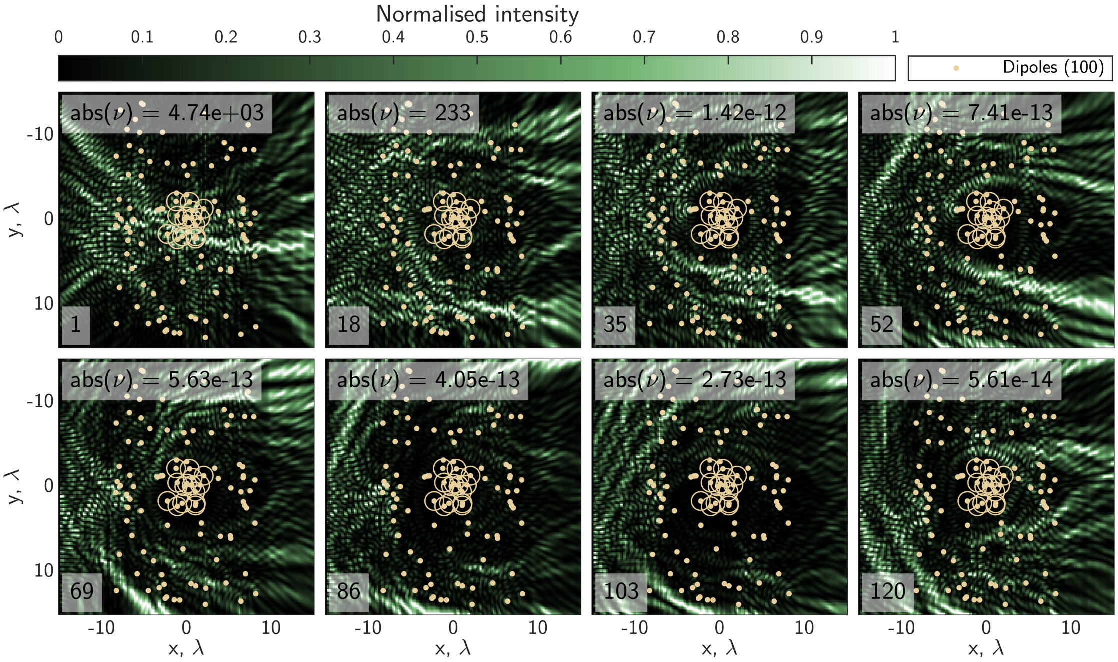

FIGURE 2.12: **Intensity heatmaps showing eigenfields of $Q_r$ for 100 randomly configured scattering dipoles in the high scattering limit** where $|\alpha| = 4k_0^{-2}$ (the maximum value). The moving dipoles are circled. The magnitude of each eigenvalue is included in the top left of each heatmap. The indices of the eigenvalues are included in the bottom left of each heatmap.

Next, the high scattering limit is considered in the same way as above. $Q_r$ for 100 randomly configured dipoles is calculated, this time with $\alpha = 4k_0^{-2}$ (the maximum physically allowed value). Fig. 2.12 and Fig. 2.13 show 8 of the 120 eigenfields for $Q_r$ on a linear and log scale, respectively. It is less obvious that the lower magnitude eigenvalues steer around all of the moving scatterers, as was seen above in Fig. 2.9. Here, the shaped fields need to not only avoid the region containing the moving dipoles themselves, but also avoid exciting all of the static dipoles in a way that causes the multiply scattered waves from these dipoles to constructively interfere onto and therefore excite the moving dipoles.

As above for the low scattering scenario, the mean intensity, standard deviation, and $\xi$ at the detectors were calculated to get a better picture of the performance of each eigenfield in the high scattering limit. Fig. 2.14 shows these normalised results. In contrast to the low scattering scenario, fewer fields exist that decrease $\xi$ by simultaneously decreasing the mean standard deviation of the intensity at the detectors and increasing (or at least maintaining) the mean intensity at the detectors.

In summary, although it is possible to find fields that thread light around pockets of moving dipoles in these scenarios, there are no constraints on what the intensity at the detectors must look like for the eigenfields. The simplest solution to minimising the

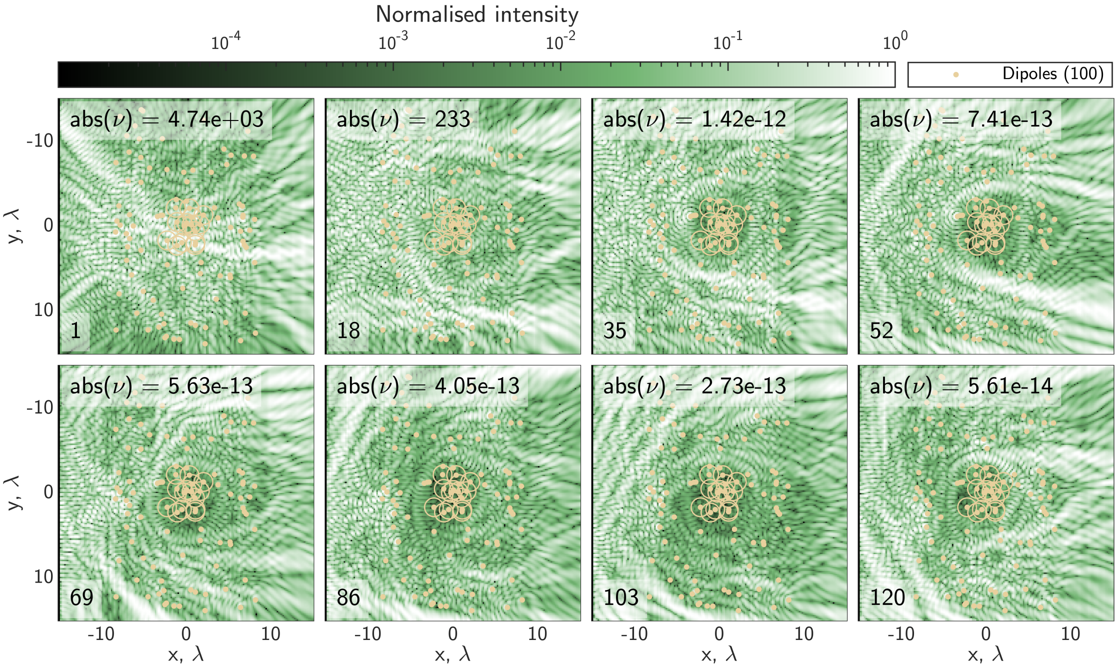

FIGURE 2.13: **Log scale intensity heatmaps showing eigenfields of $Q_r$ for 100 randomly configured scattering dipoles in the high scattering limit** where $|\alpha| = 4k_0^{-2}$ (the maximum value). The moving dipoles are circled. The magnitude of each eigenvalue is included in the top left of each heatmap. The indices of the eigenvalues are included in the bottom left of each heatmap.

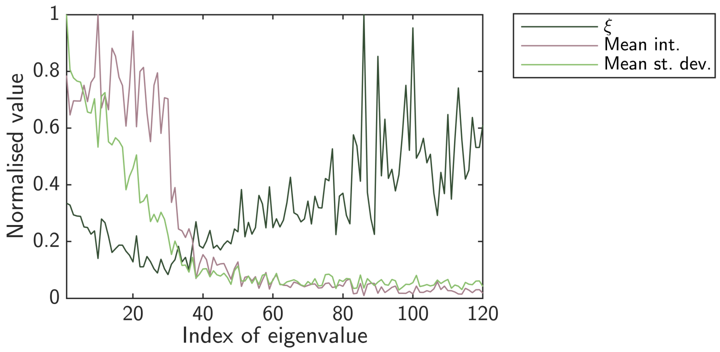

FIGURE 2.14: **Performance of the eigenfields of $Q_r$ for 100 dipoles in the high scattering limit.** Here $\alpha = 4k_0^{-2}$ (the maximum value). The normalised lines indicate $\xi$ (dark green), mean intensity (light red), and mean standard deviation (light green) of the intensity at the detectors.

interaction with the moving scattering pockets is to reduce the intensity everywhere – including the detectors. This result is clearly visible in the mean intensity at the detectors of the fields corresponding to the smallest magnitude (largest index) eigenvalues in both the low scattering and high scattering scenarios, such that only a small percentage of the total intensity reaches the detectors. Therefore, these eigenfields may not be useful for applications, such as imaging through dynamic scattering media, which rely on information extracted by probing the far side of a scattering system with light.

Furthermore, approximating $S$ with the TM works well for the low scattering case (low polarisability, $\alpha$, of scattering dipoles). For higher amounts of scattering, however, the transmission matrix and therefore the approximated GWS operator approach do not perform as well.

Another limitation of this method is that determination of the full scattering matrix in experiment is very challenging, if not impossible. Even for the simulations presented here, not all of the light is incident on the detectors – this means that the full scattering matrix is not captured, and the calculated matrix is not actually unitary. This issue is clearly seen in the decrease in performance of the GWS operator eigenfields for the high scattering case. Experimentally then, it is most feasible to apply this operator in the low scattering scenario. However, even in this limit, this method requires knowledge of, access to, and control over the moving dipoles.

An additional difficulty that the GWS operator faces in experimental implementation is that the entire scattering or transmission matrix needs to be calculated quickly (at speeds far exceeding scattering motion). In order to build the derivative of the scattering matrix in Equation 2.45, we need to measure an entire scattering or transmission matrix while the moving pockets are essentially stationary, and repeat this 3 times for 3 different configurations of scatterers. Measuring full scattering or transmission matrices in short times is challenging and already a major bottle-neck in wavefront shaping techniques based on these matrices. This strongly reduces the viability of the GWS approach for real applications.

### 2.2.5 Deposition matrix

Another existing method that uses a wavefront shaping based approach to generating fields that target certain points within scattering environments is the deposition matrix. It was recently introduced as a way to deposit energy into a specified area within a scattering region in waveguide experiments in [90]. Bender et al. defined the deposition matrix $Z$ as

$$Z_{mn} \equiv [\epsilon(y_m, z_m)A/M]^{1/2} E_n(y_m, z_m), \tag{2.49}$$

where $A$ is the deposition area uniformly sampled by $M$ points, $(y_m, z_m)$ gives the location of the $m$th sampling point, and $\epsilon$ is the dielectric constant.

Calculating the deposition matrix $Z$ and taking the eigenvalues and eigenvectors of $Z^\dagger Z$ provides input wavefronts given by the eigenstates that deposit energy equal to the magnitude of the eigenvalues into the targeted region. Eqn. 2.49 can be interpreted as stating that the deposition matrix $Z$ can be calculated by determining the transmission matrix to every point within the desired deposition area in a scattering region and normalising by the factor in square brackets in the equation.

Intuitively, this approach can be understood as determining the fields that deliver the most energy $e$ to a region which is proportional to the following:

$$e \propto E_n^\dagger(y_m, z_m)E_n(y_m, z_m) = E_{\text{in}}^\dagger \mathcal{T}^\dagger \mathcal{T} E_{\text{in}} \tag{2.50}$$

where the transmission matrix describes the transformation from input field $E_{\text{in}}$ to the field at a location within the deposition area $E_n(y_m, z_m)$ via

$$E_n(y_m, z_m) = \mathcal{T} E_{\text{in}}. \tag{2.51}$$

The fields within the deposition area are excited by the input eigenfields of $Z^\dagger Z$, ordered in terms of how much energy they deliver to the output plane (given by the magnitude of the corresponding eigenvalue) – thus revealing internal fields that minimally interact with the deposition area containing the time-varying parts of the medium. This seems like a promising approach to the problem of finding light fields that avoid a desired area in a scattering region as long as the field in that region can be probed.

This recently developed method is investigated in coupled dipole simulations, as described previously. Here, the normalising factors in Eqn. 2.49 are ignored because all that we are concerned with here is the relative amounts of energy deposited into a given area, not the absolute values.

First, the case of the forward-scattering limit is considered. For 100 randomly configured dipoles in a simulated space of dimensions 30 × 30 wavelengths, a deposition area with radius 5 wavelengths centred in the simulated region is defined. The dipoles' polarisability is set to $\alpha = 0.4k_0^{-2}$ (10% of the maximum value), and the necessary transmission matrices to each point within the deposition area are calculated. The deposition matrix $Z$ then consists of $n_s$ (number of sources) columns and $n_a$ (number of sampled points in the deposition area) rows, such that each column contains the information of how a single input mode is transformed to the field in the deposition area. Next, as described above, the matrix product $Z^\dagger Z$ is calculated, and the resulting matrix is decomposed into its eigenvectors and eigenvalues. The eigenvalues are ordered from smallest magnitude to largest, corresponding to the smallest and largest amounts of energy deposited into the deposition area, respectively.

Fig. 2.15 and Fig. 2.16 show intensity heatmaps for 8 of the 120 eigenfields of the deposition matrix in the low scattering scenario on both the linear and log scales, respectively. The eigenfields corresponding to the lowest magnitude eigenvalues completely avoid the entire scattering region. These fields deposit the least amount of light into the deposition area, as expected. The reason that these fields completely avoid the entire scattering region, and not just the deposition area, is to remove the light that would reach the deposition area through multiple scattering off of the other dipoles. Eigenfield 86 (bottom row, 2nd heatmap from left in both figures) interestingly seems to navigate completely around only the deposition area. The largest eigenvalue (eigenfield 120 – bottom row, last heatmap in both figures), on the other hand, focuses the maximum amount of light into the deposition area. Again, this is as expected because the largest magnitude eigenvalue of $Z^\dagger Z$ corresponds to the field which deposits the largest amount of energy into the deposition area.

Fig. 2.17 investigates the intensity that reaches the detectors. The normalised log scale plot reveals that the eigenfields of $Z^\dagger Z$ increase the mean intensity that reaches the detectors for increasing eigenvalue. This corresponds to an increase in the mean standard deviation of the intensity at the detectors as well. However, the intensity at the detectors increases orders of magnitude more than the standard deviation, therefore resulting in a reduction in $\xi$ for increasing eigenvalue index.

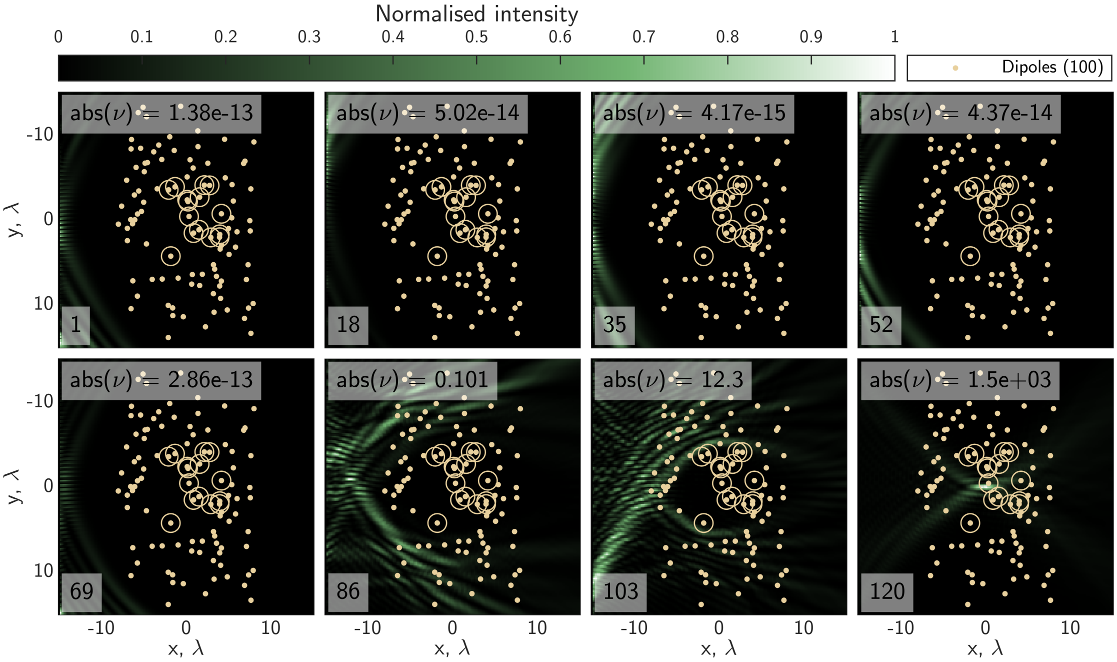

FIGURE 2.15: **Eigenfields of $Z^\dagger Z$ for 100 randomly configured scattering dipoles in the low scattering scenario** where $|\alpha| = 0.4k_0^{-2}$ (10% of the maximum value). The magnitude of the eigenvalue (top left of each heatmap) indicates the corresponding amount of energy deposition into the pocket of moving dipoles (circled) for that eigenfield. The indices of the eigenvalues are included in the bottom left of each heatmap.

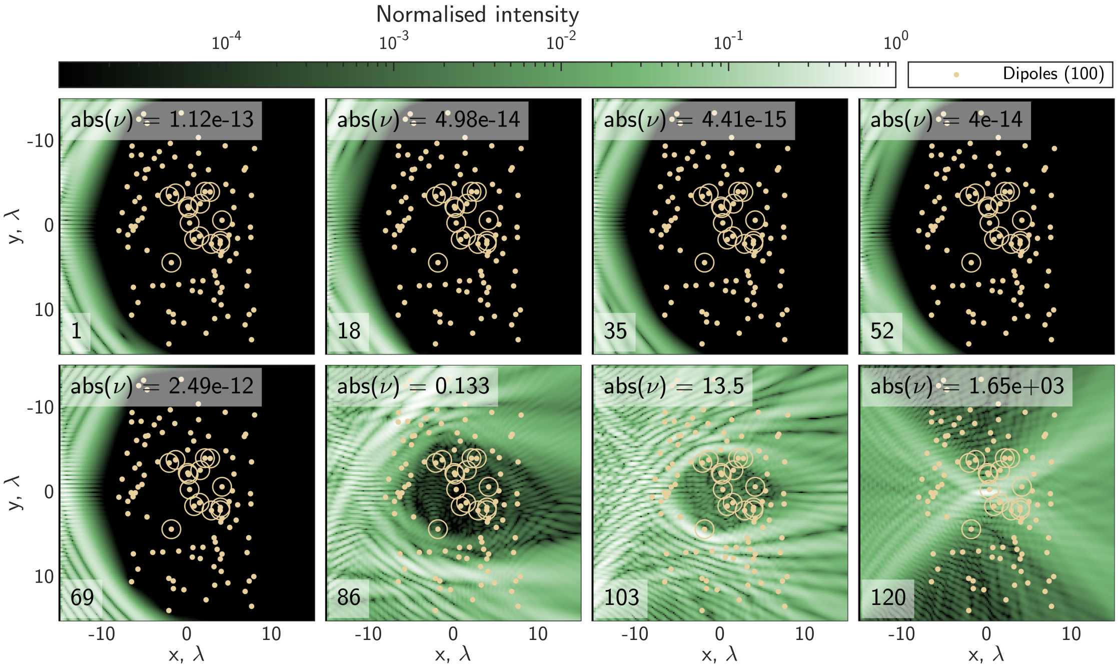

Figure 2.16: **Eigenfields of $Z^\dagger Z$ for 100 randomly configured scattering dipoles in the low scattering scenario** where $|\alpha| = 0.4k_0^{-2}$ (10% of the maximum value). The magnitude of the eigenvalue (top left of each heatmap) indicates the corresponding amount of energy deposition into the pocket of moving dipoles (circled) for that eigenfield. The indices of the eigenvalues are included in the bottom left of each heatmap.

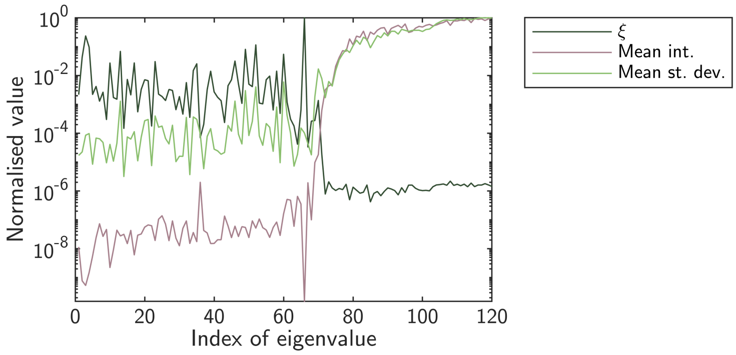

Figure 2.17: **Performance of the eigenfields of $Z^\dagger Z$ for a configuration of 100 dipoles in the low scattering scenario.** Here $\alpha = 0.4k_0^{-2}$ (10% of the maximum value). The normalised lines indicate $\xi$ (dark green), mean intensity (light red), and mean standard deviation (light green) of the intensity at the detectors.

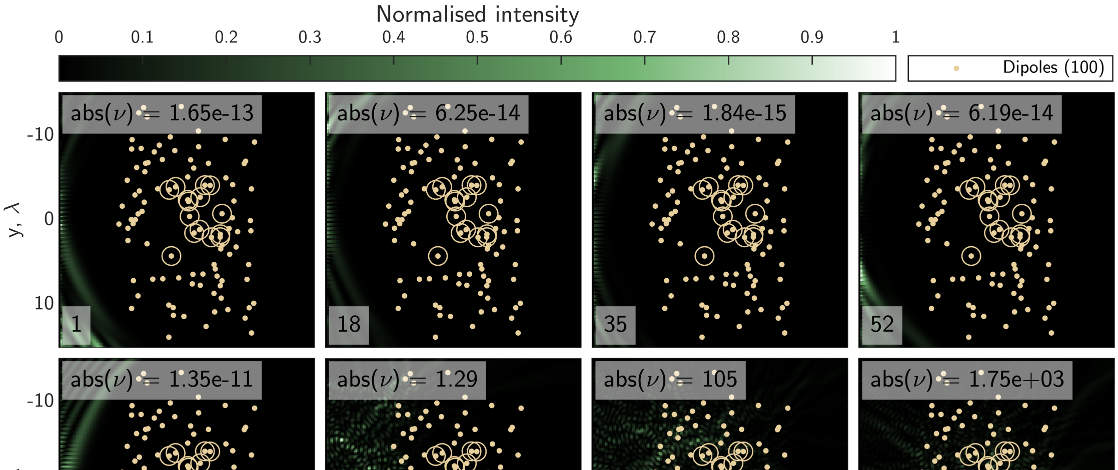

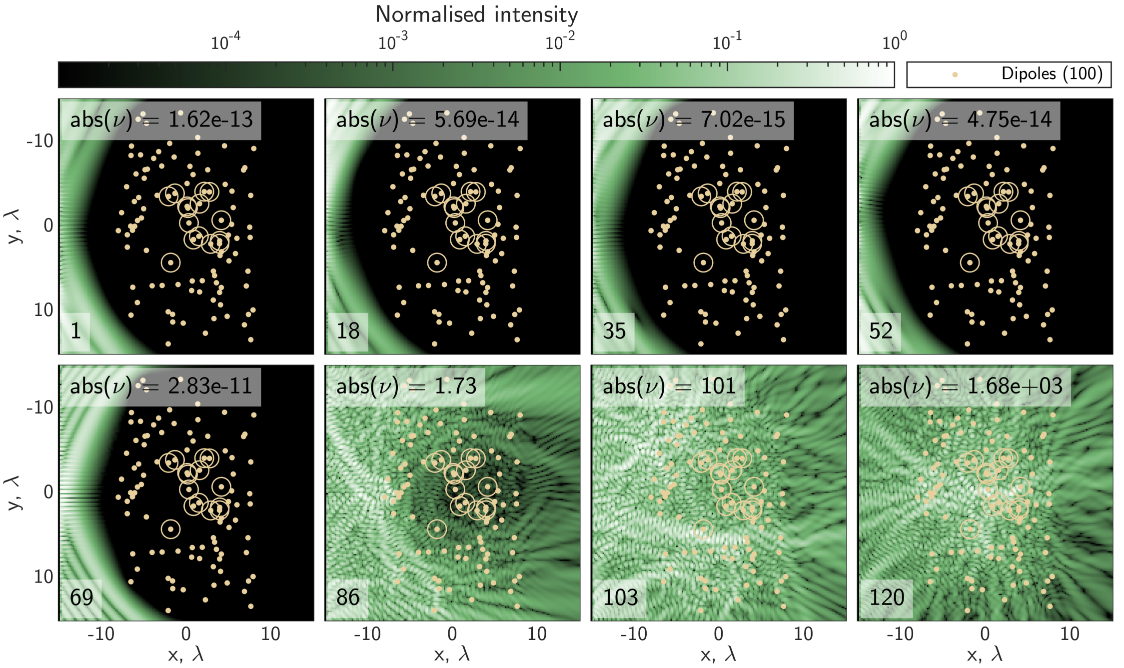

FIGURE 2.19: **Eigenfields of $Z^{\dagger}Z$ for 100 randomly configured scattering dipoles in the high scattering limit** where $|\alpha| = 4k_0^{-2}$ (the maximum value). The magnitude of the eigenvalue (top left of each heatmap) indicates the corresponding amount of energy deposition into the pocket of moving dipoles (circled) for that eigenfield. The indices of the eigenvalues are included in the bottom left of each heatmap.

Next the high scattering limit is considered for the same system of scattering dipoles. Fig. 2.18 shows 8 of the 120 eigenfields. As before, the eigenfields corresponding to the lowest magnitude eigenvalues completely avoid the scattering region. Although eigenfield 86 shows reduced intensity within the deposition area, it is not as dramatic as in the low scattering scenario shown in Fig. 2.15. Eigenfield 120, as above, focuses the light into the deposition area, therefore depositing the most energy, as anticipated.

The intensity that reaches the detectors is again analysed, this time for the high scattering limit. Fig. 2.19 shows log scale normalised plots of the mean intensity, mean standard deviation, and $\xi$ for the above describe scenario. As before, the eigenfields of $Z^{\dagger}Z$ prioritize depositing energy into the deposition area, and do not accomplish the desired task of increasing mean intensity while decreasing mean standard deviation of the intensity.

An obstacle that the deposition matrix approach faces is experimental implementation. Though possible in waveguide experiments, it is much more challenging in free-space optics to measure this matrix. Experimental implementation of the deposition matrix in such an optics experiment would prove incredibly difficult due to the necessary calculation of many transmission matrices. As mentioned in the previous section, calculating the transmission matrix is often the biggest bottleneck in an experiment. Having to calculate

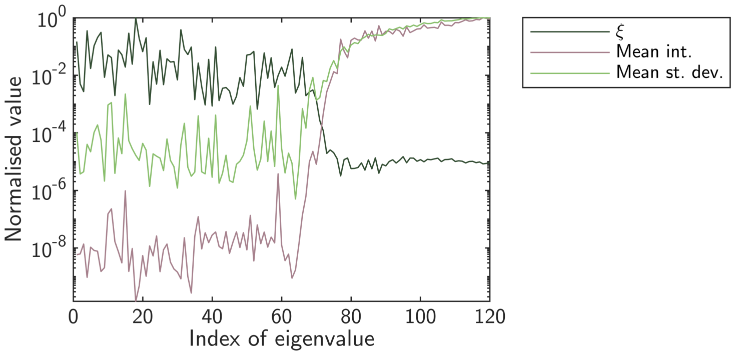

FIGURE 2.20: **Performance of the eigenfields of $Z^\dagger Z$ for a configuration of 100 dipoles in the high scattering limit.** Here $\alpha = 4k_0^{-2}$ (the maximum value). The normalised lines indicate $\xi$ (dark green), mean intensity (light red), and mean standard deviation (light green) of the intensity at the detectors.

a multitude of these transmission matrices would take an prohibitively large amount of time. Additionally, one needs access to the full field information at every point sampled in the deposition area, which would not be possible in the case of tissue, for example.

Ultimately, although the deposition matrix succeeds in finding fields that avoid a specified area in a scattering region, it seems difficult to envision its practicality in a real world scenario such as imaging through partially dynamic scattering media.

### 2.2.6 Brief conclusion on existing approaches

Although some of the methods presented in this chapter hold promise for finding light fields that carefully navigate through partially dynamic scattering media, it is clear that novel approaches are required to perform the dual objectives set out in this thesis – creating a light field that simultaneous maintains or increases the amount of intensity at the detectors while also decreasing the standard deviation of the intensity at the detectors due to the movement of pockets of dynamic dipoles. None of the methods presented so far achieve both of these objectives simultaneously.

## Chapter 3

# Novel approaches to wavefront shaping in dynamic scattering media

*The art of life lies in a constant readjustment to our surroundings.*

Kakuzo Okakura

This chapter provides a path forward in the quest to overcome the challenges posed by partially dynamic scattering media. Traditional methods have struggled to perform effectively in such complex environments, necessitating a fresh approach. Here, novel techniques are crafted specifically for the realm of partially dynamic scattering media. Wavefront shaping in the presence of dynamic scattering is a formidable challenge, and while one common solution involves speeding up the characterization of scattering materials through faster spatial light modulators (SLMs), this presents technological bottlenecks for widespread application. Instead, we venture into the uncharted territory between static and fully dynamic scattering media: partially moving scattering media. This domain features pockets of moving scatterers embedded within a predominantly static matrix of scatterers.

The motivation behind this exploration stems from a deeper examination of dynamic complex media. Many dynamic materials exhibit various decorrelation rates, potentially classifying them as partially moving scattering media if wavefront shaping techniques can operate at the pace of the slowest decorrelations. This effectively renders the slowest moving components of a dynamic scatterer as quasi-static with respect to the wavefront shaping process.

Our hope in conducting this research is to provide new tools for future technologies that enable innovation in many fields. The applications of such research extend far beyond academic research, promising breakthroughs in fields ranging from medical imaging to telecommunications, where manipulating light in complex, partially dynamic environments opens new vistas of possibility. A poignant example is found in the human body, where blood vessels carrying blood flow represent faster moving regions amidst a more slowly changing scattering material; counteracting this dynamic scattering could allow future technologies for enhanced *in vivo* medical imaging. For autonomous vehicles, imaging through dynamic scattering materials could assist in precisely navigating through challenging conditions, such as fog, rain, or snow, by providing real-time information about the environment and obstacles. The performance of free-space optical communication systems could also be enhanced, especially in adverse weather conditions, by understanding and mitigating scattering effects in dynamic atmospheric conditions.

In the preceding chapter, we introduced a performance metric denoted as $\xi$ to evaluate methods. This metric serves a dual purpose: minimizing fluctuations in detector intensity while preserving the incident light on detectors. In the current chapter, we continue to employ this metric to assess the efficacy of novel techniques. Additionally, within this chapter, we explore a range of fresh figures of merit tailored to several phase optimization algorithms. The primary objective is to guide wavefront-shaped light fields through partially dynamic scattering media while either maintaining or enhancing transmitted light levels and concurrently diminishing the standard deviation of transmitted intensity.

This chapter introduces innovative techniques, the first of which is a novel matrix operator we call the *time-averaged transmission matrix.* This matrix enables the computation of various incident wavefronts designed to circumvent the dynamic regions within partially moving scattering media. Furthermore, three novel iterative phase optimization algorithms are unveiled. The initial algorithm is a straightforward iterative phase optimizer that seeks to minimize $\xi$ in order to identify a wavefront that avoids the dynamic pocket. The subsequent two algorithms are adjoint iterative phase optimizers engineered to minimize novel figures of merit specifically designed to tackle the challenges posed by partially dynamic media. The chapter wraps up with a discussion of each approach, elucidating their respective strengths and weaknesses.

## 3.1 Time-averaged transmission matrix

Drawing inspiration from the existing wavefront shaping method of the transmission matrix, a novel matrix operator is introduced that is specifically tailored to the problem of dynamic scattering materials. The *time-averaged transmission matrix*, $\mathbf{T}_{\text{av}}$, presents an eigenvalue-based approach to a solution that provides multiple fields that carefully navigate through partially dynamic scattering materials.

This new matrix operator is developed in [91]. As the name suggests, the columns of this matrix consist of the time-averaged output field at the detectors. The intuition behind applying $\mathbf{T}_{\text{av}}$ is that, over time, the contributions of a randomly moving pocket of scatterers will average to near-zero, while the contributions of the light paths that avoid the pocket of dynamic scattering will average to constant, higher values. The information in this matrix could then be used to find fields that avoid moving scattering regions.

The total time-averaged power $P$ arriving at the detectors can be written in terms of $\mathbf{T}_{\text{av}}$ as

$$P = \mathbf{v}_{\text{av}}^{\dagger}\mathbf{v}_{\text{av}} = \mathbf{u}^{\dagger}\mathbf{T}_{\text{av}}^{\dagger}\mathbf{T}_{\text{av}}\mathbf{u}. \tag{3.1}$$

where $\mathbf{v}_{\text{av}}$ is the vectorised time-averaged field at the detectors, and $\mathbf{u}$ is the field incident on the scattering material.

Unlike the Generalized Wigner-Smith (GWS) operator and the Deposition matrix, the time-averaged transmission matrix doesn't require access to the inside of the scattering material – which often is not feasible in real optics scenarios, such as with biological tissue. Although similar concepts have been considered in the field of wireless communications [92–94], here we demonstrate the first application of this matrix in optics, and the first application to reducing temporal fluctuations in transmitted fields.

### 3.1.1 Experimental results

This approach to finding optimised wavefronts that will navigate around areas of moving scattering material is first implemented in experiment. Proof-of-principle experiments were recently uploaded in a pre-print on ArXiv [91]. These experiments were led by Dr. Chaitanya Mididoddi.

We experimentally emulate a dynamic scattering material with a cascade of phase planes separated by free-space. This type of representation has been shown to accurately simulate the scattering that occurs in the atmosphere [95–97] and multiple scattering samples [98, 99]. We implemented such a scattering scenario with an SLM and a mirror, creating a multi-pass configuration where the incident laser light is reflected multiple times between the two, incident on three separate sections of the SLM screen at each pass [99]. This experimental scatterer demonstrates this technique in the forward scattering case, where nearly all of the light that is incident on the scattering sample is transmitted to the output.

Fig. 3.1a shows a simplified schematic of the experiment: probe fields are sequentially sent through the scattering region and imaged onto a camera using off-axis digital holography [24] to recover the full complex field at the camera, where the fields are averaged to create the columns of $\mathbf{T}_{\text{av}}$. Fig. 3.1b shows the differences in eigenvalue magnitude for weak (solid red) and strong (dotted purple) fluctuations, where weak fluctuations correspond to a single small pocket such as from the slow optimisation experiment, and strong fluctuations are shown in Fig. 3.1c. Fig. 3.1d shows three snapshots in time of experimentally created transmitted eigenfields for the weakly scattering scenario at the camera from largest (left) to smallest (right) eigenvalue. The largest eigenvalue fields fluctuated very minimally, while the smallest eigenvalue fields fluctuate quite a lot. Fig. 3.1e shows

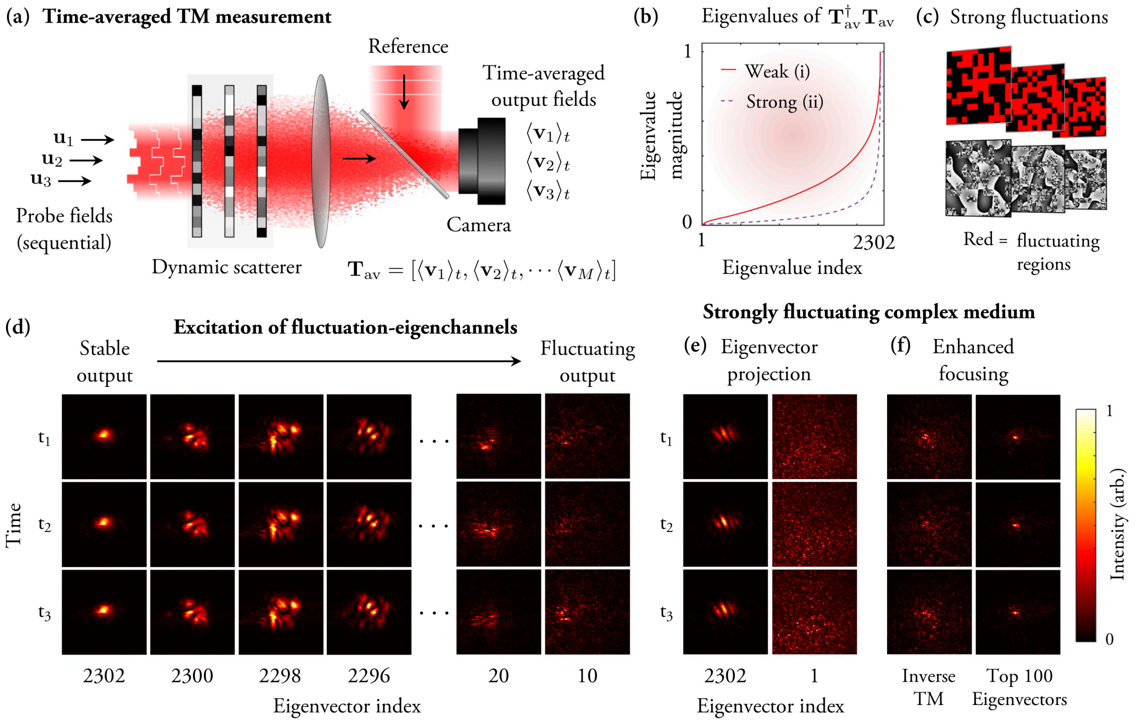

FIGURE 3.1: **Figure 3 and the corresponding caption from [91] showing experimental implementation of $\mathbf{T}_{\mathrm{av}}$.**(a) Schematic of experimental set-up. A sequence of orthogonal probe fields are individually transmitted through the medium, e.g. $\mathbf{u}_1, \mathbf{u}_2, \mathbf{u}_3$. For each input, the corresponding time-averaged output field is recorded, e.g. $\langle \mathbf{v}_1 \rangle, \langle \mathbf{v}_2 \rangle, \langle \mathbf{v}_3 \rangle$, and arranged column-by-column to build the time-averaged TM $\mathbf{T}_{\mathrm{av}}$. (b) The magnitudes of the eigenvalues of $\mathbf{T}_{\mathrm{av}}^{\dagger}\mathbf{T}_{\mathrm{av}}$, for a weakly (i) and strongly (ii) fluctuating dynamic medium. Both are arranged in ascending order and normalised to a maximum value of 1. The weakly fluctuating medium is the same as used in the earlier experiments. An example of the strongly fluctuating medium is shown in (c), with moving regions highlighted in red. (d) Excitation of selected fluctuation-eigenchannels in the weakly fluctuating medium. Each column shows the output when the medium is illuminated with different eigenvectors. Each row shows the output at a different time – i.e. for 3 different configurations of the dynamic regions of the medium. We see the high index eigenvectors are stable with respect to these movements, while the low eigenvectors are not. (e) Eigenvector projection through a strongly fluctuating medium. (f) Enhanced focusing through strongly fluctuating scattering media using the time-averaged TM. Left column: an attempt to make a focus using the conventional inverse TM, which is measured while the medium fluctuates. We see a poor contrast focus which fluctuates strongly as the medium reconfigures. Right column: An output focus created through the same medium, with the input field generated using the top 100 most stable eigenvectors of $\mathbf{T}_{\mathrm{av}}^{\dagger}\mathbf{T}_{\mathrm{av}}$. Here we see that the contrast and stability of the output focus is significantly improved.

experimentally created fields of the largest and smallest eigenvalues for a strongly fluctuation scatterer. Using the eigenvectors corresponding to the top 100 eigenvalues, enhanced focusing was demonstrated and compared to using the inverse TM for focusing through a strongly fluctuating scattering region, as seen in Fig. 3.1f.

### 3.1.2 Simulation results

The experiment presented in the previous section demonstrates the utility of the time-averaged transmission matrix in the forward scattering scenario. My role in this project was to investigate how well this new wavefront shaping technique works for more difficult scenarios when high levels of multiple scattering and the effect of diffusion are taken into account.

The time-average transmission matrix can be easily calculated using the DDA for a random configuration of scatterers, such as the one illustrated in Fig. 2.1. Each of the sources can have their amplitude and phase individually manipulated, such that any arbitrary incident wavefront can be created to create the probe fields to build the time-averaged transmission matrix. The spacing between the sources and between the detectors must be no larger than $\lambda/2$; this is to allow full control of the wavefront by sampling and creating fields at the diffraction limit.

The array of sources can be described by a vector containing complex numbers that describe the phase and amplitude of each individual source, which can be easily manipulated to generate the needed fields. The results below offer insight into the typical behavior of this method in simulation for highly diffusive samples. Because this is a high-dimensional problem, and the numerical simulation has many parameters that can be individually adjusted, several scenarios are considered.

First, a region of size $\sim 30 \times 30$ wavelengths is considered. The simulation space contains a slab of 100 randomly positioned dipoles, with a dynamic pocket in the centre of the slab containing 15 dynamic dipoles. For these simulations, the high scattering limit ($|\alpha| = 4k_0^{-2}$) is used unless otherwise stated. In these situations, the least amount of light reaches the detectors, with much of the scattered light lost by the multiple highly scattering events in the light's path. In comparison to the forward scattering experiments presented in the previous section, these simulations represent a more difficult scenario wherein the wavefront shaping process must compensate for the maximum physically allowable scattering of a sample containing many scattering dipoles within a relatively small area.

The time-averaged TM is calculated as described above for the scattering system. Next, the matrix product $\mathbf{T}_{\text{av}}^{\dagger}\mathbf{T}_{\text{av}}$ is calculated and the resulting matrix's eigenvectors and eigenvalues are determined. The magnitude of the eigenvalues corresponds directly to the amount of power transmitted to the detectors through the scattering region. The corresponding eigenvectors provide the wavefronts that are launched from the sources.

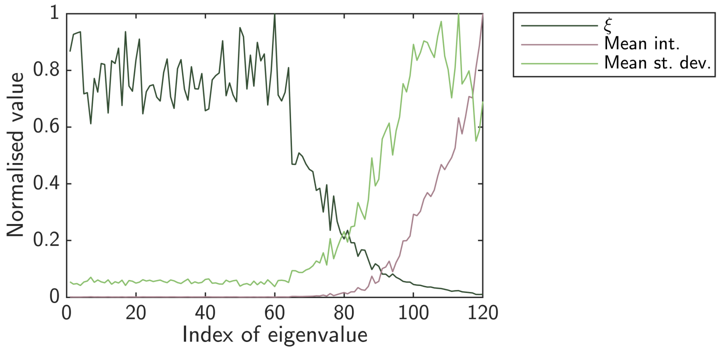

FIGURE 3.2: **Fluctuations of transmitted field for each eigenfield** of $\mathbf{T}_{\mathrm{av}}^{\dagger}\mathbf{T}_{\mathrm{av}}$ for a system of 100 dipoles, 15 of which move, in the high scattering limit ($|\alpha| = 4k_0^{-2}$). The standard deviation of movement of the dynamic dipoles is $1.25\lambda$, and the fields are averaged over $n = 55$ configurations. The sources and detectors are spaced evenly $\lambda/4$ apart. The normalised values of the level of fluctuation $\xi$ (dark green), mean transmitted intensity (light red), and mean standard deviation of the transmitted amplitude over time (light green) are plotted.

Here, these eigenvalues and eigenvectors are sorted by ascending magnitude of the eigenvalues.

Fig. 3.2 shows values of the mean transmitted intensity, mean standard deviation of the transmitted field amplitude, and fluctuations of the transmitted field quantified by $\xi$ for each of the eigenvalues. As expected from Eqn. 3.1, there is a trend of increasing intensity transmitted to the detectors for larger eigenvalues. Notably, there are a few fields corresponding to some of the largest eigenvalues that see a decrease in the mean

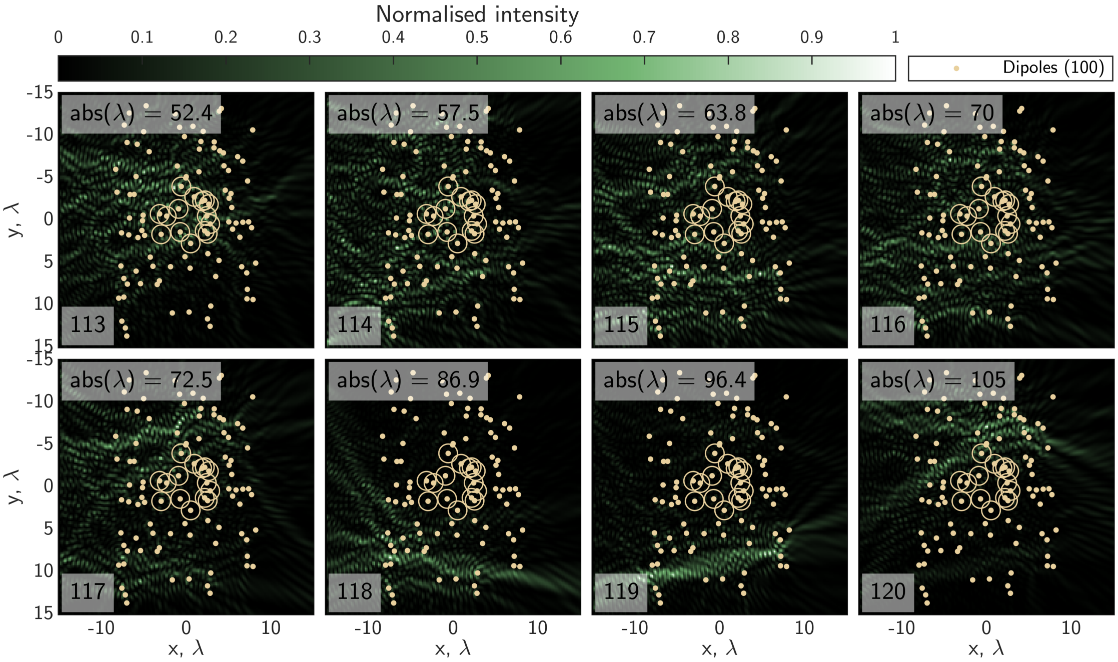

FIGURE 3.3: **Last 8 eigenfields of $\mathbf{T}_{\mathrm{av}}^{\dagger}\mathbf{T}_{\mathrm{av}}$ for a system of 100 dipoles, 15 of which move, in the high scattering limit ($|\alpha| = 4k_0^{-2}$).** The standard deviation of movement of the dynamic dipoles is $1.25\lambda$, and the fields are averaged over $n = 55$ configurations. The sources and detectors are spaced evenly $\lambda/4$ apart.

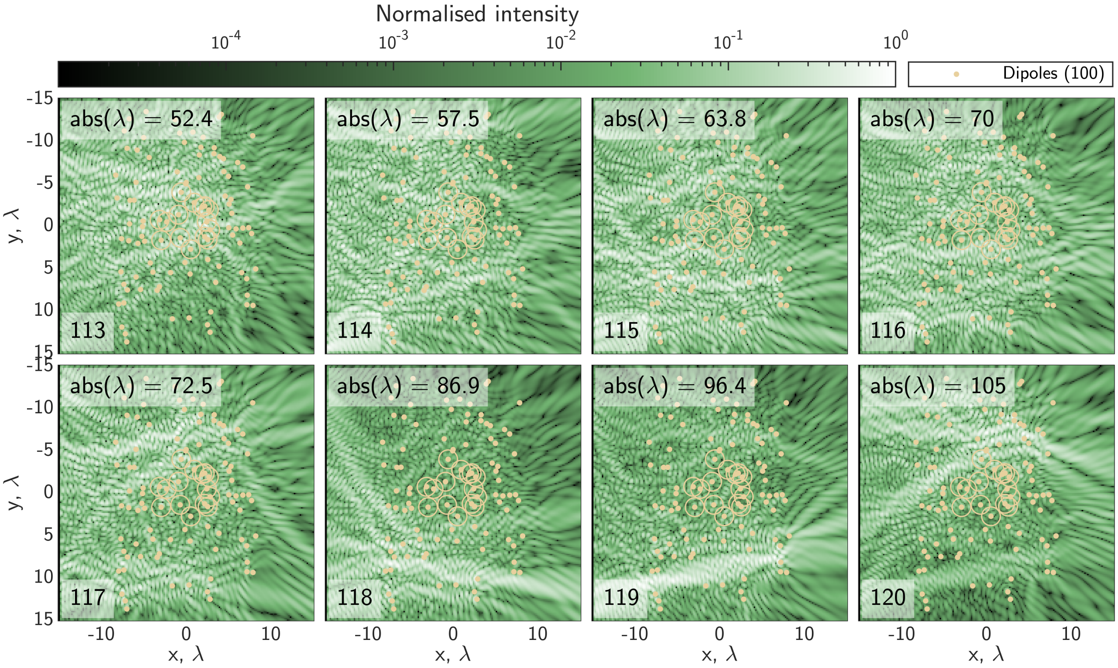

FIGURE 3.4: **Log scale version of eigenfield heatmaps from Fig. 3.3.**

standard deviation of the field amplitude as well. The last 8 eigenfields are plotted in Fig. 3.3 and Fig. 3.4, the last few of which clearly steer light around the pocket of dynamic dipoles.

The optimiser does not rely on knowledge about the pocket of dipoles, including the actual location of this pocket within the scattering material. To illustrate this, the simulation is re-run where the pocket of dynamic scatterers is moved to a different location. Fig. 3.5 shows that several eigenfields exist that show a reduced mean standard deviation of the transmitted field amplitude with an increased mean transmitted intensity for this new situation. Fig. 3.6 and Fig. 3.7 show the last 8 eigenfields for the time-averaged TM in this scenario. As before, the last few eigenfields send most of the light into the regions around the dynamic dipoles.

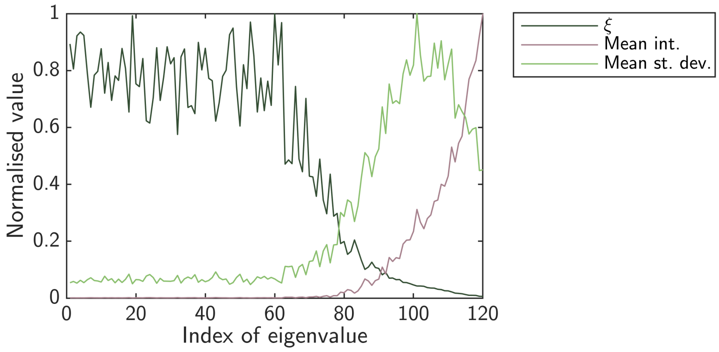

FIGURE 3.5: **Fluctuations of transmitted field for each eigenfield** of $\mathbf{T}_{\mathrm{av}}^{\dagger}\mathbf{T}_{\mathrm{av}}$ for a system of 100 dipoles, 15 of which move, in the high scattering limit ($|\alpha| = 4k_0^{-2}$), where the pocket has been translated away from the centre of the scattering region. The standard deviation of movement of the dynamic dipoles is $1.25\lambda$, and the fields are averaged over $n = 55$ configurations. The sources and detectors are spaced evenly $\lambda/4$ apart. The normalised values of the level of fluctuation $\xi$ (dark green), mean transmitted intensity (light red), and mean standard deviation of the transmitted amplitude over time (light green) are plotted.

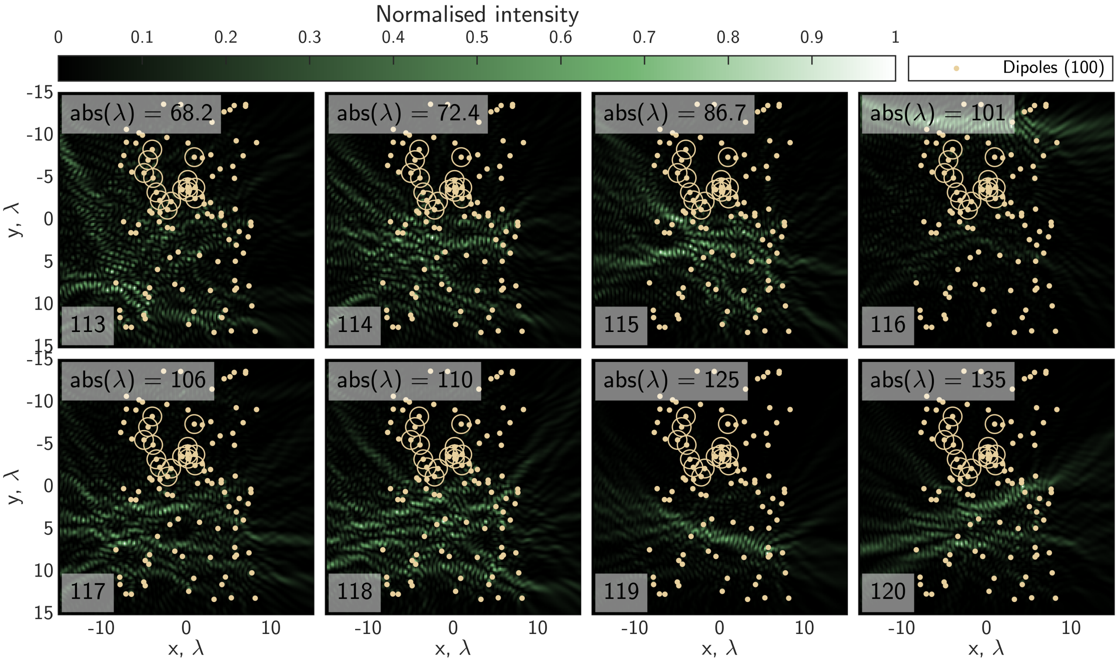

FIGURE 3.6: **Last 8 eigenfields of $\mathbf{T}_{\mathrm{av}}^{\dagger}\mathbf{T}_{\mathrm{av}}$ for a system of 100 dipoles, 15 of which move, in the high scattering limit** ($|\alpha| = 4k_0^{-2}$), where the pocket of dynamic dipoles has been translated to a new location. The standard deviation of movement of the dynamic dipoles is $1.25\lambda$, and the fields are averaged over $n = 55$ configurations. The sources and detectors are spaced evenly $\lambda/4$ apart.

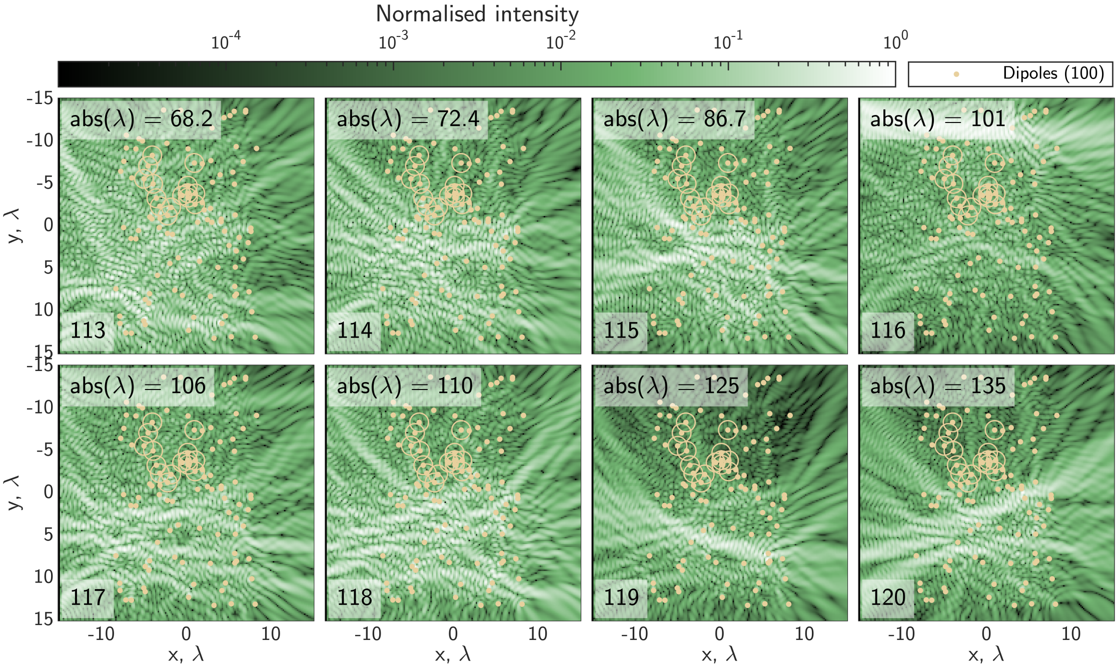

FIGURE 3.7: **Log scale version of eigenfield heatmaps from Fig. 3.6.**

This method also works if the dynamic dipoles' motion is larger. To demonstrate this, the standard deviation of the motion of the dynamic dipoles is doubled to $2.5\lambda$. Fig. 3.8 shows the performance of each eigenfield. Notably, there are now less fields for which the intensity is increased while the standard deviation is also decreased when compared with the previous scenario with a smaller standard deviation of movement. Fig. 3.9 and Fig. 3.10 show the last 8 eigenfields for this simulation.

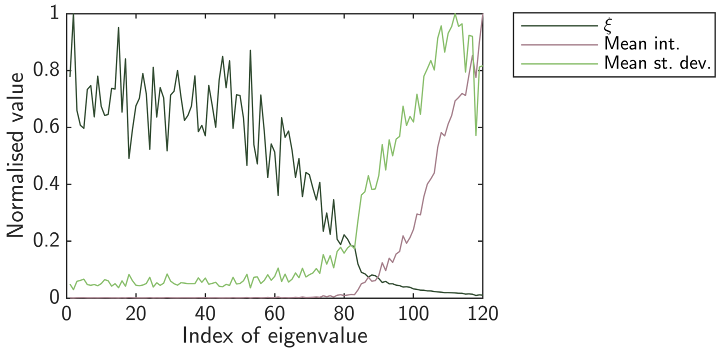

FIGURE 3.8: **Fluctuations of transmitted field for each eigenfield** of $\mathbf{T}_{\mathrm{av}}^{\dagger}\mathbf{T}_{\mathrm{av}}$ for a system of 100 dipoles, 15 of which move, in the high scattering limit ($|\alpha| = 4k_0^{-2}$). The standard deviation of movement of the dynamic dipoles is $2.5\lambda$, and the fields are averaged over $n = 200$ configurations. The sources and detectors are spaced evenly $\lambda/4$ apart. The normalised values of the level of fluctuation $\xi$ (dark green), mean transmitted intensity (light red), and mean standard deviation of the transmitted amplitude over time (light green) are plotted.

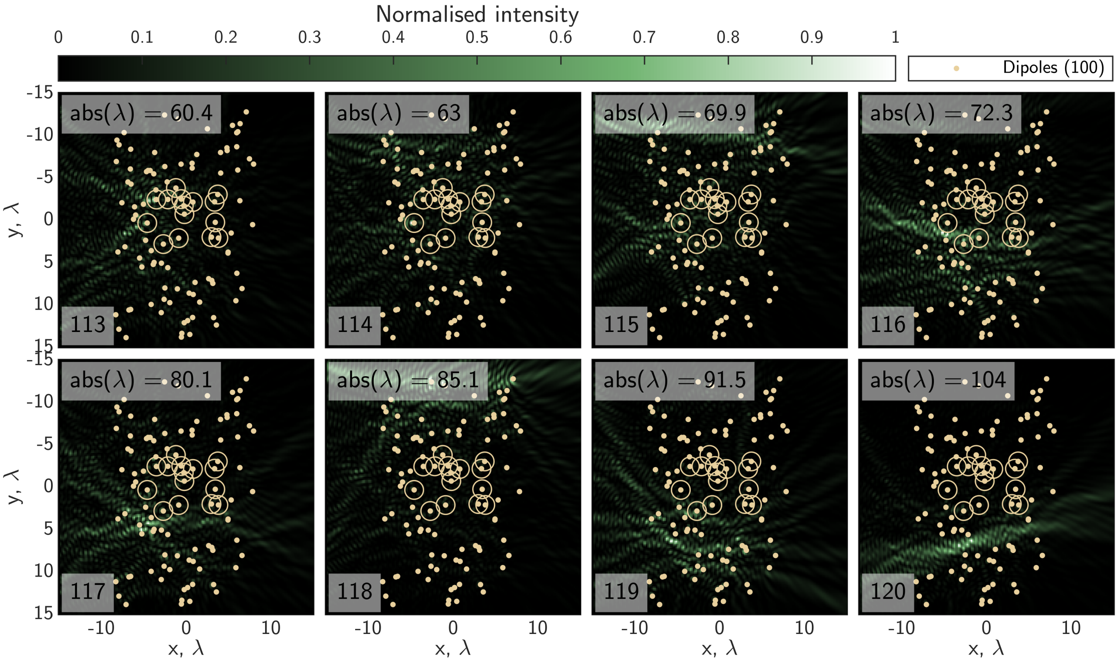

FIGURE 3.9: **Last 8 eigenfields of $\mathbf{T}_{\mathrm{av}}^{\dagger}\mathbf{T}_{\mathrm{av}}$ for a system of 100 dipoles, 15 of which move, in the high scattering limit** ($|\alpha| = 4k_0^{-2}$). The standard deviation of movement of the dynamic dipoles is $2.5\lambda$, and the fields are averaged over $n = 200$ configurations. The sources and detectors are spaced evenly $\lambda/4$ apart.

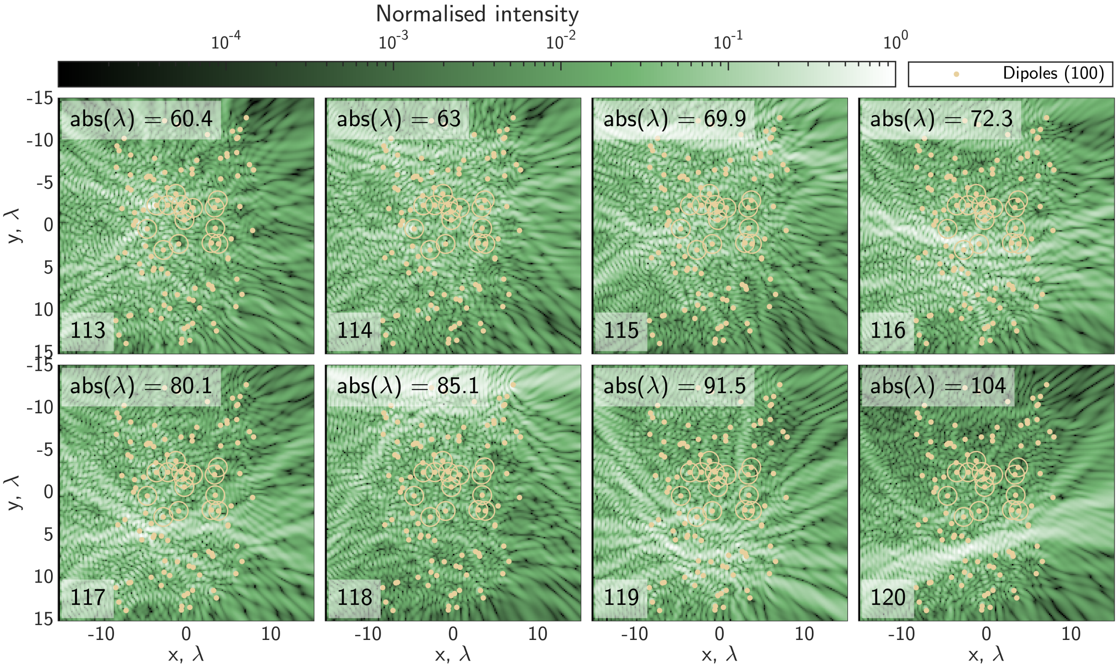

FIGURE 3.10: **Log scale version of eigenfield heatmaps from Fig. 3.9.**

Finally, the low scattering case is considered. Fig. 3.11 shows the performance of the eigenfields for this scenario. Here the forward transmission of as much light as possible is prioritised over reducing the fluctuations due to the movement of the dynamic dipoles. However, there are still a few fields that avoid the moving scatterer (most obviously eigenfield 100). Fig. 3.12 and Fig. 3.13 show heatmaps of some of the last eigenfields, including eigenfield 100.

This method for the low scattering case does not perform as well as for the high scattering limit because it increases time-averaged power levels on the detector plane. There are two ways this can happen: first the way we want, by reducing the fluctuations (hence the moving media is avoided) so the field doesn't time-average to near zero. However, if the fluctuations don't average to zero, then the time-average intensity on the detector plane can also be increased a second way, by shaping the input wavefront to transmit more scattered light to the output plane, regardless of if the fluctuating region is avoided or not. This second way is dominating here, because lower levels of scattering mean a dipole's movement makes less of a difference to the structure of the output field. Therefore, the field doesn't average away as effectively as in the highly scattering case.

Notably, the fluctuations of the field don't go completely to zero in any of the situations considered here. This is due to the highly multiply scattering nature of the samples. Even if the incident wavefront is shaped such that all of the light is focused to the furthest point from the dynamic pocket within the scattering material, the dynamic dipoles will still be excited by the incident light. This is because each of the dipoles scatters circular waves in response to the incident wavefront, allowing such a focused field to interact with the dynamic pocket after multiple scattering events. The eigenfields feature 'stripes' of intensity which increase in spatial frequency as the eigenvalue increases. We speculate that a possible explanation for this phenomenon is that by avoiding diffraction out to the side similar to the behavior of a Bessel beam [100], such that the maximum amount of power is transmitted to the detector plane.

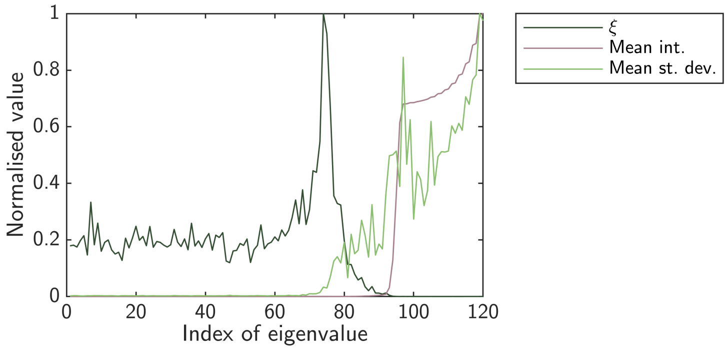

FIGURE 3.11: **Fluctuations of transmitted field for each eigenfield** of $\mathbf{T}_{\mathrm{av}}^{\dagger}\mathbf{T}_{\mathrm{av}}$ for a system of 100 dipoles, 15 of which move, in the low scattering scenario ($|\alpha| = 0.4k_0^{-2}$). The standard deviation of movement of the dynamic dipoles is $1.25\lambda$, and the fields are averaged over $n = 55$ configurations. The sources and detectors are spaced evenly $\lambda/4$ apart. The normalised values of the level of fluctuation $\xi$ (dark green), mean transmitted intensity (light red), and mean standard deviation of the transmitted amplitude over time (light green) are plotted.

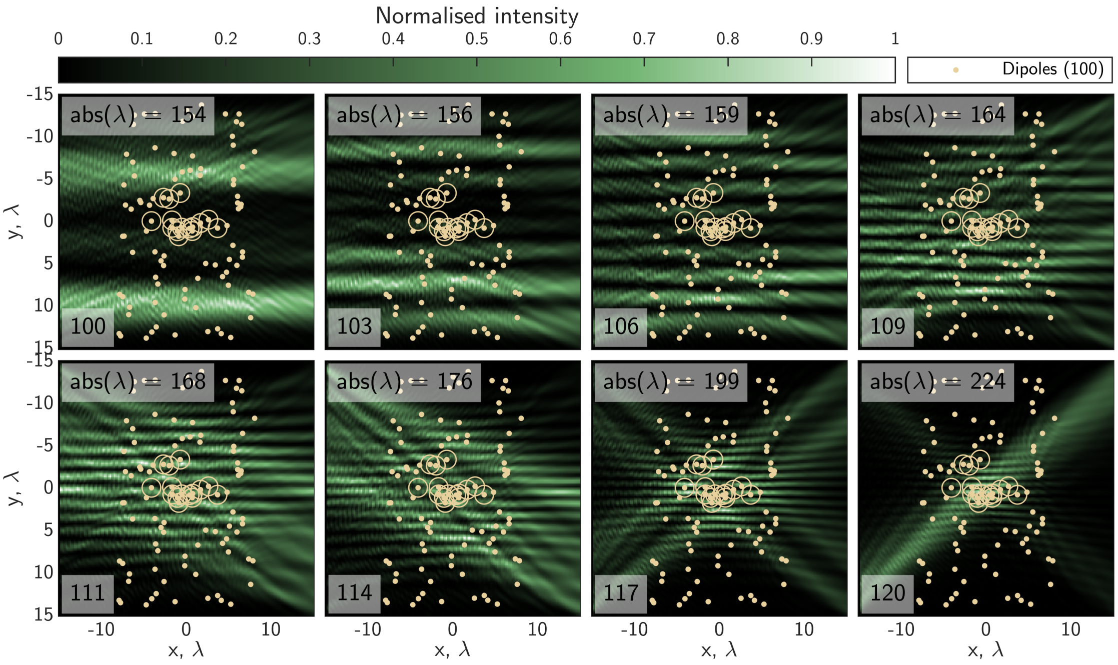

FIGURE 3.12: **Last 8 eigenfields of $\mathbf{T}_{\mathrm{av}}^{\dagger}\mathbf{T}_{\mathrm{av}}$ for a system of 100 dipoles, 15 of which move, in the low scattering scenario** ($|\alpha| = 0.4k_0^{-2}$). The standard deviation of movement of the dynamic dipoles is $1.25\lambda$, and the fields are averaged over $n = 55$ configurations. The sources and detectors are spaced evenly $\lambda/4$ apart.

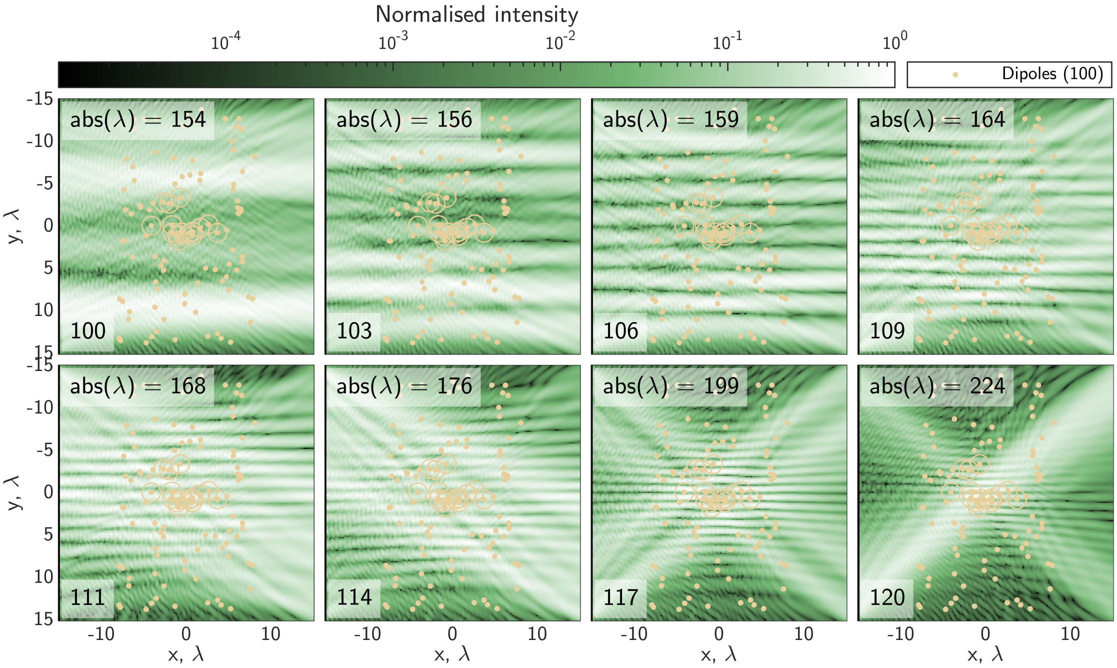

FIGURE 3.13: **Log scale version of eigenfield heatmaps from Fig. 3.12.**

Although this approach finds multiple eigenfields that navigate around the dynamic pocket in the highly scattering scenario, the exact behavior of the eigenfields and subsequently which of those eigenfields successfully avoid the pocket is highly dependent on the scattering material. Choosing the best eigenfield is not straight-forward. This limits the applicability of the time-averaged transmission matrix because one would need to test each eigenfield to determine how it fluctuates at the detectors before being certain the field avoids the dynamic pocket of scatterers. This limitation does not apply to the experiments presented above, because in the experiments all of the light is forward scattered. Therefore, the eigenvalues are well correlated with the light fields that avoid the moving regions.

## 3.2 Simple iterative phase optimisation

Another method for finding fields that navigate around pockets of moving scatterers within a sample of static scatterers is to introduce an iterative phase optimiser which attempts to minimise the intensity fluctuations quantified by $\xi = \overline{\sigma}_{\sqrt{I}} / \overline{I}$ in Eqn. 2.36 for a light field that travels through a partially moving scatterer. This simple iterative phase optimisation iteratively adjusts the phase of each source such that the light in the scattering region interacts minimally with the moving scatterers, resulting in a reduction in $\xi$ at the detectors, and thereby choosing a path that selectively avoids these regions.

This straight-forward algorithm is detailed below:

1. For the $i$th source, a small phase change $\Delta\phi$ is added to the complex amplitude such that the phase of the source $\phi_i$ is now given by $\phi_i + \Delta\phi$.

2. The total input field is propagated through the partially dynamic scattering medium, and the intensity at the detectors is recorded for $n_m$ random movements of the dynamic dipoles. This is analogous to recording the intensity at a camera for a fixed integration time, for example. Each measurement is saved separately, not averaged at this point.

3. The figure of merit (FOM) $\xi_{\Delta\phi}$ is calculated from these intensities.

4. Steps 1-3 are repeated, this time for a small phase change $-\Delta\phi$, such that $\xi_{-\Delta\phi}$ can be calculated.

5. Steps 1-3 are again repeated, this time for the initial phase of the source, such that $\xi_0$ can be calculated.

6. From these three scenarios, the phase configuration which minimises the FOM $\xi$ is selected.

7. The chosen phase configuration that minimises $\xi$ is saved and becomes the initial phase of the chosen source for the start of next iteration, when these steps are repeated for the next consecutive source.

Subsequently, one iteration of the optimiser will refer to one optimisation of every source (i.e. $n_s$ repetitions of the above described steps).

We have chosen to use the pixel basis - this basis is easy to handle in simulation where there are no problems due to the signal-to-noise ratio. Other bases may be chosen [15, 18, 101] where multiple pixels are changed at once, however there is no strong reason why any basis would be better than any other for the scenarios considered here.

### 3.2.1 Experimental results

Proof-of-principle experimental implementations of this method were recently released in an ArXiv pre-print [91]. A version of this paper is currently under review in a peer-reviewed journal as of the time of this writing.

Fig. 3.14 shows these results from [91]. The experiment consisted of a basic wavefront shaping optical setup, briefly sketched in the simple schematic in Fig. 3.14a, wherein an expanded laser beam has its phase modulated by an SLM. This shaped beam then propagates through a mock dynamic scattering region – here, three phase masks displayed side-by-side on another SLM with a mirror placed parallel to the SLM screen such that the propagating laser beam is reflected off of each phase mask in sequence. To create the necessary phase masks, random phase matrices were created, up-scaled in size, and interpolated across to create smoothly varying, random phase masks.

Each of these three phase masks contains a dynamic pocket – labelled ‘Fluctuating regions’ in Fig. 3.14e, top row – wherein the phase is randomly fluctuating. The locations of the pockets are different for each phase mask. The optimised transmitted field reduces the fluctuation levels compared to the initial transmitted field before optimisation, as seen in the difference between the standard deviation of the intensity fluctuations in Fig. 3.14c and d.

The simple iterative optimisation succeeded in finding fields that navigate through the scattering region, avoiding all three pockets of movement. Off-axis holography was used to determine the amplitude and phase of the field on each of the three phase masks, shown by the color (phase) and brightness (amplitude) of the field in Fig. 3.14e, middle row, which clearly shows the field avoiding the pocket of movement on each plane of the scattering region containing the dynamic scatterers. The intensity on each of these planes is shown in Fig. 3.14e, bottom row, and illustrates the same thing.

These proof-of-principle experimental results show that it is possible to experimentally find fields that navigate through a scattering region with multiple fluctuating pockets. This experiment demonstrates the utility of this technique in the low scattering scenario, because the scattering material was digitally mimicked by a reflective SLM, such that minimal light was lost via scattering in other directions. The simulations presented in the previous section demonstrate that this technique can work even in the high scattering limit.

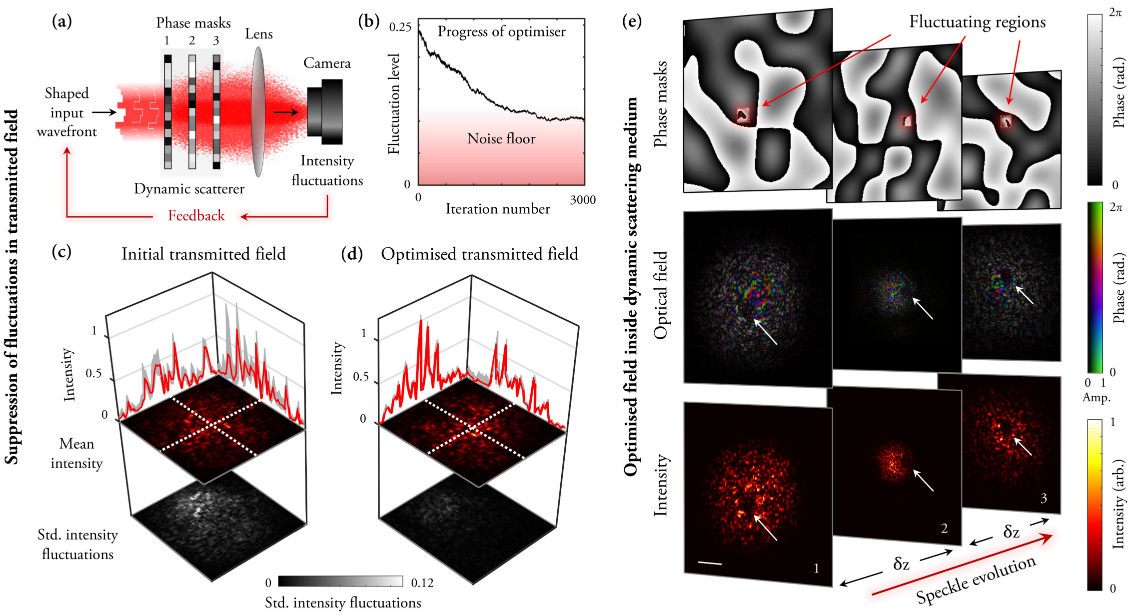

FIGURE 3.14: **Experimental results for simple iterative optimiser.** Recreated from Fig. 1 and the corresponding caption in [91]. a) Schematic of experimental set-up. An input wavefront is iteratively modified to reduce the intensity fluctuations in transmitted light. (b) A plot of fluctuation level as a function of iteration number throughout the optimisation procedure. Convergence is reached after several thousand iterations: the fluctuation level does not fall to zero, but plateaus when the residual fluctuations fall below the experimental noise floor, indicated (approximately) in pink. (c) Fluctuations in the output field for a randomly chosen input field used as the starting point of the optimisation. Upper heat maps show the mean intensity of transmitted light at the output plane, and lower heat maps show the fluctuation level around the mean, represented as a standard deviation around the mean. The line-plots show line-profiles through the output field along the lines marked with white hatched lines, with mean intensity (red line) and fluctuations about the mean (gray shading). (d) Equivalent plot to (c) but now showing the optimised transmitted field. We see the fluctuations have been strongly suppressed in (d) compared to (c). (e) Measured shape of the optimised field inside the dynamic scattering sample. The top row shows the 3 phase planes that form the scattering system, with a fluctuating region on each plane highlighted by a red box. The middle and bottom rows show the optical field (middle row) and intensity pattern (absolute square of the field – bottom row) incident on each plane. We see that the optimised field arriving at each plane has a low intensity region corresponding to the location of the fluctuating region – highlighted by white arrows – thus ‘avoids’ these regions.

### 3.2.2 Simulation results

Next, this iterative optimisation approach to finding light fields that navigate through partially dynamic scattering media is investigated numerically. As before with the time-average transmission matrix, the simple iterative phase optimiser can be easily integrated with the DDA for a random configuration of scatterers, such as the one illustrated in Fig. 2.1. Each of the sources can have their amplitude and phase individually manipulated, such than any arbitrary incident wavefront can be created. The same scenarios are considered as in the previous section.

The intensity heatmaps in Fig. 3.15 show an example of both a plane wave (left) and an optimised wavefront (right) propagating through this array of 100 randomly configured dipoles. The circled dipoles explore a normally distributed area about their initial locations, with a standard deviation of 1.25$\lambda$. To emphasize the path that the shaped wavefront takes through the scattering region, Fig. 3.15b shows the same intensity heatmaps as Fig. 3.15a, but on a log scale. From these intensity plots it is clear that the light bends around the pocket of dynamic dipoles.

Fig. 3.16 shows the progression of the optimiser. One iteration consists of optimising every one of the sources consecutively once. Throughout the 100 iterations, the chosen phase configurations simultaneously maintain the mean intensity reaching the detectors, while also decreasing the mean standard deviation of the amplitude at the detectors. This is seen by the decrease in the FOM, $\xi$ over the course of the simulated optimisation to $\sim$ 20% of its initial value. For each iteration, the moving dipoles explore 55 random locations, chosen as described above.

To demonstrate that this method works for situations with more movement, this optimisation is simulated again with the same parameters as above but with a higher standard deviation of motion of the dynamic dipoles. Fig. 3.17 and Fig. 3.18 show the results of this simulation with a standard deviation of motion of 2.5$\lambda$, twice the value considered above. To ensure that this does not also mean that the calculated FOM suffers from higher error

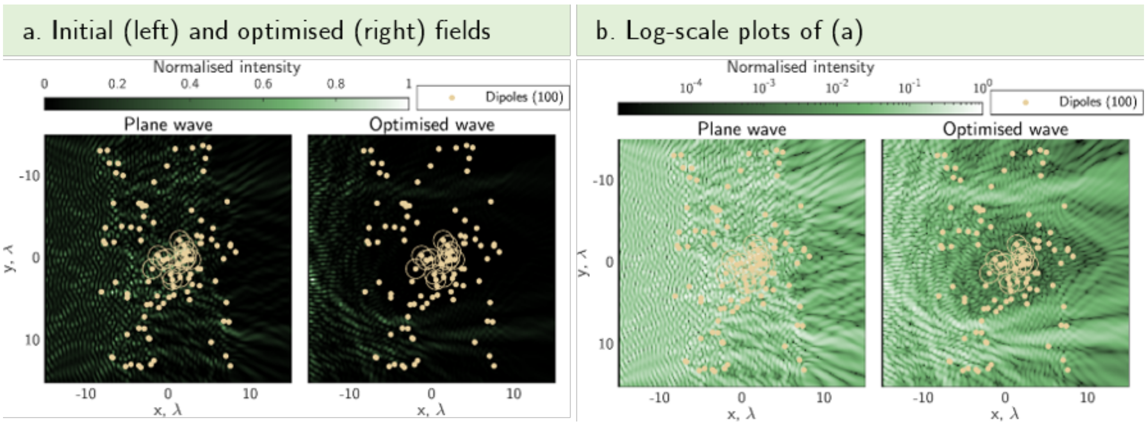

FIGURE 3.15: **Simulation of simple iterative phase optimisation in the high scattering limit**. Sources are spaced $\lambda/2$. St. dev. of motion of dipoles is 1.25$\lambda$, $n_{\mathrm{m}} = 55$ configurations are used for fluctuation quantification. $\Delta\phi = \pi/10$. (a) Intensity heatmaps showing plane wave (left) and optimised wavefront (right) propagating through 100 scattering dipoles (yellow dots), 15 of which are dynamic (circled). (b) Log scale versions of plots in (a). (c) Progression of the optimisation.

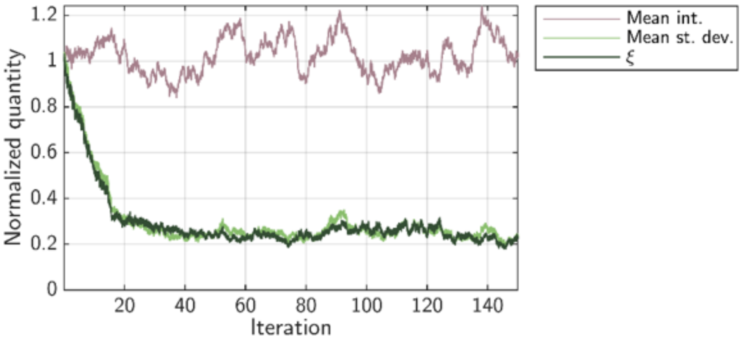

FIGURE 3.16: **Progression of the simple iterative phase optimisation in the high scattering limit**.

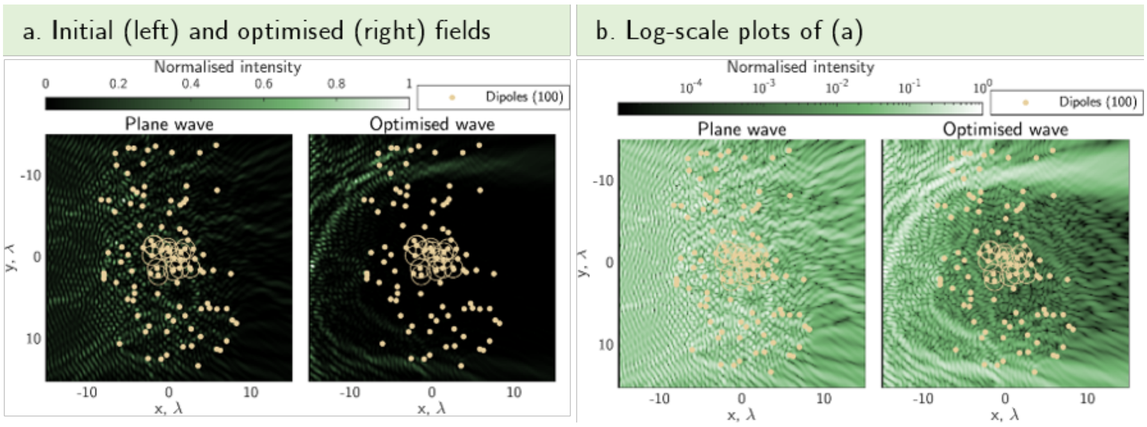

FIGURE 3.17: **Simulation of simple iterative phase optimisation in the high scattering limit**. Sources are spaced $\lambda/2$. St. dev. of motion of dipoles is $2.5\lambda$, $n_{\mathrm{m}} = 200$ configurations are used for fluctuation quantification. $\Delta\phi = \pi/10$. (a) Intensity heatmaps showing plane wave (left) and optimised wavefront (right) propagating through 100 scattering dipoles (yellow dots), 15 of which are dynamic (circled). (b) Log scale version of plots in (a).

introduced by under-sampling the moving dipoles' movement, $n_m = 200$ configurations are used for quantifying the level of fluctuations (previously used $n_m = 55$).

For the case of larger random movements of the dipoles, less of the final optimised field is transmitted to the detectors. The mean intensity of the field at the detectors decreases to $\sim 70\%$ of the initial value. This is due to the overall locations sampled by the larger movement occupying a larger percentage of the total simulated space, meaning that the wavefront must be shaped more dramatically to bend the incident light completely around the dynamic pocket. Doing so becomes more difficult for larger pockets within the same area, and subsequently fewer detectors directly behind the pocket receive any transmitted light.

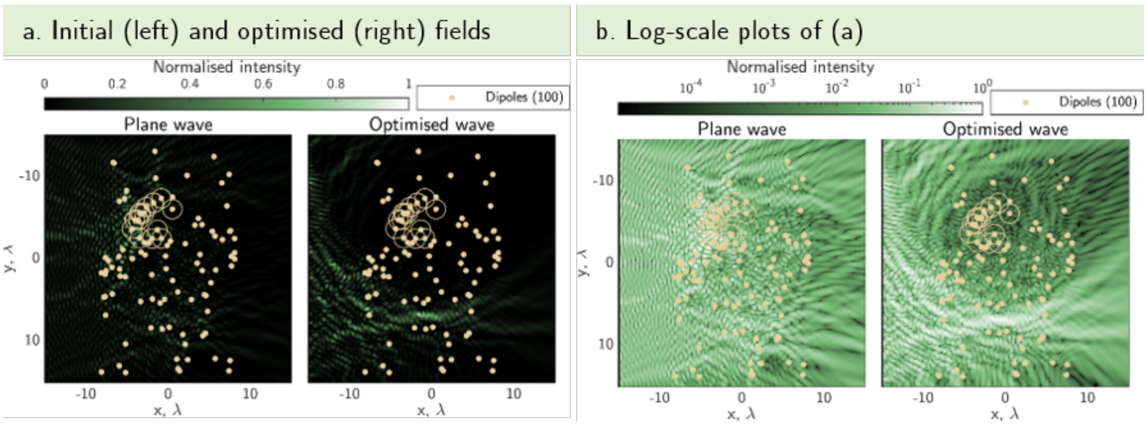

FIGURE 3.19: **Simulation of simple iterative phase optimisation in the high scattering limit**. Sources are spaced $\lambda/2$. St. dev. of motion of dipoles is $1.25\lambda$, $n_{\mathrm{m}} = 55$ configurations are used for fluctuation quantification. $\Delta\phi = \pi/10$. (a) Intensity heatmaps showing plane wave (left) and optimised wavefront (right) propagating through 100 scattering dipoles (yellow dots), 15 of which are dynamic (circled). (b) Log scale version of plots in (a).

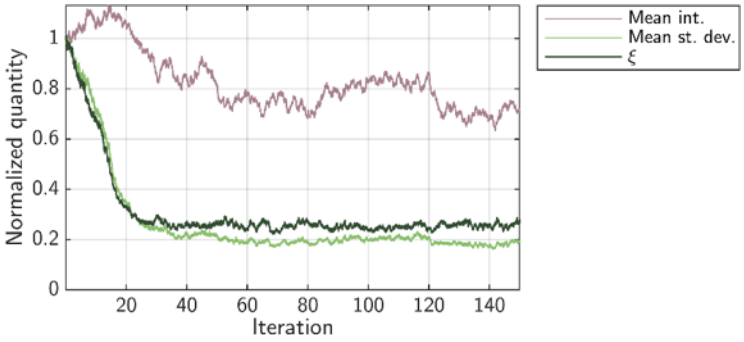

FIGURE 3.18: **Progression of the simple iterative phase optimisation in the high scattering limit with more movement.**

Next, the pocket of dynamic dipoles is translated to a different location within the scattering region, as before. Fig. 3.19ab show heatmaps of the intensity of the initial plane wave (left) and an optimised wavefront (right) propagating through an array of 100 scatterers, containing a pocket of 15 moving dipoles. Here, the pocket has been moved to the upper left area of the scattering region. The optimised wavefront clearly avoids this pocket of dynamic dipoles, as emphasized by the log scale heatmaps in Fig. 3.19b, where most of the light navigates through the lower portion of the scattering region.

The progression of the optimiser is plotted in Fig. 3.20, showing the decrease in the fluctuations of the field at the detectors, quantified by $\xi$ (dark green line), as the optimiser converges to a solution. The mean intensity at the detectors decreases to $\sim$ 80% of its initial value, while the standard deviation of the intensity decreases to less than $\sim$ 20% of its initial value. This results in a reduction of the $\xi$, as anticipated.

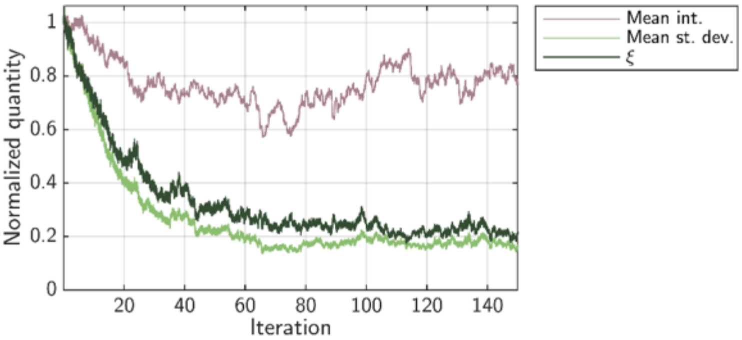

FIGURE 3.20: **Progression of the simple iterative phase optimisation in the high scattering limit with translated dynamic pocket.**

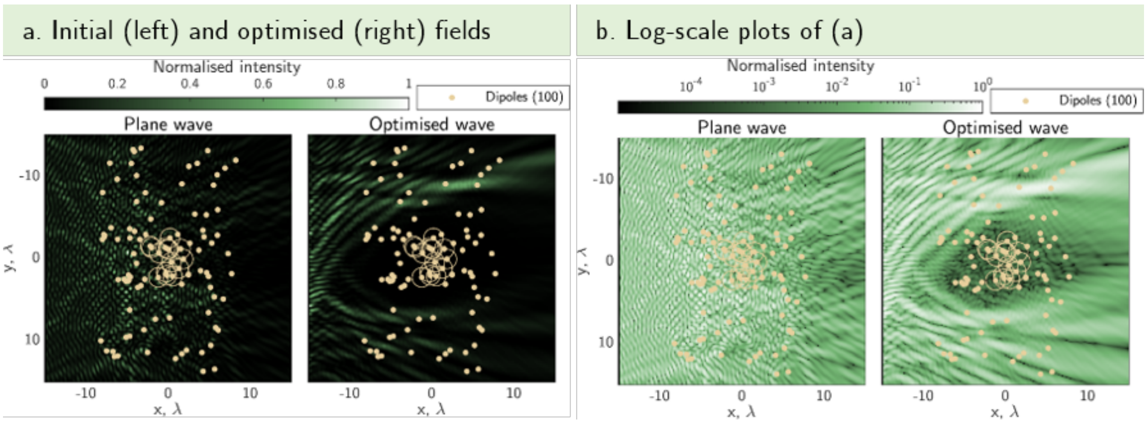

FIGURE 3.21: **Simulation of simple iterative phase optimisation in the low scattering scenario**. Sources are spaced $\lambda/2$. St. dev. of motion of dipoles is $1.25\lambda$, $n_{\mathrm{m}} = 55$ configurations are used for fluctuation quantification. $\Delta\phi = \pi/10$. (a) Intensity heatmaps showing plane wave (left) and optimised wavefront (right) propagating through 100 scattering dipoles (yellow dots), 15 of which are dynamic (circled). (b) Log scale version of plots in (a).

Finally, the low scattering scenario is considered. Fig. 3.21 and Fig. 3.22 show the results for similar parameters as above, but with $|\alpha| = 0.4k_0^{-2}$. The mean intensity at the detectors decreases alongside the standard deviation of the intensity in this scenario. This is because most of the light from the initial, un-optimised wavefront still reaches the detectors in the low scattering scenario. By wavefront shaping the wavefront to avoid the dynamic scattering pocket, some of the light is diffracted away from the detectors to create the final intensity distribution that avoids the pocket. However, the standard deviation of the intensity at the detectors decreases more than the mean intensity at the detectors, resulting in a reduction in $\xi$ and an optimised field that successfully avoids the dynamic pocket.

To summarise, the numerical simulations and experimental results in this section have demonstrated the following. This simple iterative optimisation is a powerful tool, capable of finding fields that selectively avoid pockets of dynamic dipoles within a larger scattering

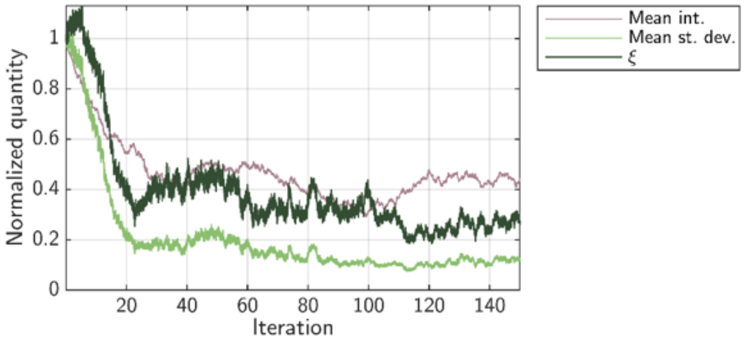

FIGURE 3.22: **Progression of the simple iterative phase optimisation in the low scattering scenario.**

region, in both the forward scattering and diffusive regimes. This method requires no *a priori* knowledge about the exact behavior or location of the moving region. It does not require access to or control of the dynamic region. However, this approach takes an objectively slow route to this solution. Ideally, such solutions would be found as quickly as possible.

## 3.3 Adjoint iterative optimisation

The above described method succeeds in the main objective of this research – finding light fields that carefully navigate around moving parts of a scattering region. However, it is a slow process, because each source mode is adjusted individually. This can quickly become a very high-dimensional problem to solve in macroscopic optical systems. Ideally, to efficiently optimise fields, all of the source modes should be adjusted at the same time. To do this, a fast way of calculating the gradient of the objective function of the optimiser is needed. In the coming sections, several different figures of merit (used to quantify the performance of the optimisation) and objective functions (the function that will be optimised) are investigated to this end. It is interesting to note, that many other figures of merit exist that could be used for similar optimisations. One must decide, for a specific application, how much knowledge of and control over a system one has, and choose an appropriate FOM from this information.

### 3.3.1 Figure of merit 1: Overlap of fields at all times

One FOM that is explored through this research is the overlap of the fields at the detectors over time. Intuitively, if the field is the same at all times (for all configurations of the pocket of moving scatterers), the overlap would be maximised, and the fluctuations of the field would be minimised. The following derivation was led by Dr. Simon Horsley.

For a 2D system such as those considered in this work, this the overlap of the fields at the detectors, FOM $F$, can be written as

$$F = \left| \sum_t \sum_{t'} \int dx \ \mathbf{v}_t(x) \mathbf{v}^*_{t'}(x) \right|^2 \tag{3.2}$$

where $\mathbf{v}_t(x)$ is the field at time $t$ at the detectors located at $x$. This FOM will be referred to as FOM 1 later.

From this it follows that the objective function of this adjoint optimisation is to maximise the FOM from Eqn. 3.2.

The field at the detectors $v_t(x)$ can be written as

$$\mathbf{v}_t(x) = \int G_t(x, x')\mathbf{u}(x')dx, \tag{3.3}$$

where the integral over the Green's function $G_t$ for the configuration of particles at time $t$ is equivalent to multiplying the transmission matrix $\mathcal{T}$ by the source field - the notation used previously to describe this propagation.

In order to understand how to iteratively maximise $F$, it is necessary to determine how a small change in the output field $\delta \mathbf{v}_t$ affects $F$.

$$F = \left| \sum_t \sum_{t'} \int dx \ \left[\mathbf{v}_t(x) + \delta \mathbf{v}_t\right] \left[\mathbf{v}^*_{t'}(x) + \delta \mathbf{v}^*_{t'}\right] \right|^2 \tag{3.4}$$

$$= \left| \sum_t \sum_{t'} \int dx \ \left[\mathbf{v}_t(x)\mathbf{v}^*_{t'}(x) + \mathbf{v}_t(x)\delta \mathbf{v}^*_{t'} + \delta \mathbf{v}_t \mathbf{v}^*_{t'}(x) + \delta \mathbf{v}_t \delta \mathbf{v}^*_{t'}\right] \right|^2, \tag{3.5}$$

where the red term is dropped because it is the product of two small numbers, and therefore can be considered negligible compared to the rest of the sum. One can write $z = \delta \mathbf{v}_t \mathbf{v}^*_{t'}(x)$ and its complex conjugate $z^* = \mathbf{v}_t(x)\delta \mathbf{v}^*_{t'}$, such that the above equations become

$$F \sim \left| \sum_t \sum_{t'} \int dx \ \left[\mathbf{v}_t(x)\mathbf{v}^*_{t'}(x) + z^* + z\right] \right|^2 \tag{3.6}$$

$$\sim \left| \sum_t \sum_{t'} \int dx \ \left[\mathbf{v}_t(x)\mathbf{v}^*_{t'}(x) + 2\mathrm{Re}[z]\right] \right|^2 \tag{3.7}$$

$$\sim \left| \sum_t \sum_{t'} \int dx \ \left(\mathbf{v}_t(x)\mathbf{v}^*_{t'}(x) + 2\mathrm{Re}\left[\delta \mathbf{v}_t \mathbf{v}^*_{t'}(x)\right]\right) \right|^2 \tag{3.8}$$

$$\sim \left| M + 2\mathrm{Re}\left[ \sum_t \sum_{t'} \int dx \ \delta \mathbf{v}_t \mathbf{v}^*_{t'}(x) \right] \right|^2, \tag{3.9}$$

where $M = \sum_t \sum_{t'} \int dx \ \mathbf{v}_t(x)\mathbf{v}^*_{t'}(x) = \int dx \left(\sum_t \mathbf{v}_t\right) \cdot \left(\sum_{t'} \mathbf{v}_{t'}\right)^\star$, which is always positive and real. In the second term on the right of Eqn. (3.9) the sum over $t'$ can be moved inside the integral and onto $\mathbf{v}^*_{t'}$ as this is the only quantity that depends on $t'$. The change in the FOM then becomes

$$F \sim \left| M + 2\mathrm{Re}\left[ \sum_t \int dx\ \delta \mathbf{v}_t \sum_{t'} \mathbf{v}^*_{t'}(x) \right] \right|^2 . \tag{3.10}$$

The sum of $\mathbf{v}^*_{t'}$ over $t'$ can be rewritten in terms of the time average of the transmitted field,

$$\sum_{t'} \mathbf{v}^*_{t'}\left(x\right) = n \left\langle \mathbf{v}^*\left(x\right) \right\rangle , \tag{3.11}$$

where $n$ is the total number of time points and $\langle \mathbf{v}^* \rangle$ is the time averaged field. In terms of this averaged field the FOM now equals

$$F \sim \left| M + 2\mathrm{Re}\left[ \sum_t \int dx\ \delta \mathbf{v}_t\ n \left\langle \mathbf{v}^*\left(x\right) \right\rangle \right] \right|^2 . \tag{3.12}$$

From this, to determine the change needed in the input field $\delta \mathbf{u}(x')$ (which should not depend on time) to induce this small change in the transmitted field, use Eqn.3.3:

$$\delta \mathbf{v}_t\left(x\right) = \int dx'\ G_t\left(x, x'\right) \delta \mathbf{u}(x'). \tag{3.13}$$

Combining this with Eqn. 3.12, the FOM can now be written in terms of changes to the input field $\delta \mathbf{u}$:

$$F \sim \left| M + 2n\mathrm{Re}\left[ \sum_t \int dx \int dx' G_t\left(x, x'\right) \delta \mathbf{u}(x') \left\langle \mathbf{v}^*(x) \right\rangle \right] \right|^2 . \tag{3.14}$$

Multiplying out the absolute square in this expression yields

$$\begin{aligned} F \sim M^2 + & \left| 2n\mathrm{Re} \sum_t \int dx \int dx' G_t(x, x') \delta \mathbf{u}(x') \left\langle \mathbf{v}^*(x) \right\rangle \right|^2 \\ & + 4nM\mathrm{Re}\left[ \sum_t \int dx \int dx' G_t(x, x') \delta \mathbf{u}(x') \left\langle \mathbf{v}^*(x) \right\rangle \right] . \end{aligned}$$

The red term, which is the square of a small number and so negligible compared to the other terms, is dropped. To increase the FOM (the overlap of the field at the detectors at all times) it is thus required that

$$\delta F = 4nM\mathrm{Re}\left[ \sum_t \int dx \int dx' G_t(x, x') \delta \mathbf{u}(x') \left\langle \mathbf{v}^*(x) \right\rangle \right] > 0 \tag{3.15}$$

Assuming that the system is reciprocal $G_t(x, x') = G_t(x', x)$, Eqn. 3.15 states that to increase the FOM, the conjugate of the time averaged field must be propagated back through the time varying system, this result averaged (the sum over $t$) on the input side, and then $\delta\mathbf{u}$ must be chosen so that its overlap with this averaged field has the largest possible real part. There are several ways of achieving this, but because only the phase of the source field is being modulated the input field is adjusted by a fixed amplitude $\delta A$ and a spatially varying phase denoted by column vector $\boldsymbol{\theta}(x)$:

$$\delta\mathbf{u}(x) = \delta A \mathrm{e}^{i\boldsymbol{\theta}(x)}, \tag{3.16}$$

where each element of the column vector $\boldsymbol{\theta}(x)$ is exponentiated on an element-by-element basis. Applying Eqn. 3.16 to Eqn.3.15, this phase $\theta$ can be determined via

$$\delta F = 4nM\mathrm{Re}\left[\delta A \sum_t \int dx\, \mathrm{e}^{i\boldsymbol{\theta}(x)} \int dx' G_t(x, x') \left\langle \mathbf{v}^*(x) \right\rangle \right]. \tag{3.17}$$

To maximize the value of Eqn. 3.17 the phase $\theta$ is chosen such that it equals the negative of the argument of the term highlighted in blue in Eqn. 3.17

$$\boldsymbol{\theta}(x) = -\arg\left[\sum_t \int G_t(x', x) \left\langle \mathbf{v}^*(x) \right\rangle dx \right] \tag{3.18}$$

With this choice the FOM $F$ will be increased by the largest amount, for a fixed small value of $\delta A$.

This result is encouraging; it implies that it is possible to find fields that avoid pockets of dynamic scattering by minimising fluctuations without any measurements inside of the scattering region, and without any prior knowledge about the location or behavior of the dynamic pocket.

### Experimental results

To perform this optimisation in experiment proved incredibly intricate, and required hours of painstaking alignment and unwavering dedication by postdoctoral researcher Dr. Chaitanya Mididoddi. The optical system required for this experiment ended up spanning the vastness of most of a large optical table, and involved a maze of multiple spatial light modulators, mirrors, lenses, and cameras. Briefly, this optimisation passes a wavefront backwards and forwards through a scattering system, and the wavefront is iteratively adapted to travel a path that avoids areas of time-varying scattering. Fig. 3.23a shows a simplified schematic of this process. Fig. 3.23b shows the progression of this optimisation. Fig. 3.23c shows the field at each plane of the scattering system avoids the moving pockets (outline in white dashed lines).

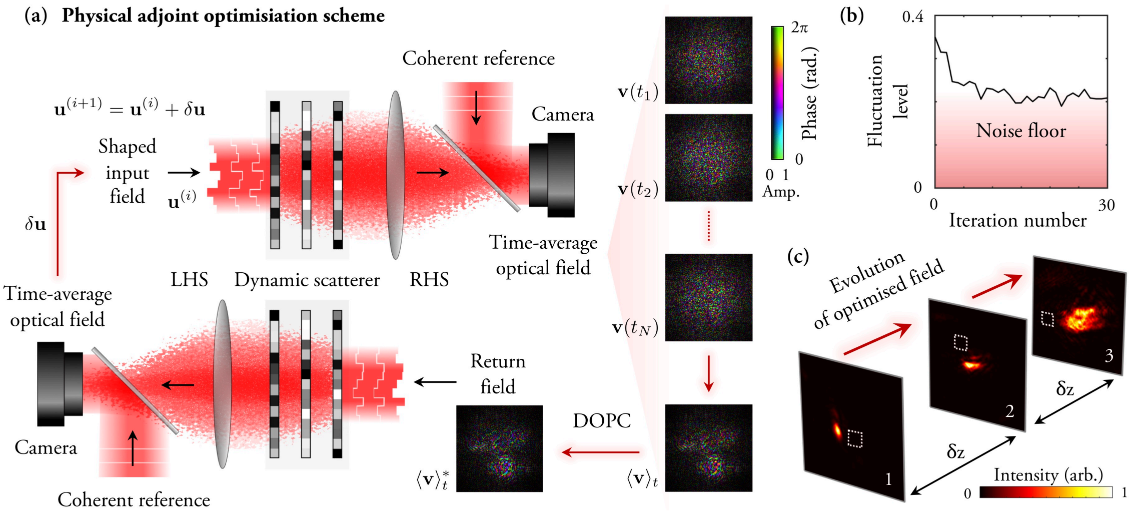

FIGURE 3.23: **Experimental adjoint phase optimisation.** Recreated from Fig. 2 and the corresponding caption in [91].(a) Schematic of experimental set-up. On iteration $i$ an input field $\mathbf{u}(i)$ is transmitted through the dynamic medium from the left-hand-side (LHS). The output field is time-averaged on the right-hand-side (RHS) – the schematic shows output fields recorded at individual times $\mathbf{v}(t_1), \mathbf{v}(t_2), ... \mathbf{v}(t_N)$ (where $N$ is the total number of recorded output fields). These are averaged to yield $\langle\mathbf{v}\rangle_t$. Digital optical phase conjugation (DOPC) is carried out to transmit the phase conjugate of $\langle\mathbf{v}\rangle_t$ back through the medium. The resulting field emerging on the LHS is then time-averaged, and used to calculate $\delta\mathbf{u}$, such that the input of the next iteration $(i+1)$ is given by $\mathbf{u}^{(i+1)} = \mathbf{u}^{(i)} + \delta\mathbf{u}$. (b) A plot of fluctuation level as a function of iteration number throughout the optimisation procedure. In this scheme, convergence is reached after $\sim 15$ iterations. (c) The experimentally recorded intensity of the optimised field arriving at the three phase planes. The maximum intensity at each plane is normalised to 1. The white squares indicated the location of the moving region on each plane. We see that, once again, the optimised field avoids these moving regions of the sample.

### Simulation results

As with the time-averaged transmission matrix and the simple iterative phase optimiser, I next investigate this adjoint phase optimisation in simulations where the scattering material is no longer only forward scattering. The same scenarios as before are considered for high and low scattering, higher levels of motion of the dynamic dipoles, and for a translated dynamic pocket. Again, a $\sim 30 \times 30$ wavelength simulation area is set up containing a region of 100 scattering dipoles. 15 of these dipoles are allowed to randomly move within a pocket at the centre of the scattering region.

Fig. 3.24 and Fig. 3.25 show numerical results for the adjoint phase optimisation using the overlap of the fields at the detectors over time as the FOM, as described in Eqn. 3.2, for motion of the moving dipoles with a standard deviation of $1.25\lambda$. The figures here are

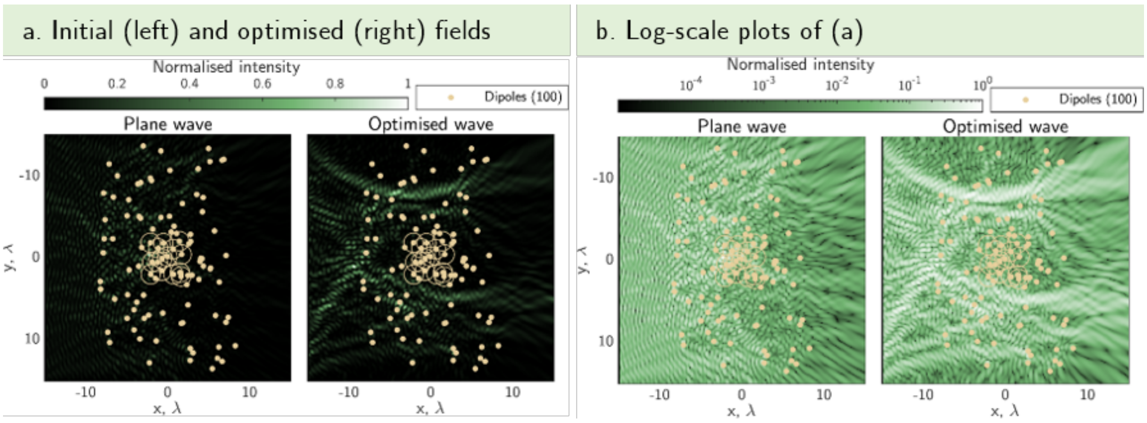

FIGURE 3.24: **Simulation of adjoint phase optimisation in the high scattering limit** using the overlap of the fields at the detectors over time as the FOM. Sources are spaced $\lambda/4$. St. dev. of motion of dipoles is $1.25\lambda$, $n_\mathrm{m} = 55$ configurations are used for fluctuation quantification. $dj = 0.1$. (a) Intensity heatmaps showing plane wave (left) and optimised wavefront (right) propagating through 100 scattering dipoles (yellow dots), 15 of which are dynamic (circled). (b) Log scale version of plots in (a).

formatted in the same way as in the previous section. This optimisation performed as it should – increasing the overlap of the field with each iteration. It also increases the mean intensity transmitted to the detectors. The mean standard deviation of the amplitude of the field at the detectors has reduced slightly to $\sim 85\%$ of its initial value. Hence, $\xi$ decreases to $\sim 40\%$ of its initial value. The optimised field is mostly focused below the dynamic pocket.

Fig. 3.26 and Fig. 3.27 show results for the low scattering scenario with $|\alpha| = 0.4k_0^{-2}$. In this case, the seemingly poor performance of the optimisation is similar to that seen for the time-averaged transmission matrix for the low scattering scenario. Again, this is due to the reduced contribution of the scattered field to the overall field at the detectors. Here, the duality of the desired outcome in this situation becomes clearer and points to potential

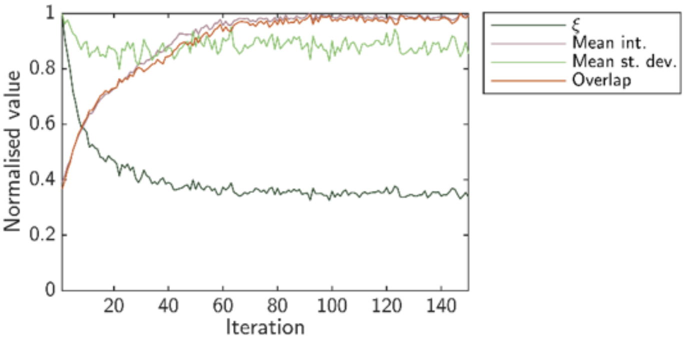

FIGURE 3.25: **Progression of the adjoint phase optimisation in the high scattering limit** using the overlap of the fields at the detectors over time as the FOM.

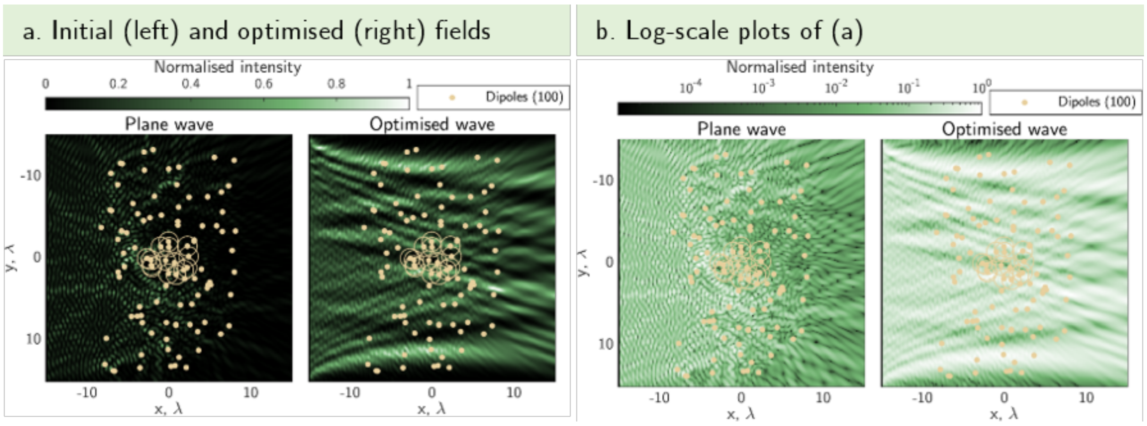

FIGURE 3.26: **Simulation of adjoint phase optimisation in the high scattering limit** using the overlap of the fields at the detectors over time as the FOM. Sources are spaced $\lambda/4$. St. dev. of motion of dipoles is $1.25\lambda$, $n_\mathrm{m} = 55$ configurations are used for fluctuation quantification. $dj = 0.1$. (a) Intensity heatmaps showing plane wave (left) and optimised wavefront (right) propagating through 100 scattering dipoles (yellow dots), 15 of which are dynamic (circled). (b) Log scale version of plots in (a).

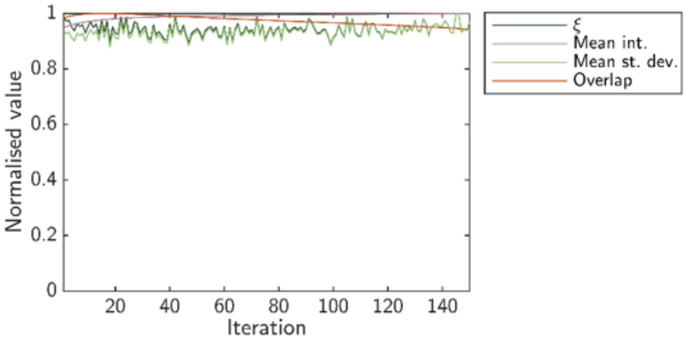

FIGURE 3.27: **Progression of the adjoint phase optimisation in the low scattering scenario** using the overlap of the fields at the detectors over time as the FOM.

short-comings of this FOM. We desire the optimised field to simultaneously navigate around the dynamic pocket while also ensuring at least constant intensity transmission through the scattering region, and FOM 1 prioritizes the latter.

The scenarios of a translated dynamic pocket and higher levels of movement of the dipoles for the high scattering limit are investigated in Appendix B.3.1. In short, the optimised fields also successfully maximise the FOM in these situations, and the optimised fields navigate around the pocket of moving dipoles. The intensity and standard deviation at the detectors also follow the same trend as above for the high scattering scenario.

In summary, the adjoint optimisation with the FOM given by the overlap of the fields over time in Eqn. 3.2 succeeds in threading light around a moving region within a scattering material in higher scattering scenarios. It decreases $\xi$ while also increasing the FOM, as anticipated. However, it does not necessarily decrease the standard deviation of the amplitude of the field at the detectors; in some scenarios, the standard deviation actually increases, but because the mean intensity transmitted to the detectors increases a larger amount, this still results in an overall decrease in the levels of fluctuations of the field. Ultimately, this approach will prioritize increasing the overlap of the fields over time at the detectors over decreasing the standard deviation of the field over time, because the FOM does not constrain the standard deviation in any way.

### 3.3.2 Figure of merit 2: Normalised variance of fields over time

Next, inspired by the success of the FOM $\xi$ from the simple iterative optimisation, and with knowledge of how FOM 1 only prioritizes half of our objective, another FOM is investigated numerically. The following derivation was provided by Dr. Simon Horsley.

We let $F$ be the variance of the field at the detectors over time

$$\begin{aligned} F &= \int \mathrm{Var}(x)\ dx && (3.19) \\ &= \frac{1}{N}\int |\phi_t|^2 dx - \frac{1}{N^2}\sum_t \sum_{t'} \int \phi_t(x)\phi^*_{t'} dx && (3.20) \\ &= 1 - \frac{1}{N^2}\sum_t \sum_{t'} \int \phi_t(x)\phi^*_{t'}(x) dx, && (3.21) \end{aligned}$$

this is more similar to the ratio $\xi$ than the previous FOM 1 (overlap of the fields).

Dropping the pre-factor and addition of one, as they will make no difference in the optimisation, this simplifies to the same as FOM 1 from Eqn. 3.2 with an added normalisation. The new FOM $F$ can then be written as

$$F = -\sum_t \sum_{t'} \frac{\int \phi_t(x)\phi^*_{t'}(x) dx}{\left[\int |\phi_t(x)|^2 dx\ \int |\phi_{t'}(x)|^2 dx\right]^{1/2}}. \tag{3.22}$$

If the same derivation as above in Section 3.3.1 is performed on this FOM, the resulting change that needs to be made to the phase of each mode of the input field becomes

$$\boldsymbol{\theta}(x) = -\arg\left[\sum_t \int dx \frac{G_t(x', x)}{N_t}\left[\langle \phi^*(x)\rangle - \frac{\phi^*_t(x)}{N_t} A_t\right]\right] \tag{3.23}$$

where

$$A_t = \mathrm{Re}\left[\int \frac{\phi_t(x)}{N_t}\langle \phi^*(x)\rangle dx\right] \tag{3.24}$$

and the normalisation factors are given by

$$N_t = \int |\phi_t(x)|^2 dx \tag{3.25}$$

and similar for $t'$.

Interestingly, Eqn. 3.23 is very similar to the change in phase for FOM 1 in the previous section. The first term in the inner square brackets is the complex conjugated of the time-averaged field at the detectors – this is FOM 1! The second term in the inner square brackets is new for FOM 2 – this term is the complex conjugated of the field at the detectors at all measurement times $t$, scaled by the factors $N_t$ and $A_t$.

In contrast to FOM 1, FOM 2 should decrease (thus the negative sign), and the field must propagate through the same configurations of the moving dipoles going forwards and backwards (due to the second term). Unlike FOM 1 introduced for the adjoint optimisation, this FOM requires control of or extensive knowledge of the movements of the dipoles in the moving pocket or the ability to perform the measurements and wavefront shaping faster than the movement of the dynamic dipoles such that the second term in the inner square brackets of Eqn. 3.23 can be experimentally created.

This approach was developed after the conclusion of Dr. Mididoddi's experimental work. Therefore, no experiments were conducted for this approach. However, I investigated this adjoint phase optimisation numerically as before for the other optimisation algorithms.

Fig. 3.28 shows simulated results of adjoint optimisation using the normalised variance FOM (FOM 2) with similar simulation parameters as above. The optimised field forks around the dynamic pocket. Fig. 3.29 shows the levels of fluctuation (solid dark green line) and the FOM (solid light red line) decreasing as the optimisation progresses, converging to a solution that reduces $\xi$ to approximately 40% its initial value. This method seems to check all of the boxes: the mean intensity at the detectors has increased slightly, the mean standard deviation of the amplitude of the field at the detectors has decreased, the ratio $\xi$ has decreased, the FOM has decreased, and the optimised field skirts the edges of the pocket of dynamic dipoles.

Next, the low scattering scenario is considered with this method. Fig. 3.30 and Fig. 3.31 show the results for the scenario where $|\alpha| = 0.4k_0^{-2}$ for a similar configuration of 100 dipoles as seen above. The heatmaps in Fig. 3.30 show the intensity of the initial (left) and optimised (right) wavefronts, which show the later field clearly avoiding the pocket of moving dipoles. The plots showing the performance of the optimiser across all iterations in Fig. 3.31 show that the mean intensity remains nearly constant throughout the optimisation, but the standard deviation, FOM, and $\xi$ decrease significantly, with the levels of fluctuation falling to $\sim$ 20% of their initial value.

The scenarios of a translated dynamic pocket and higher levels of movement of the dipoles for the high scattering limit are investigated in Appendix B.3.2. In short, the optimised fields also successfully minimise the FOM and $\xi$, and the optimised fields navigate around the pocket of moving dipoles. The intensity and standard deviation at the detectors also follow the same trend as above for the high scattering scenario.

If the motion of the dynamic pocket is periodic, we expect that the requirement of fast wavefront shaping could be relaxed. To investigate this numerically, I simulated a

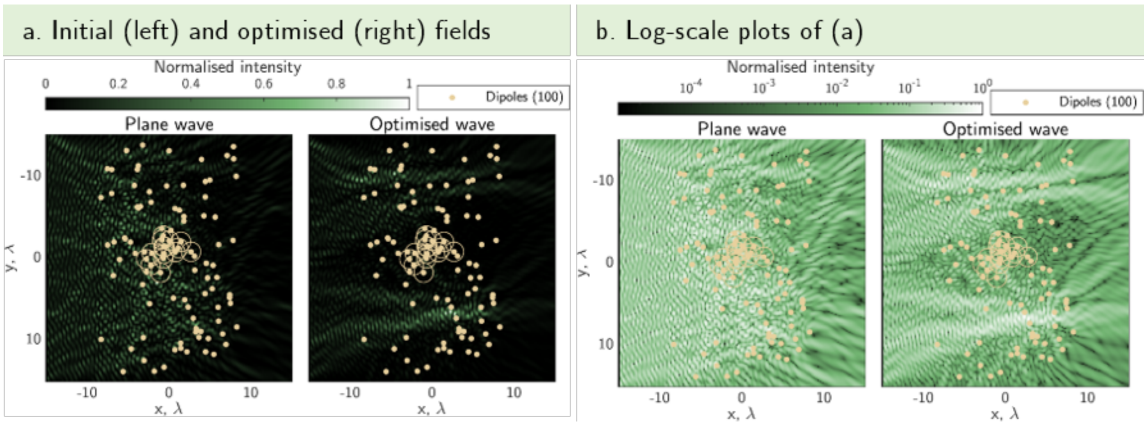
a. Initial (left) and optimised (right) fields
b. Log-scale plots of (a)

FIGURE 3.28: **Simulation of adjoint phase optimisation in the high scattering limit** using the normalised variance of the fields at the detectors over time as the FOM. Sources are spaced $\lambda/4$. St. dev. of motion of dipoles is $1.25\lambda$, $n_\mathrm{m} = 55$ configurations are used for fluctuation quantification. $dj = 0.1$. (a) Intensity heatmaps showing plane wave (left) and optimised wavefront (right) propagating through 100 scattering dipoles (yellow dots), 15 of which are dynamic (circled). (b) Log scale version of plots in (a).

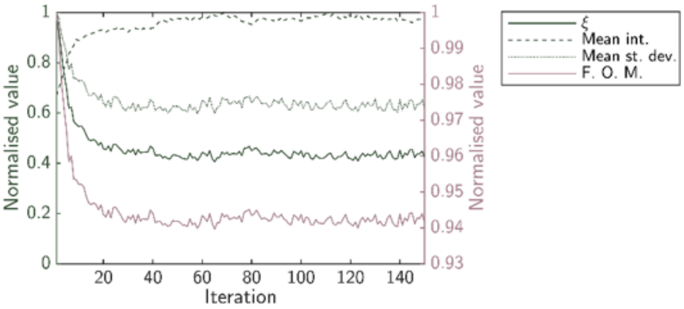

FIGURE 3.29: **Progression of adjoint phase optimisation in the high scattering limit** using the normalised variance of the fields at the detectors over time as the FOM.

scenario wherein the dynamic dipoles are allowed to move to random new locations for the measurement of the conjugate field $\phi_t^*(x)$. Because the movement of the dipoles used here are normally distributed about some initial location, we believe that this method should still successfully optimise the phase of an incident wavefront.

Fig. 3.32 and Fig. 3.33 show the results for the scenario where $|\alpha| = 4k_0^{-2}$ for a similar configuration of 100 dipoles as seen above. As before, the dynamic dipoles explore 55 different normally distributed positions for each iteration. The heatmaps in Fig. 3.32ab show the intensity of the initial (left) and optimised (right) wavefronts, which show the latter field clearly steering around the pocket of moving dipoles. The plots showing the performance of the optimiser across all iterations in Fig. 3.33 show that the mean intensity increases slightly throughout the optimisation, and the standard deviation, FOM, and $\xi$ decrease, with the levels of fluctuation falling to $\sim 60\%$ of their initial value.

The performance of this optimisation was decreased in comparison to the previously considered scenarios where the dipoles are considered to be static over each calculation of the average and instantaneous fields at the detectors. Because of the normally distributed nature of the motion considered here, we believe that increasing the number of time steps over which the optimised phases are calculated should also increase the performance of the optimisation. To test this, I simulated the same scenario as above but for 200 different normally distributed positions for each iteration, effectively increasing the number of time steps considered by $\sim 4\times$.

Fig. 3.34 and Fig. 3.35 show the results for this scenario. Notably, the final fluctuations are decreased to $\sim 40\%$ of their initial value, indicating that higher sampling rates improve the performance of this phase optimisation in this situation. Additionally, the progress curves are smoother in this case of 200 time steps in comparison to those from Fig. 3.33 where 55 time steps were used. This is due to better sampling the overall periodic nature of the dynamic pocket's motion.

The adjoint optimisation with the FOM given by the normalised variance of the fields over time in Eqn. 3.19 succeeds in threading light around a moving region within a scattering material in all considered scattering scenarios. It decreases $\xi$ while also decreasing the FOM, as anticipated. It also decreases the standard deviation of the amplitude of the field at the detectors while also increasing the mean intensity transmitted to the detectors. Ultimately, this approach allows the desired control over the field through the scattering material, but it also requires fast wavefront shaping for the measurement of the field at the detectors or knowledge that the motion of the dynamic regions is periodic.

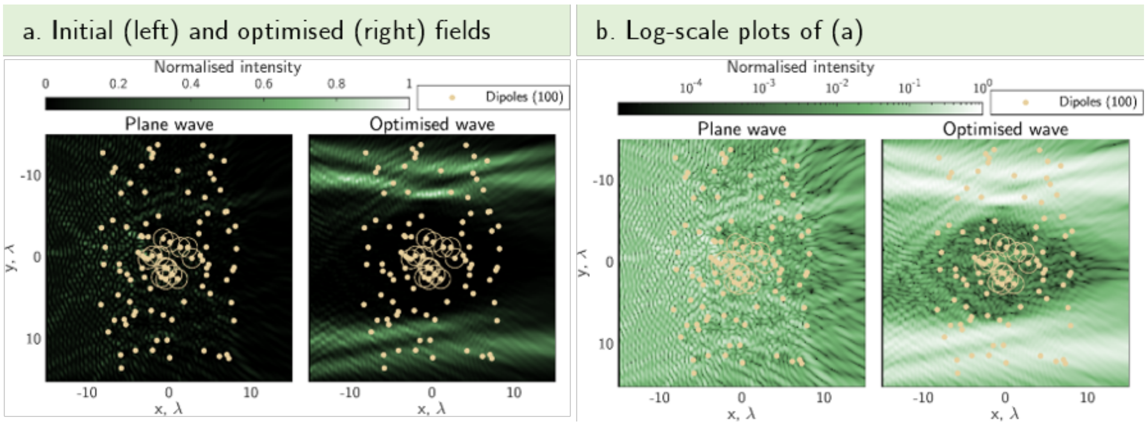

FIGURE 3.30: **Simulation of adjoint phase optimisation in the low scattering scenario** using the normalised variance of the fields at the detectors over time as the FOM for an off-centre pocket of dipoles. Sources are spaced $\lambda/4$. St. dev. of motion of dipoles is $1.25\lambda$, $n_{\mathrm{m}} = 55$ configurations are used for fluctuation quantification. $dj = 0.1$. (a) Intensity heatmaps showing plane wave (left) and optimised wavefront (right) propagating through 100 scattering dipoles (yellow dots), 15 of which are dynamic (circled). (b) Log scale version of plots in (a).

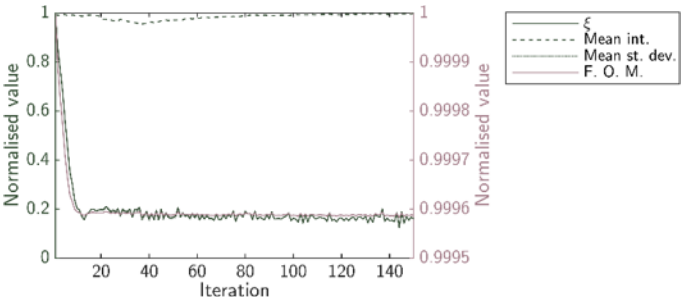

FIGURE 3.31: **Progression of adjoint phase optimisation in the low scattering scenario** using the normalised variance of the fields at the detectors over time as the FOM for an off-centre pocket of dipoles.

## 3.4 Discussion of approaches

There are many parameters that can be adjusted in the simulations presented here, but the general trends seen across each method are summarised in this section. The advantages and disadvantages of each method are also discussed below.

The time-averaged transmission matrix requires no knowledge or control of the dynamic pocket. This method exploits the eigenchannels of $\mathbf{T}_{\text{av}}^{\dagger}\mathbf{T}_{\text{av}}$, where the channels corresponding to the highest magnitude eigenvalues fluctuate the least as the dynamic scatterers move. There are always at least a handful of eigenchannels that steer clear of the dynamic pocket. Another advantage of this method is that measuring $\mathbf{T}_{\text{av}}$ in experiments is reasonably easy; this technique could be implemented in any existing optical system where the standard transmission matrix can be measured. The biggest drawback to this approach is that we cannot determine which eigenfields will perform best for a

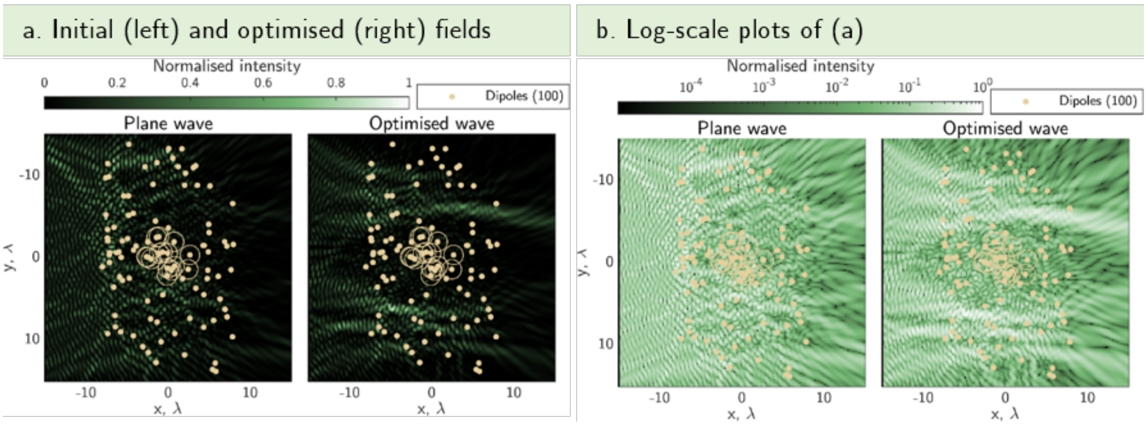

FIGURE 3.32: **Adjoint phase optimisation with FOM 2 with continuous movement.** Sources are spaced $\lambda/4$. St. dev. of motion of dipoles is $1.25\lambda$, $n_{\text{m}} = 55$ configurations are used for fluctuation quantification. $dj = 0.1$. (a) Intensity heatmaps showing plane wave (left) and optimised wavefront (right) propagating through 100 scattering dipoles (yellow dots), 15 of which are dynamic (circled). (b) Log scale version of plots in (a).

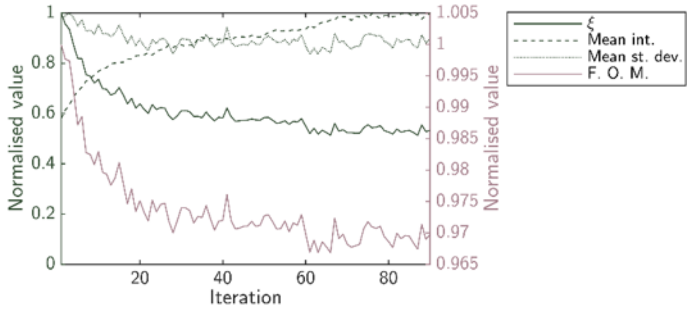

FIGURE 3.33: **Progress of adjoint phase optimisation with FOM 2 with continuous movement** over $n_\mathrm{m} = 55$ configurations.

given scattering material without testing each eigenfield.

The simple iterative phase optimiser requires the least information on and control of a scattering system. The downside of this approach is the large number of iterations required for it to converge to a solution ($n_s \times n_i$ total loops of the optimisation steps, where $n_s$ is the number of sources/modes and $n_i$ is the total number of iterations). However, this method succeeds in reliably and repeatably finding fields that carefully navigate through scattering regions with a pocket of dynamic scatterers, for every set of parameters tested. This approach could be implemented in any wavefront shaping experiment where a researcher has only intensity fluctuation information on the far side of a partially dynamic scattering material.

The first adjoint phase optimisation using the overlap of the fields at the detectors over time as the FOM requires the ability to send light through the scattering material from two directions – very challenging in experiment. However, no control of the scattering material

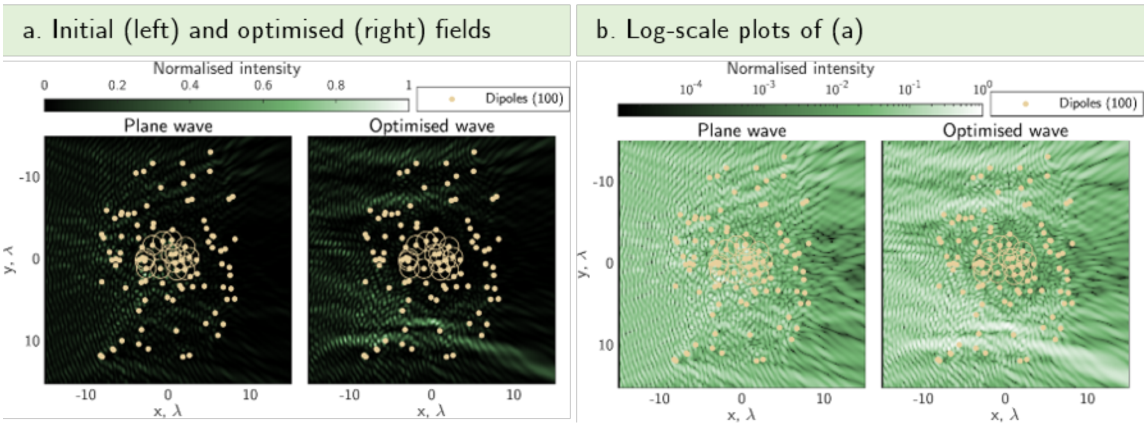

FIGURE 3.34: **Adjoint phase optimisation with FOM 2 with continuous movement.** Sources are spaced $\lambda/4$. St. dev. of motion of dipoles is $1.25\lambda$, $n_\mathrm{m} = 200$ configurations are used for fluctuation quantification. $dj = 0.1$. (a) Intensity heatmaps showing plane wave (left) and optimised wavefront (right) propagating through 100 scattering dipoles (yellow dots), 15 of which are dynamic (circled). (b) Log scale version of plots in (a).

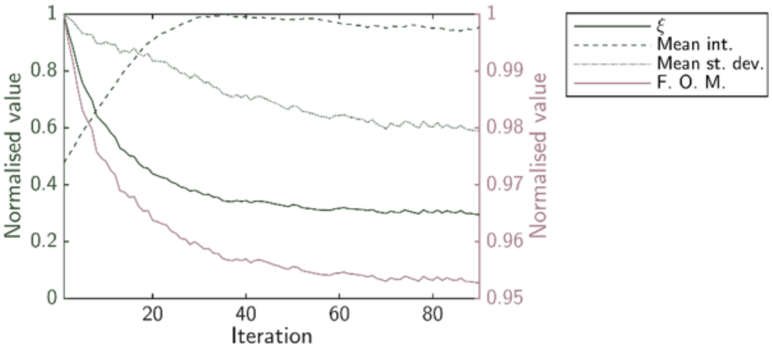

FIGURE 3.35: **Progress of adjoint phase optimisation with FOM 2 with continuous movement** over $n_{\mathrm{m}} = 200$ configurations.

itself is necessary. This method succeeds in increasing the intensity at the detectors, which corresponds to avoiding the pocket of moving scatterers in most situations. For the low scattering scenario, however, this method is less effective because the increase in intensity outweighs the fluctuations induced by the scattering scenarios considered here. This is due to the chosen FOM and objective function, not a failing of the optimiser – in short, it does exactly what it should: increase the overlap of the field at the detectors over time.

The second adjoint optimisation using the normalised variance of the fields at the detectors over time as the FOM also requires the ability to send light through the scattering material from both sides of the material, and additionally requires that the configuration of the scatterer is known so the appropriate correction can be made to send backwards through the medium. This means experimentally one of three things must be true: the fields must be created at the rate of the motion of the dynamic pocket, the motion of the dynamic pocket must be controllable, or the motion of the dynamic pocket must be periodic such that higher sampling rates of this motion accurately capture this periodicity. In many experiments the former may be more feasible. Unlike the previous figure of merit, this FOM performs well for all scattering scenarios tested here, even the low scattering case. To perform this optimisation in experiment 'as is' would require the ability to chose the configuration of the dynamic scattering region while simultaneously launching the corresponding fields forwards and backwards through the system. This faces the same experimental difficulties as the first adjoint optimisation FOM.

There is a trade-off that needs to be considered between the amount of control one has of a scattering system, and the amount of control one can expect to have of the wavefront shaped field. We have investigated a handful of scenarios here, but as mentioned before there are countless possible combinations of figures of merit and objective functions that can be tailored to a specific situation or experiment. In waveguide experiments, for example, it is possible to have exact control over the location and movements of scatterers, which are typically centimetre-scale cylinders in this case. However, in living tissue this level of information on and control over the scattering system is not possible. The different approaches are compared in the table below, providing a basic overview of the trade-offs of the different optimisation algorithms.

| **Wavefront optimisations in partially dynamic scattering scenarios** | | | |
|---|---|---|---|
| **Method** | **Pros (+) & cons (−)** | **Relative time to solution** | **Suitable applications** |
| Time-averaged TM | + Finds multiple fields, ordered from least to most fluctuating<br>+ Beam-shaping can be done slower than the movement<br>− Forward scattering only | High ($\sim 10^6 - 10^7$ measurements) | Atmosphere, thin (forward scattering) tissue, optical fibres, and other forward scattering scenarios. |
| Simple iter. phase opt. | − Finds one field<br>+ Beam-shaping can be done slower than the movement<br>+ All levels of scattering | High ($\sim 10^3 - 10^4$ measurements) | Any scattering scenario |
| Adjoint opt., FOM 1 | − Finds one field<br>+ Beam-shaping can be done slower than the movement<br>− Forward scattering only | Low ($\sim 10^2$ measurements) | Atmosphere, thin (forward scattering) tissue, optical fibres, and other forward scattering scenarios. |
| Adjoint opt., FOM 2 | − Finds one field<br>− Beam-shaping must be done at the rate or faster than the movement<br>+ All levels of scattering | Low ($\sim 10^2$ measurements) | Any scattering scenario |

The findings presented in this section demonstrate important progress in the field and have significant implications for future wavefront shaping applications in dynamic situations. In scenarios with precise control, such as waveguide experiments, these methods offer great promise. However, in more complex environments, like living tissue, where control over the scattering system is limited, careful consideration is needed to select the most suitable approach. We hope that our research in combination with breakthroughs in other areas will pave the way for the development of tailored wavefront shaping strategies and ultimately advancing their application in a wide range of dynamic scattering situations.

# Part II

# Enhancing optical tweezers

*Out of that childhood country what fools climb*
*To fight with tyrants Love and Life and Time?*

Patrick Kavanagh

In this part, wavefront shaping and scattering play as much of a role as they did in the previous chapters. Here however, the focus is on the momentum transfer from light to a mesoscopic particle. In a way, while Part 1 of this thesis concentrated on creating light fields that avoid regions within a scattering material to minimise light-matter interactions in this region, Part 2 probes the possibility of generating light fields that specifically maximise momentum transfer between light and an optically trapped particle.

Chapter 4 introduces the concept of optical tweezers and explores previous work done to optimise the stiffness of optical traps, as well as introduces the novel numerical 3D optical trap enhancement optimisation developed for this research project. Chapter 5 details the experimental holographic optical tweezers setup and procedures developed to create high quality optical traps through aberration correction. Chapter 6 presents, to our knowledge, the first ever experimental realisations of 3D enhanced holographic optical traps.

The main contributors to this project are Dr. Unė G. Būtaitė (UGB), Dr. Michael Horodynski (MH), Dr. Graham M. Gibson (GMG), Prof. Miles J. Padgett (MJP), Prof. Stefan Rotter (SR), Prof. Jonathan M. Taylor (JMT), Prof. David B. Phillips (DBP), and me. UGB, JMT and DBP conceived the idea for the project, and developed it with all other contributors. DBP and JMT supervised the project. UGB led the development of the optimiser and performed all simulations, with support from me. MH and SR developed the theory of the GWS operators and derived the gradients and Hessians used in the optimisation. JMT derived the analytical expressions for the differential of the scattering matrix used in the optimisation. GMG and I built the optical setup, with support from DBP and MJP. UGB and I modified the experimental control software. I performed the experiments and data analysis with support from UGB and DBP.

# Chapter 4

# Wavefront shaping and optical tweezers

In this chapter, we provide an overview of the background theory of optical tweezers. Previous work that focuses on enhancing optical tweezers via wavefront shaping is highlighted and discussed. Simulations of the Generalized-Wigner Smith approach to finding optimum traps are presented, demonstrating one previously developed approach to enhancing optical traps via wavefront shaping.

Finally, in this chapter, a numerical treatment of the problem of three dimensional optical trap enhancement using wavefront shaping is developed. Ultimately, three dimensional optical trap enhancement is shown in simulation for the first time with up to two orders of magnitude reduction in the confinement volume of optically trapped microspheres using a novel constrained optimisation. Later, in Chapter 5, the experimental setup needed to attempt such an optical tweezing experiment is detailed, and finally in Chapter 6 the first ever experimental realisations of 3D enhanced optical traps are presented.

## 4.1 Light and momentum

James Clerk Maxwell theorised the existence of radiation pressure in the 1860s in his groundbreaking work developing electromagnetic theory [102]. This effect was not proven experimentally until nearly half a century later in 1901 by Lebedew [49]. Because the laser had not been invented yet, the first experiments proving the existence of radiation pressure [49, 50] seemed to show that it would never be possible to exploit optical forces for anything practical. This is due to the tiny scale of the forces – on the order of picoNewtons ($10^{-12}$). The technology at the beginning of the 20th century, when Lebedew and Nichols published their findings, was not advanced enough to harness these forces.

The invention of the laser in the mid-21st century opened new doorways across physics, and one of those doors led to optical tweezers. A laser (**l**ight **a**mplification by the **s**timulated **e**mission of **r**adiation) emits photons which are identical in their wavelength and propagation direction, unlike a flashlight or the sun. This enables a lot of power to be tightly focused into a small region of space. For researchers this meant that it became easier to investigate optical forces, and exploit them for many practical applications.

Thanks to the laser, today the field of optical tweezers, a tool that has proven powerful as a mesoscale matter manipulator, is thriving [103]. Additionally, optical forces are also being harnessed for many other applications, such as in integrated photonic circuits [51], damping of mechanical oscillations [52], and solar sails in outer space [53].

## 4.2 Optical tweezers

As mentioned above, the invention of the laser in the mid-1900s made it possible to exploit the minuscule optical forces of light. Ashkin discovered in the 1970s and 1980s that, with tightly focused laser light, it is possible to manipulate micro-particles. The future Nobel laureate found that a focused Gaussian laser beam could not only propel particles forward via radiation pressure, but also stably trap them near the focal point of the beam [55, 104]. This can be explained using simple ray optics.

Let's consider a pair of highly focused rays (such as those emerging from a high numerical aperture (NA) microscope objective) incident on a spherical glass micro-particle submerged in water. Fig. 4.1, reproduced from Fig. 1a in [56], shows this pair of rays changing direction at the interfaces between the water and glass. This change in direction of a light ray can be calculated using Snell's law:

$$n_w \sin\theta_w = n_g \sin\theta_g \tag{4.1}$$

where $n_w$ and $n_g$ are the refractive indices and $\theta_w$ and $\theta_g$ are the angles between the normal and the ray's direction in water and glass, respectively.

This change in direction also indicates a change in the momentum of the rays. Newton's 3rd law dictates that the micro-sphere must experience an equal and opposite change in momentum (force) such that momentum is conserved. The forces felt by the micro-sphere due to the change in direction of the pair of rays A is indicated by $\mathbf{F}_\mathrm{A}$ in Fig. 4.1. The transverse components of the force are equal and opposite, such that they sum to zero. The axial components add together to give a net backwards force – a restoring force. The combination of this restoring force, which pulls the micro-sphere towards the focal point, and radiation pressure from the incident laser beam, which pushes the micro-sphere in the direction of laser propagation, creates a stable equilibrium position for the micro-sphere where the particle is said to be *optically trapped* slightly downstream of the focal point.

The initial experiments by Ashkin proved to be the conception of an entire field in physics, and optical tweezers have since been used to stably trap myriad particles, from simple spheres [56] to cells [58, 59]. It is now also possible to create arrays of multiple stable traps [64], create a "tractor beam" that pulls particles in the opposite direction of light propagation [65], rotate particles [66], image surfaces using trapped particles [68], indirectly trap particles using hydrodynamic flows from micro-machines [63], and even cool

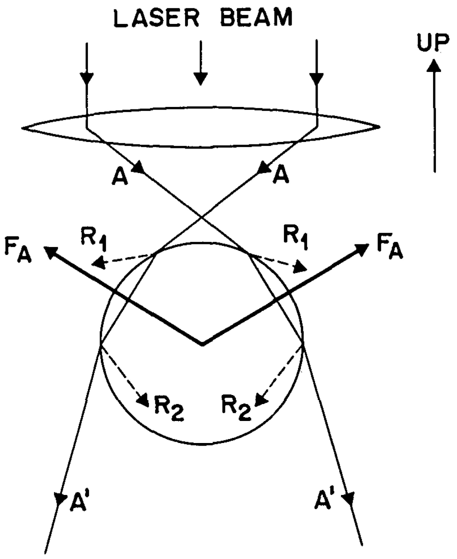

Figure 4.1: **Spherical Mie particle trapped in water by the highly convergent light of a single-beam gradient force trap.** Image reproduced from Fig.1a [56].

a single atom to its quantum ground state [69], all using optical tweezers. Potential future applications of optical tweezers include probing and imaging photosensitive biological systems [73], or creating micro- or nano-scale robots to assemble matter piece by piece [105, 106].

In the dipole approximation, the gradient force can be written as [107]

$$F_{\text{grad}}(\mathbf{r}) = \frac{1}{2}\frac{\alpha}{c\epsilon_0}\nabla I(\mathbf{r}) \tag{4.2}$$

where $\mathbf{r}$ is the position, $\alpha$ is the polarisability of the trapped dipole, and $I$ is the intensity of the optical trap. This equation provides intuition for the behavior of optical traps – the forces felt by a particle are dependent on the intensity gradient of the focused laser beam. Changing the intensity distribution of the optical trap in turn changes the optical forces experienced by an optically trapped particle. This concept is at the core of this research, where we ask how an intensity distribution can be manipulated using wavefront shaping to enhance the optical forces on a particle.

In the field of optical tweezing, it is a well known fact that the forces on an optically trapped particle in three-dimensions can be approximated as Hookean restoring forces for small displacements from the equilibrium position:

$$F_x \approx -\kappa_x \Delta x. \tag{4.3}$$

Here $F_x$ is the $x$-force felt by a trapped particle, $\kappa_x$ is the so-called stiffness of the optical trap, and $\Delta x$ is the displacement of the particle from its equilibrium position. Similar

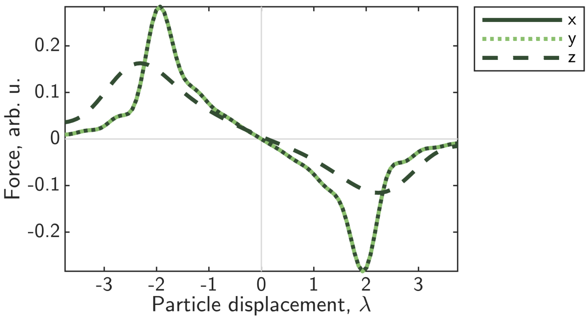

FIGURE 4.2: **Optical force curves** for a 1.5 µm radius silica ($n = 1.45$) microsphere in a Gaussian trap of NA = 1.3 and $\lambda$ =1064 nm in water ($n_w = 1.33$).

equations can be written for the $y$ and $z$ directions. The stiffness is a commonly used quantity to determine the performance of an optical trap. Hence, we use it to quantify the enhancement of our wavefront-shaped traps.

The Optical Tweezers Toolbox (OTT) [108] is an open source code enabling users to model optical tweezers, and calculate optical forces. The toolbox uses the T-matrix approach which is discussed later. Here we use it for such a calculation of the force curves for a 1.5 µm radius silica microsphere in water trapped in a Gaussian beam. Fig. 4.2 shows these forces in the $x$ (solid dark green), $y$ (dotted light green), and $z$ (dashed dark green) directions.

The linear Hookean force described above is clearly visible in Fig. 4.2 about the equilibrium location of the trap where the forces go to zero. This plot demonstrates how a particle displaced from equilibrium experiences a force that pulls it back to said equilibrium. As the sphere is displaced enough so that only its edge is immersed in the beam, the linear force-displacement response breaks down. The force increases to a certain point before sharply dropping off – at this point the particle is moved entirely out of the beam and has escaped the trap. This maximum magnitude of force can be thought of as the energy barrier preventing the particle from escaping the optical trap.

### Brownian motion and the confinement volume

If micro-particles are suspended in water and allowed to a freely move (i.e. in the absence of an optical trap), the water molecules around the particle continuously jostle it. This causes the particle to undergo a random walk through the surrounding space, also called Brownian motion. This motion is dependent on the temperature of the water, as this dictates how energetically the water molecules are moving. Optical traps suppress this motion by exerting a restoring force every time a trapped micro-particle is bumped out of the equilibrium position. The particle is restricted to randomly exploring a small volume around the equilibrium trapping position.

To quantify the enhancement of the optimised traps presented in the coming sections, the thermal motion of an optically trapped particle is considered. The extent of this motion can be described by a *thermal ellipsoid* [109] which characterises the 3D motion of the centre of mass (CoM) of an optically trapped particle as a tri-variate normal distribution. This thermal ellipsoid is hereafter dubbed the *confinement volume*, $V_c$ of the trapped particle.

For each direction, the empirical rule for normally distributed data states that the probability of finding the CoM of the particle within 3 standard deviations of the mean position in that direction is $p \approx 0.997$. Therefore, in 3D, the confinement volume is the region of space in which there is a $p \approx 0.997^3 \approx 0.99$ ($\sim 99\%$) probability of finding the particle's CoM.

This volume is given by

$$V_{\mathrm{c}} = \frac{4}{3}\pi(3\sigma_x)(3\sigma_y)(3\sigma_z) \tag{4.4}$$

where $\sigma_x$, $\sigma_y$, and $\sigma_z$ are the standard deviations of the motion in the $x$, $y$, and $z$ directions, respectively.

The confinement volume can be written in terms of the optical trap stiffness by considering the Equipartition Theorem. This theorem states that, for a system in thermal equilibrium, each degree of freedom of the system contributes, on average, $\frac{1}{2}k_{\mathrm{B}}T$ to the kinetic energy. The energy stored in an optical trap in 1D can be written as

$$U(x) = \frac{1}{2}\kappa(\Delta x)^2. \tag{4.5}$$

This expression can be used to directly link the thermal motion of a trapped particle to the stiffness of the optical trap:

$$\frac{1}{2}k_{\mathrm{B}}T = \frac{1}{2}\kappa_x\sigma_x^2 \tag{4.6}$$

where $k_{\mathrm{B}}$ is Boltzmann's constant, T is the absolute temperature, and $\sigma_x^2$ is the variance of $x$ motion equivalent to $\langle(\Delta x)^2\rangle$.

Consequently, the standard deviation of the motion along the $x$ direction can be written in terms of the optical trap stiffness $\kappa_x$:

$$\sigma_x = \sqrt{\frac{k_{\mathrm{B}}T}{\kappa_x}}. \tag{4.7}$$

Similar expressions can be written for $\sigma_y$ and $\sigma_z$, which combined with 4.4 yield an equation for the confinement volume in terms of optical trap stiffness:

$$V_{\mathrm{c}} = 36\pi\sqrt{\frac{k_{\mathrm{B}}^3T^3}{\kappa_x\kappa_y\kappa_z}}. \tag{4.8}$$

Enhancing the stiffness of an optical trap corresponds to a decrease in the confinement volume $V_c$ of a micro-particle in the trap. The aim of our work is to exert tighter control over an optically trapped particle by enhancing the stiffness in all directions simultaneously using wavefront shaping – thus reducing the volume the particle can explore.

## 4.3 Optical tweezers and the T-matrix

In order to allow us to investigate stiffness enhancements of optical traps, we make use of the T-matrix method to model optical tweezers. The matrix $T$ is similar to the scattering matrix, $S$, in that it provides information on how a field incident on a scattering medium is transformed into outgoing fields. The basis for $T$ is conventionally the vector spherical wavefunctions (VSWFs), as they are a complete set of solutions to the free space Helmholtz Equation (see Appendix A) in spherical coordinates. The incident and scattered fields can be written as linear combinations of these VSWFs:

$$E_{\text{inc}} = \sum_{n=1}^{\infty} \sum_{m=-n}^{n} \left( a_{mn} \mathbf{M}^1_{mn} + b_{mn} \mathbf{N}^1_{mn} \right) \tag{4.9}$$

and

$$E_{\text{scat}} = \sum_{n=1}^{\infty} \sum_{m=-n}^{n} \left( f_{mn} \mathbf{M}^3_{mn} + g_{mn} \mathbf{N}^3_{mn} \right). \tag{4.10}$$

The VSWFs are given by

$$\mathbf{M}^{(j)}_{nm}(k\mathbf{r}) = N_n h^{(j)}_n(k\mathbf{r}) \mathbf{C}_{nm}(\theta, \phi) \tag{4.11}$$

$$\mathbf{N}^{(j)}_{nm}(k\mathbf{r}) = \frac{h^{(j)}_n(k\mathbf{r})}{k\mathbf{r} N_n} \mathbf{P}_{nm}(\theta, \phi) + N_n \left( h^{(j)}_n(k\mathbf{r}) - \frac{n h^{(j)}_n(k\mathbf{r})}{k\mathbf{r}} \right) \mathbf{B}_{nm}(\theta, \phi) \tag{4.12}$$

where $N_n$ is a normalization constant, $h^{(j)}_n$ are spherical Hankel functions of order $j$, and $\mathbf{B}_{nm}$, $\mathbf{C}_{nm}$, and $\mathbf{P}_{nm}$ are the vector spherical harmonics. These are given by

$$\begin{aligned} N_n &= [n(n+1)]^{-1/2} \\ \mathbf{B}_{nm}(\theta, \phi) &= r Y^m_n(\theta, \phi) \\ \mathbf{C}_{nm}(\theta, \phi) &= \nabla \times (\mathbf{r} Y^m_n(\theta, \phi)) \\ \mathbf{P}_{nm}(\theta, \phi) &= \hat{r} Y^m_n(\theta, \phi) \end{aligned}$$

where $Y^m_n$ are normalized scalar spherical harmonics.

The sum over $n$ in Eqn. 4.9 and Eqn. 4.10 will be truncated at $n_{\text{max}}$, determined by [110]

$$n_{\text{max}} = (kr) + 4.05(kr)^{1/3} + 2 \tag{4.13}$$

This choice of $n_{\text{max}}$ ensures that the field is accurately captured over the volume of interest containing the particle of radius $r$.

The T-matrix is defined as

$$\begin{pmatrix} \mathbf{f} \\ \mathbf{g} \end{pmatrix} = T \begin{pmatrix} \mathbf{a} \\ \mathbf{b} \end{pmatrix} \tag{4.14}$$

which relates the beam shape coefficients (BSCs) of the incident ($\mathbf{a}$, $\mathbf{b}$) and scattered ($\mathbf{f}$, $\mathbf{g}$) VSWFs from Eqn. 4.9 and Eqn. 4.10. These BSCs are the respective weights of each individual VSWF which is included in the total linear combination of a given field.

The BSCs can be combined into a single vector, and Eqn. 4.14 can be rewritten as

$$\mathbf{u} = T\ \mathbf{v}. \tag{4.15}$$

The *T-matrix method* is useful because the matrix depends only on the geometry of the particle to be investigated. The freely available library known as the Optical Tweezers Toolbox (OTT) [108] in MATLAB utilizes this approach to model optical tweezers. The toolbox has the built-in capability to do many things, ranging from optical force calculations, to trapping landscape visualisations, to modelling optical trapping of multiple shapes of micro-particle. Here we utilised this library and extended it by adding new functions to explore three-dimensional optical trap enhancement.

### 4.3.1 The Bessel basis transformation

The Bessel basis is ideally suited to modelling light passing through the hard-edged aperture of a microscope objective, as it would in an experiment. Therefore, transformations from the Bessel basis to the VSWFs are implemented here.

In the pupil plane, each basis vector in the Bessel basis consists of an infinitely thin ring with an origin coinciding with the centre of the pupil. Each ring has constant amplitude and azimuthally varying phase described by $l\theta$, where $l$ denotes the orbital angular momentum of the beam (the number of times that the phase of a ring wraps between 0 and $2\pi$) and $\theta$ is the azimuthal angle.

For infinitely thin Bessel rings, the resulting fields are infinite in extent in the particle plane. Here a finite Bessel basis is considered, such that the rings have finite width. This limits the extent of the field needed to model the plane of the particle. The electric field of such a finite-width Bessel beam can be described by [111]

$$E_{\text{Bess}}(\mathbf{r}) = E_0 \int_0^{2\pi} e(\alpha,\theta) \mathrm{e}^{iK(\alpha,\theta)\cdot \mathbf{r}} \mathrm{e}^{il\theta} d\theta \tag{4.16}$$

where $E_0$ is the complex amplitude of the Bessel beam in the far field, $e$ is the polarisation vector, $\alpha$ is the cone angle, $\theta$ is the azimuthal angle, and $\mathbf{r}$ is the point at which we are evaluating the electric field.

One can think of a single finite Bessel ring in the pupil plane as a continuum of plane waves emitting from the points around the ring, propagating towards a focus with a set cone angle $\alpha$, and interfering to form an intensity pattern consisting of a series of dark and bright rings.

For the finite-sized discrete basis we consider here, these transformations from a finite Bessel basis to the VSWFs can be represented in matrix form. The T-matrix equation (Eqn. 4.15) can thus be rewritten as

$$\mathbf{u} = T(M_{\mathrm{B2V}}\mathbf{v}_{\mathrm{B}}) \tag{4.17}$$

where $\mathbf{v} = M_{\mathrm{B2V}}\mathbf{v}_{\mathrm{B}}$. The matrix $M_{\mathrm{B2V}}$ transforms from the Bessel basis to the VSWF basis.

## 4.4 1D optimum stiffness optical traps

It has been shown that the globally optimum optical trap capable of most stiffly trapping a micro-particle in one dimension can be found using techniques based on the Generalized Wigner-Smith (GWS) operator [86], which was already discussed in detail in Section 2.2.4. We note that other methods are also able to identify such a field [89, 112–114].

To begin investigating the concept of spatially shaping optical traps for stiffness enhancement, this global optimum solution was simulated by integrating such techniques based on the GWS operator into the OTT. This problem was previously detailed in [111]. We recall from Section 2.2.4 that the GWS operator is given by

$$Q_\alpha = -iS^{-1}\frac{dS}{d\alpha}, \tag{4.18}$$

where $S$ is the scattering matrix and $\alpha$ is a configurational degree of freedom of the system of interest. We also recall that the eigenvectors of e.g. $Q_x$ corresponding to the largest eigenvalues form the fields that apply maximum momentum in the $x$ direction.

It has also been shown that the operator that provides information about the stiffest possible optical trap in 1D is given by the derivative of the GWS operator with respect to a given direction [86]:

$$K_x = -\frac{\partial Q_x}{\partial x}. \tag{4.19}$$

Here, $K_x$ is this stiffness operator, $Q_x$ is the GWS operator for the $x$ degree of freedom.

To calculate $K_x$, the derivatives are replaced with finite differences as before with the GWS operator. For $K_x$, for example:

$$K_x \approx \frac{Q_x(\Delta x) - Q_x(-\Delta x)}{2\Delta x} \tag{4.20}$$

where $Q_x$ is the GWS operator for optimum momentum along $x$, evaluated at $\pm\Delta x$. Similar equations can be written for $K_y$ and $K_z$. The inverses needed to calculate the GWS operators $Q_x$ are estimated using the conjugate transpose.

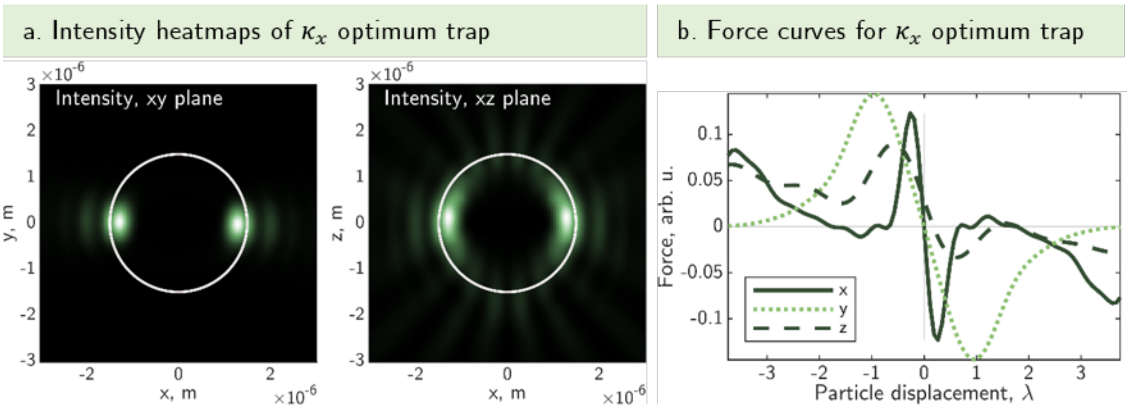

FIGURE 4.3: **Solution for optimum $\kappa_x$ trap** for a 1.5 µm radius silica ($n = 1.45$) microsphere in an optical trap of NA=1.3 with circularly polarised 1064 nm light. (a) Heatmaps showing cross-sections of the intensity distribution of the optimum field at the $z$ equilibrium position. The cross-sections show the two focused lobes just inside the surface of the microsphere (white circle), aligned along the $x$ direction. (b) Force curves showing the stiffness of the optimum field along $x$ (solid), $y$ (dotted), and $z$ (dashed).

In order to integrate this stiffness operator with the capabilities of the OTT, a transformation matrix from the the Bessel basis to the VSWF is used. This also effectively constrains the maximum angle of the light used to create the simulated optical traps and provide an easy and intuitive way to modulate the complex wavefront. This also accurately simulates the experimental setup used later to create optimised optical traps in the lab.

The Bessel basis used in this section consists of 50 cone angles, spaced evenly in radius across the pupil plane, and orbital angular momentum up to $l = 10$. Smaller rings have a lower maximum $l$, because small radii and high OAM rings correspond to an intensity distribution in the object plane where most of the light is concentrated well outside of the trapping area. Here, a total of 560 different modes is used. We choose this number to simultaneously keep the computational time as low as possible while still incorporating enough degrees of freedom to find a solution. Additionally, we choose to use circularly polarized light to remain consistent between simulations and experiments discussed later. Using circularly polarized light counteracts the changes in polarization induced by a high NA objective lens on the highest angle rays.

We apply this GWS-based approach to determine the optical trap with the highest stiffness $\kappa$ for a 1.5 µm radius silica microsphere with a refractive index of $n = 1.45$.

First, for this set of particle parameters, $K_x$ is calculated. Fig. 4.3 shows the $\kappa_x$ optimum trap for this operator. Fig. 4.3a shows normalised heatmaps of the intensity of the $\kappa_x$ optimum trap in the $xy$ plane along the transverse direction (left), and in the $xz$ plane along the propagation direction (right). The field forms bright intensity lobes along the $x$ direction just inside the surface of the microsphere – this is where the majority of the exchange in momentum between the light and particle now takes place. Fig. 4.3b shows the force curves for this trap in all three dimensions. As expected, the stiffnesses along $y$ and $z$ are not as large as along $x$. the trap

Fig. 4.4 compares the $x$ force curve for a Gaussian (light red line) and the $\kappa_x$ optimum traps (dark green line). In this case, there is an 11.7× enhancement in the optical trap stiffness (the slope of the force curve for small displacements from equilibrium) for the $x$ direction. Additionally, the maximum magnitude of the optical force is lower for the optimised trap – this means that the energy barrier preventing a particle from escaping the trap is reduced for the optimised trap. This suggests a trade-off between stiffness enhancement and ability to keep a particle trapped that must be considered for such an optimised trap.

Next, for the same set of particle parameters, $K_y$ is calculated. Given the circular symmetry of the particle and pupil plane, we predict that we will see the lobes of the optimised $\kappa_x$ field rotated. Indeed, the optimised field in Fig. 4.5a shows the $\kappa_y$ optimum trap for this operator forms bright intensity lobes along the $y$ direction just inside the surface of the microsphere. The force curves in Fig. 4.5b show similar results as above in Fig. 4.3b for the $\kappa_x$ optimum optical trap, but with $x$ and $y$ swapped. Here, the force curve along the $y$ direction shows a higher stiffness/steeper slope of the curve about the origin.

Fig. 4.6 compares the $y$ force curve for a Gaussian (light red line) and the $\kappa_y$ optimum traps (dark green line). Here, as above for the case of $K_x$, the stiffness was enhanced by a factor of 11.7, as expected because the particle is spherical and therefore rotationally symmetric. Intuitively, one would imagine the optimum field for stiffness along any arbitrary axis lying in the transverse to be the same solution, rotated to align with that arbitrary axis. Also, the energy barrier keeping the particle inside the optical trap is again reduced.

Finally, $K_z$ is calculated. Fig. 4.7 shows the $\kappa_z$ optimum trap for this operator. The field forms two bright, adjacent foci just inside the back surface of the microsphere in the $xz$-plane. Fig. 4.7b shows the force curves for this field in all three dimensions. As was explored in [111], the $K_z$ operator does not explicitly find the highest stiffness, stable

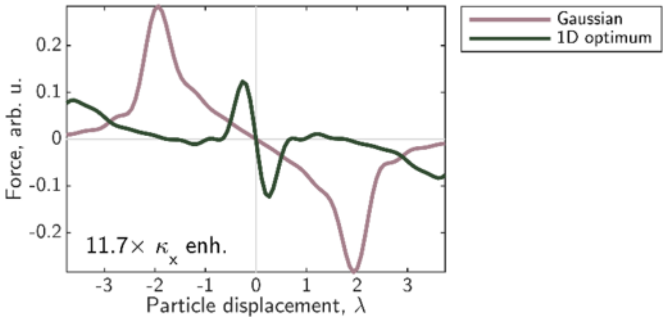

FIGURE 4.4: **Force curves along $x$ of the optimum $\kappa_x$ trap (dark green) vs. Gaussian trap (light red)** for a 1.5 µm radius silica ($n = 1.45$) microsphere in an optical trap of NA=1.3 with circularly polarised 1064 nm light. The stiffness along $x$ is enhanced by a factor of 11.7.

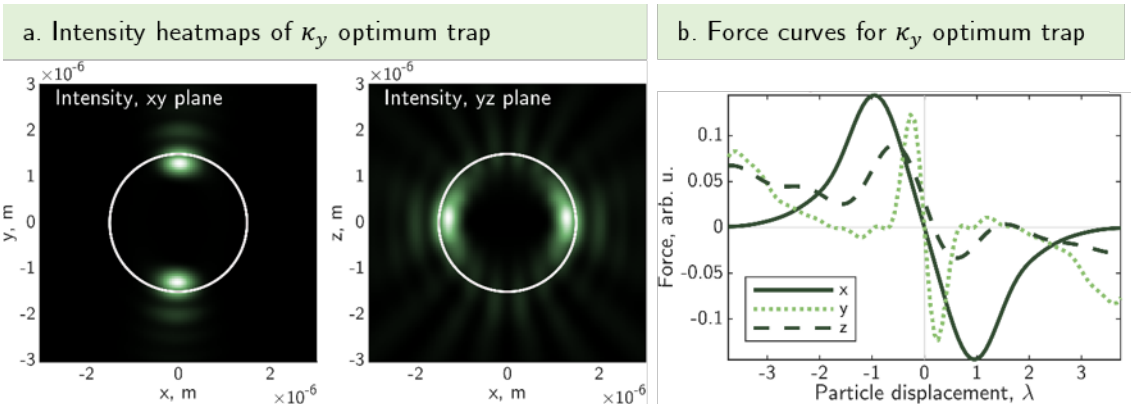

FIGURE 4.5: **Solution for optimum $\kappa_y$ trap** for a 1.5 µm radius silica ($n = 1.45$) microsphere in an optical trap of NA=1.3 with circularly polarised 1064 nm light. (a) Heatmaps showing cross-sections of the intensity distribution of the optimum field at the $z$ equilibrium position. The cross-sections show the two focused lobes just inside the surface of the microsphere (white circle), aligned along the $y$ direction. (b) Force curves showing the stiffness of the optimum field along $x$ (solid)), $y$ (dotted), and $z$ (dashed).

trap - instead, it finds the steepest negative force gradient at $z = 0$. The force does not necessarily cross from positive to negative in this region to create a stable trapping equilibrium. the z-force itself is positive over the entire diameter of the bead, as can be seen in Figure 5.16(b). An equilibrium does exist, at about $z = -5$ µm but the stiffness there is two orders of magnitude smaller than in a Gaussian beam trap.

Fig. 4.8 compares the $z$ force curve for a Gaussian (light red line) and the $\kappa_z$ optimum traps (dark green line). Although the slope of the force curve is increased by a factor of 5.82, this ‘trap’ is not stable due to the lack of an equilibrium position. This is indicated by the force not crossing zero in the region of linear slope. This optimum beam would continuously push the particle downstream, and away from the trap entirely.

These improvements in one-dimensional optical trap stiffness are encouraging to the

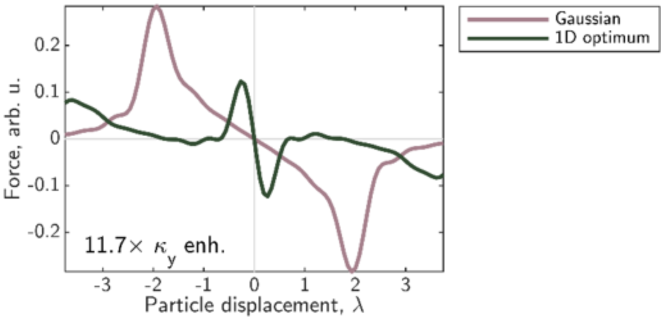

FIGURE 4.6: **Force curves along $y$ of the optimum $\kappa_y$ trap (dark green) vs. Gaussian trap (light red)** for a 1.5 µm radius silica ($n = 1.45$) microsphere in an optical trap of NA=1.3 with circularly polarised 1064 nm light. The stiffness along $y$ is enhanced by a factor of 11.7.

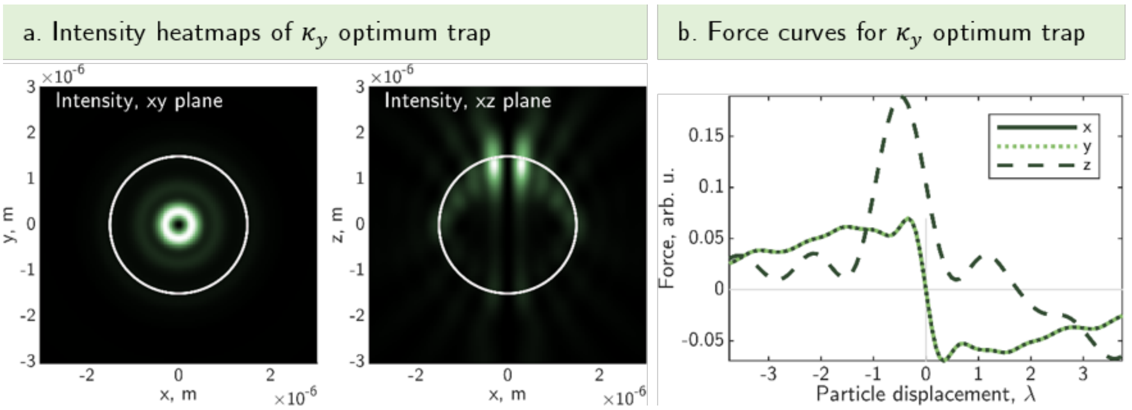

FIGURE 4.7: **Solution for optimum $\kappa_z$ trap** for a 1.5 µm radius silica ($n = 1.45$) microsphere in an optical trap of NA=1.3 with circularly polarised 1064 nm light. (a) Heatmaps showing cross-sections of the intensity distribution of the optimum field at the $z$ equilibrium position. The cross-sections show a focused ring just inside the back surface of the microsphere (white circle). (b) Force curves showing the stiffness of the optimum field along $x$ (solid)), $y$ (dotted), and $z$ (dashed).

goal of this project, but no constraints are placed on the other dimensions. This means that the optical traps need not be enhanced or even stable at all in these dimensions [103], as seen in Fig. 4.7. Additionally, extending one-dimensional optimum stiffness enhancement to three dimensions is not straight forward. In fact, the naive solution of finding the optimum in multiple dimensions and superimposing those results does not yield straightforward results [111], because the different optimum beams interfere and therefore affect one another and altering the overall intensity distribution of the optical trap. Analytically solving for the globally optimum solution in all dimensions is not possible because the operators for each dimension do not commute – the stiffnesses in each direction are not independent of one another. This remains an open problem in the field [103].

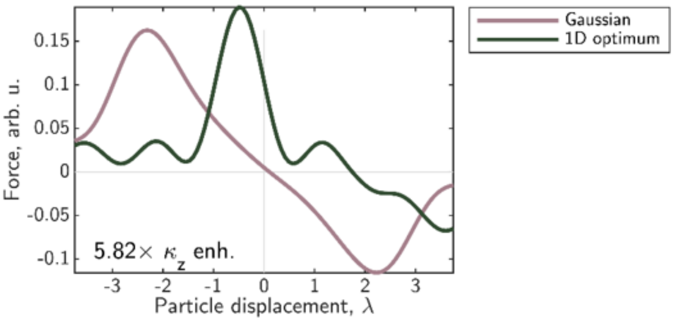

FIGURE 4.8: **Force curves along $z$ of the optimum $\kappa_z$ trap (dark green) vs. Gaussian trap (light red)** for a 1.5 µm radius silica ($n = 1.45$) microsphere in an optical trap of NA=1.3 with circularly polarised 1064 nm light. The stiffness along $z$ is enhanced by a factor of 5.82.

Therefore, a novel approach to 3D optical trap enhancement is needed to solve this challenging problem facing the field of optical tweezers. In the next section, an optimisation-based approach is introduced that has the ability to numerically determine 3D-enhanced optical traps.

## 4.5 Novel numerical approach for 3D trap enhancement

In this section, a novel approach to provide a solution to the problem of 3D optical trap enhancement is presented. This approach and its results were recently released in an ArXiv pre-print [115]. In it, a constrained interior point optimisation algorithm is used to create complex-modulated optical traps that demonstrate up to two orders of magnitude reduction in the confinement volume of a trapped particle.

This novel optimisation addresses two of the biggest challenges for this project. The first being the lack of an analytical solution, and the second being the computational bottleneck. Previous optimisations in the field, which have only been in 1D [116] or 2D [111], have been computationally expensive and taken on the order of days to converge to a solution. In comparison, the optimisation presented in the coming sections takes seconds to minutes to converge to a 3D solution using a desktop PC.

### 4.5.1 Constrained interior point optimisation

The optical trap to be optimised is expressed in the pupil plane in terms of finite Bessel rings, each with an associated amplitude and phase which can be modulated during the optimisation to affect wavefront shaping. Dr. Unė G. Būtaitė led the effort of developing this numerical optimisation and the simulations included in this section were carrier out by her.

Using the T-matrix approach in combination with the GWS operator and a constrained interior point optimisation, we find 3D enhanced optical traps. The details of this optimisation are elaborated on in [115]. Briefly, we describe the optical trap incident on a particle as a set of Bessel rings in the pupil plane, where we can perform wavefront shaping on the beam. Using a transformation from the Bessel to the VSWF basis, we then express these fields in the near-field of the particle as VSWFs – this allows us to use the OTT to calculate the T-matrix and subsequently calculate the GWS operators for force and stiffness. By using the scattered representation of the T-matrix in the OTT, we can write the operators as follows:

$$f_x^{\mathrm{opt}} = \mathbf{u}^\dagger Q_x \mathbf{u} = \mathbf{u}^\dagger \left( -\mathrm{i}\mathbf{S}^\dagger \partial_x \mathbf{S} \right) \mathbf{u}, \tag{4.21}$$

$$\kappa_x = \mathbf{u}^\dagger K_x \mathbf{u} = \mathbf{u}^\dagger \left( -\partial_x Q_x \right) \mathbf{u}, \tag{4.22}$$

where $f_x^{\text{opt}}$ is the force in the $x$ direction acting on the particle due to the incident wavefront $\mathbf{u}$, $\mathbf{S}$ is the scattered representation of the T-matrix describing how the light interacts with the particle, $\partial_x$ indicates a partial derivative with respect to the $x$-position of the particle, and $^\dagger$ indicates a conjugate transpose. The vector $\mathbf{u}$ describes the incident field contains the BSCs in the VSWF basis.

The operators $Q_x$ and $K_x$ are the cornerstones for this novel approach, allowing us to calculate the force and stiffness for any incident beam quickly because the T-matrix need only be calculated once at the start of the optimisation. This significantly reduces the computational time for 3D stiffness enhancement optimisations.

Fig. 4.9, reproduced from [115], shows results for 3D optimised traps found using our novel approach for 900 different microspheres of varying refractive index and radius. The heatmaps show the levels of enhancement to the stiffnesses and confinement volumes, as well as the corresponding reduction in needed power for the same trapping performance as a conventional Gaussian trap at 1064 nm. For a sizable portion of these optimised traps, the stiffnesses are increased by over $\sim 10\times$ in all dimensions and the confinement volumes are reduced by over $\sim 50\times$. Interestingly, these traps are stable for situations in which microparticles in a conventional trap are unstable (lilac regions of the enhancement plots in Fig. 4.9a-e).

Fig. 4.10 shows a handful of these 900 optimised traps. The common thread between the scenarios plotted here is that the intensity is mainly focused to just inside the surface of the microsphere. This can be understood by considering that the momentum transfer occurs at the interface between the particle and the surrounding medium, so concentrating the light there maximises the momentum transfer, thereby increasing the stiffness of the optical trap.

These results are encouraging, demonstrating for the first time that it is possible to make better use of available light by wavefront shaping the incident light to a shape that increases the resulting optical trap's stiffness. There are two sides to this: it is possible with these traps to either trap a particle over an order of magnitude more stiffly, or use over an order of magnitude less laser power to achieve the same trapping stiffness as a conventional Gaussian trap.

However, it was not expected that these traps would be easily implementable in an experiment. There are a multitude of reasons for this. The performance of the optical traps is strongly dependent on the precise intensity distributions and gradients, and slight deviations in these values result in immediate deterioration of the performance of the trap, as explored in the Supplementary material in [115], and commercially available silica microspheres have a statistical variation in their size. Because the optimised traps presented here are very sensitive to the exact size of the microsphere, and because we do not know the exact size of a trapped microsphere in experiments, implementing one of the numerically optimised traps in experiment is not straight forward. Additionally, optical aberrations in the created field cause deviations in the generated intensity distribution,

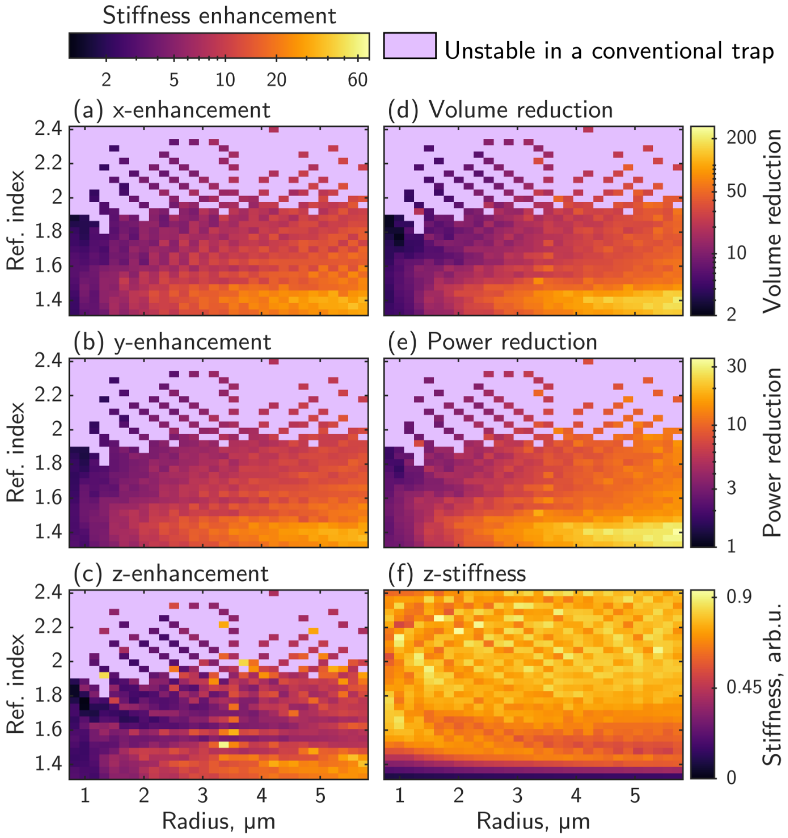

FIGURE 4.9: **Part of Figure 2 from** [115] showing the levels of enhancement for a range of 900 microspheres with different radii and refractive indices. The lilac colored areas correspond to beads that are unstable in a conventional Gaussian optical trap. The wavelength of the optical trap in these simulations was 1064 nm.

which would directly reduce the performance of the optical trap. The equipment used in a typical holographic optical tweezers system also introduces elements with some degree of uncertainty or deviation from simulation, such as the cross-talk between SLM pixels and the behavior of high angle rays in high NA microscope objectives.

Nonetheless, in the next chapter, we introduce the experimental set up used to try and experimentally demonstrate such 3D trap enhancements for the first time.

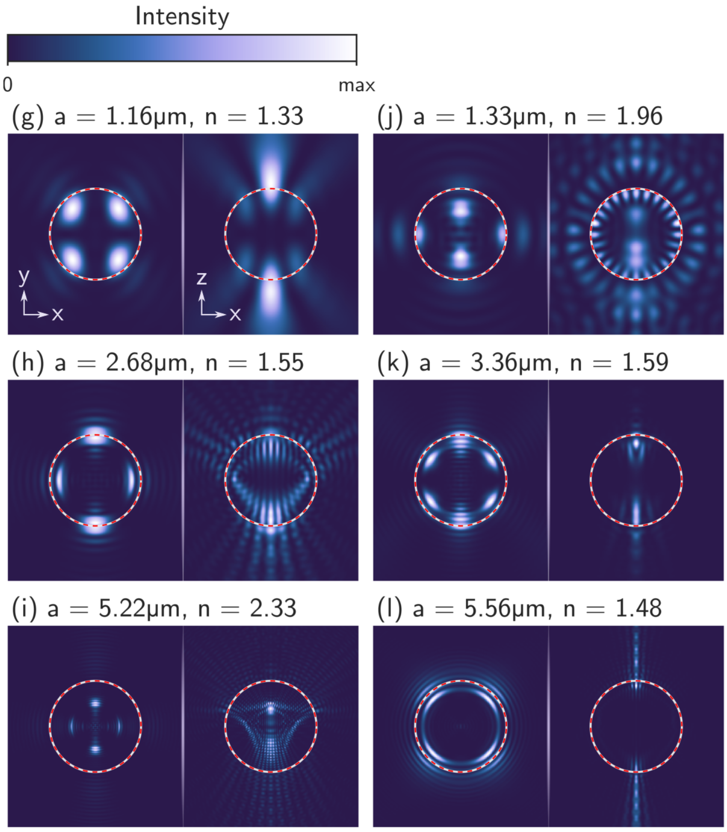

FIGURE 4.10: **Part of Figure 2 from [115]** showing intensity cross-sections of 6 numerically optimised optical traps. Each trap is optimised for the microsphere with radius $a$ and refractive index $n$ indicated above each subfigure (g-l). The cross-sections show the transverse (left) and axial (right) planes at the equilibrium position.

## Chapter 5

# Holographic optical tweezers setup

WITH the aim of enhancing optical trapping in three dimensions, and heeding the sensitivity of numerically optimised optical traps to minute differences in micro-sphere properties, it was clear that the experimental implementation of this approach needed to be incredibly precise. With this goal in mind, I redesigned and rebuilt the holographic optical tweezers (HOT) system I was provided at the start of my postgraduate research.

The finalised system is described in the next section, followed by details of various methods of aberration correction performed on the system, with the goal of generating the highest quality optical traps possible with this HOT setup.

## 5.1 Experimental setup

### The laser path in the HOT

The HOT system used for the experiments presented in this thesis is shown schematically in Figure 5.1. A 1064 nm continuous wave laser (Laser Quantum: VentusIR, 3 W) is expanded (5×) onto the screen of a liquid crystal spatial light modulator (Boulder Non-linear Systems: XY-series, 512×512 resolution). The phase is spatially adjusted here by displaying a phase mask such as the one inset above the SLM in the schematic. The polarization of the laser is converted from linear polarisation to circular polarisation. The laser beam is then passed through a lens of focal length $f_1$ before splitting into two paths. A dichroic beamsplitter designed to reflect the laser wavelength diverts the laser into the main beam path, through a lens of focal length $f_2$, and onto the back of a 1.3 NA 100x microscope objective (Olympus, Thorlabs, RMS100X-PFO). This objective tightly focuses the wavefront-shaped laser beam to create the desired optical traps in the sample plane. A secondary laser path consists of the beam transmitted through the imperfect dichroic beamsplitter, which allows a fraction of a percentage of the incident laser to transmit instead of reflect. This transmitted beam is then collimated by a lens of focal length $f_3$, and then focused onto Camera 2 (Thorlabs, DCC1545M) by a lens of focal length $f_4$. The

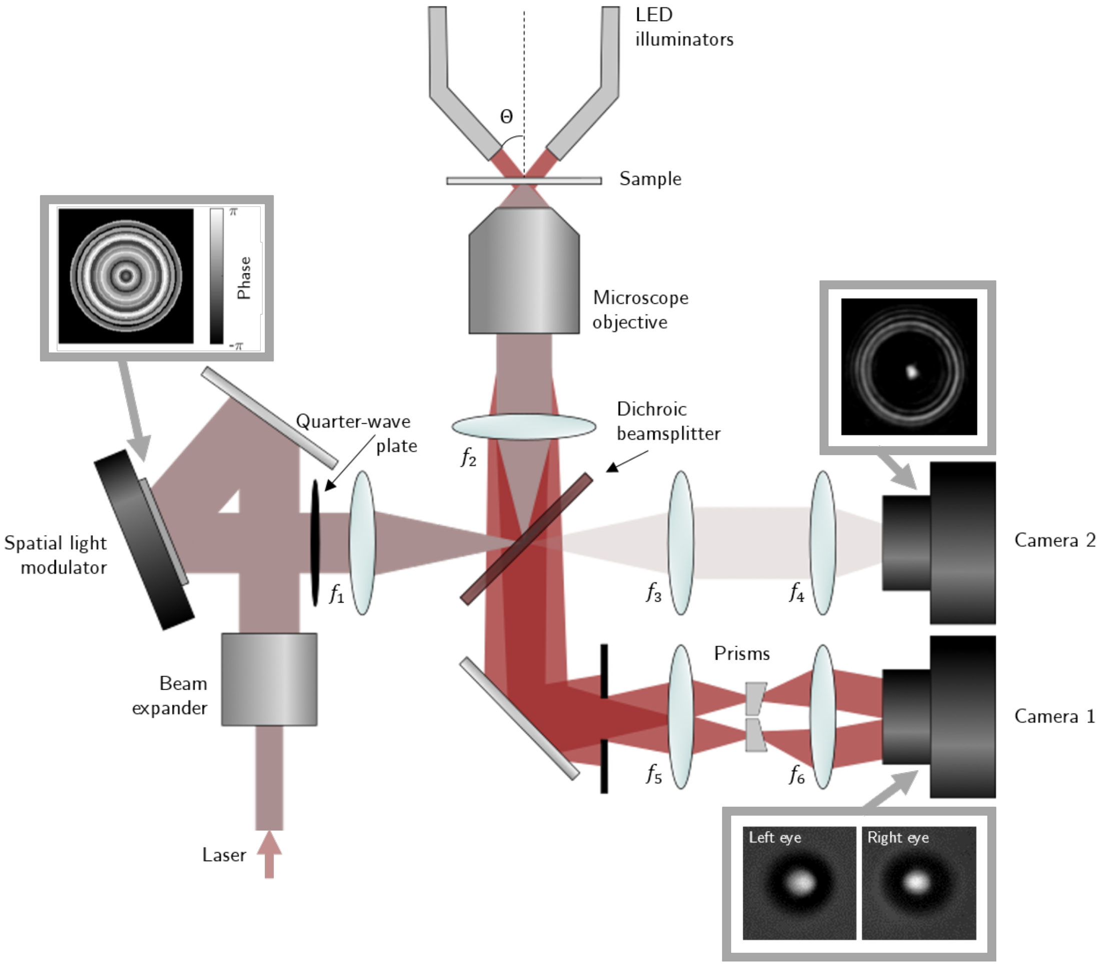

FIGURE 5.1: **Schematic of the HOT setup.** The laser is expanded to fill a liquid crystal spatial light modulator. An example of the phase mask displayed on the SLM is shown in the inset on the top left. The SLM is then re-imaged onto the back of the objective lens. The sample slide is placed in the front focal plane of the objective, where the micro-spheres can be manipulated using wavefront-shaped optical traps. The sample is back-illuminated with two red LED sources, forming twin views of the sample from different angles. The two images are collected by the same objective lens and later passed through two spatially adjacent prisms, positioned in the Fourier plane of the sample, to separate the two 'eyes' of the stereo-vision system. Finally the two spatially separated views of the sample are imaged side-by-side onto Camera 2, as seen in the inset on the bottom right. The intensity distribution of the wavefront-shaped optical trap can be recorded using Camera 2, as seen in the inset on the middle right.

inset above Camera 2 in the schematic shows an example of such an image of an optimised beam.

### Live 3D position measurements with stereomicroscopy in the HOT

We need to track trapped microparticles in 3D. To do this we use stereomicroscopy, which gives images of the sample from two different perspectives – enabling 3D tracking of particle positions using 2D image analysis of each image and combining the information from these two images using parallax.

Displacement of an object in $z$ corresponds to opposite displacements in the two 2D images along the direction parallel to the axis that the illuminators are mounted along. For example, if the illuminators are mounted along $x$, a displacement of a trapped microparticle in $z$ results in a displacement in $\pm x$ according to

$$\Delta z = \frac{(\Delta x_1 - \Delta x_2)}{2 \tan \Theta} \tag{5.1}$$

where $\Theta$ is the separation half-angle between the illuminators (as seen in Fig. 5.1), $\Delta z$ is the calculated displacement along $z$, and $\Delta x_1$ and $\Delta x_2$ are the displacements of the object along $x$ in the left (1) and right (2) images respectively. This approach allows nanometric tracking precision [117].

Experimentally, the necessary stereomicroscope is created by back-illuminating the sample with two LED illuminators angled at $\Theta$ from the normal to the sample. The light from the illuminators passes through the sample and the front of the microscope objective, is collimated by the lens of focal length $f_2$, before transmitting through the dichroic beamsplitter. The illumination is then filtered through a rectangular aperture, which reduces the field of view so both images of the sample fit side-by-side on the camera, before passing through a lens of focal length $f_5$. The light from the two 'eyes' of the system is separated by two prisms at the focal plane of the lens, and the rectangular images are finally collimated by a lens of focal length $f_6$ and reach Camera 1 (Mikrotron, EoSens CL)). The inset above Camera 1 shows a cropped region of interest of the left and right eye images.

### Details of the lenses used in the HOT

For the experiments presented in this thesis, the focal lengths of the lenses were: $f_1 =$ 150 mm (Thorlabs, LA1433-YAG); $f_2 =$ 100 mm (Thorlabs, ACA254-100-1064); $f_3 =$ 125 mm (Thorlabs, LA4235-1064); $f_4 =$ 75 mm (Thorlabs, LA1608-YAG); $f_5 =$ 150 mm (Thorlabs, LA1433-A); and $f_6 =$ 175 mm (Thorlabs, LA1229-A). The lenses in the laser beam path are AR coated for 1064 nm.

The focal lengths of the lenses were carefully chosen to achieve the proper magnifications $M$ throughout the system, which are calculated by

$$M_{ab} = -\frac{f_b}{f_a} \tag{5.2}$$

where $f_a$ and $f_b$ are the focal lengths of lens $a$ and $b$ respectively.

Lenses 1 and 2 (which yield a magnification of $M_{12} = -0.67$) were used to de-magnify the SLM, which has a screen diameter of 7.68 mm, to fill the back aperture of the objective lens, which has a diameter of 4.7 mm. This means that a circular area with diameter 7.05 mm on the SLM screen – 92% of the total SLM screen width – is needed to be able to modulate the phase of the entire numerical aperture (NA) of a created optical trap. Lenses 3 and 4 ($M_{34} = -0.60$)) create a focused image of the phase modulated optical trap on Camera 2, with high enough resolution for it to capture the details of the trap (see inset by Camera 2 in Fig. 5.1). Lenses 5 and 6 ($M_{56} = -1.17$) create slightly magnified, collimated images of the left and right eyes on Camera 1 to generate the stereo-images necessary for live 3D centre-of-mass symmetry tracking (see inset by Camera 1 in Fig. 5.1).

### Sample and objective mounting in the HOT

The sample is mounted in a spring loaded microscope slide holder, which is in turn mounted on a motorised 2D translation stage, allowing the entire sample to be viewed easily. To adjust the height of the focal plane within the sample, the microscope objective was mounted on a motorised 1D translation stage. In the experiments detailed in Chapter 6, the focal plane was translated 25 µm from the bottom of the sample by translating the objective lens, to ensure that a trapped microsphere does not bounce into the coverslip, and can freely explore its full 3D confinement volume. For details about sample preparation, see Appendix C.

One fact which we neglected to take into account at the time is the impact of boundary effects within the water of the sample. This interaction is created when an object moves close to a wall of the container, and is described by Faxén's law. This law is a correction to Stokes' law for the friction on spherical objects in a viscous fluid between two parallel boundaries [118]. However, we do not believe that this impacted the performance of our optimization. Plotting a histogram of the movement of an optically trapped microsphere displaced 25 µm above the bottom of the sample revealed a normal distribution of positions, lacking the asymmetry to indicate interactions of the microsphere with the boundary of the sample.

### Software control of the HOT

To control the system for experiments, the *Red Tweezers* LabVIEW software from [119] was modified. Custom LabVIEW subVIs were written and integrated with this existing experimental software framework to generate the desired phase patterns on the SLM (inset by the SLM in Fig. 5.1) and perform the aberration correction and optical trap enhancement experiments detailed in this and the next chapters. Appendix E details the use of this software and provides and overview of the back panel of the program.

## 5.2 Aberration corrections

Optical aberrations introduced into the focused laser cause distortions in the intensity gradients, which are extremely detrimental to the desired performance of a generated optical trap. In an attempt to reduce the effect of such aberrations in experiments, aberration correction of the optical system can be performed. In the case of the experiments presented here, this is done using the SLM in the optical setup. The SLM counteracts the optical aberrations by adding the inverse of the phase aberrations to the laser beam reflecting from it.

These optical aberrations are caused by misalignments, manufacturing imperfections, etc. of components within the setup. They can be corrected by subtracting a fixed, pre-calculated phase mask from every hologram displayed on the SLM. Several methods of aberration correction were tested and implemented throughout the course of the work presented in this thesis, and are discussed in detail below. They include a superpixel, Gerchberg-Saxton, and Zernike optimisation approach, as well as simply reducing the NA used in the system. Naturally, the resulting phase corrections are highly dependent on the exact configuration of the optical system, requiring re-measurement anytime the system changes (i.e. an optical component is adjusted).

Notably, aberration correction has been used in the past to increase the stiffness of optical traps. Previous work has included 2D optical trap enhancement through aberration correction [120–123]and the use of Laguerre-Gaussian beams [124]. This highlights the sensitivity of optical trap performance to the precise intensity distribution of the trap, and the importance of aberration correction in the quest for 3D-optimised optical tweezing stiffness.

### 5.2.1 Superpixel method

One method to correct aberrations along the laser path in a coherent optics setup was introduced in 2010 in [17]. Čižmár et al. demonstrated diffraction limited focusing through strongly scattering media by shaping the field incident on the scattering material using an SLM in the Fourier plane of the focus. In this approach, the SLM screen displaying some diffraction grating is divided into $n \times n$ superpixels – individual modes on a rectangular lattice of lower resolution than the number of SLM pixels available – which splits the incident wavefront into $n^2$ independent spatial modes. Here, $n$ is the 1D resolution of the superpixel grid.

Next, a reference superpixel is chosen, which will have constant global phase delay with respect to the other superpixels. We iterate over each of the other superpixels to determine the phase aberrations across the superpixel grid. Two such reference and tester spatial modes are seen in Fig. 5.2a – in this case the simulated SLM screen is split into $10 \times 10$ superpixels. All other superpixels except the reference and tester superpixels are turned off (zero phase in these locations). A camera is used to re-image the focused laser;

this image is in turn used to probe the intensity of the generated focus. The phase delays of the other superpixels which are needed to correct the aberrations are determined as follows.

Fundamentally, this method works by determining the relative phase differences between all $n^2$ modes of the incident field, such that they all maximally constructively interfere at a chosen location. This interference between fields due to the reference and a single tester superpixel is described in [17] by

$$I_p(t) \propto |E_t|^2 + |E_r|^2 + 2|E_t||E_r| \cos(\psi_t - \psi_r + vt) \tag{5.3}$$

where $E_t$ and $E_r$ are the fields on the camera due to the tester and reference superpixels, respectively, and $\psi_t$ and $\psi_r$ are their phases. The phase term $vt$, where $0 = \psi_t - \psi_r + vt$, corresponds to the optimal phase delay for maximum constructive interference between the reference and tester superpixel modes.

To determine the optimal phase delay, the intensity at the location of the first diffracted order on the camera (or indeed at the location of a chosen camera pixel) is sequentially probed for values of $vt$ between 0 and $2\pi$. The optimal phase delay for one pair of reference and tester superpixels can be extracted by Fourier-transforming the interference signal $I_p(t)$. Once all of the relative phases for each of the superpixels is determined, the $n \times n$ phase delays are turned on together to form a grid of phase corrections.

To understand this method in more detail, it was simulated in LabVIEW using a $10 \times 10$ grid of superpixels. Fig. 5.2 illustrates the approach for a single tester superpixel. The reference superpixel was chosen near the middle of the lattice, where the intensity incident on the SLM is expected to be maximum in experiments. The fields from the

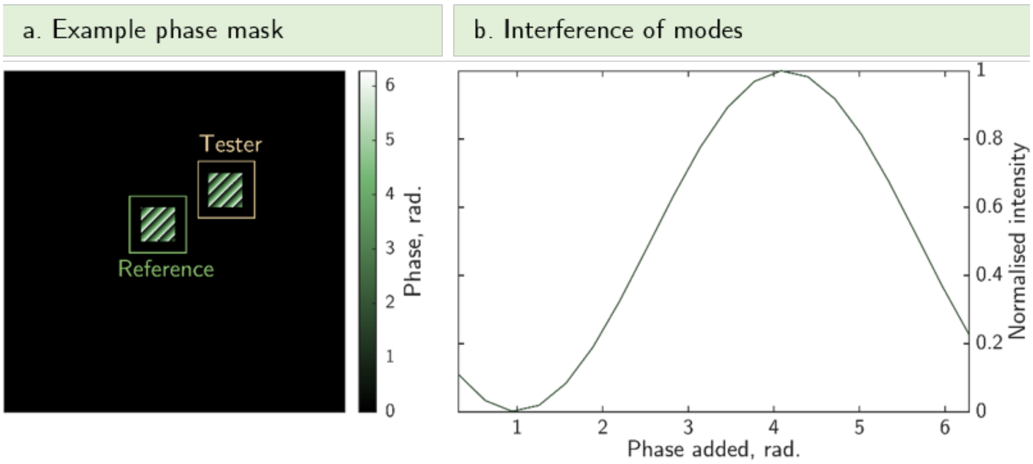

FIGURE 5.2: **Simulated superpixel aberration correction**, as demonstrated in [17]. (a) An example phase mask showing 2 superpixels – 1 tester and 1 reference – from a $10 \times 10$ grid of superpixels. (b) The modulation of the intensity of a selected pixel in the Fourier plane of the simulated SLM due to the shifting of the interference fringes created by the two superpixels.

tester and reference superpixels will interfere at the location of the 1st diffractive order focus, generating interference fringes which will have a bright maximum at the location of the focus if the appropriate phase delay is added to the tester superpixel.

Fig. 5.2b shows the simulated intensity of one pixel of the camera image within the image of the interference fringes, illustrating how adding a global phase to the tester superpixel causes this intensity to sinusoidally vary with respect to the added phase. For this superpixel, an added phase of $\sim 4$ radians optimises the constructive interference at the chosen pixel in the camera image. This process is then repeated for all other tester superpixels within the superpixel grid.

In addition to determining the phase delays between all superpixels to perform the aberration correction, it is possible to measure the intensity distribution of the laser profile on the SLM screen by iteratively probing the intensity of the 1st diffractive order focus for individual superpixels. This is useful to perform complex modulation of the wavefront, if needed, and also to provide information on alignment of the laser path. The latter application of the intensity distribution information was applied in this thesis to ensure precise alignment: if the circular region of intensity is not centred on the SLM, the laser is not aligned.

Fig. 5.3 shows experimental results of applying the above method in the HOT system shown in Fig. 5.1 used for the experiments detailed in this thesis. The intensity distribution in Fig. 5.3a indicates that the laser is well-aligned, as it is centred on the SLM; it also provides insight into the actual size of the expanded laser beam in the system. From the configuration of the system, it was calculated that $\sim 92\%$ of the SLM screen corresponds to the full NA of the system; this is experimentally verified by the spatial extent of the intensity distribution shown here.

The measured phase delays in Fig. 5.3b illustrate the aberrations present in the laser path of the system. The noise present at the edges is due to a lack of light reflecting from those superpixels. Fig. 5.3c shows the same intensity and phase information in the form of a complex plot where the phase is represented by the color and the amplitude is represented by the brightness.

The camera images shown in Fig. 5.4 were obtained before (left) and after (right) aberration correction with this superpixel method. The images were taken using the same camera exposure settings, so that they are directly comparable. The quality of the focus has improved - the shape is more symmetric, and the intensity has increased.

This method of aberration correction relies on the light reflected from the glass-water interface of the sample reaching the camera that re-images this plane (Camera 1 in Fig. 5.1). An issue that arose in the implementation of this method was the low percentage of the laser light incident on the sample that actually made it to the imaging camera. This light has to be both reflected from the sample and also transmitted through the dichroic beamsplitter (designed to reflect light at the laser wavelength) to the imaging arm of the system. To address these low levels of light on the camera, special samples were

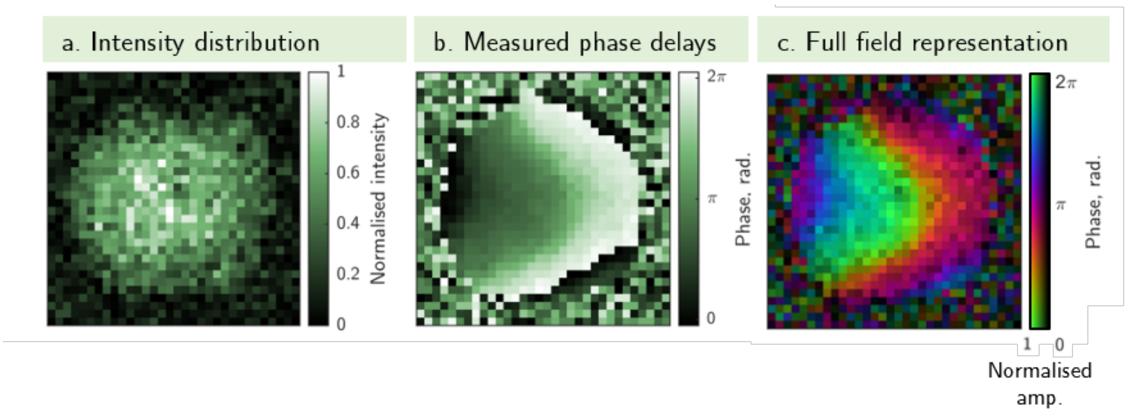

FIGURE 5.3: **Experimentally measured aberration correction of the HOT system** for 30 × 30 superpixels, using the method described in [17]. (a) Intensity distribution of the laser on the SLM screen. (b) Phase delays of individual superpixels, which taken together form the necessary phase corrections to remove aberrations. (c) Full field representation of the results in (a) and (b); here the color represents phase and the brightness represents amplitude.

fabricated in which half of the coverslip was covered with ∼ 40 nm of sputtered gold. This half-gold coverslip was used to create a sample such that the gold interface was between the glass of the coverslip and the water of the sample chamber (i.e. inside the sample). For a photograph of such a sample see Appendix C, Fig. C.4. In principle, a better (more reflective) metal could be used, however 40 nm of gold coverslips were readily available thanks to Dr. William Wardley, who provided then for my use. This enhanced the level of reflected light reaching the imaging arm sufficiently to perform higher resolution superpixel aberration correction, such as the one presented in Fig. 5.3 for a grid of 30 × 30 superpixels. Without such a sample, the system was limited to correction using a grid of ∼ 10 × 10 superpixels.

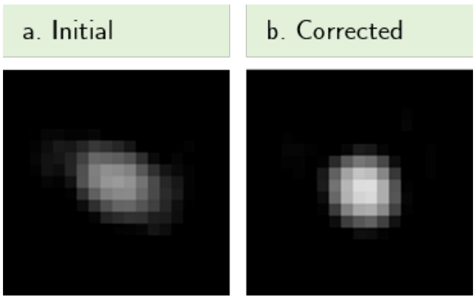

FIGURE 5.4: **Camera images of a focused laser beam.** (a) Initial focus. (b) Focus after superpixel aberration correction. Both images were taken with the same exposure settings; this means the increase in brightness is due to more light being focused to the desired location, and not due to changes in the camera settings.

### 5.2.2 Gerchberg-Saxton method

A method to correct for the surface deviations of the SLM screen, specifically to avoid reduction in optical trapping performance due to aberrations of the trapping beam, was introduced in 2007 by Jesacher et al. which relies only on a camera image of an aberrated beam in the focal plane [125]. Jesacher et al. induced aberrations by transmitting a beam through an angled piece of glass. Using a camera image of an aberrated beam in a Gerchberg-Saxton (GS) algorithm, the phase errors that constitute the phase aberrations of the experimental focus can be quickly calculated.

The GS algorithm is a well-known iterative algorithm [126–132] to find the unknown phase profile of an optical field from intensity only measurements. It relies on the fact that the phase affects how a beam diffracts as it propagates through space, so two planes of intensity-only measurements can reveal information about the phase of the field.

The algorithm is briefly described here, but it is discussed in greater detail in [125]. In short, we follow the same approach but with a beam reflected from a glass-water interface instead of transmitted through it. The algorithm functions as follows:

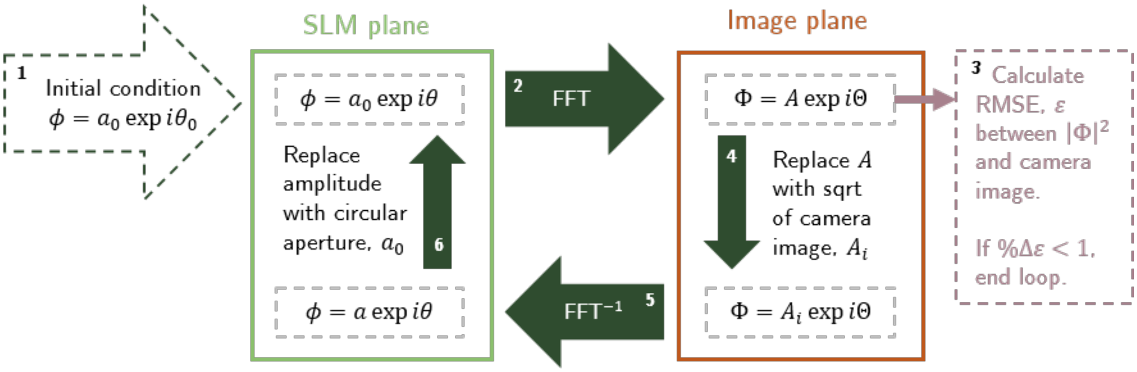

FIGURE 5.5: **Flowchart illustrating the Gerchberg-Saxtion aberration correction procedure.**

1. An initial condition (initial field, $\phi$) is chosen – a complex field with a circular aperture for its amplitude $a_0$ and a vortex for its phase $\theta_0$.
2. A fast Fourier transform (FFT) is performed on the initial field to propagate the field from the SLM plane to the image plane. The field in the image plane is called $\Phi$.
3. The root-mean-square error (RMSE), $\varepsilon$, between $|\Phi|^2$ and the intensity image of the aberrated beam from the camera is calculated. If the percent change of $\varepsilon$ from one iteration to the next is less than 1% ($\%\Delta\varepsilon < 1$), this procedure ends.
4. The amplitude $A$ of the complex array representing the field $\Phi$ is replaced with the square-root of the intensity image of the aberrated beam, $A_i$.
5. An inverse FFT ($\mathrm{FFT}^{-1}$) is performed on $\Phi$ to propagate it back to the SLM plane.

6. At the SLM plane the amplitude $a$ of the complex array representing the field $\phi$ is replaced by the circular aperture $a_0$ which was used as the amplitude of the initial field in Step 1.

These steps are repeated until $\%\Delta\varepsilon < 1$. The phase array $\theta$ from the last loop of these steps can then be subtracted from the initial phase mask used in the SLM plane to correct for the recovered aberrations.

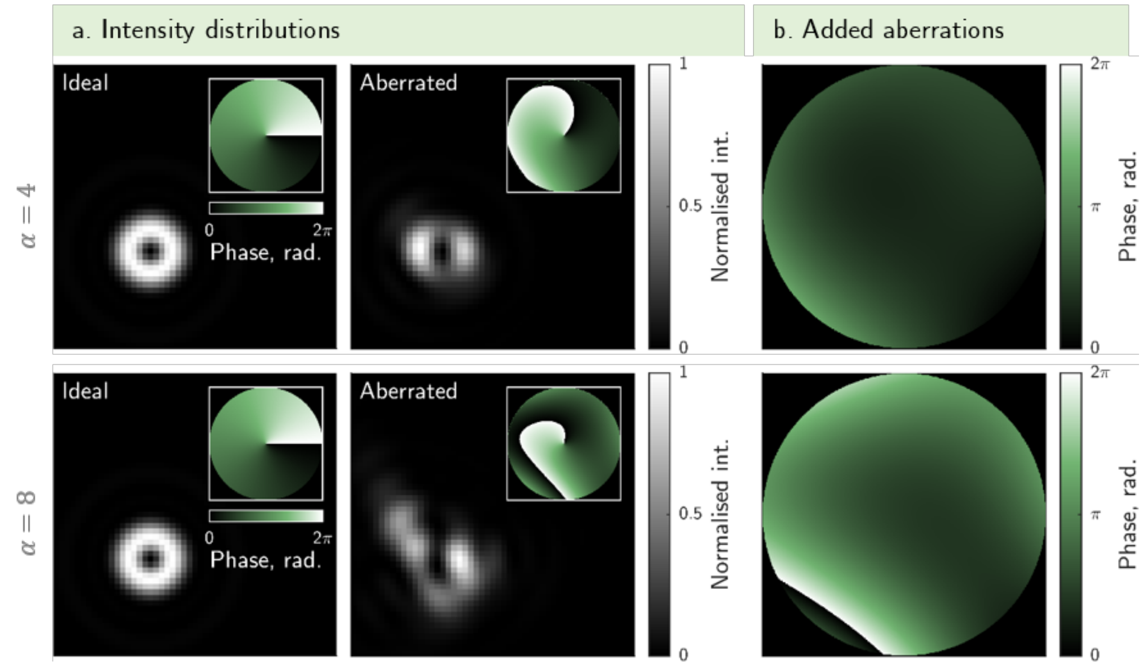

FIGURE 5.6: **Simulated intensity distributions and aberrations for the Gerchberg Saxton aberration correction method for a Laguerre Gaussian beam with $l = 1$.** (a) Ideal and aberrated images of the beam; the insets show the corresponding phase in the SLM plane. (b) The phase distortions added in the SLM plane, to generate the aberrated beam shown in (a). The top row corresponds to results for levels of aberration with the same maximum variation of phase as demonstrated in [125]; the bottom row corresponds to larger variations of phase and therefore larger levels of aberration.

As with the superpixel method discussed above, this approach to aberration correction was first investigated in simulations. The phase of a Laguerre Gaussian beam with radial index $r = 0$ and azimuthal index $l = 1$ was chosen as the initial phase in the SLM plane. The initial amplitude was a circular aperture with the same diameter as the resolution of the field, which was chosen to be $512 \times 512$ pixels to match the size of the SLM screen used in the optical tweezing experiments presented in this thesis.

In our test simulation, we are able to specify the degree of aberration, and then run the algorithm to see if we are able to recover the aberrations. To simulate the aberrations that would be corrected by this method experimentally, a weighted combination of the first 8 radial Zernike polynomials, as defined in [133], was calculated. This is done using

$$\zeta = \alpha \sum_{m,n} c_m^n R_n^m \tag{5.4}$$

to generate the aberrating phase $\zeta$, consisting of individual radial Zernikes $R_n^m$ each weighted by a different randomly chosen constant $c_n^m$, such that the sum is normalised to 1. This is in turn normalised to a maximum value of $\alpha$. A value of $\alpha = 4$ is approximately the level of phase distortions presented for the simulations in [125].

These aberrations were added to the Laguerre Gaussian phase in the SLM plane, and Fourier-transformed to generate the aberrated beam in the image plane. Fig. 5.6a shows the intensity distributions of the ideal and aberrated Laguerre Gaussian beams in the image plane, as well as their corresponding phases in the SLM plane, for two levels of aberrations. The added phase distortions used to generate the aberrated beams are shown in Fig. 5.6b.

The beams in Fig. 5.6 were used to initialise the Gerchberg-Saxton optimisation algorithm. The phase of the ideal beam in the SLM plane was used as the initial field's phase. The intensity of the aberrated field in the image plane was used in place of the experimental camera image to calculate the RMSE, $\varepsilon$. Fig. 5.7 shows the optimisation results for the algorithm described above. The progression of the algorithm is shown in Fig. 5.7a with the normalised RMSE, $\varepsilon$. Included are the intensities in the image plane of the initial aberrated and final corrected fields, after subtraction of the recovered aberrations. Fig. 5.7b shows the aberrations that were recovered by the algorithm and the remaining aberrations.

For levels of aberration similar to those considered in [125], the remaining aberrations consist of mostly flat and uniform phase without any visible distorting phase features missed by the phase retrieval of the GS-algorithm, indicating this method of aberration correction succeeded. The remaining distortion in the centre is due to the singularity in the initial field phase, which was explained in [125] as being due to a violation of the sampling criteria in the central region of the phases. However, for larger levels of aberrations, the algorithm failed to retrieve the phase aberrations. This indicates that this algorithm is not reliable for cases in which the aberrations become more extreme. This is because the GS algorithm optimises towards a local solution which could be far from the globally optimum solution if the initial field is too distorted in comparison to the ideal field, i.e. the case where aberrations are severe.

In the experimental implementation of this technique, it is important to properly resize the initial field such that the FFT that generates the field in the image plane is the same size in pixels as the real experimental image on the camera. This is done here by padding the initial condition with the needed number of rows and columns of zeros. Fig. 5.8 shows experimental results for aberration corrections found using this method. The figure shows camera images of the reflected laser beam on Camera 1 in the HOT

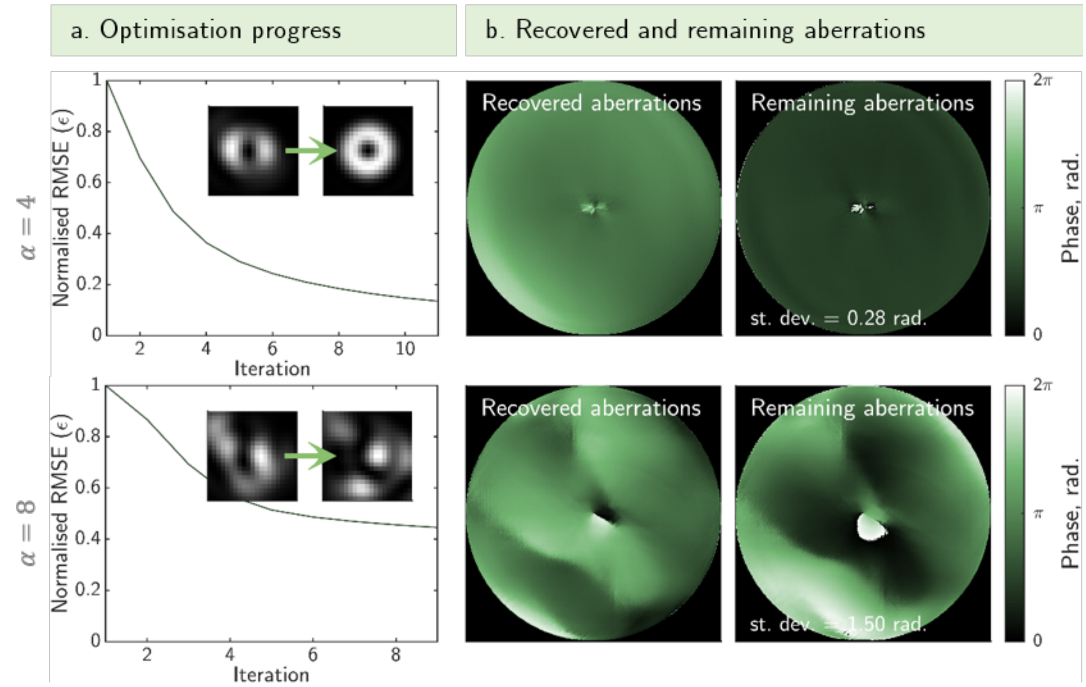

FIGURE 5.7: **Simulated performance of the Gerchberg-Saxton aberration correction method** (top) for lower levels of aberration and (bottom) higher levels of aberration. (a) Progression of the optimiser, showing the decrease in the RMSE $\varepsilon$ with increasing iterations. The insets show the intensity of the initial aberrated and final corrected fields in the image plane. (b) Phases recovered by the algorithm, and remaining aberrations calculated by subtracting the recovered phases from the full aberrations in Fig. 5.6b. For higher levels of aberration, this algorithm fails to retrieve the phases and therefore cannot correct the aberrations.

setup; the insets show the phase masks displayed on the SLM, minus the diffraction grating phases, used to generate the traps. As was also presented in [125], multiple cycles of this method can be used to further improve the quality of the focused image, as seen in Fig. 5.8b.

This method of aberration correction does not perform as well for the HOT system used in this research, as the optical setup presented in [125], which was much simpler. The optical setup there images the Fourier plane of the SLM directly, while the HOT setup used here re-images reflections of the tightly focused laser from the glass-water interface of a sample. A combination of effects from the high NA objective in the HOT setup and differences in using the reflected or transmitted light may be at the root of this reduction in algorithm performance.

### 5.2.3 Zernike method

The focal plane of the objective lens for the previously described aberration techniques is located at the glass-water interface of the sample, and therefore these techniques only

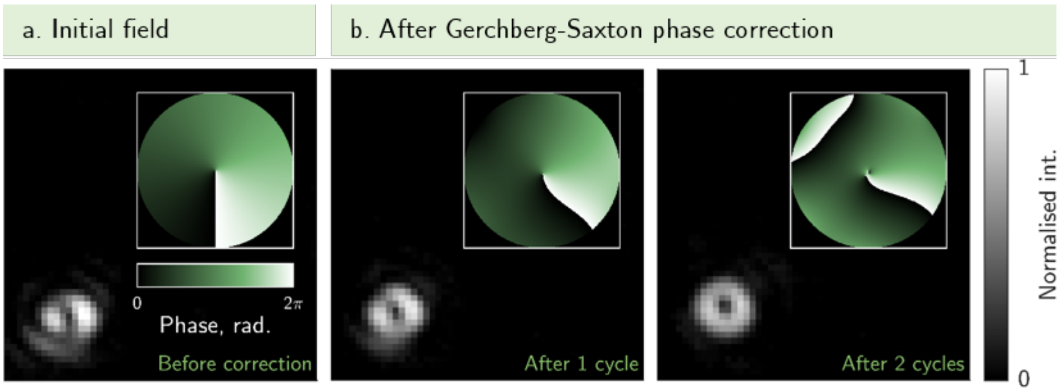

FIGURE 5.8: **Experimental aberration correction performed using the Gerchberg-Saxton algorithm.** (a) Camera image showing the initial aberrated, focused beam. The inset shows the phase mask, minus the necessary diffraction grating, displayed on the SLM screen to generate the camera image.

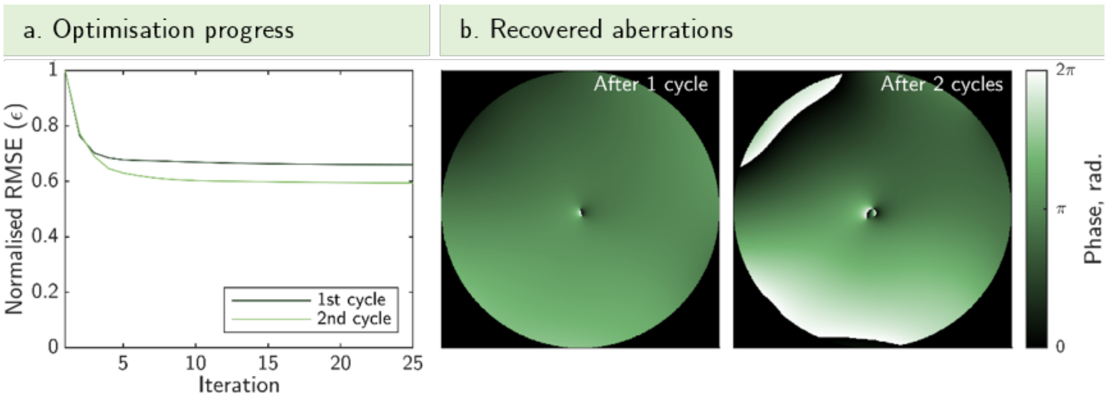

FIGURE 5.9: **Performance of experimental Gerchberg-Saxton aberration correction algorithm.** (a) Progression showing normalised RMSE $\varepsilon$ for two consecutive cycles of the optimiser. (b) The recovered phases after each of the two consecutive cycles.

correct aberrations to the glass-water interface. They use the light reflected at this interface, which is re-imaged onto a camera, as the marker to measure aberrations. Therefore, the superpixel and Gerchberg-Saxton methods of aberration correction neglect any aberrations introduced between the interface and the trapped particle itself. As it turns out, this is not a negligible omission, as discussed below.

In this section, a novel approach to aberration correction in HOT setups is detailed which uses live feedback from an optically trapped microsphere in an optimiser to retrieve the necessary linear combination of Zernike radial polynomials to recreate the aberrating phases present in the HOT system.

### Note about the aberrating effect of the glass-water interface

The glass-water interface introduces additional aberrations to the focused optical trap, which cannot be measured with either the superpixel or GS methods described previously because these methods use light reflected from the interface itself, not the location within the water at which experiments will be performed. This is a well known problem in the field of optical tweezers and microscopy [107, 134, 135] that results in the distortion of a focus through an interface, mainly through spherical aberration. Of the methods introduced here, only this Zernike optimisation approach can inherently take these additional aberrations into account.

### Zernike optimiser for aberration correction

Instead of using an image of the reflected laser light to extract information about the system's aberrations, here a new method is proposed using live tracking data from a trapped micro-sphere as the marker for these aberrations. Ideally, a focused laser beam would form an ellipsoidal trap in three dimensions, such that it is elongated along the axial direction (propagation direction) of the laser beam. In the presence of aberrations, however, this ellipsoid becomes distorted.

Because optical tweezers fundamentally rely on the exchange of momentum between the incident laser and the trapped micro-particle, the precise intensity distribution of the focused trap including aberrations impacts how tightly the micro-particle is trapped, for better or (usually) for worse. For spherical particles it intuitively follows that aberrations of a focused Gaussian beam will induce a reduction in the three dimensional trapping stiffness. The optimisation algorithm detailed here attempts to correct these distortions by extracting information about the trap stiffness from live tracking data of a trapped micro-sphere and compensating for the aberrations on the displayed phase hologram used to generate the optical traps.

Before starting the optimisation, a 15.03 µm diameter silica micro-sphere was trapped in the zero-th diffractive order focus. The bead was translated 25 µm from the bottom of the sample using the translation stage, to ensure its 3D motion in the trap is not restricted by the coverslip.

The basis for this optimiser consists of the first 12 radial Zernike polynomials as defined by Zernike in [133]. Using an algorithm relatively robust to noise, similar to the one presented in [91], it is possible to extract the optical aberrations present within an HOT system such as the one used here. These aberrations can be expressed as a linear combination of each of the radial polynomials. Because of the configuration of the HOT setup (see Appendix C), the phase correction patterns were generated within a circular aperture centred on the SLM screen with a diameter of 92% of total SLM screen width.

Each polynomial is considered consecutively, so that only one is probed at a time. The amplitude of each radial polynomial needed to create the total sum of all aberrations is determined as follows.

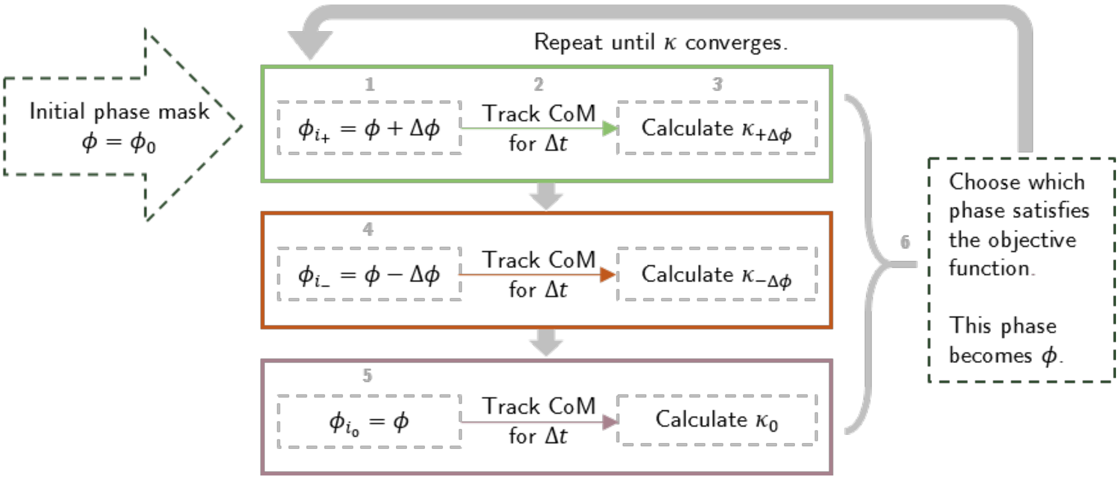

FIGURE 5.10: **Flowchart illustrating the Zernike aberration correction optimisation.**

1. For a chosen radial polynomial, a small amount $\Delta\phi$ of it is added to the phase mask $\phi$ displayed on the SLM.
2. The centre-of-mass (CoM) of the trapped micro-sphere in three dimensions is tracked for a time $\Delta t = 10$ s, an integration time that is long enough to accurately calculate statistics from the tracking data – a full discussion of the choice of integration time is presented in Section 6.2.3.
3. From the 3D tracking data, the standard deviation of the three dimensional motion of the CoM of the microparticle is calculated. Using the Equipartition Theorem as in Eqn. 4.6, the stiffness of the current aberrated optical trap $\kappa_{+\Delta\phi}$ is calculated.
4. Steps 1-3 are repeated, this time with a small amount $\Delta\phi$ of the chosen radial polynomial subtracted from the starting phase mask, such that $\kappa_{-\Delta\phi}$ can be calculated.
5. Steps 1-3 are then repeated for the initial phase mask, and $\kappa_0$ is calculated.
6. From these three scenarios, the phase configuration $\phi$ which maximises the objective function is selected. The objective function chosen here was that the average of stiffness in the $x$ and $y$ directions, $\bar{\kappa}_{xy}$, must increase, and the stiffness in the $z$ direction, $\kappa_z$, must not decrease. The chosen phase configuration that maximises the objective function then becomes the initial phase mask displayed on the SLM for the start of next iteration, when these steps are repeated for the next consecutive radial polynomial.

The optimiser is allowed to cycle through the polynomials, trying to find the optimum amount of each needed to correct the aberrations, until it is manually stopped once it has converged.

Fig. 5.11a shows the experimentally measured confinement volume of the centre of mass of a 15.03 µm silica micro-sphere. This size – the largest available within the research group

– was used because it was anticipated that larger micro-particles will be more heavily impacted by trap aberrations and therefore less stiffly trapped due to the distortions of the beam. The left subplot shows the confinement volume of the micro-sphere in a conventional Gaussian trap before aberration correction. The right subplot shows the same micro-sphere in the trap after optimisation as described above to determine aberrations present in the system. Fig. 5.11b shows (top left) the recovered aberrations, (top right) the stiffness enhancements between the aberration corrected beam and the original Gaussian beam, and (bottom) the progression of the optimisation as the stiffness enhancement vs. iteration. For the optimisation included in Fig. 5.11, correcting the aberrations of the focused trap resulted in a stiffness enhancement of 1.15× in $x$, 1.90× in $y$, and 1.18× in $z$, and an overall 1.61× confinement volume reduction.

Unfortunately, I was unable to successfully repeat this experiment. This is believed to be due to the many local minima that may exist on the complicated landscape of 3D optical trap enhancement. Perhaps the signal-to-noise ratio was too low for the algorithm to make correct choices about how to change the Zernike coefficients. A variety of microsphere radii and laser power settings were tested to try and recreate the above presented result, to no avail.

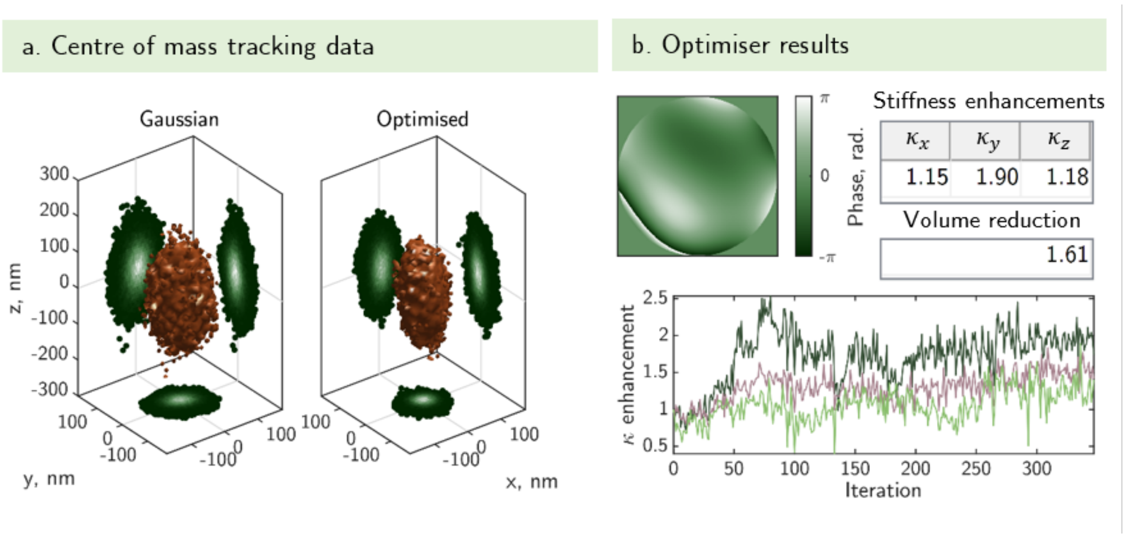

**Figure 5.11: Experimental Zernike Aberration Correction results.** (a) CoM tracking data showing the confinement volume of an optically trapped 15.03 µm diameter silica microsphere in a Gaussian (left) and in an optimised (right) trap. The 2D projections show the probability of finding the particle in a given location. (b) Results of the optimiser, including the recovered phase aberrations (top left), stiffness enhancements and volume reduction (top right), and the live stiffness enhancement progression (bottom).

### Future improvements to the Zernike aberration correction method

In future work, possible improvements to this method include a more spohisticated objective function; perhaps one, similar to the one described in the previous chapter in the constrained interior point optimiser section, in which the diagonal axes between $x$ and $y$ are also considered, would be sufficiently constraining to ensure convergence. Additionally, beginning the optimisation with a more stiffly trapped micro-particle may enhance the method's sensitivity to the aberrations because stiffer traps' performance is more affected by the presence of optical aberrations. Such a stiffer trap may be one like the 3D-enhanced optical traps discussed later in this thesis. Expanding the optimiser to include more Zernike polynomials, as well as allowing the optimiser to change multiple polynomials at once, may also prove beneficial to the process. Also, a metric could be easily built in to automatically end the optimiser once it has converged on a solution. This was not done here due to the sensitive nature of the experiment, which requires careful supervision to ensure the trapped micro-sphere is not ejected from the trap for any reason during the optimisation.

## 5.2.4 Reduced numerical aperture method

The previously introduced methods of aberration correction did not correct optical traps that extended over larger regions of the image plane than Gaussian beams, beams carrying low values of OAM. Because the optical traps generated in the experiments detailed in the coming sections were more spatially spread out than this, a new method to correct aberrations was needed.

The most reliable aberration correction for the optical tweezers experiments presented in this thesis was determined to be simply reducing the NA of the system by displaying a circular aperture on the SLM screen, limiting the region of the SLM used to generate the 1st diffractive order. This was discovered much to my disdain, as I had spent many long hours in the lab performing the previously described methods of aberration correction.

The aberrations cut out by reducing the NA are hypothesized to be due to a combination of aberrating effects of the SLM itself [99, 136] and the behavior of the high NA objective lens [137–139]. The SLM itself causes aberrations due to its potentially non-flat surface, and this warping is potentially more severe at the edges – therefore, cutting out light from these regions improves the quality of the laser beam's intensity distribution. The objective lens suffers from what is known as apodization, wherein rays exiting the objective at different angles may experience different loss and/or phase delays.

The NA of the objective lens is 1.3. With the specific lenses in the optical system, this corresponds to a circular region on the SLM with a diameter of $\sim 92\%$ of the SLM screen width. Utilizing this full NA results in a more aberrated optical trap as seen on the left in Fig. 5.12. The right of the figure corresponds to a circular aperture of 80% of the SLM screen width, and displays significantly reduced aberrations. This discovery was critical to the success of the experimental trap enhancement results in the next section, as the

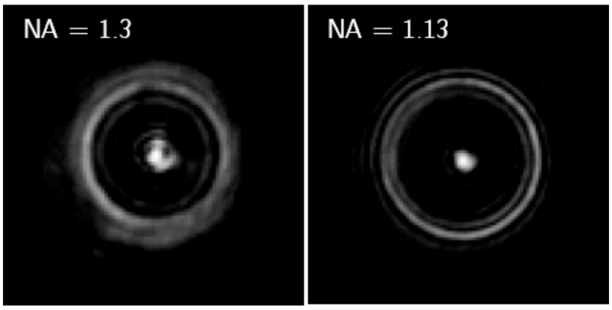

Figure 5.12: **The same focused optical trap with different NA,** taken using Camera 2. Reducing the numerical aperture from 1.3 to 1.13 reduced the levels of aberration significantly.

previously discussed methods of aberration correction failed to correct optical traps with a larger footprint in the sample.

# Chapter 6

# Enhancing optical tweezers by wavefront shaping

*If you liked it then you shoulda put a ring on it*
*Oh, oh, oh, oh, oh, oh, oh, o-ohh*

Beyoncé Giselle Knowles-Carter

ARMED with the experimental tools from the previous chapter, this chapter will address the problem posed in detail in Chapter 4 – can the stiffness enhancement of an optimised optical trap such as those presented previously be attained in experiment? For the many reasons discussed at the end of Chapter 4, the pre-designed traps presented earlier cannot be directly implemented experimentally with the capabilities of the holographic optical tweezers (HOT) used for this research. To briefly summarise, these reasons include aberrations of the laser beam, uncertainty in the exact parameters for experimental micro-spheres, cross-talk between pixels on the spatial light modulator (SLM), and apodization due to the high numerical aperture (NA) objective. Although we address the distortions of the laser through the aberration correction techniques described in Chapter 5, it is important to note that these techniques are not perfect – the remaining small imperfections of the laser intensity distribution are enough to disrupt the performance of a pre-designed optimised trap.

Instead, to overcome these issues, a live optimisation strategy is developed which allows the incident trap to be slowly adapted from a conventional Gaussian trap to a 3D enhanced trap, which ensures the particle is stably trapped for the entirety of the experimental optimisation. The experimentally optimised traps presented in this chapter demonstrate order of magnitude reduction in the confinement volume of the centre of mass of trapped microspheres for the first time.

Because spherical micro-particles are used in these experiments, the finite Bessel basis is ideally suited for this approach, as before for the pre-designed optimal traps. The traps generated with the Bessel ring phases in the pupil plane are also ring-shaped in the focal plane where the optical trapping occurs. In other words, the answer was to put a (wavefront-shaped) ring on it (the SLM).

## 6.1 Live 3D stiffness optimisation strategy

To perform a live optimisation, the HOT system (Fig. 5.1) introduced previously is used here. Using only feedback from the live centre-of-mass (COM) symmetry tracking of a trapped microsphere, the phase mask displayed on the SLM is iteratively adjusted to optimise the stiffness of said trap. The strategy is the same as that described in Section 5.2.3, but instead of Zernike polynomials as the basis of the phase masks displayed on the SLM a basis of finite Bessel rings (as described in Section 4.3.1) is used.

$N = 30$ rings are typically used here. The phase between these rings is linearly interpolated to prevent abrupt jumps in the phase displayed on the SLM. Abrupt jumps in the phase masks reduce the efficiency with which the trap is generated. This reduction in efficiency appears as a false reduction in the enhancement of the optical trap due to a reduction in the total laser power that is used to create the wavefront-shaped trap.

The phase of each ring is determined as follows:

1. For a randomly chosen half of the $N$ rings, a small amount $\Delta\phi$ is added to the phase of each chosen ring in the phase mask displayed on the SLM.

2. The centre-of-mass (CoM) of the trapped micro-sphere in three dimensions is tracked for a time (normally $\Delta t = 10\,\mathrm{s}$ is sufficient, this is discussed in detail in Section 6.2.3), an integration time that is long enough to accurately calculate statistics from the tracking data.

3. From the 3D tracking data, the standard deviation of the particle motion is calculated. This is related to the stiffness of the current aberrated optical trap $\kappa_{+\Delta\phi}$ via the Equipartition Theorem, as previously shown in Eqn. 4.6.

4. Steps 1-3 are repeated, this time with a small amount $\Delta\phi$ subtracted from the phase of the chosen half of the rings, such that $\kappa_{-\Delta\phi}$ can be calculated.

5. Steps 1-3 are then repeated for the initial phase mask, and $\kappa_0$ is calculated.

6. From these three scenarios, the phase configuration which maximises the objective function is selected. The objective function chosen can vary – a full list of tested objective functions and their constraints will be discussed later. An example of an objective function and its constraints that was used is that the stiffness in the $x$, $\kappa_x$, must increase, and the stiffness in the $z$ direction, $\kappa_z$, must not decrease. The chosen phase configuration that maximises the objective function then becomes the initial phase mask displayed on the SLM for the start of next iteration, when these steps are repeated for a new randomly chosen half of the rings.

The live 3D stiffness optimiser is allowed to repeat the above steps until it is manually stopped.

Ordinarily, such an optimisation takes on the order of a few hours to converge to a solution, due to the necessary integration times and number of iterations (typically a few hundred). To ensure that drift of the laser power over time or changes in the sample's temperature do not influence the results, the 3D tracking data in the initial conventional trap are remeasured at the end of the optimisation. This remeasured data can then be directly compared to the 3D tracking data for the optimised optical trap to extract enhancement factors of the stiffnesses in all directions, and subsequently the reduction of the confinement volume of the trapped microsphere.

### 6.1.1 LabVIEW implementation of the live 3D stiffness optimiser

The optical tweezers experiment is controlled using a modified version of the *Red Tweezers* software [119]. This program, which was originally developed by Richard Bowman, allows all-in-one control of the HOT system in a single interface. The ability to perform 3D COM symmetry tracking with the stereo-vision capabilities of the HOT used here is added to the software, as well as the above described optimisation algorithm. Using parallax, the LabVIEW software implements 3D live symmetry tracking by extracting the 3D motion of the CoM of a trapped micro-sphere from the two 2D camera images (left eye and right eye images) of the micro-sphere. This is discussed in more detail in Chapter 5.

**Phase holograms**

The hologram generation method included in the *Red Tweezers* is also replaced with a custom piece of LabVIEW code that creates the needed Bessel rings and phase gratings. Although slower, we did not need fast GPU-based hologram generation included in the

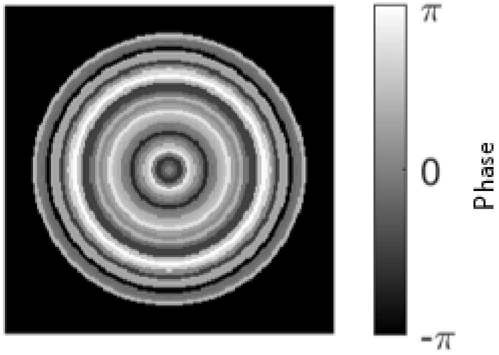

FIGURE 6.1: **Example of finite Bessel ring phase hologram** with 30 rings.

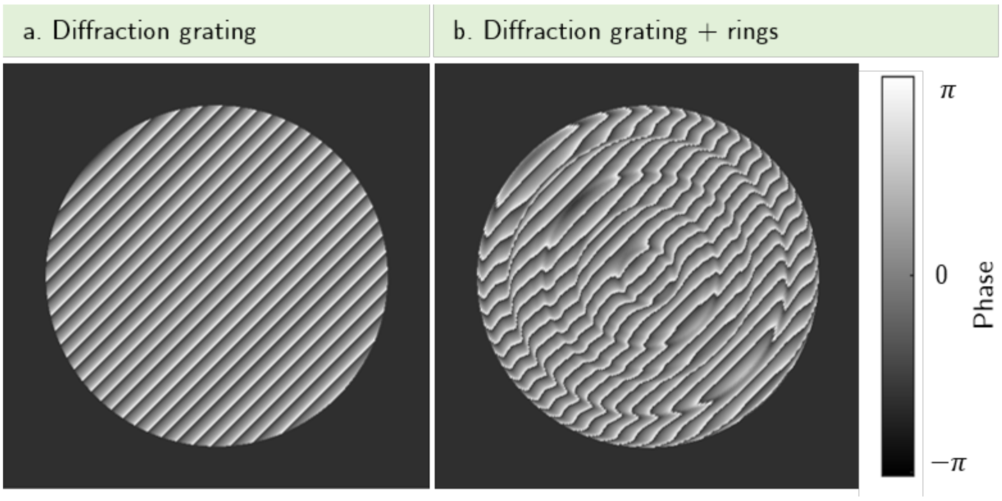

FIGURE 6.2: **Example phase holograms** showing (a) diffraction grating and (b) diffraction grating and interpolated Bessel rings.

software [119] for our optimisation experiments. The holograms are scaled to the appropriate size dependent on the HOT setup (magnifications, size of SLM pixels, size of camera pixels, etc.) using built-in parameters in the RedTweezers software (see Appendix E for more details).

The Bessel rings are generated at the resolution of the SLM ($512 \times 512$ pixels), with a programmable number (here $N = 30$) of rings which are linearly interpolated between with 4 sub-rings for each main Bessel ring. Fig. 6.1 shows an example of a phase hologram created with these Bessel rings.

The diffraction gratings used to create the first order focus which is used as the optical trap in experiments are generated using the WaveTrace library for LabVIEW originally written by Johannes Courtial at the University of Glasgow. Fig. 6.2a shows an example of such a diffraction grating. The Bessel rings and the diffraction grating can be added together to produce the phase hologram that is displayed on the SLM screen, as seen in Fig. 6.2b. The Bessel rings are interpolated over 4 sub-rings per ring to ensure that the phase does not abruptly jump – abrupt jumps in phase reduce the efficiency of the SLM, negatively impacting the performance of our optimisation.

### 6.1.2 Discussion of different objective functions and constraints

The choice of objective function and which constraints it is subject to is of course important for any optimisation. For this research, several different options are considered. The objective functions and constraints detailed below are not the only options – these could be tailored to a researcher's specific needs and adapted to other scenarios. For example, because spherical microparticles and traps with cylindrical symmetry were used in this research, the $x$ and $y$ stiffnesses were assumed to be the same. However, for non-spherical particles the constraints would need to be adjusted.

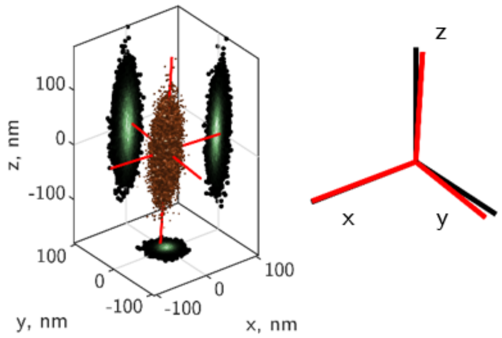

FIGURE 6.3: **Example of measurement axes** showing the lab axes (black) and major axes of the thermal ellipsoid (red) for a 9 µm diameter silica micro-sphere.

### Choice of measurement axes

The live 3D stiffness optimiser presented above minimises the standard deviation of the 3D motion of a trapped micro-sphere. This is a selectable parameter in the optimisation. This standard deviation can be calculated along different sets of axes. The live 3D stiffness optimiser here has the following three choices for these sets of axes.

1. **Lab axes**
   The first set of axes considered is the lab axes, such that the $xy$ plane is parallel to the floor of the lab, and the $+z$ axis points towards the ceiling (which is also the laser propagation direction). This choice of axes doesn't take into account any misalignments in the laser or imaging systems, such that the axes do not necessarily correspond to the major axes of the confinement volume.

2. **Evolving thermal ellipsoid axes**
   Next, to account for any misalignments in the laser or the stereo-microscope imaging systems, the thermal ellipsoid made up of the 3D tracking data are chosen for the measurement axes. As a reminder, the thermal ellipsoid, or confinement volume, is the volume of space explored by the CoM of a trapped micro-particle (this is discussed in detail in Chapter 4). The axes of the ellipsoid are remeasured for each configuration of the phase of the rings on the SLM. The axes are given by the eigenvectors of the covariance matrix of the 3D tracking positions. This choice allows the major axes of the ellipsoid to vary over time, which corresponds to a rotation of the thermal ellipsoid which is not desirable here because the goal is to optimise the stiffness of the optical trap along specified directions and compare these stiffnesses over the course of the optimisation.

3. **First measurement thermal ellipsoid axes**
   To address the shortcomings of the previous two choices of measurement axes, the major axes of the thermal ellipsoid corresponding to the initial Gaussian optical trap is chosen. Again, the eigenvectors of the covariance matrix of the 3D tracking

positions provide the major axes. In this case, the live 3D stiffness optimiser can take any misalignments into account and also prevent the thermal ellipsoid from rotating, consistently comparing the same axes throughout the course of the optimisation.

### Objective functions and constraints

The specific objective functions and constraints can be tailored to fit a desired scenario. The following combinations were included in the live 3D stiffness optimiser LabVIEW program.

1. **mean(XY) & Z**
   One possible set of objective function and constraints to the optimisation is to ensure that the average standard deviation of the motion in the $x$ and $y$ directions (the objective function) must decrease, while the $z$ standard deviation must not increase (the constraint). In principle this combination would allow a phase pattern that increases $x$ at the expense of $y$ stiffness to be found, as there were no additional constraints in place to prevent this from happening.

2. **X & Z**
   Another possible combination that takes advantage of the symmetries of the microspheres and traps considered in this research is to ensure $x$ standard deviation decreases (the objective function) and $z$ standard deviation does not increase (the constraint). By symmetry the $y$ standard deviation should also decrease.

3. **Y & Z**
   Alternatively, the $y$ standard deviation should decrease (objective function) and $z$ must not increase (constraint).

4. **Z & Y**
   Finally, the $z$ standard deviation should decrease (objective function) and $y$ standard deviation must not increase (constraint).

At a first glance it may seem that items 3 and 4 are identical, however they are indeed different. Item 3 prioritizes $y$ stiffness enhancement; in theory the live 3D stiffness optimiser could choose a path that never enhances the $z$ stiffness of the optical trap. Alternatively, item 4 prioritizes $z$ stiffness enhancement without the need to enhance the $y$ stiffness. In practice, these two objective functions behave identically, however there may be scenarios where this is not the case (i.e. non-spherical particles or a different basis for SLM phase patterns that lacks cylindrical symmetry).

## 6.2 Results: Experimental trap enhancement

The main experimental results of this project were recently released in the previously mentioned ArXiv pre-print [115], demonstrating an order of magnitude reduction factor in the confinement volume of silica microspheres with radii between 2.5 and 5 µm.

The above described live optimisation strategy was applied to this range of microsphere sizes. First, for a 4.99 µm radius silica microsphere, the results for this optimisation are shown in Fig. 6.4. The integration time for this scenario is $\Delta t = 10$ s, and a diffraction grating resulting in a shift of (5 µm, 5 µm, −1 µm) of the generated optical trap is used. The objective function for this run of the live 3D stiffness optimiser is the standard deviation of the motion along the lab axes, with Y&Z constraints as discussed above.

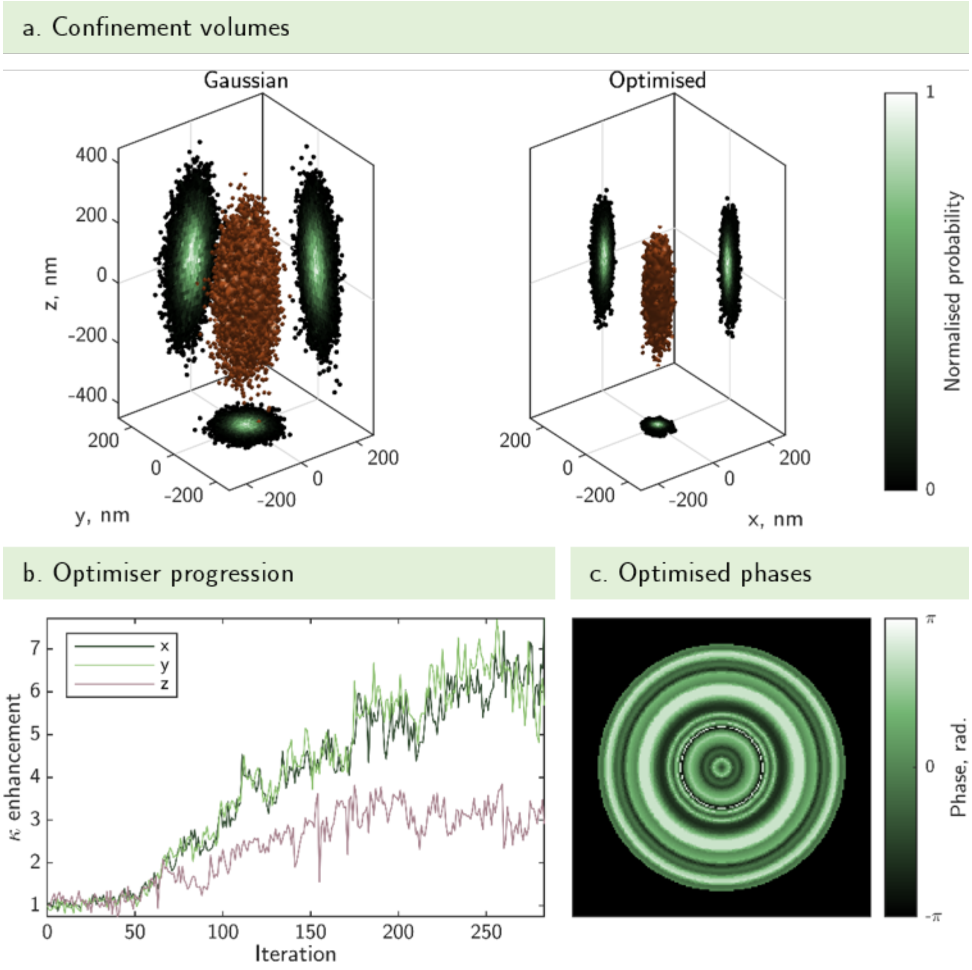

FIGURE 6.4: **Experimental 3D enhancement of an optical trap** for a 4.99 µm radius silica microsphere. (a) Live 3D tracking data for the microsphere trapped in the initial Gaussian trap (left) and the final optimised trap (right), demonstrating 11.0× reduction in $V_c$. (b) Progression of the live 3D stiffness optimiser, resulting in final stiffness enhancements of (7.1, 6.1, 2.8) for each direction respectively. (c) Final optimised phases of the rings on the SLM.

The confinement volumes for the microsphere trapped in an initial Gaussian (left) and final optimised (right) trap are shown in Fig. 6.4a, illustrating a volume reduction factor of 11.0× after optimisation. The progress of the live 3D stiffness optimiser is shown in Fig. 6.4b for the enhancement of all three stiffnesses over the course of the optimisation. The final stiffness enhancement factors are 7.1, 6.1, and 2.8 for $x$, $y$, and $z$ stiffnesses, respectively. Fig. 6.4c shows the final optimised phases of the rings that are added to the diffraction grating to generate the final optimised optical trap.

While the $x$ and $y$ stiffnesses are enhanced approximately the same amount, the $z$ stiffness is enhanced to a lesser extent. To investigate if a different set of constraints would impact this outcome, the experiment is repeated for a 4.99 µm radius microsphere, with 10 s integration time, and an underlying diffraction grating resulting in a shift of

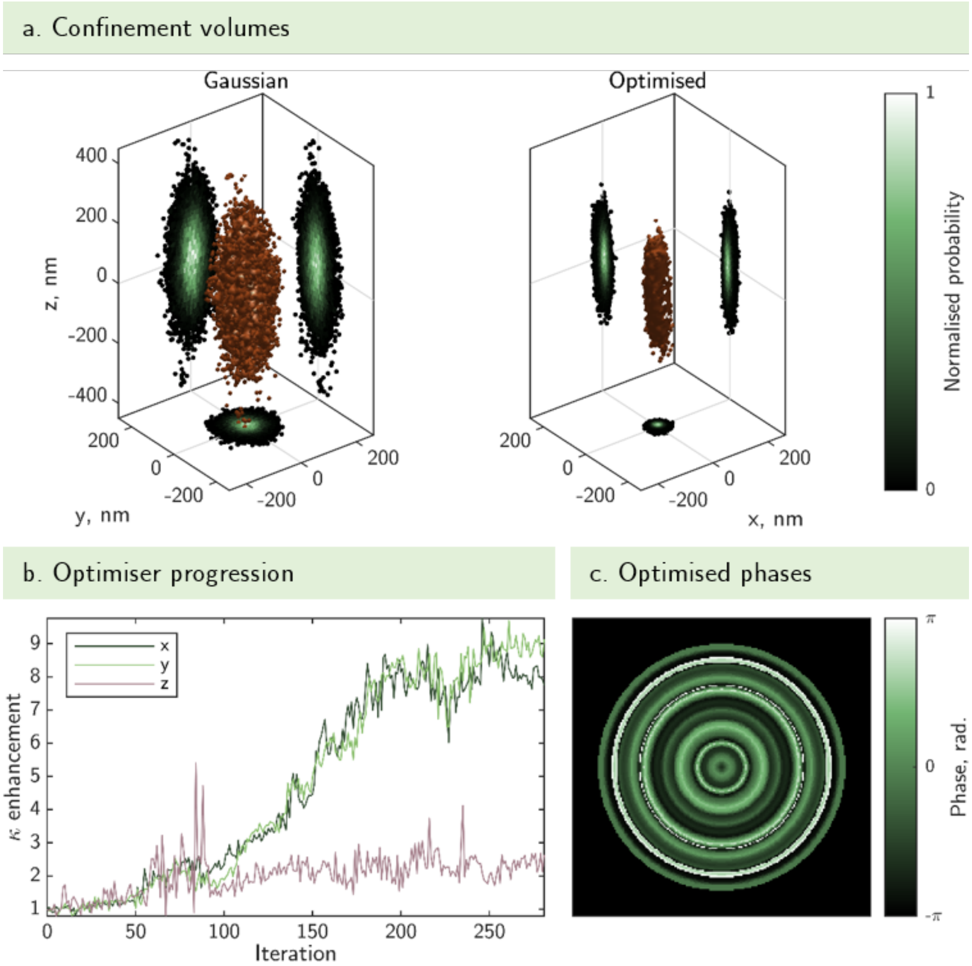

FIGURE 6.5: **Experimental 3D enhancement of an optical trap** for a 4.99 µm radius silica microsphere. (a) Live 3D tracking data for the microsphere trapped in the initial Gaussian trap (left) and the final optimised trap (right), demonstrating 13.3× reduction in $V_c$. (b) Progression of the live 3D stiffness optimiser, resulting in final stiffness enhancements of (8.0, 8.9, 2.5) for each direction respectively. (c) Final optimised phases of the rings on the SLM.

the optical trap of (5 µm, 5 µm, −2.5 µm). In this case, the objective function was the standard deviation of the stiffness along the major axes of the thermal ellipsoid of the initial Gaussian trap, constrained by Z&Y, as described above.

Fig. 6.5 shows the results for this experiment. In this case, the stiffnesses are enhanced by factors of 8.0, 8.9, and 2.5 respectively, resulting in a total reduction in the confinement volume of 13.3×. Notably, there is no improvement in the amount of enhancement in $\kappa_z$ due to prioritizing $z$ enhancement over $y$ enhancement (the constraints Z&Y vs. Y&Z).

To investigate a different size particle, next a 2.59 µm radius silica microsphere is considered, using the same parameters as above (10 s integration time, objective function as the st. dev. of the major axes of first measurement of thermal ellipsoid, Z&Y constraints) and a diffraction grating that translates the trap to (5 µm, 5 µm, −0.5 µm). Fig. 6.6 shows

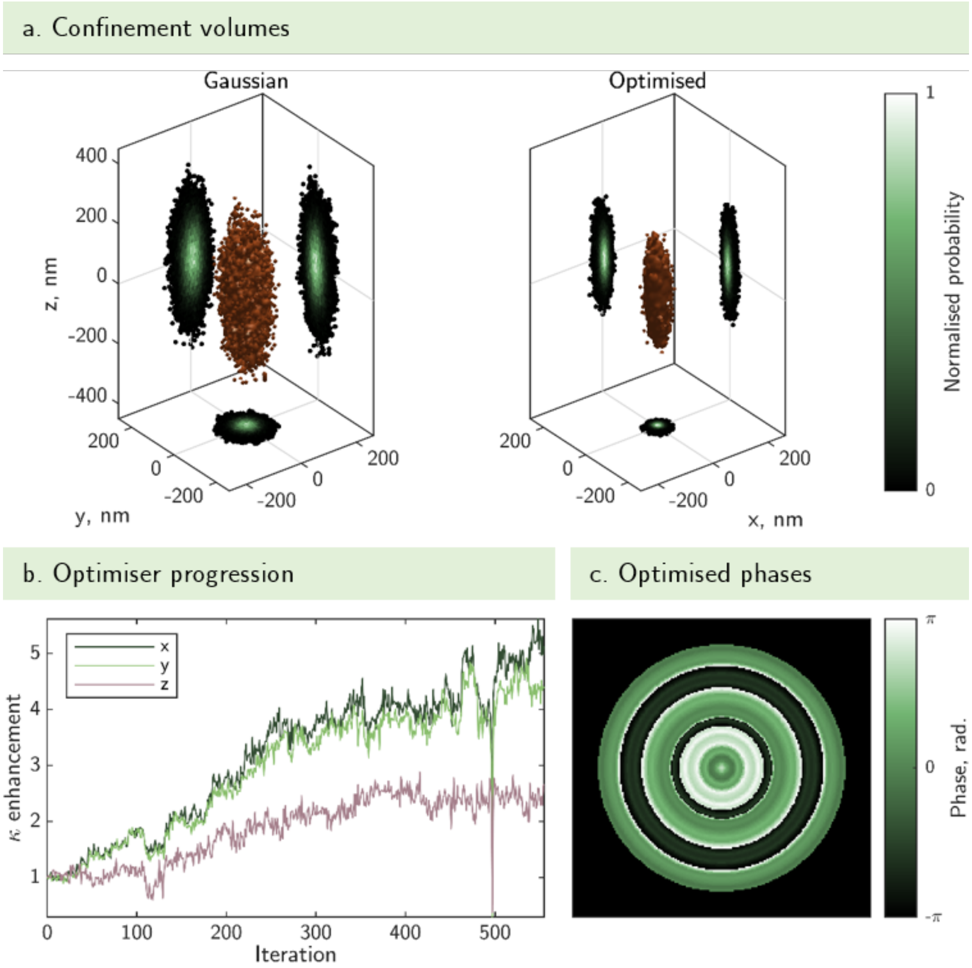

FIGURE 6.6: **Experimental 3D enhancement of an optical trap** for a 2.59 µm radius silica microsphere. (a) Live 3D tracking data for the microsphere trapped in the initial Gaussian trap (left) and the final optimised trap (right), demonstrating 7.0× reduction in $V_c$. (b) Progression of the live 3D stiffness optimiser, resulting in final stiffness enhancements of (4.8, 4.5, 2.3) for each direction respectively. (c) Final optimised phases of the rings on the SLM.

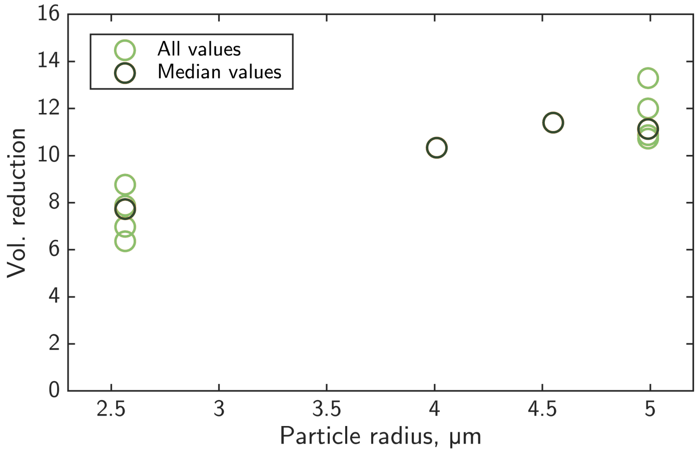

FIGURE 6.7: **Experimental 3D enhancement results** for a range of microsphere sizes.

the experimental results for this scenario.

The optimisation was repeated for a range of microsphere radii between 2.59 µm and 4.99 µm. Fig. 6.7 shows the volume reduction factors for these experiments. The light green circles indicate volume reductions for each repeated run of the live 3D stiffness optimiser with different microspheres in the same sample. The dark green circles indicate the median volume reduction run, where applicable, for each size. For the largest 3 sizes of microspheres tested, this optimisation strategy consistently enhances the confinement of the trapped microsphere by over an order of magnitude. The smallest size microspheres tested are enhanced slightly less than 10×.

The error for the median results (dark green circles in Fig. 6.7) are analysed in Fig. 6.8 and Fig. 6.9. The error bars on these plots are calculated as described in Section 6.2.3.

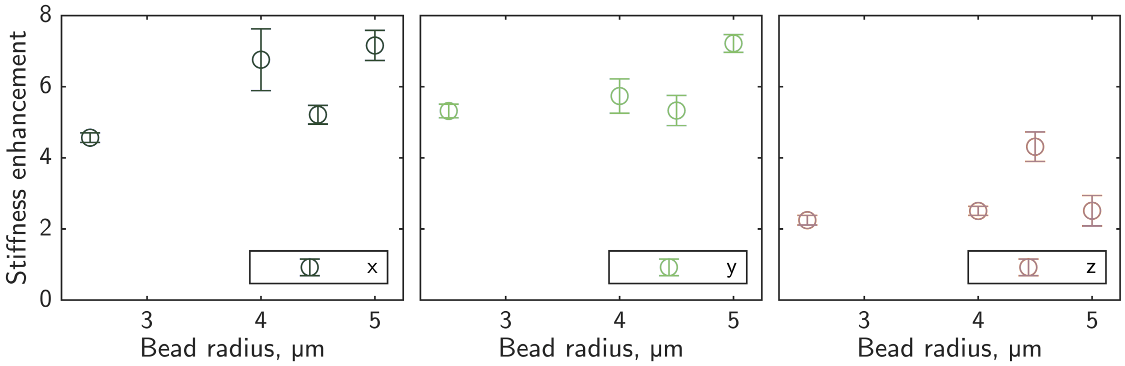

FIGURE 6.8: **Stiffness enhancement for all three dimensions for the median runs of the live 3D stiffness optimiser indicated by the dark green circles in Fig. 6.7.** Error bars determined as described in Section 6.2.3.

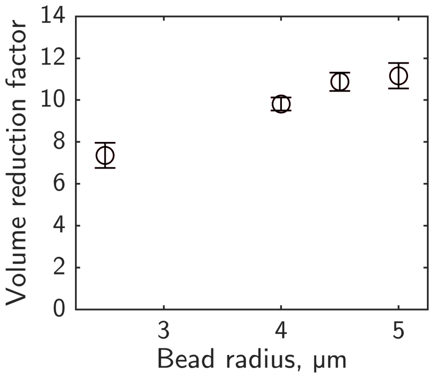

FIGURE 6.9: **Volume reduction factors for the median runs of the live 3D stiffness optimiser indicated by the dark green circles in Fig. 6.7.** Error bars determined as described in Section 6.2.3.

### 6.2.1 Sensitivity of optimised traps to micro-sphere radius

Optimised optical traps are also extremely sensitive to the exact size of the microsphere. This is true for both numerically designed traps and live optimised ones. Experimentally, for example, optimising the trap for a specific micro-particle in a given sample does not mean that all micro-particles in the sample will experience higher confinement. This is due to the statistical variation of the size of the commercially available micro-spheres. This was tested in the sample of 4.99 µm radius silica microspheres presented in Fig. 6.4. Of the 10 total microparticles tested, none except for the bead that was optimised for had their confinement enhanced by 11.0×. Fg. 6.10 shows 3 of these 10 micro-spheres: the optimised (Bead 1), worst (Bead 2), and next best (Bead 3) volume reductions.

An important thing that this experiment accounts for is that, by translating to different areas in the sample to select different beads, the thickness of the coverslip, and therefore the amount of spherical aberration introduced by the glass-water interface, varies across

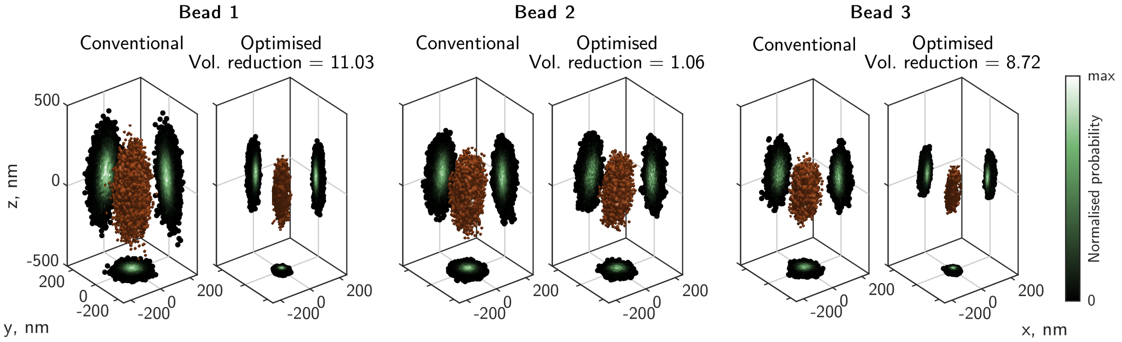

FIGURE 6.10: **Experimental 3D tracking data of different** 4.99 µm **micro-spheres** within the same sample. The optimised trap was optimised for Bead 1. Beads 2 and 3 show no/reduced enhancement of the confinement volume for the optimised trap for Bead 1.

the sample. The volume reductions quoted in the figure compare each optimised trap measurement with its corresponding conventional trap measurement – the differences in the confinement volumes of different beads in the conventional trap illustrate a combination of effects from the minute differences in micro-sphere radii to variations in the spherical aberrations.

To understand the differences in the Gaussian confinement volumes, we need to consider which factors in the experiment can impact the changes in stiffness from bead to bead. The beads could all have slightly different radii, due to statistical variations arising from the manufacturing of the micro-spheres. This is an unavoidable part of these experiments. We also wondered about possible laser drift causing variations in the total power of the incident laser, and the effects this could have on this experiment with multiple beads. To investigate this I tracked a single micro-sphere in a Gaussian trap for several hours – there was no recognizable drift in the stiffness of the optical trap, indicating that this is not a problem for our experiments.

Due to these findings, we think that the differences in the conventional Gaussian confinement volumes across the different beads in this experiment are mainly due to variations in the coverslip thickness throughout the sample. This thickness directly impacts the levels of spherical aberration of an optical trap, which directly effects the 3D stiffness of the trap. The manufacturer-quoted variation in the coverslip thickness is 0.17—0.19 mm, which indicates even small variations in the thickness of the coverslip significantly impact the intensity distribution of the final optimized optical trap.

### 6.2.2 Micro-particle size constraints of current HOT setup

The range of sizes of microspheres that can be used in the 3D stiffness optimiser is strongly dependent on the wavefront shaping capabilities of the HOT system. For the system used here, for example, 1.5 µm radius microspheres were too small, because they are only a few wavelengths in size and it is difficult to create precise fields on this scale. On the other hand, 5.99 µm and 7.52 µm radius microspheres were too large. This is believed to be due to limitations of the SLM/objective lens system in generating fields over a larger area in the sample plane. Larger traps require more space throughout the optical system, meaning the path that these fields take comes closer to the edges of lenses, even potentially clipping the edges. This introduces aberrations, which is extremely detrimental to the performance of the optimised optical traps.

Fig. 6.11 shows an example of the live 3D stiffness optimiser failing to enhance the trapping stiffness of a 5.99 µm radius microsphere. The confinement volumes shown in Fig. 6.11a are not significantly different between the initial conventional Gaussian trap and the final ‘optimised’ trap. The noise between iterations is much higher than in previously presented results, and there is no general trend of increasing stiffness in Fig. 6.11b.

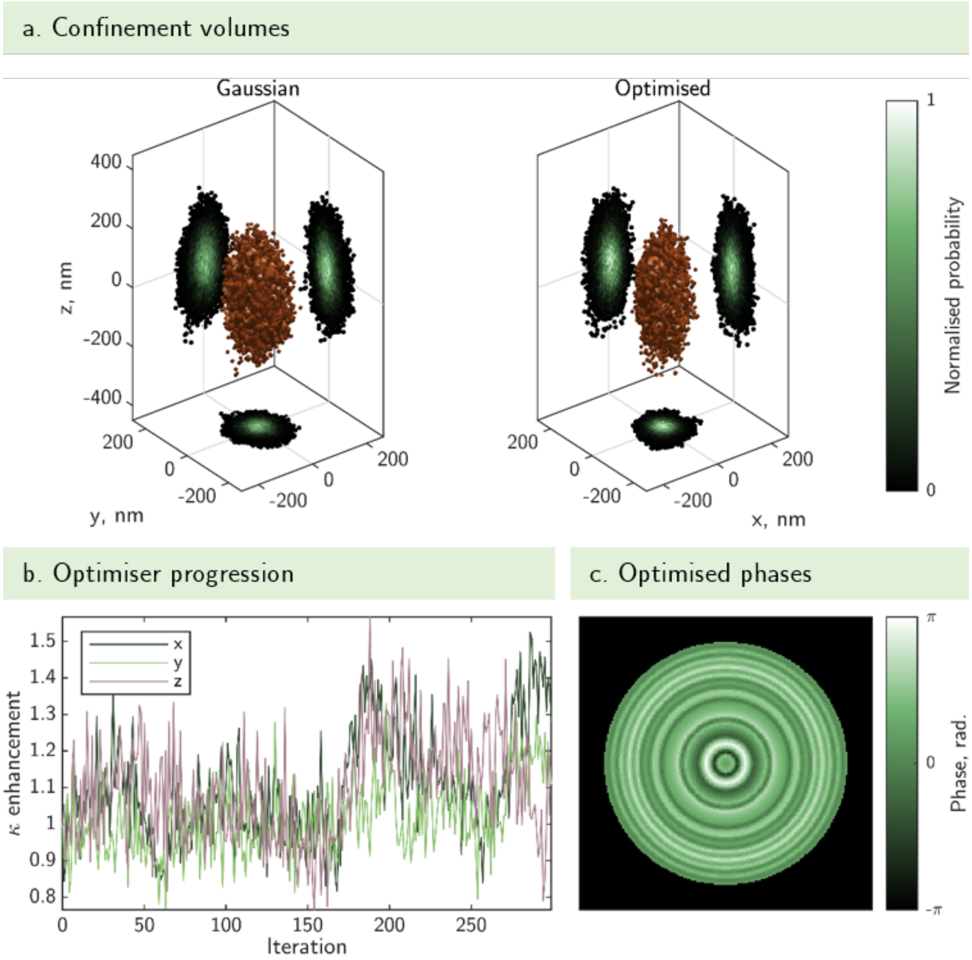

FIGURE 6.11: **Failed experimental 3D enhancement of an optical trap** for a 5.99 µm radius silica microsphere. (a) Live 3D tracking data for the microsphere trapped in the initial Gaussian trap (left) and the final optimised trap (right), demonstrating 1.2× reduction in $V_c$. (b) Progression of the live 3D stiffness optimiser, resulting in final stiffness enhancements of (1.3, 1.2, 1.0) for each direction respectively. (c) Final optimised phases of the rings on the SLM.

### 6.2.3 Measurement errors and noise

Errors and noise are, unfortunately, a fact of life for experimental optics. Here several sources of these and steps taken to account for their impact are discussed.

#### 3D tracking error

The inherent error on the 3D tracking is investigated in Appendix C. There it is determined that it is possible to track the centres-of-mass of microspheres with nanometer precision, as was previously also shown in [140]. The error on the 3D tracking data is determined to be less than 1 nm in $x$ and $y$, and less than 3 nm in $z$.

### Error in stiffness calculations from 3D tracking data

The integration time $\Delta t$ plays a large role in the amount of error introduced by the noise on the live 3D tracking data used to calculate the stiffnesses of a given optical trap. To determine the integration needed for sufficiently low-noise measurements while also minimising the duration of the experiment, the coefficient of variation (CV) of the stiffness across different chunks of time was investigated.

Fig. 6.12 shows the CV for a 2.57 µm radius micro-sphere in a conventional Gaussian trap for integration times between 0 and 30 seconds. An integration time of $\Delta t = 10$ s is chosen as a 'happy medium' to simultaneously reduce the error on stiffness calculations while also keeping the total time needed to optimise an optical trap to a few hours.

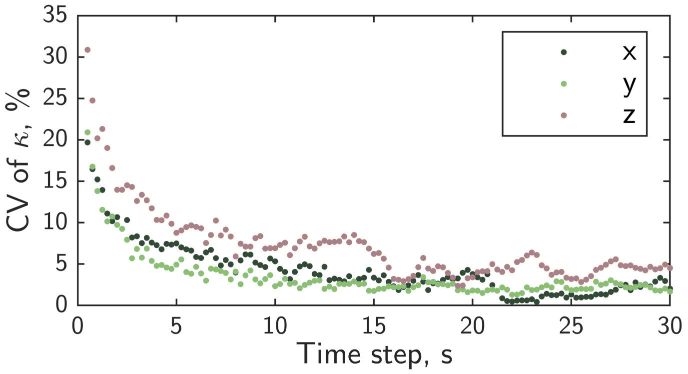

FIGURE 6.12: **Coefficient of variation of the stiffness for different integration times for a 2.57 µm radius micro-sphere in a conventional Gaussian trap.** Figure from Supplementary Information of [115].

### Errors on stiffness enhancement and volume reduction factors

The confinement volume of an optically trapped microsphere is given by

$$V_c = 36\pi\sqrt{\frac{k_B^3 T^3}{\kappa_x \kappa_y \kappa_z}} \tag{6.1}$$

The error on this quantity is determined by the individual errors on the three stiffness measurements. Assuming that the errors are independent of one another and obey a normal distribution, such an error is then given by

$$s_f = \sqrt{\left(\frac{\delta f}{\delta x}\right)^2 s_x^2 + \left(\frac{\delta f}{\delta y}\right)^2 s_y^2 + \left(\frac{\delta f}{\delta z}\right)^2 s_z^2} \tag{6.2}$$

where in this case, $f$ is the volume $V_c$ such that

$$s_{V_c} = \sqrt{\left(\frac{\delta V_c}{\delta \kappa_x}\right)^2 s_{\kappa_x}^2 + \left(\frac{\delta V_c}{\delta \kappa_y}\right)^2 s_{\kappa_y}^2 + \left(\frac{\delta V_c}{\delta \kappa_z}\right)^2 s_{\kappa_z}^2}. \tag{6.3}$$

The partial derivatives are given by

$$\frac{\delta V_c}{\delta \kappa_x} = -18\pi\sqrt{\frac{k_B^3 T^3}{\kappa_x^3 \kappa_y \kappa_z}} \tag{6.4}$$

and similar equations for $\kappa_y$ and $\kappa_z$.

Additionally, the error for the ratio of volumes $R = V_{\text{Gauss}}/V_{\text{opt}}$ is given by

$$s_R = \frac{V_{\text{Gauss}}}{V_{\text{opt}}}\sqrt{\left(\frac{s_{V_{\text{Gauss}}}}{V_{\text{Gauss}}}\right)^2 + \left(\frac{s_{V_{\text{opt}}}}{V_{\text{opt}}}\right)^2} \tag{6.5}$$

where the individual volume errors are calculated as above in Eqn. 6.3.

### Contamination of samples

Another source of error in experiments is the microbiological contamination of the silica microsphere samples. Although precautions were taken to reduce this contamination, the sample fabrication facilities used were not sterile environments. For a detailed discussion of the sample fabrication steps, and precautions against contamination, see Appendix C. Nonetheless, the contamination occurs and is a common issue in the field [141].

If microorganisms are present in the sample, given enough time they will inevitably find their way towards the optical trap location in the sample. If they are then also sucked into the optical trap, the 3D tracking data for a trapped microsphere will be impacted. The microsphere could even be knocked out of the trap entirely by a particularly energetic bacterium, for example.

It is sometimes possible to 'rescue' a trapped microsphere from surrounding contamination by translating the trap to a different, cleaner location within the sample. This is done with the translational stage, *not* by changing the diffraction grating used on the SLM because this changes the efficiency with which the optimised trap is generated. The sharp dip in $x$ and $y$ stiffness enhancement around 500 iterations in Fig. 6.6b is due to such a rescue mission, where I sprinted from my office to the lab to save the microsphere in its time of need when a rogue contaminant was spotted approaching the optical trap during routine monitoring. One iteration of the optimisation is sacrificed (seen in the sharp dip of the enhancement) to quickly translate the bead within the sample. Such rescues are not without their own risks, however, as the thickness of the coverslip could vary between locations, impacting the levels of spherical aberrations present and potentially altering the achieved enhancements thus far in the optimisation.

## 6.3 Comparison with pre-designed optimised traps

Although this chapter has presented order of magnitude enhancement in microsphere confinement, it is fair to ask why there is such a large disparity between these experimental results and the previously presented pre-designed optimised trap enhancements that demonstrated up to ∼ 200× enhancement. To investigate where this difference arises, further simulations were performed. This is also discussed in the Supplementary Material for [115].

First, in addition to the complex amplitude modulation presented in Chapter 4, the same constrained interior point optimisation was performed with phase only modulation of the incident field. Next, a simulation of the live iterative optimisation presented in this chapter was run. Fig. 6.13 shows the comparison of these methods. The pre-designed traps generated using the complex amplitude optimisation see the greatest reduction in confinement volume, as expected. The pre-designed traps generated with phase only optimisation see the next greatest reduction in confinement volume, about 60% lower than the best case scenario.

The iterative optimisation used for experiments was simulated, with and without noise. Without noise, the phase only iterative optimised traps performed about 50-90% as well as the phase only pre-designed traps. Upon addition of noise, the levels of volume reduction fell another 10-30%. The levels of noise used for these simulations were determined by the coefficient of variation (as in Fig. 6.12). Finally, all of these simulations were compared to the actual experimental results, which achieved approximately 70-90% of the anticipated volume reduction presented by the simulation of the iterative optimisation with noise.

It is possible that, with more intricate knowledge of one's HOT system, the experimental phase only iterative optimisation approach could reach it's full, simulated potential.

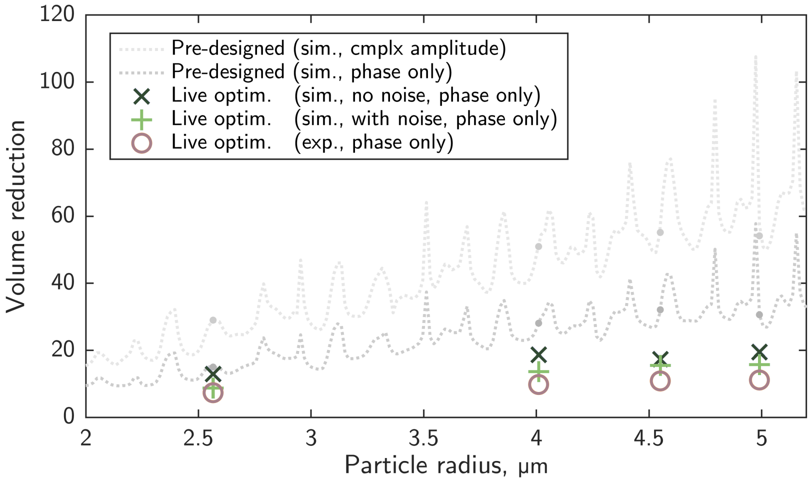

FIGURE 6.13: **Comparison of optimisation methods for 3D optical trap enhancement** for various sizes of silica ($n = 1.45$) micro-spheres at 1064 nm. Plot originally from Supplementary Information of [115].

Additionally, this analysis has made it clear that it is very much possible to further increase the trapping enhancement in optical tweezers experiments. There are plenty of stones left unturned, and rabbit holes yet unexplored. One could, for example, anticipate an increase in performance of the experimental optimiser if the ability to do complex amplitude modulation were added.

## 6.4 Discussion

The experiments presented here demonstrate the first known attempts to enhance the stiffness of an optical trap in all three dimensions with passive methods, i.e. wavefront shaping. For microparticles ranging in radii from 2.57 µm to 4.99 µm, significant improvements in the confinement of such particles in optical traps is demonstrated, with average increases of an order of magnitude for all but the smallest size micro-spheres. Larger particles have larger enhancements - in simulation and experiment - because wavefront shaping is diffraction limited, so that the wavefront can be better shaped for larger particles for which the optimum traps themselves are larger than the diffraction limit.

Comparing these experimental results with the previously discussed numerically optimised traps, there are a few major differences. In its current form, the live iterative optimisation exhibits no control over the aspect ratio of the final 3D stiffnesses/confinement volume, unlike in simulations of pre-designed traps. This could be addressed with more rigorous constraints to the objective function. Another difference is that the number of degrees of freedom tested is much lower for the experimentally optimised traps, due to the time requirements of such experiments. Additionally, with the current HOT system, complex amplitude modulation in such an optimisation is not feasible due to e.g. changes in the total power in the generated optical trap, which is already an important issue for phase only modulation discussed next. The action of the SLM itself plays a big role in the performance of the optimisation, as discussed below.

The 'steepness' of the diffraction grating plays a large role as well. This is one parameter that was critical to the success of the optimisation – if the optical trap generated in the first order is translated too far from the zero order focus, the performance of the live 3D stiffness optimiser decreases drastically. This was probed in two different ways: by translating a live-optimised trap and bead at the end of an experiment, and by experimentally optimising a trap at a location further from the zero order focus.

In the case of the former scenario, a trap for a 4.99 µm was optimised for experimentally with the same parameters as in Fig. 6.4, and then the final optimised trap was translated a distance of (13 µm, 13 µm) in $x$ and $y$ in the sample plane, respectively. The achieved enhancement of the confinement volume dropped from 10.4× at the location nearer the zero order focus to 6.3× at the translated location.

The latter scenario (optimising a trap further from the zero order focus) was also investigated experimentally. Typically, the optimisation was performed on a first order trap located between 4 µm and 6 µm from the zero order in the $x$ and $y$ directions, depending on the radius of the microsphere. These distances were sufficiently far enough away that the zero order does not also exert an optical force on the particle. The translations were induced using a phase grating on the SLM. Here, however, a location (10 µm, 10 µm) was used for the optical trap, requiring a steeper phase grating with more phase wrapping lines where the phase goes from $2\pi$ to 0. The resulting enhancement of the optical trap was minimal – the confinement volume was only reduced by a factor of 2.6×.

Another important note about the method presented in this chapter for enhancing the stiffness of an optical trap in 3D is the repeatability of results. Due to the nature of the live optimisation performed and the lack of an analytical global solution, we do not find the global optimum trap for 3D-enhanced stiffness. Instead, we converge on (different) local maxima each time we perform the experimental optimisation.

As noted previously, the exact size of a given microsphere heavily impacts the result of the optimisation. The microspheres used in these experiments (purchased from microParticles Gmb) exhibit a statistical variation of sizes. For the batches used here, the diameters of the microspheres have a standard deviation of between 0.02 and 0.2 µm depending on the exact spheres used. This minuscule distribution of the size of the microspheres (2% or less variation in diameter) was enough to significantly impact the performance of an optimised trap.

The optimisations presented here required on the order of $\sim 10^2$ iterations to converge to a solution. Each of these iterations included 3 measurements of the optically trapped particle's 3D motion, meaning these experiments took on the order of hours (typically 2-4 hours). This process could be sped up in the future by beginning with a better starting optical trap – perhaps one informed by a numerically optimised trap such as those described in Chapter 4.

Finally, we compare our approach to other approaches for increasing the stiffness of optical traps. One such method is position clamping [142–144], in which an optical trap is translated in real-time to more effectively counteract the thermal motion of a trapped particle, have demonstrated order of magnitude improvements in trapping stiffness in 1D and 2D. This method differs from what is presented here because position clamping is an active approach to suppressing the motion of an optically trapped particle, which uses feedback from the trapped particle to adjust the optical trap in real time. In contrast, the optimisations presented here are passive. However, it should theoretically be possible to also perform 3D optical trap enhancement using a position clamping approach, though this would require higher speed control of the phase mask displayed on the SLM.

# Chapter 7

# Conclusions

Wavefront shaping approaches hold promise, proposing answers to many challenging problems in modern optics situations. In this thesis, two novel applications of wavefront shaping have been investigated – navigating light through partially dynamic scattering materials and optimising the confinement of optically trapped particles in all three dimensions simultaneously. The work presented in this thesis marks a significant milestone in the field of wavefront shaping and its applications in optics. As we look to the future, it is clear that there are numerous exciting possibilities and unexplored avenues for these research projects.

In Part I of this thesis, wavefronts were optimised to carefully navigate through scattering regions containing pockets of dynamic scattering. Using both iterative optimisation techniques and the time-averaged transmission matrix, stable, non-fluctuation fields were found. The results presented here illustrate the duality of optimising the fields in this way. Fields must be found that simultaneously satisfy two competing interests: increase or maintain the average intensity transmitted to the output; and decrease the amount of light within the dynamic pocket to prevent interactions of the field with the moving dipoles, thereby causing fluctuations of the field at the output.

It is the unfortunate reality of research that not every avenue can be explored. I believe experimental proof-of-principle experiments for the adjoint iterative optimisation using the normalised variance of the field at the output holds great promise. Sadly, we did not have the time to pursue this.

One can envision further advancements in the optimization techniques and the objective functions used to generate fields that can traverse complex dynamic media. Although we have successfully found fields that navigate around a dynamic pocket within scattering material using, in part, the two adjoint optimisations, we wonder what better objective functions may be out there for similar optimisations. Additionally, the simulations included here were performed in 2D. Extending such models to 3D provides an interesting road ahead for future investigations. This may provide more insight into the capabilities that future experiments could require.

The potential to extend this research to even more intricate scatterers, including biological tissues, opens up a vast frontier of applications. As technology continues to advance, we can anticipate the development of more sophisticated spatial light modulators

(SLMs) with faster modulation times, enabling the transformation of currently dynamic scattering materials into near-static media for various applications, including biomedical imaging and laser-based communication systems.

In the far future, it is our hope that the methods for finding light fields that carefully traverse dynamic scattering media become a part of the solution to controlling light in highly dynamic situations. We imagine the techniques presented here will find use in exotic future technologies that will enable seeing through fog and mist, peering into clouds, and looking deep into the human body.

Part II of this thesis focused on a totally different application of wavefront shaping – 3D enhancement of optical trap stiffness. Notably, the numerically designed traps exhibited up to $\sim 200\times$ reduction in the confinement volume of optically trapped micro-spheres for a wide range of refractive indices and radii. Experimentally, $\sim 10\times$ reduction in the confinement volume was demonstrated for a range of silica micro-sphere radii. An important thing to note is that the confinement volume reduction and laser power reduction are two sides of the same coin – the numerically optimised traps presented in this thesis can either confine given particles up to $200\times$ more tightly, or achieve the same trapping performance as a conventional Gaussian trap but with up to $\sim 30\times$ less power in the trap.

In the case of 3D enhancement of optical trapping, the experimental demonstrations presented in the thesis offer a tantalizing glimpse of what can be achieved. Future research may delve deeper into the underlying mechanisms of holographic optical tweezers (HOT). I have often referred to the many possible directions for these stiffness enhancement experiments as rabbit holes, each one deeper than the last. In the future, it would be interesting to explore in depth how exactly SLMs produce various modulated beams with varying efficiency. The impact of high numerical aperture objectives on such modulated fields is also of future interest. Integrating complex amplitude modulation into the existing HOT represents another intriguing frontier, promising even greater enhancements in optical trapping performance. This work could have profound implications in fields like biophysics and nanotechnology, where precise manipulation of micro- and nanoparticles is essential.

We envision our approaches detailed herein will be an integral part of the toolkit required to attain the fundamental minimum amount of light to precisely manipulate mesoscale matter. We hope these methods will support the development of future technologies that will enable the study of photosensitive cells and their mechanics and the creation of successful quantum computing arrays of trapped atoms and ions.

Overall, the possibilities for these wavefront shaping techniques are intriguing. They have the potential to revolutionize a wide range of optical applications, from imaging to biophotonics and materials science. As the research community continues to explore and innovate, we can expect to see an exciting future filled with novel applications and breakthroughs in the field of wavefront shaping. In particular, I believe that even greater experimental enhancements of the 3D stiffness of optical traps are just out of reach.

# Appendix A

# The Helmholtz equation

## A.1 The free-space Helmholtz equation

This derivation of the free-space Helmholtz equation follows that found in [145].

We start from Maxwell's equations in the absence of charges and currents ($\rho = 0$ and $J_i = 0$ respectively), which describe the propagation of light:

$$\nabla \cdot \mathbf{E} = 0, \tag{A.1}$$

$$\nabla \cdot \mathbf{B} = 0, \tag{A.2}$$

$$\nabla \times \mathbf{E} = -\frac{\partial}{\partial t}\mathbf{B}, \tag{A.3}$$

$$\nabla \times \mathbf{B} = \mu_0 \epsilon_0 \frac{\partial}{\partial t}\mathbf{E} \tag{A.4}$$

where $\nabla \cdot \mathbf{A}$ denotes div$\mathbf{A}$, the divergence of vector $\mathbf{A}$, and $\nabla \times \mathbf{A}$ denotes curl$\mathbf{A}$, the curl of vector $\mathbf{A}$.

Applying the curl to both sides of Eqn. A.3 leads to

$$\nabla \times (\nabla \times \mathbf{E}) = -\nabla \times \left(\frac{\partial}{\partial t}\mathbf{B}\right). \tag{A.5}$$

This can be rewritten by using the following identity:

$$\nabla \times (\nabla \times \mathbf{A}) = \nabla(\nabla \cdot \mathbf{A}) - \nabla^2 \mathbf{A}. \tag{A.6}$$

Applying the above identity, Eqn. A.5 can be rewritten as

$$\nabla(\nabla \cdot \mathbf{E}) - \nabla^2 \mathbf{E} = -\frac{\partial}{\partial t}\nabla \times \mathbf{B}. \tag{A.7}$$

From Eqns. A.1 and A.4, this becomes the well-known *electromagnetic wave equation* in free space:

$$\left(\nabla^2 - \frac{1}{c^2}\frac{\partial^2}{\partial t^2}\right)\mathbf{E}(\mathbf{r}, t) = 0. \tag{A.8}$$

A similar equation can be derived for the magnetic field.

For monochromatic waves, the time-dependence can be separated such that $\mathbf{E}(\mathbf{r},t) = \mathbf{E}(r)\cdot\exp(i\omega t)$ where $\omega$ is the frequency. Substituting this into Eqn. A.8 yields the *vectorial free-space Helmholtz equation*:

$$(\nabla^2 + k^2)\mathbf{E}(\mathbf{r}) = 0, \tag{A.9}$$

where $k = \omega/c$ is the wave number.

In the scalar wave approximation, this reduces to the *scalar free-space Helmholtz equation*:

$$(\nabla^2 + k^2)U(\mathbf{r}) = 0. \tag{A.10}$$

## A.2 The inhomogeneous Helmholtz equation

In contrast to the free-space Helmholtz equation, the inhomogeneous Helmholtz equation describes the propagation of light in the presence of localised sources.

To derive this equation, the wave equation (Eqn. A.8) can be modified to become

$$\left(c^2\nabla^2 - \frac{\partial^2}{\partial t^2}\right)\mathbf{E}(\mathbf{r},t) = F(\mathbf{r},t). \tag{A.11}$$

where $F(\mathbf{r},t)$ is a function describing the source wavefunction. Time-harmonic solutions to this *homogeneous wave equation* are given by

$$U(\mathbf{r},t) = e^{i\omega t}u(\mathbf{r}) \tag{A.12}$$

$$F(\mathbf{r},t) = e^{i\omega t}f(\mathbf{r}). \tag{A.13}$$

From here, it follows that the scalar inhomogeneous Helmholtz equation is given by

$$(\nabla^2 + k^2)u(\mathbf{r}) = -f(\mathbf{r}). \tag{A.14}$$

### A.2.1 Point sources and the inhomogeneous Helmholtz equation

For point sources, $f$ becomes the Dirac delta function $\delta$ located at $r_s$, the position of the point source. The Green's function can then be substituted for $u(\mathbf{r})$ to satisfy Eqn. A.14:

$$(\nabla^2 + k^2)G(\mathbf{r}, r_s) = -\delta(\mathbf{r} - r_s). \tag{A.15}$$

Notably, linear combinations of the above solution are also solutions to Eqn. A.14, meaning the solution to multiple point sources at different locations $r_i$ is given by $f(\mathbf{r}) = \sum_i a_i\delta(\mathbf{r} - r_i)$ where $a_i$ is the amplitude of each source field. This solution to the homogeneous Helmholtz equation is used in Chapters 2 and 3 to create the source field from an assortment of point sources in 2D.

# Appendix B

# More data for the DDA optimisations

This Appendix contains information on the DDA MATLAB code as well as more results of the phase optimisations described in Chapter 3.

## B.1 MATLAB code

The discrete dipole approximation code I used for the work presented in this thesis is available on GitHub: `https://github.com/structuredlightlab/dynamicScattererDDA.git`.

## B.2 Simple iterative phase optimisation

### B.2.1 Repeated runs of the simple iterative phase optimisation

Each of the results presented below were generated with a new random array of scattering dipoles to show the repeatability of the resulting optimised fields.

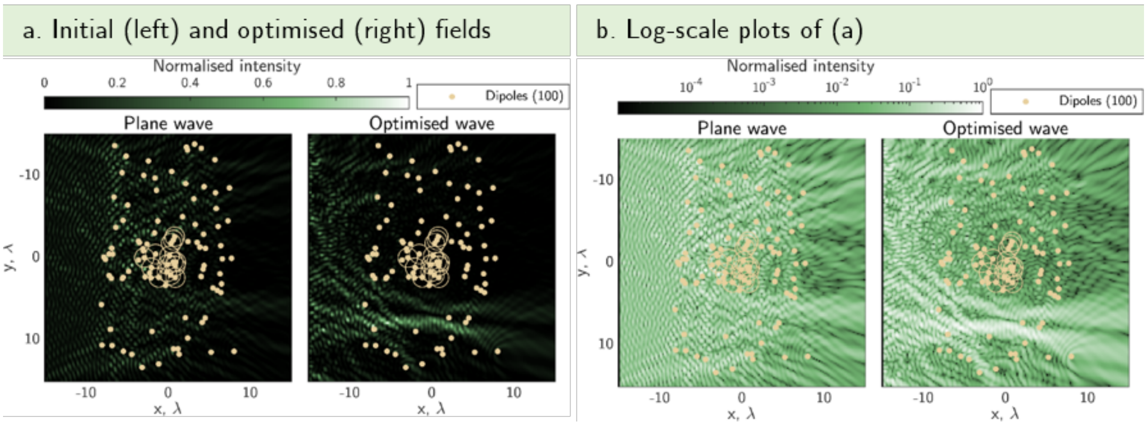

FIGURE B.1: **Run 1 of simple iterative phase optimisation in the high scattering limit**. Sources are spaced $\lambda/2$. St. dev. of motion of dipoles is $1.25\lambda$, $n_{\mathrm{m}} = 55$ configurations are used for fluctuation quantification. $\Delta\phi = \pi/10$. (a) Intensity heatmaps showing plane wave (left) and optimised wavefront (right) propagating through 100 scattering dipoles (yellow dots), 15 of which are dynamic (circled). (b) Log scale versions of plots in (a).

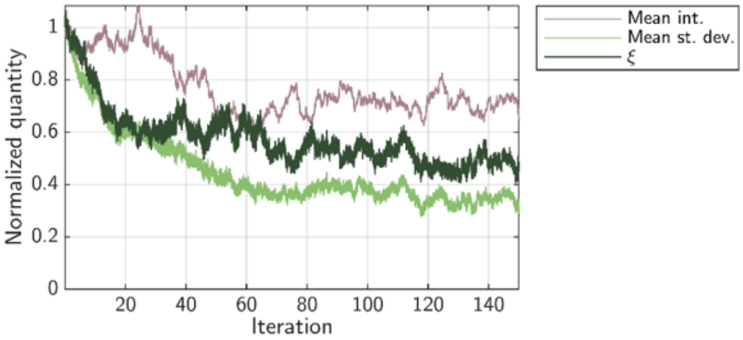

FIGURE B.2: **Progression of run 1 of simple iterative phase optimisation in the high scattering limit.**

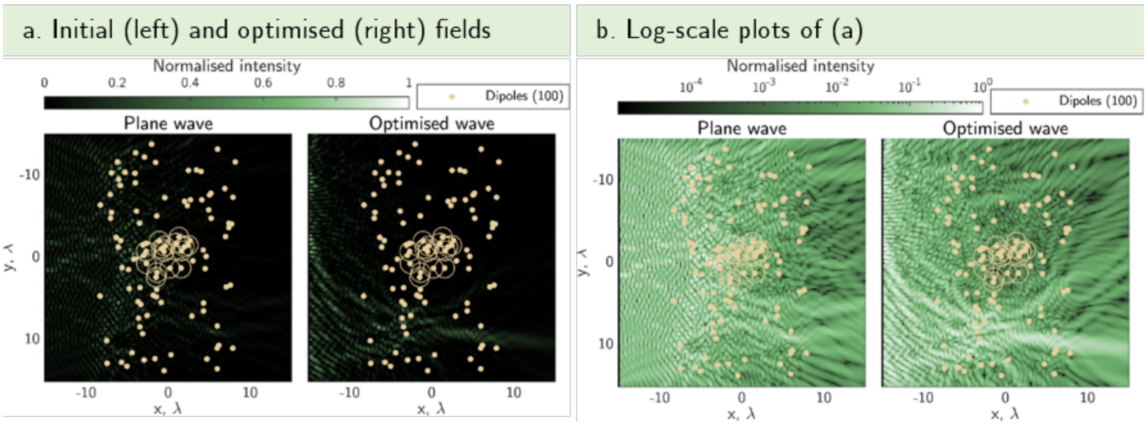

FIGURE B.3: **Run 2 of simple iterative phase optimisation in the high scattering limit**. Sources are spaced $\lambda/2$. St. dev. of motion of dipoles is $1.25\lambda$, $n_\mathrm{m} = 55$ configurations are used for fluctuation quantification. $\Delta\phi = \pi/10$. (a) Intensity heatmaps showing plane wave (left) and optimised wavefront (right) propagating through 100 scattering dipoles (yellow dots), 15 of which are dynamic (circled). (b) Log scale versions of plots in (a).

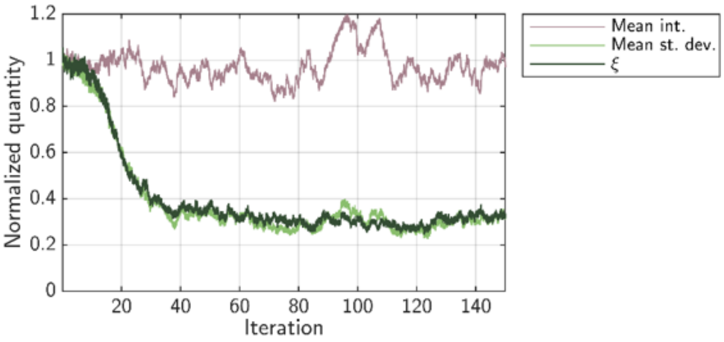

FIGURE B.4: **Progression of run 2 of simple iterative phase optimisation in the high scattering limit.**

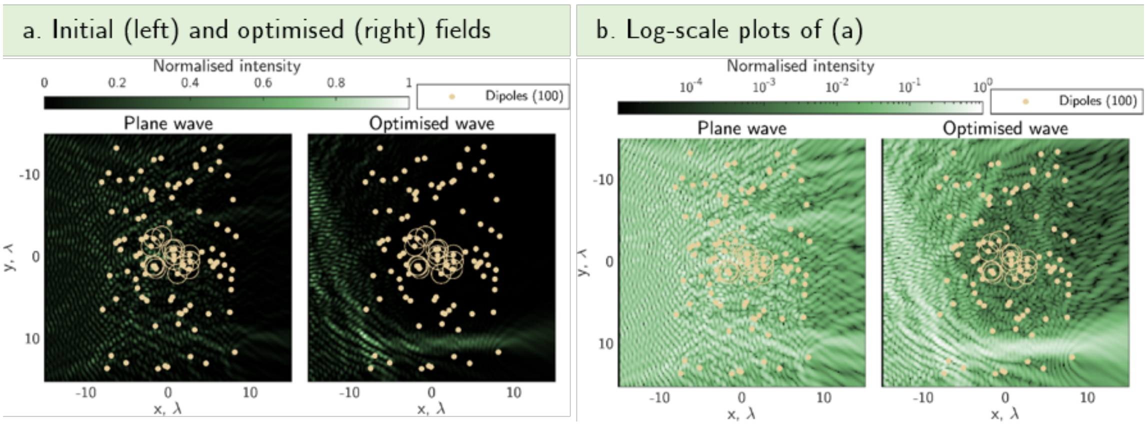

FIGURE B.5: **Run 3 of simple iterative phase optimisation in the high scattering limit**. Sources are spaced $\lambda/2$. St. dev. of motion of dipoles is $1.25\lambda$, $n_{\text{m}} = 55$ configurations are used for fluctuation quantification. $\Delta\phi = \pi/10$. (a) Intensity heatmaps showing plane wave (left) and optimised wavefront (right) propagating through 100 scattering dipoles (yellow dots), 15 of which are dynamic (circled). (b) Log scale versions of plots in (a).

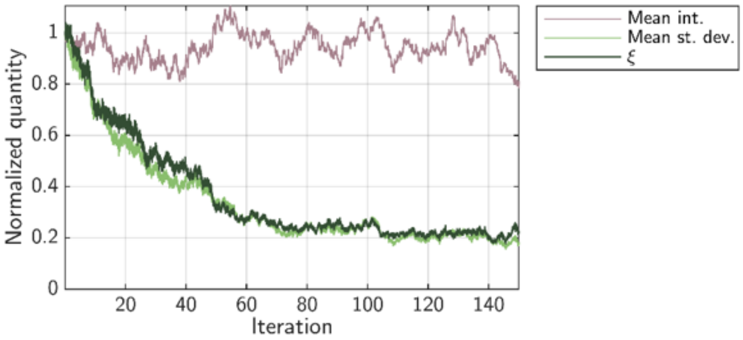

FIGURE B.6: **Progression of run 3 of simple iterative phase optimisation in the high scattering limit.**

## B.3 Adjoint iterative phase optimisation

### B.3.1 FOM 1

**Simulation results for translated dynamic pocket for adjoint optimisation with FOM 1**

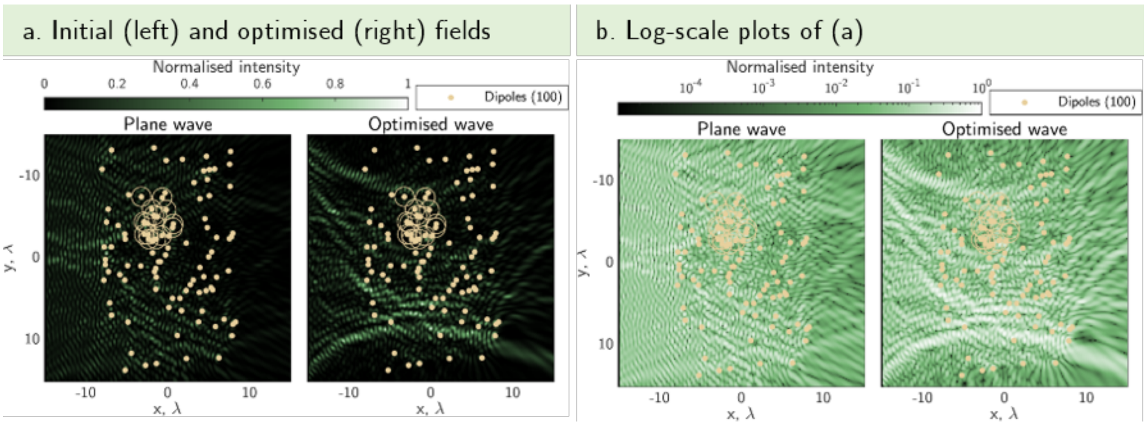

FIGURE B.7: **Simulation of adjoint phase optimisation in the high scattering limit** using the overlap of the fields at the detectors over time as the FOM with the pocket of dynamic dipole at a different location in the scattering region. Sources are spaced $\lambda/4$. St. dev. of motion of dipoles is $1.25\lambda$, $n_\mathrm{m} = 55$ configurations are used for fluctuation quantification. $dj = 0.1$. (a) Intensity heatmaps showing plane wave (left) and optimised wavefront (right) propagating through 100 scattering dipoles (yellow dots), 15 of which are dynamic (circled). (b) Log scale version of plots in (a).

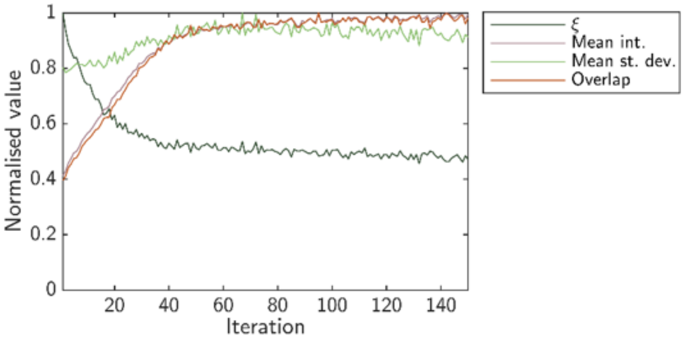

FIGURE B.8: **Progression of adjoint phase optimisation in the high scattering limit** using the overlap of the fields at the detectors over time as the FOM with the pocket of dynamic dipole at a different location in the scattering region.

Fig. B.7 and Fig. B.8 show numerical results for this adjoint phase optimisation using the FOM described in Eqn. 3.2 for a translated pocket of dipoles with standard deviation of their motion equal to $1.25\lambda$. As before, this optimisation performed as it should – increasing the overlap of the field with each iteration. It also increases the mean intensity transmitted to the detectors. The mean standard deviation of the amplitude of the field at the detectors has increased slighty, but overall $\xi$ decreases to $\sim 50\%$ of the initial value. The optimised field is mostly focused below the pocket of dynamic dipoles.

### Simulation results for higher levels of movement of dynamic dipoles using the adjoint optimisation with FOM 1

Next, higher levels of movement are investigated. Fig. B.9 and Fig. B.10 show simulated results for this method with a standard deviation of motion of $2.5\lambda$, twice the amount considered above. Again, the overlap of the output fields over time increases and $\xi$ decreases over the course of the optimisation. The optimised field forks around the dynamic pocket of dipoles.

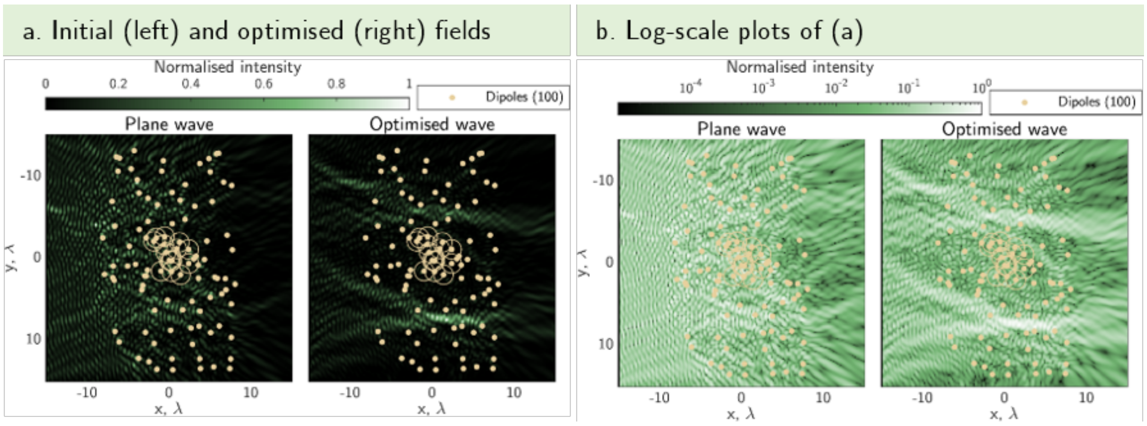

FIGURE B.9: **Simulation of adjoint phase optimisation in the high scattering limit** using the overlap of the fields at the detectors over time as the FOM with the pocket of dynamic dipole at a different location in the scattering region. Sources are spaced $\lambda/4$. St. dev. of motion of dipoles is $2.5\lambda$, $n_{\mathrm{m}} = 200$ configurations are used for fluctuation quantification. $dj = 0.1$. (a) Intensity heatmaps showing plane wave (left) and optimised wavefront (right) propagating through 100 scattering dipoles (yellow dots), 15 of which are dynamic (circled). (b) Log scale version of plots in (a).

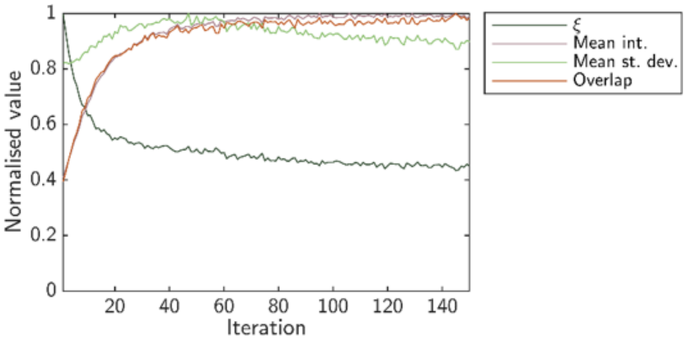

FIGURE B.10: **Progression of adjoint phase optimisation in the high scattering limit** using the overlap of the fields at the detectors over time as the FOM with the pocket of dynamic dipole at a different location in the scattering region.

### Repeated simulations of the adjoint optimiser with FOM 1

Each of the results presented below were generated with a new random array of scattering dipoles to show the repeatability of the resulting optimised fields.

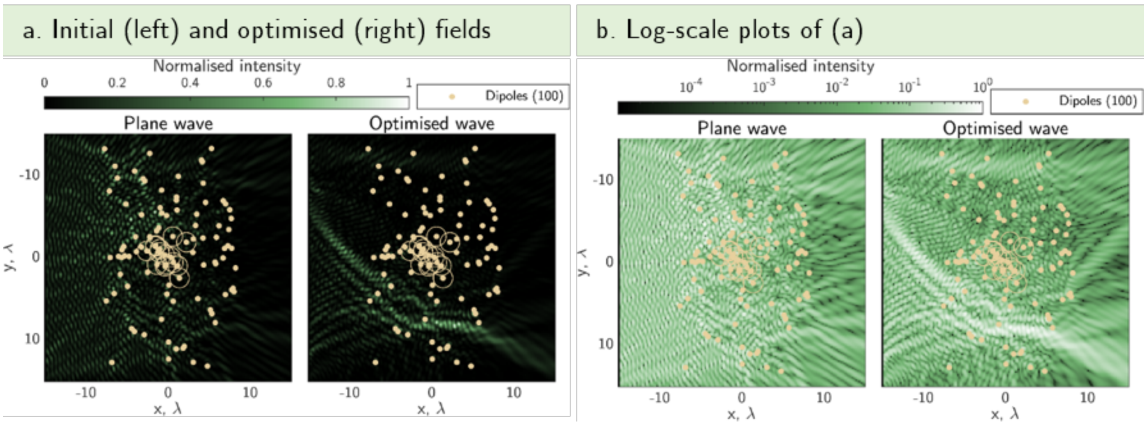

FIGURE B.11: **Run 1 of adjoint phase optimisation in the high scattering limit** using the overlap of the fields at the detectors over time as the FOM. Sources are spaced $\lambda/4$. St. dev. of motion of dipoles is $1.25\lambda$, $n_\mathrm{m} = 55$ configurations are used for fluctuation quantification. $dj = 0.1$. (a) Intensity heatmaps showing plane wave (left) and optimised wavefront (right) propagating through 100 scattering dipoles (yellow dots), 15 of which are dynamic (circled). (b) Log scale version of plots in (a).

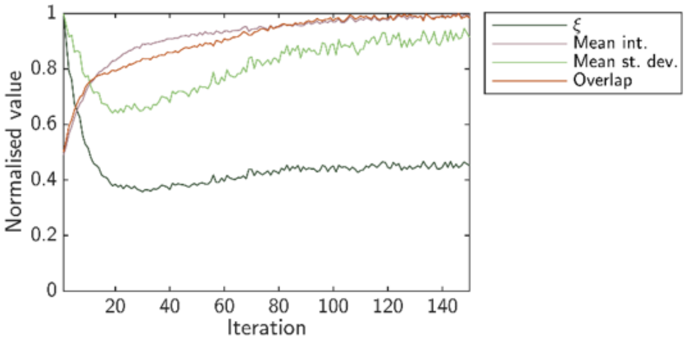

FIGURE B.12: **Progress of run 1 of adjoint phase optimisation with FOM 1 in the high scattering limit.**

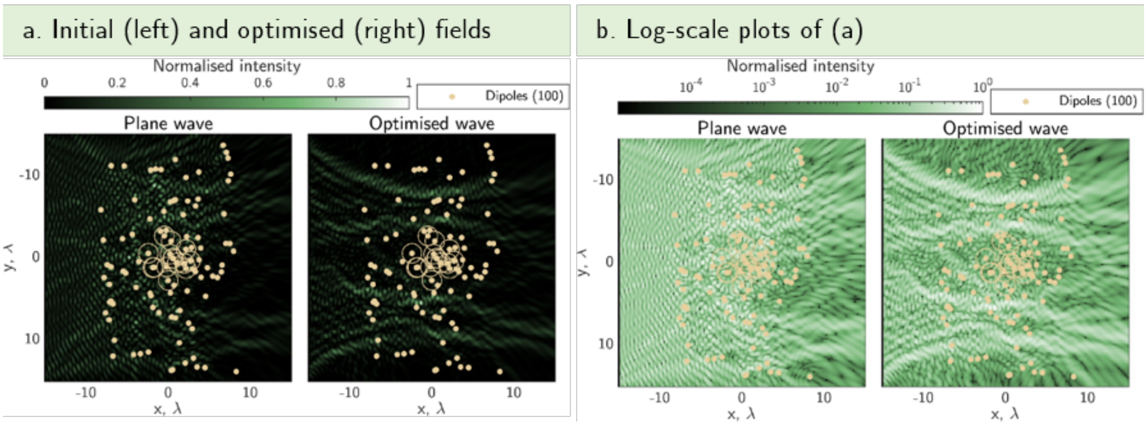

FIGURE B.13: **Run 1 of adjoint phase optimisation in the high scattering limit** using the overlap of the fields at the detectors over time as the FOM. Sources are spaced $\lambda/4$. St. dev. of motion of dipoles is $1.25\lambda$, $n_\mathrm{m} = 55$ configurations are used for fluctuation quantification. $dj = 0.1$. (a) Intensity heatmaps showing plane wave (left) and optimised wavefront (right) propagating through 100 scattering dipoles (yellow dots), 15 of which are dynamic (circled). (b) Log scale version of plots in (a).

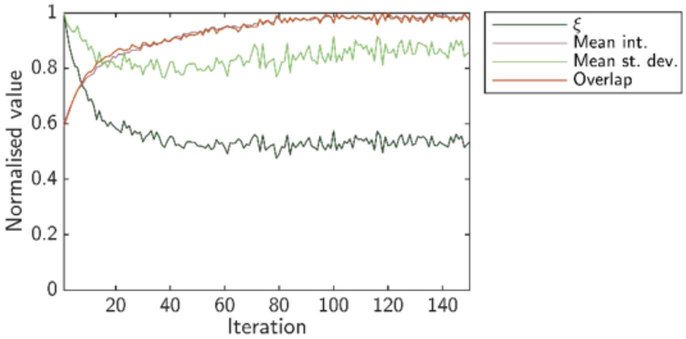

FIGURE B.14: **Progress of run 1 of adjoint phase optimisation with FOM 1 in the high scattering limit.**

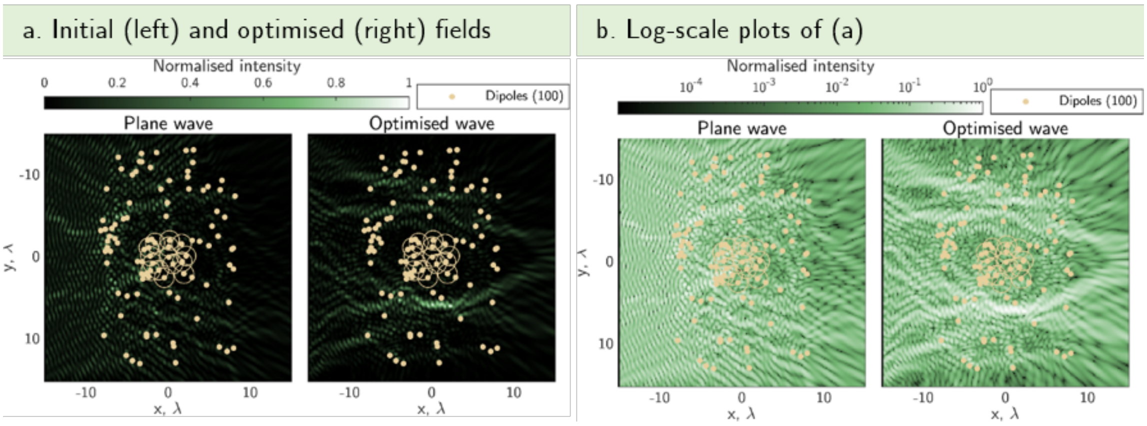
a. Initial (left) and optimised (right) fields

b. Log-scale plots of (a)

Figure B.15: **Run 1 of adjoint phase optimisation in the high scattering limit** using the overlap of the fields at the detectors over time as the FOM. Sources are spaced $\lambda/4$. St. dev. of motion of dipoles is $1.25\lambda$, $n_{\mathrm{m}} = 55$ configurations are used for fluctuation quantification. $dj = 0.1$. (a) Intensity heatmaps showing plane wave (left) and optimised wavefront (right) propagating through 100 scattering dipoles (yellow dots), 15 of which are dynamic (circled). (b) Log scale version of plots in (a).

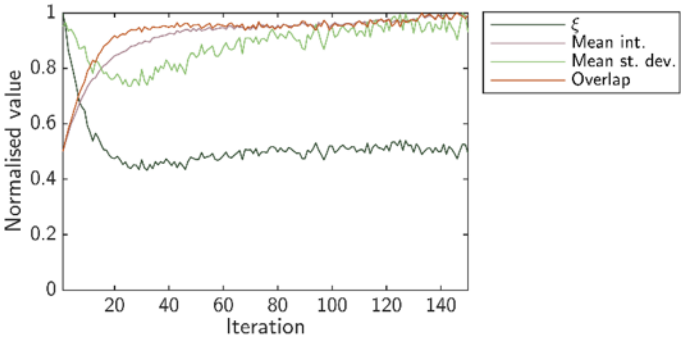

Figure B.16: **Progress of run 1 of adjoint phase optimisation with FOM 1 in the high scattering limit.**

## B.3.2 FOM 2

### Simulation results for translated dynamic pocket for adjoint optimisation with FOM 2

To demonstrate that this method also does not rely on any *a priori* knowledge of the location of behavior of the dynamic dipoles, this simulation was repeated with a translated pocket of dipoles. Fig. B.17 and Fig. B.18 show the results for the scenario where the pocket of dipoles has been translated to the top portion of the scattering material. The fluctuations have been reduced to $\sim 40\%$ of their initial value.

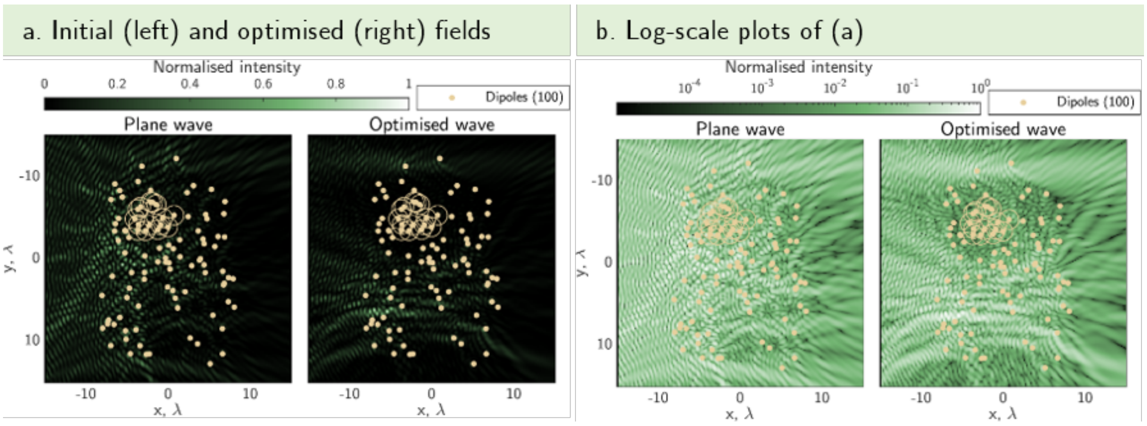

Figure B.17: **Simulation of adjoint phase optimisation in the high scattering limit** using the normalised variance of the fields at the detectors over time as the FOM for an off-centre pocket of dipoles. Sources are spaced $\lambda/4$. St. dev. of motion of dipoles is $1.25\lambda$, $n_{\mathrm{m}} = 55$ configurations are used for fluctuation quantification. $dj = 0.1$. (a) Intensity heatmaps showing plane wave (left) and optimised wavefront (right) propagating through 100 scattering dipoles (yellow dots), 15 of which are dynamic (circled). (b) Log scale version of plots in (a).

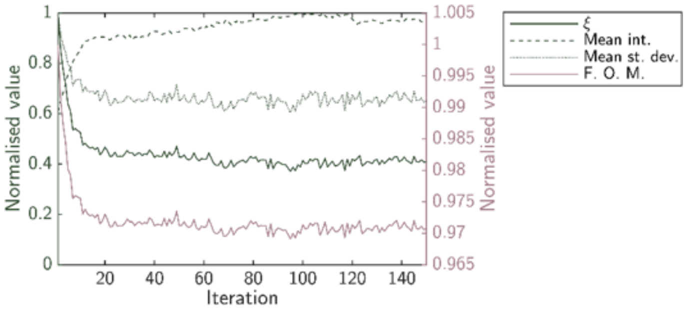

Figure B.18: **Progression of adjoint phase optimisation in the high scattering limit** using the normalised variance of the fields at the detectors over time as the FOM for an off-centre pocket of dipoles.

### Simulation results for higher levels of movement of dynamic dipoles using the adjoint optimisation with FOM 2

To further explore the capabilities of this optimisation, and compare it with previously introduced approaches, next the amount of movement of the dynamic dipoles and the number of configurations averaged over is increased. Fig. B.19 shows the results for a run of the optimisation with an increased standard deviation of motion of $2.5\lambda$ of the dynamic dipoles. The heatmaps of the intensity throughout the simulation area in Fig. B.19a and the log scale version of this data in Fig. B.19b show the optimised wavefront branching around the pocket of moving dipoles.

Fig. B.20 plots the progression of the optimisation, showing the FOM decreasing (solid light red line), and the fluctuations quantified by $\xi$ (solid green line) decreasing to approximately 55% of their initial value. This figure of merit in combination with the adjoint optimisation algorithm has succeeded in simultaneously increasing the mean intensity transmitted to the detectors (dashed green line) and decreasing the mean standard deviation of the field at the detectors (dotted green line).

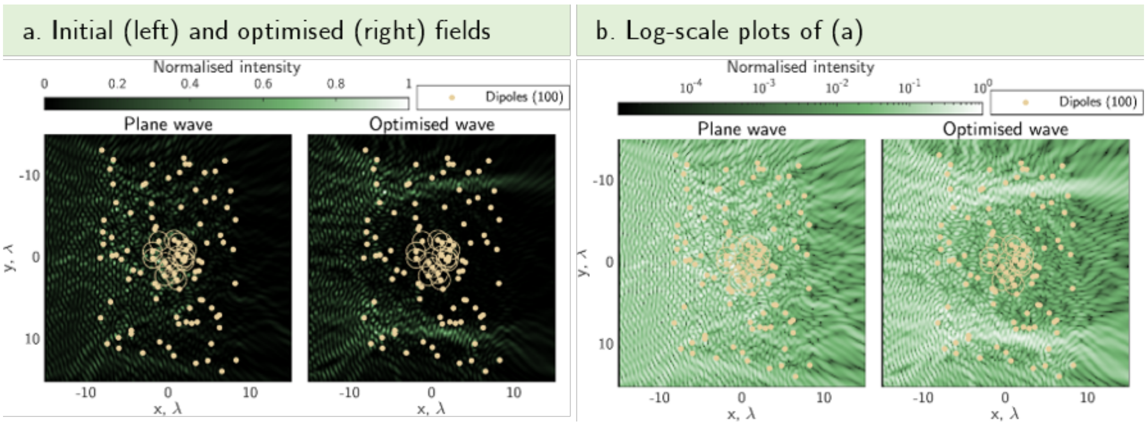

FIGURE B.19: **Simulation of adjoint phase optimisation in the high scattering limit** using the normalised variance of the fields at the detectors over time as the FOM. Sources are spaced $\lambda/4$. St. dev. of motion of dipoles is $2.5\lambda$, $n_{\mathrm{m}} = 200$ configurations are used for fluctuation quantification. $dj = 0.1$. (a) Intensity heatmaps showing plane wave (left) and optimised wavefront (right) propagating through 100 scattering dipoles (yellow dots), 15 of which are dynamic (circled). (b) Log scale version of plots in (a).

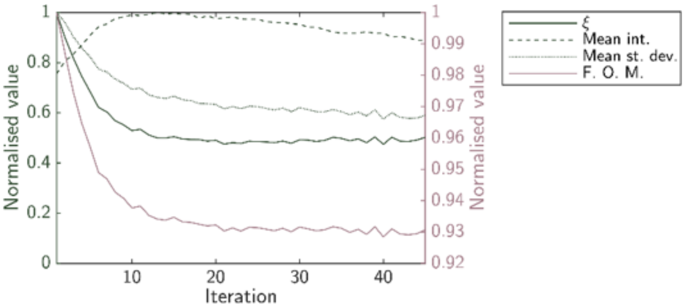

FIGURE B.20: **Progression of adjoint phase optimisation in the high scattering limit** using the normalised variance of the fields at the detectors over time as the FOM.

### Repeated simulations of the adjoint optimiser with FOM 2

Each of the results presented below were generated with a new random array of scattering dipoles to show the repeatability of the resulting optimised fields.

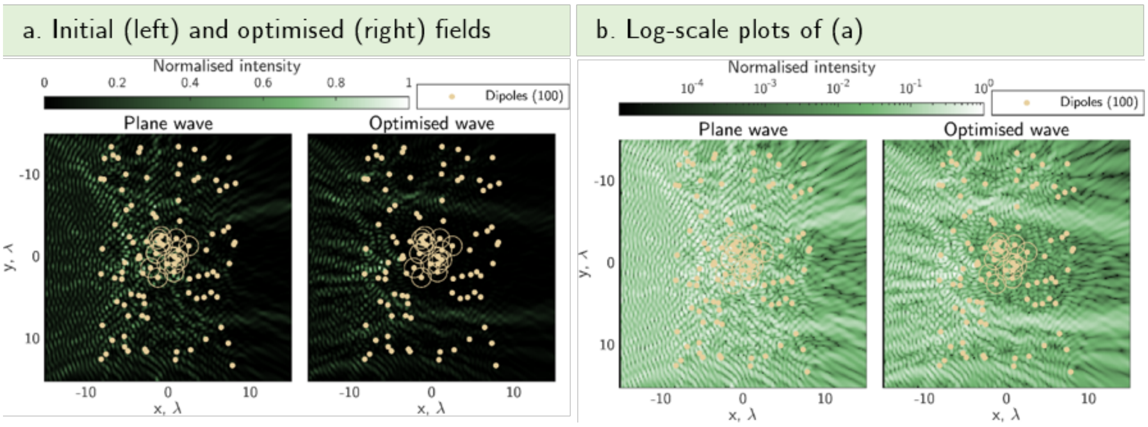

FIGURE B.21: **Run 1 of adjoint phase optimisation in the high scattering limit** using the normalised variance of the fields at the detectors over time as the FOM. Sources are spaced $\lambda/4$. St. dev. of motion of dipoles is $1.25\lambda$, $n_{\mathrm{m}} = 55$ configurations are used for fluctuation quantification. $dj = 0.1$. (a) Intensity heatmaps showing plane wave (left) and optimised wavefront (right) propagating through 100 scattering dipoles (yellow dots), 15 of which are dynamic (circled). (b) Log scale version of plots in (a).

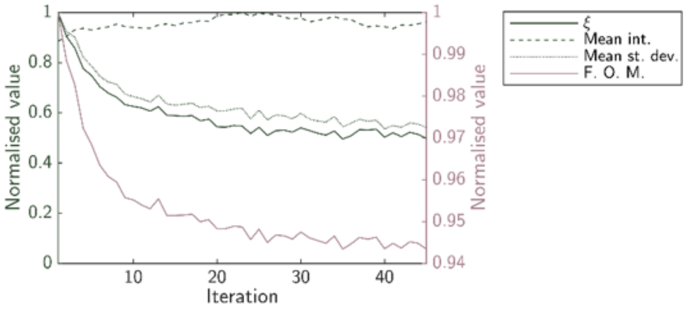

FIGURE B.22: **Progress of run 1 of adjoint phase optimisation with FOM 2 in the high scattering limit.**

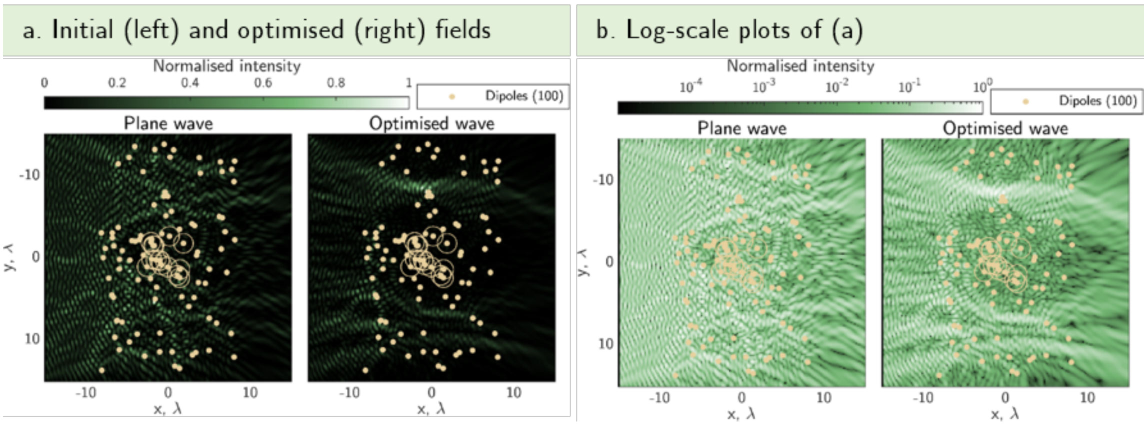

FIGURE B.23: **Run 2 of adjoint phase optimisation in the high scattering limit** using the normalised variance of the fields at the detectors over time as the FOM. Sources are spaced $\lambda/4$. St. dev. of motion of dipoles is $1.25\lambda$, $n_\mathrm{m} = 55$ configurations are used for fluctuation quantification. $dj = 0.1$. (a) Intensity heatmaps showing plane wave (left) and optimised wavefront (right) propagating through 100 scattering dipoles (yellow dots), 15 of which are dynamic (circled). (b) Log scale version of plots in (a).

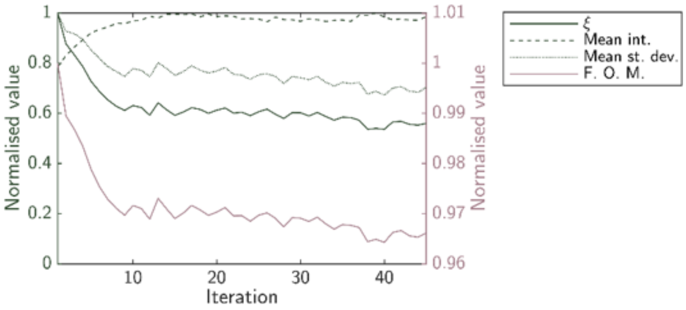

FIGURE B.24: **Progress of run 2 of adjoint phase optimisation with FOM 2 in the high scattering limit.**

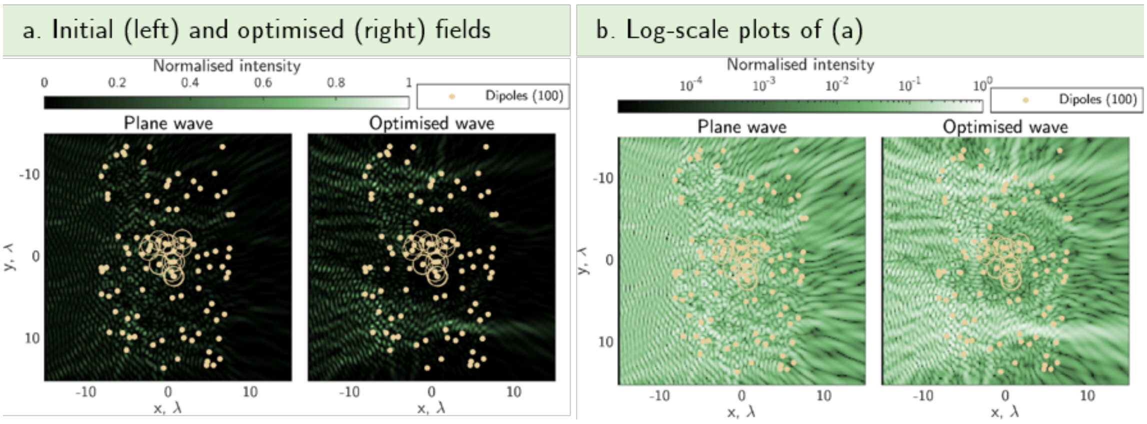

FIGURE B.25: **Run 3 of adjoint phase optimisation in the high scattering limit** using the normalised variance of the fields at the detectors over time as the FOM. Sources are spaced $\lambda/4$. St. dev. of motion of dipoles is $1.25\lambda$, $n_{\mathrm{m}} = 55$ configurations are used for fluctuation quantification. $dj = 0.1$. (a) Intensity heatmaps showing plane wave (left) and optimised wavefront (right) propagating through 100 scattering dipoles (yellow dots), 15 of which are dynamic (circled). (b) Log scale version of plots in (a).

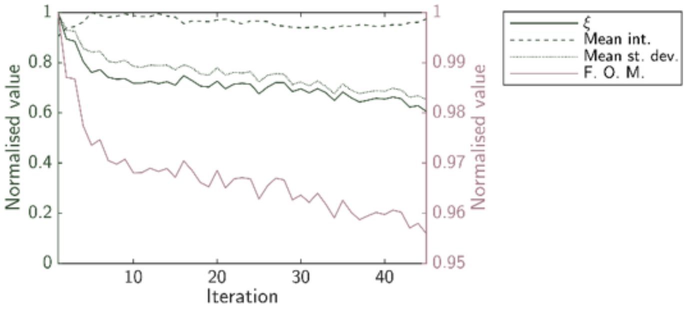

FIGURE B.26: **Progress of run 3 of adjoint phase optimisation with FOM 2 in the high scattering limit.**

## B.4 Time-averaged transmission matrix

### B.4.1 Repeated simulations of the time-averaged transmission matrix

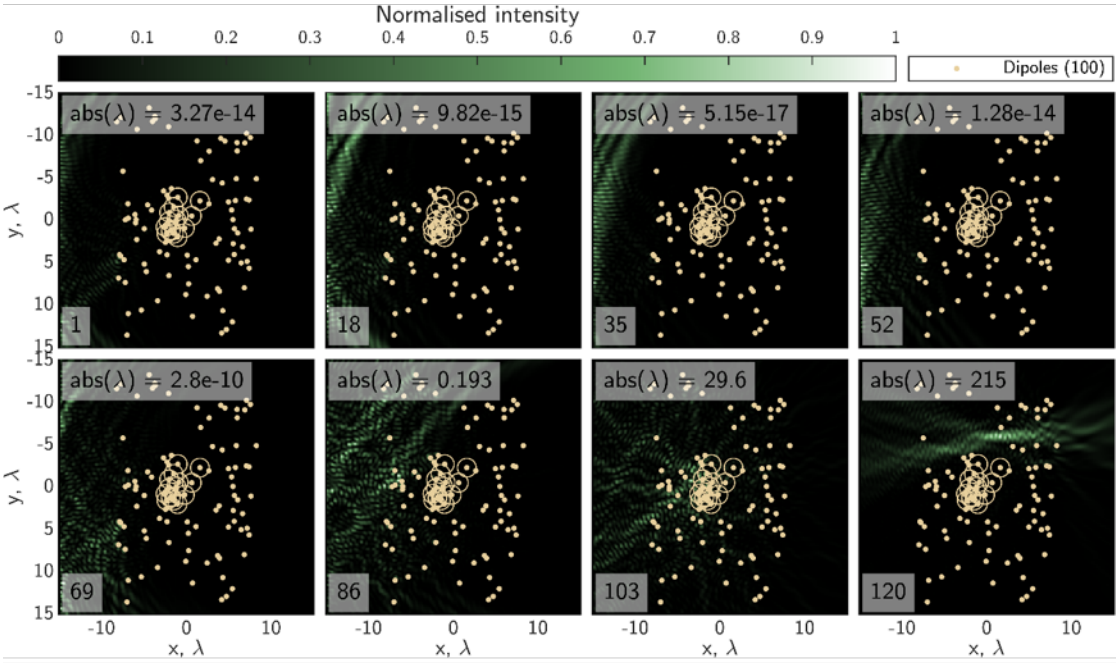
a. Intensity heatmaps of 8 eigenfields of $T_{avg}$

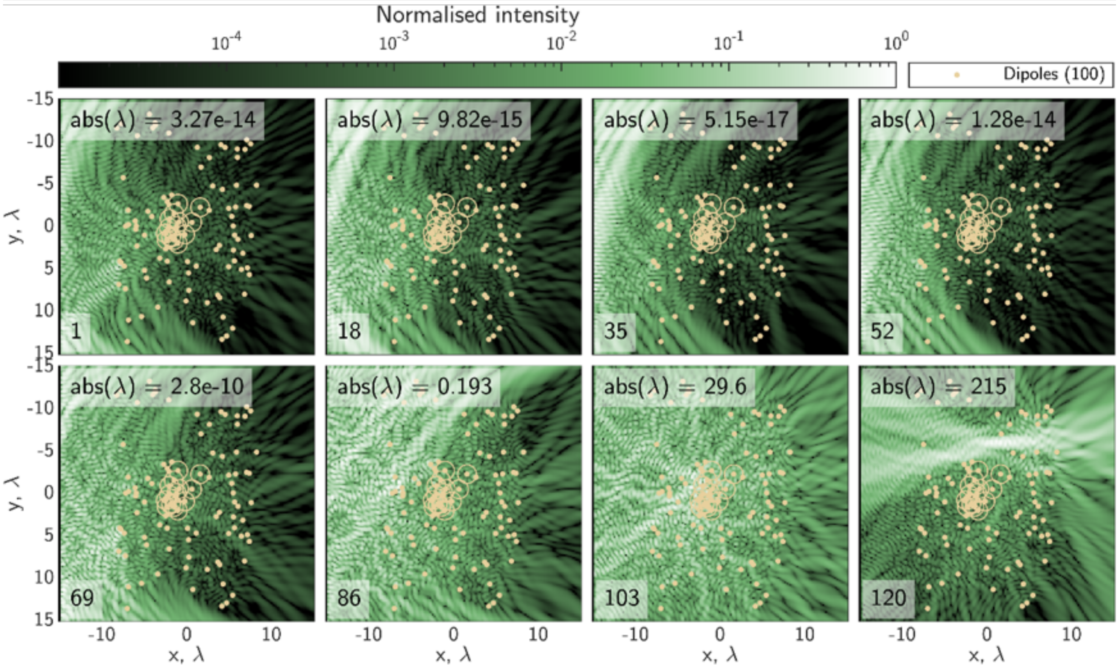
a. Log-scale intensity heatmaps of 8 eigenfields of $T_{avg}$

FIGURE B.27: **8 eigenfields of $\mathbf{T}_{\mathrm{av}}^{\dagger}\mathbf{T}_{\mathrm{av}}$ for a system of 100 dipoles, 15 of which move, in the high scattering limit** ($|\alpha| = 4k_0^{-2}$). The standard deviation of movement of the dynamic dipoles is $1.25\lambda$, and the fields are averaged over $n = 55$ configurations. The sources and detectors are spaced evenly $\lambda/4$ apart.

a. Intensity heatmaps of 8 eigenfields of $T_{avg}$

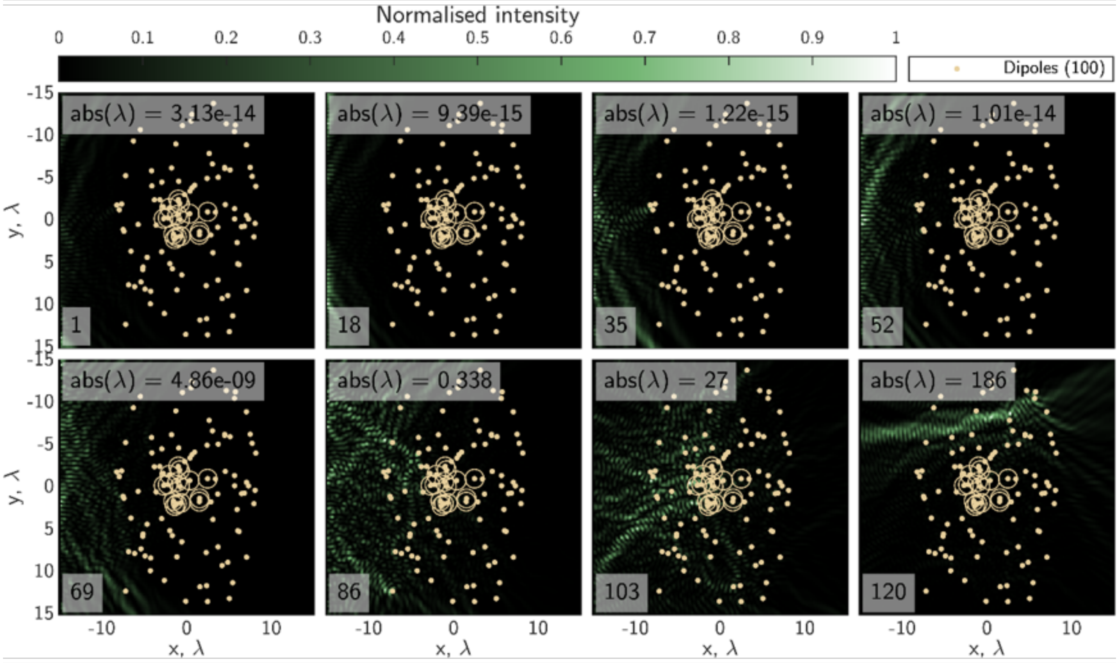

b. Log-scale intensity heatmaps of 8 eigenfields of $T_{avg}$

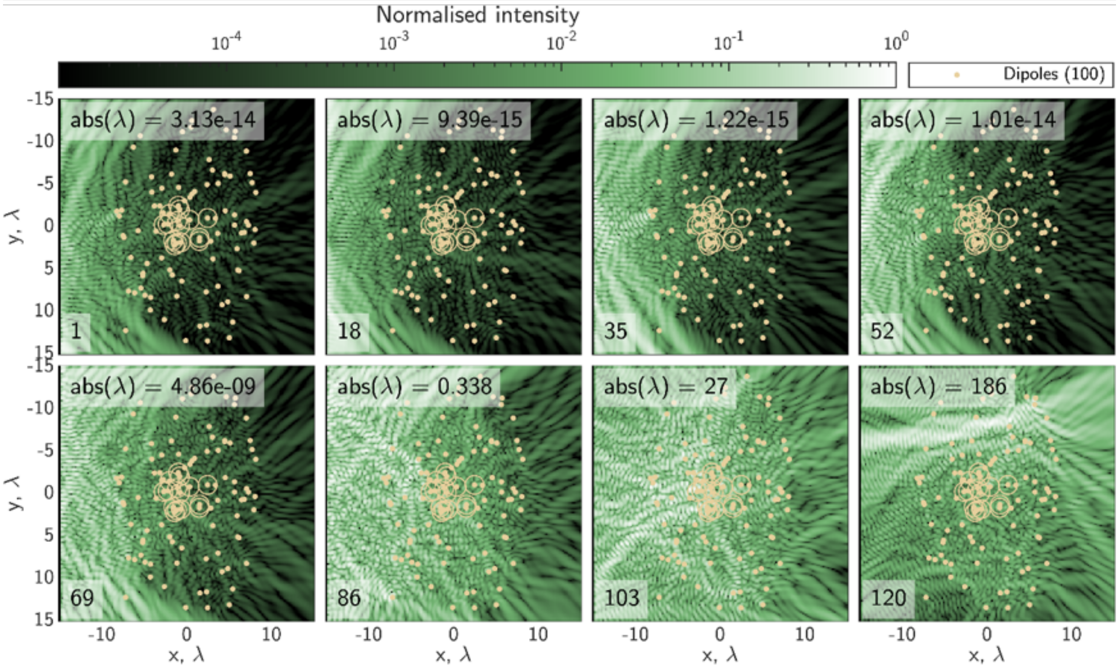

FIGURE B.28: **8 eigenfields of $\mathbf{T}^{\dagger}_{\mathrm{av}}\mathbf{T}_{\mathrm{av}}$ for a system of 100 dipoles, 15 of which move, in the high scattering limit** ($|\alpha| = 4k_0^{-2}$). The standard deviation of movement of the dynamic dipoles is $1.25\lambda$, and the fields are averaged over $n = 55$ configurations. The sources and detectors are spaced evenly $\lambda/4$ apart.

a. Intensity heatmaps of 8 eigenfields of $T_{\text{avg}}$

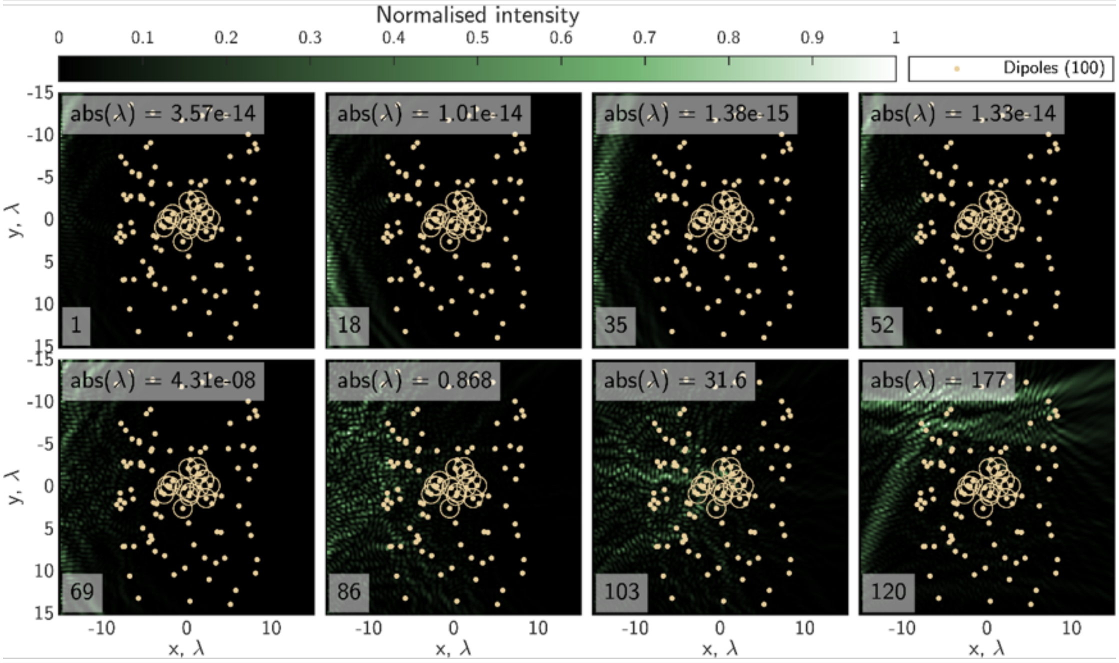

b. Log-scale intensity heatmaps of 8 eigenfields of $T_{\text{avg}}$

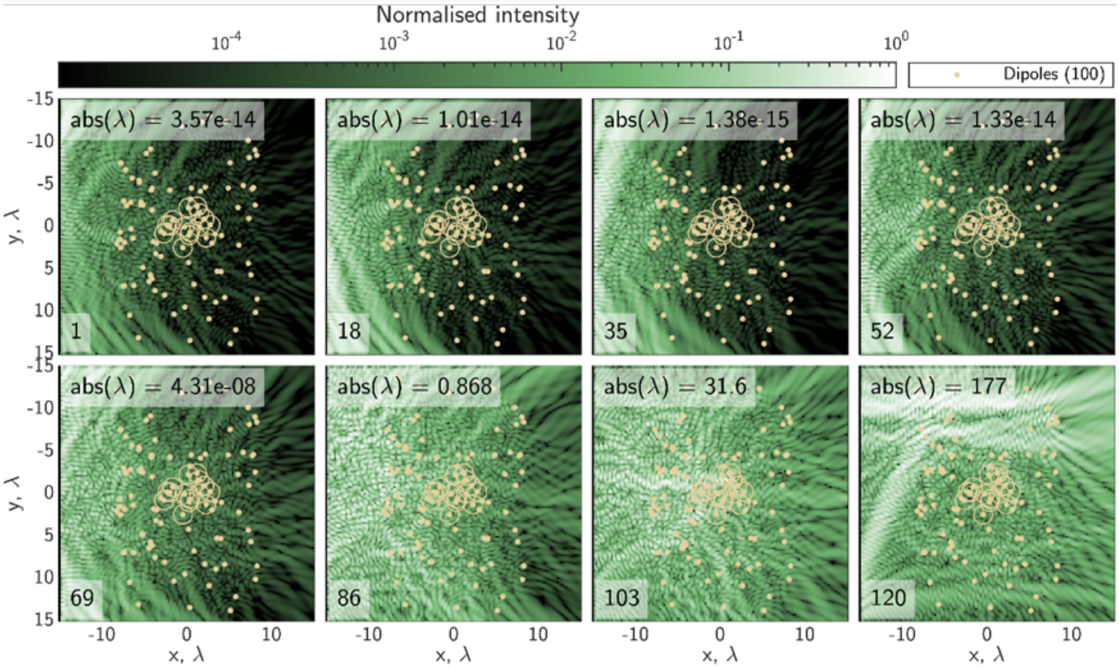

FIGURE B.29: **8 eigenfields of $\mathbf{T}_{\text{av}}^{\dagger}\mathbf{T}_{\text{av}}$ for a system of 100 dipoles, 15 of which move, in the high scattering limit ($|\alpha| = 4k_0^{-2}$).** The standard deviation of movement of the dynamic dipoles is $1.25\lambda$, and the fields are averaged over $n = 55$ configurations. The sources and detectors are spaced evenly $\lambda/4$ apart.

# Appendix C

# More details of the holographic optical tweezers system

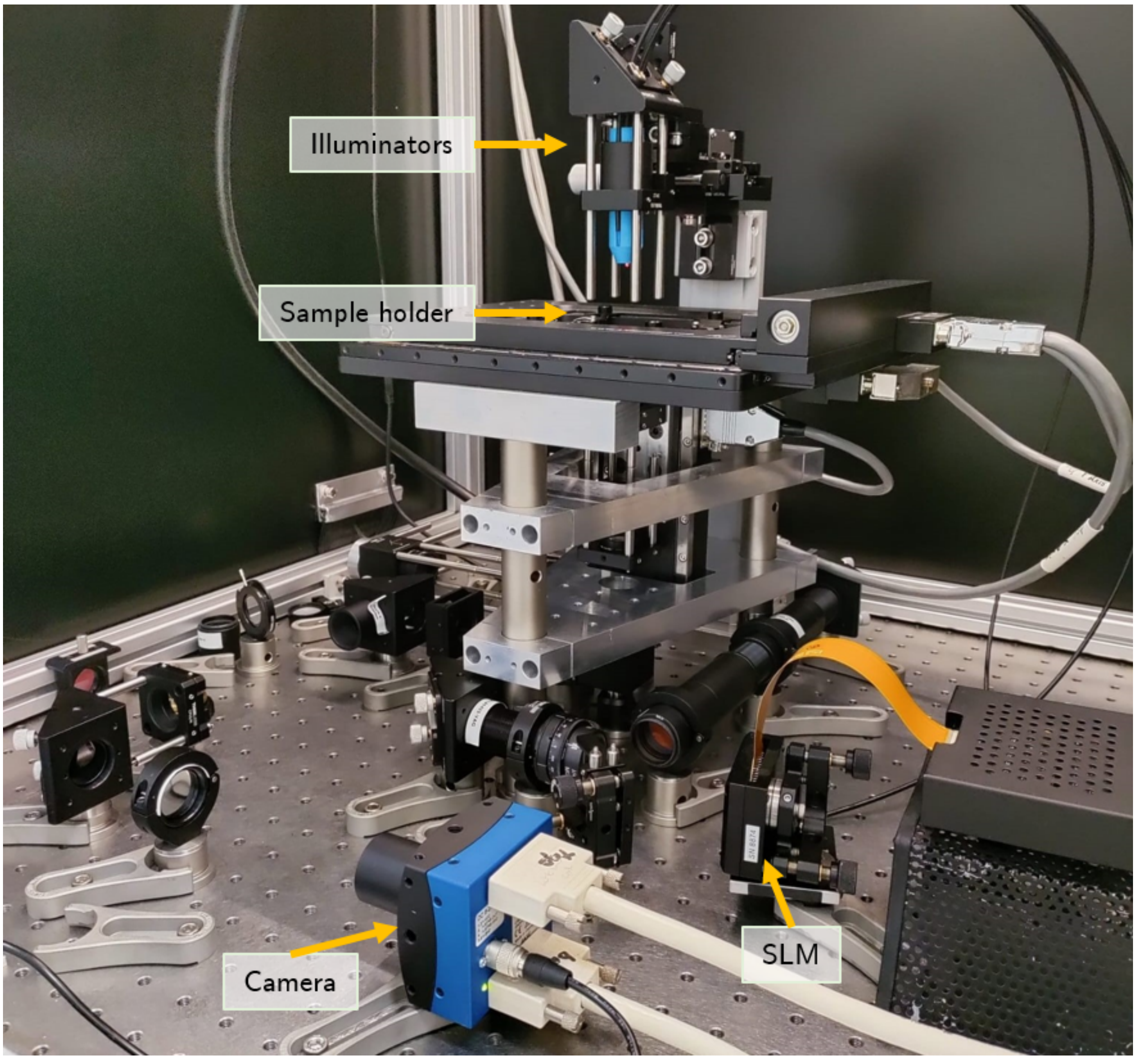

Figure C.1: **Image of the holographic optical tweezers system** used for the experiments presented in this thesis.

## C.1 Laser alignment for the holographic optical tweezers

Alignment of all parts of the holographic optical tweezers is critically important for the generation of accurate wavefront shaped optical traps and reliable 3D tracking data of optically trapped particles. A 1064nm laser can be tricky to align, since it is invisible to the human eye. Accurate alignment of the stereo-illuminators used to generate the left and right eye images needed to perform 3D tracking is necessary for low-error measurements. The following information will hopefully contain some useful ‘tips and tricks’ for alignment of the laser and imaging arms of a holographic optical tweezers such as the one used for the experiments presented in this thesis for any potential future researchers who may stumble across this thesis.

The author of this thesis also notes the importance of checking the system alignment before every experiment. Especially important, is to ensure that the plastic back of the inverted microscope objective has not melted off and fallen onto the lens directly below it. One cannot aberration correct or form an optical trap through a solid chunk of melted plastic.

Laser alignment is done sequentially from the laser head, along the beam path, to the sample anytime the laser path is adjusted. Because this laser is invisible, an infrared detector card (ThorLabs VRC4) is necessary to ‘see’ the beam path. It is very important to wear laser safety goggles (such as ThorLabs LG09 for this laser) for this work.

Firstly, the laser is centred on all lenses, mirrors, and other optical elements. Optionally, once the laser is satisfactorily aligned to the spatial light modulator, a phase pattern consisting of at least two rings varying in phase by $\pi$ is displayed on it. Such a phase mask will generate a bright ring of light with a dark centre. This intensity distribution is useful in alignment work for at least two reasons. Firstly, if the laser is not centred on the SLM (and therefore not centred on the phase pattern), the beam will have an uneven intensity distribution around the ring. Secondly, the exact centre of the intensity pattern is easier to determine than that of an expanded Gaussian intensity profile.

If necessary, the alignment of the expanded laser beam onto the SLM can now be adjusted, using the uniformity of the intensity around the ring as a marker of alignment. Then, after confirming that the laser is still centred on the remaining optics between the SLM and the sample, two irises are fitted at extreme ends of the vertical beam path. In the case of the HOT setup used here, the first iris is fitted immediately above the mirror that steers the beam upwards, and the second iris is mounted to a tube and placed in the microscope objective (which has been removed for this step) mount, as seen in Fig. C.2.

Because the mirror that reflects the beam upwards has no tip and tilt control, the SLM and the single mirror between the SLM and the vertical beam path are needed to align the vertical beam path. The top iris is initially kept open, and the bottom is gradually closed. Using the detector card above the sample mount (i.e. behind both irises in the beam path) to see the laser beam, the tip and tilt of the SLM is adjusted until the laser beam is centred going through the closed bottom iris. The bottom iris is then opened, and

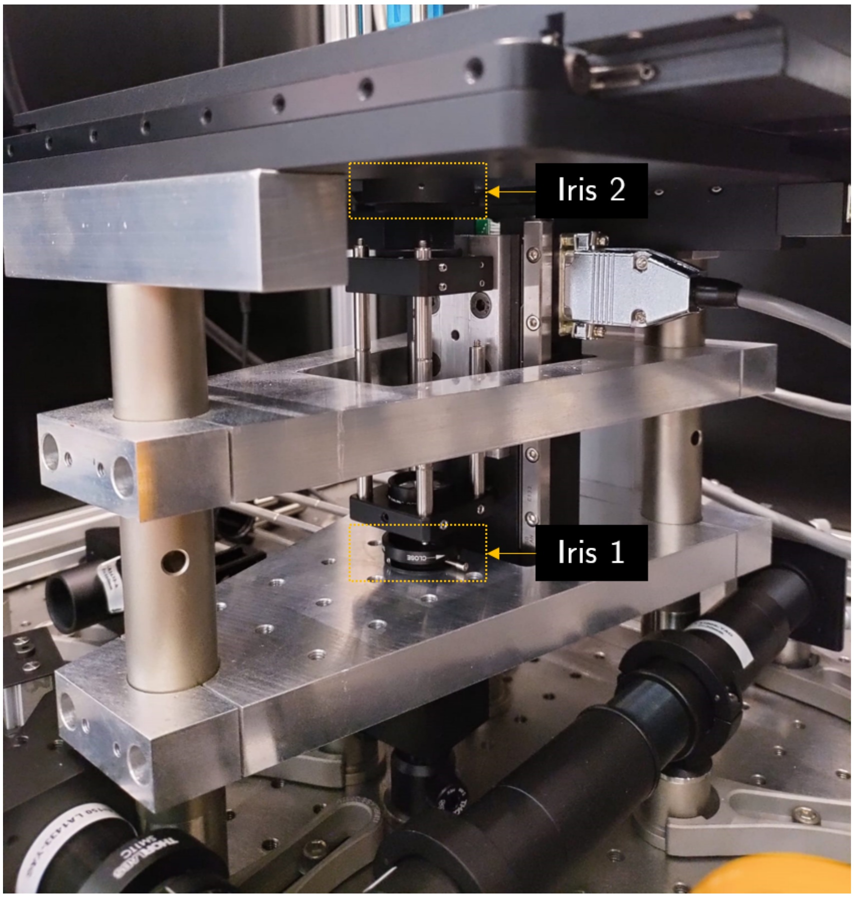

FIGURE C.2: **Location of irises for laser alignment.** Iris 1 screws into the metallic vertical housing of the tweezers. Iris 2 is attached to a small length of SM1 tubing that is screwed into the cage mount that normally holds the microscope objective lens.

the top iris is gradually closed. Again using the detector card above the sample mount, the tip and tilt of the mirror after the SLM is gradually adjusted to centre the laser beam through the top, closed iris. These steps are iteratively repeated - first closing the bottom iris, aligning the laser with the SLM tip and tilt, then opening the bottom iris and closing the top iris, and aligning with the mirror tip and tilt - until both irises can be closed at the same time and the laser beam remains centred through both irises. Once this is achieved, the irises can be removed.

To test the alignment of the laser and fine-tune it if necessary, a sample is placed in the sample mount and the reflection of the laser is imaged onto the camera. This requires the removal of the laser filter and, if applicable, the two prisms in the imaging arm towards the camera. The camera image of the reflected laser beam should show a circularly symmetric spot that does not change position on the camera as the $z$-stage is moved up and down. If the beam is not normally incident on the sample, the spot will change $(x, y)$ location on the camera as $z$ is adjusted. Additionally, the spot should retain a circularly symmetric intensity profile as $z$ is changed. If either of these things are untrue, the tip and tilt of the

SLM and mirror after the SLM will need to be adjusted in tandem. Keeping an eye on the camera image to see which direction the spot moves, the tip on the SLM is adjusted to move the spot in one direction before immediately being moved back to the initial camera location using the tip of the mirror in the opposite direction. This is repeated with tip and tilt as often as is needed until the laser beam is largely stationary and symmetric for different $z$ heights of the stage.

## C.2 Stereo-microscope alignment

The ability to track a trapped microsphere in 3D using 2D camera images is possible using stereo-vision. To facilitate minimally low errors in experiments, it is important to align the stereo-illuminators as well as possible. To make this easier, the illuminators are mounted on translational stages. A dummy sample of micro-spheres in water placed in the sample holder is useful for aligning the illuminators.

Aligning the illuminators in $x$ and $y$ is fairly straight-forward. After turning the camera and illuminators on such that the images of the sample are visible, at least one micro-sphere should be visible in both ‘eyes’ of the camera. The appearance of the micro-sphere is a good indicator of illuminator alignment – the spheres act as tiny lenses and will focus the illumination light to a point, causing them to appear as dark circles with bright centres if the stage is at the appropriate distance from the microscope objective lens (such as in the inset in Fig. 5.1). If the illuminators are misaligned, this bright focus will be off-centre and/or oblong. The $xy$ translation stage that the illuminators are mounted on can be iteratively adjusted in tandem with the mirror steering the light through the two prisms until the bright focus in the images of the micro-sphere appear centred in both eyes.

In addition to proper alignment in the $x$ and $y$ directions above the sample using the stages, it is important that the angle between the illuminators is as wide as possible, i.e. the illuminators are low and close to the back of the sample at an optimal $z$ position.

To investigate exactly how close the illuminators need to be to the sample, stationary micro-spheres were ’tracked’ using stereo-vision. To fabricate samples with stationary micro-spheres, a drop of micro-sphere dilution in water is left on a clean coverslip to air dry. This cover slip is included in a new sample, which then allows the 3D tracking of a stuck micro-sphere for the measurements presented in the tables and figure below.

The experiment to collect the 3D tracking data involved allowing the centre-of-mass (CoM) symmetry tracking built into the LabVIEW software that controls the HOT system to track one of the stationary micro-spheres, without the laser on. It is also important to sample several stuck micro-spheres, as some of them may not be truly stuck to the coverslip and will begin to wiggle free in the water. Once a fully-stuck micro-sphere is located in the sample, the LabVIEW software is used to record 3D CoM tracking data. The exact duration varies slightly from bead to bead, but each was tracked for between

a. Measuring height of illuminator

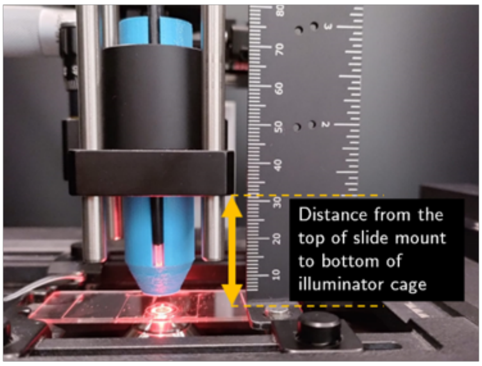

Distance from the top of slide mount to bottom of illuminator cage

b. 3D tracking data for stuck 2.59µm silica micro-sphere

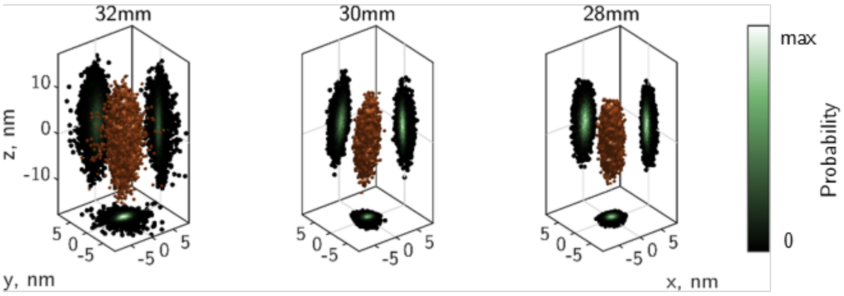

c. 3D tracking data for stuck 4.99µm silica micro-sphere

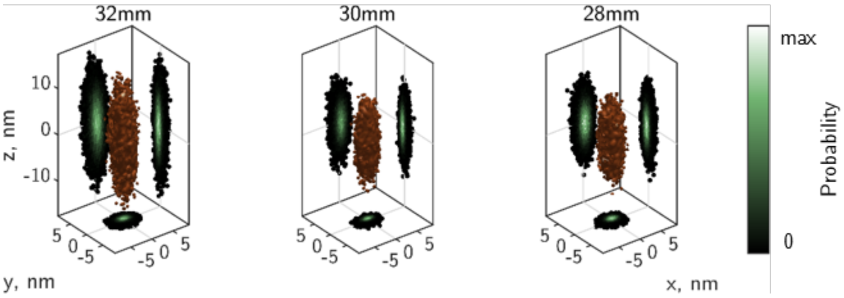

Figure C.3: **3D tracking error vs illuminator height.**

30 and 50 seconds, at a camera frame rate of 250 fps. Each bead was tracked for three different illuminator heights above the sample. These heights were measured as seen in Fig. C.3a, from the top of the slide mount holding the sample to the bottom of the first black cage mount holding the illuminator mount.

The optimum illuminator height was investigated for two radii of silica micro-spheres - 2.59 µm and 4.99 µm. The height of the illuminators was measured by eye as seen in Fig. C.3a, from the top of the sample holder/slide mount to the top of the illuminator cage mount.

The 3D CoM data for a stationary 2.59 µm sphere is seen in Fig. C.3b for illuminator heights of 32, 30, and 28 mm. This data was analysed for the error on the CoM position, $\epsilon_{\text{CoM}}$, which is the standard deviation of the data in each dimension. Results for the errors are shown in Table C.1 below. Clearly, from both the visualisations of the volumes 'explored' and the table of the errors, the illuminators should be mounted no higher than 30 mm.

**Tracking error for 2.59 µm bead**

| Illuminator height | $\epsilon_{\mathrm{CoM}_x}$, nm | $\epsilon_{\mathrm{CoM}_y}$, nm | $\epsilon_{\mathrm{CoM}_z}$, nm |
|---|---|---|---|
| **32 mm** | 0.88 | 1.13 | 3.71 |
| **30 mm** | 0.66 | 0.73 | 2.62 |
| **28 mm** | 0.66 | 0.79 | 2.55 |

Table C.1: **Experimentally determined 3D tracking error for a** 2.59 µm **radius silica micro-sphere at different illuminator heights.**

This same process was repeated for a 4.99 µm silica micro-sphere (see Fig. C.3c for the 3D CoM tracking data). Table C.2 contains the experimentally determined tracking errors for this size micro-sphere.

**Tracking error for 4.99 µm bead**

| Illuminator height | $\epsilon_{\mathrm{CoM}_x}$, nm | $\epsilon_{\mathrm{CoM}_y}$, nm | $\epsilon_{\mathrm{CoM}_z}$, nm |
|---|---|---|---|
| **32 mm** | 0.66 | 0.92 | 4.03 |
| **30 mm** | 0.51 | 0.80 | 2.73 |
| **28 mm** | 0.65 | 0.84 | 2.76 |

Table C.2: **Experimentally determined 3D tracking error for a** 4.99 µm **radius silica micro-sphere at different illuminator heights.**

As above, these results indicate that the illuminators should be positioned at most 30 mm above the sample, for minimal errors in the 3D tracking data. In addition to optimising the height of the illuminators, these results allow confirmation that this experimental setup, has the capability to track the 3D CoM of stuck micro-spheres with nanometric precision, as in [117].

## C.3 Mono-vision alignment

The stereo-illuminators can be replaced by a single illuminator normal to the sample surface. This allows standard 2D microscope imaging and tracking, if desired. The alignment for this is straight-forward: the *xy* translational stages that the illumination is mounted on should be iteratively adjusted until the image created is centred through all optics and creates an image on the camera wherein the micro-particles are illuminated properly from directly above.

## C.4 Sample preparation

The samples used in the optical tweezers experiments consisted of dilutions of $SiO_2$ microspheres in water. To create the samples, glass microscope slides (1.0—1.2 mm thick)

a. Sample of 4.01µm radius micro-spheres dilution in water

b. Superpixel aberration correction sample with Au

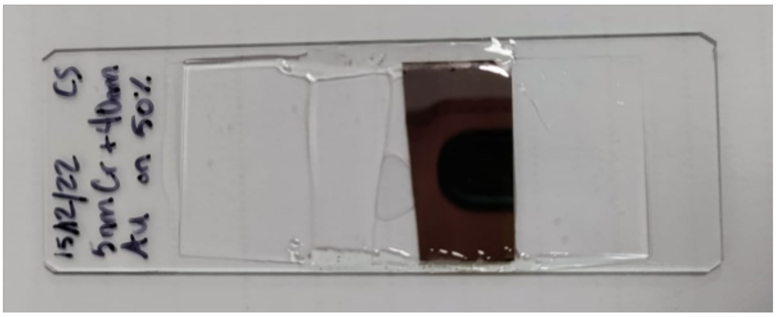

FIGURE C.4: **Images of samples.** (a) Example sample of 1:1000 4.01 µm silica micro-sphere dilution in water. (b) Half reflective sample used for superpixel aberration correction.

and coverslips (24×24 mm, 0.17—0.19 mm thickness) were glued together using Norland Optical Adhesives (NOA) 68 and 81.

First, the slides and coverslips were placed in holders which were submersed in ethanol in glass beakers. They were then sonicated for 10 minutes before being removed from the ethanol and dried. After this cleaning step, two coverslips were glued to the microscope slide using NOA 81 and promptly placed in a UV curing box (RS Components, LV202E) - this created the basis for the trough which would be filled with the microsphere dilution. Next, a third coverslip was glued to the top of the sample with NOA 81 to cover the trough. The sample was again UV cured. At this point, there were only two 'open' sides of the sample, one on either end of the trough created by the coverslips. After assembling the empty sample slide, a dilution of glass microspheres was pipetted into the trough which was immediately sealed using NOA 68 and UV cured.

Typically, a sample remained 'clean' enough (i.e. not micro-biologically contaminated) for one to two weeks. To ensure the cleanliness of the sample, ultra-pure water was used to make dilutions, and the glass slides and coverslips were sonicated in ethanol before sample fabrication.

## C.5 Using the SLM

The spatial light modulator is used to shape the laser beam in the far field (Fourier plane) to generate a given optical trap inside the sample (image plane). Typically, the patterns used in the experiments detailed in this thesis consisted of a combination of the following phase components:

1. A *phase grating*, used to position the first diffractive order at an arbitrary location within the sample. This phase mask can consist of a standard diffraction grating and a lens phase, allowing control of an optical trap in all three dimensions.
2. A *circular aperture*, used to limit which areas of the SLM will send light to the first diffractive order.
3. A *primary wavefront-shaping phase*, used to create the desired intensity distribution in the sample.

# Appendix D

# More experimental 3D enhancement results

This appendix contains the results of all 3D stiffness enhancement experiments presented in Fig. 6.7, showing successful trap optimisation for micro-spheres ranging from 2.59 to 4.99 µm.

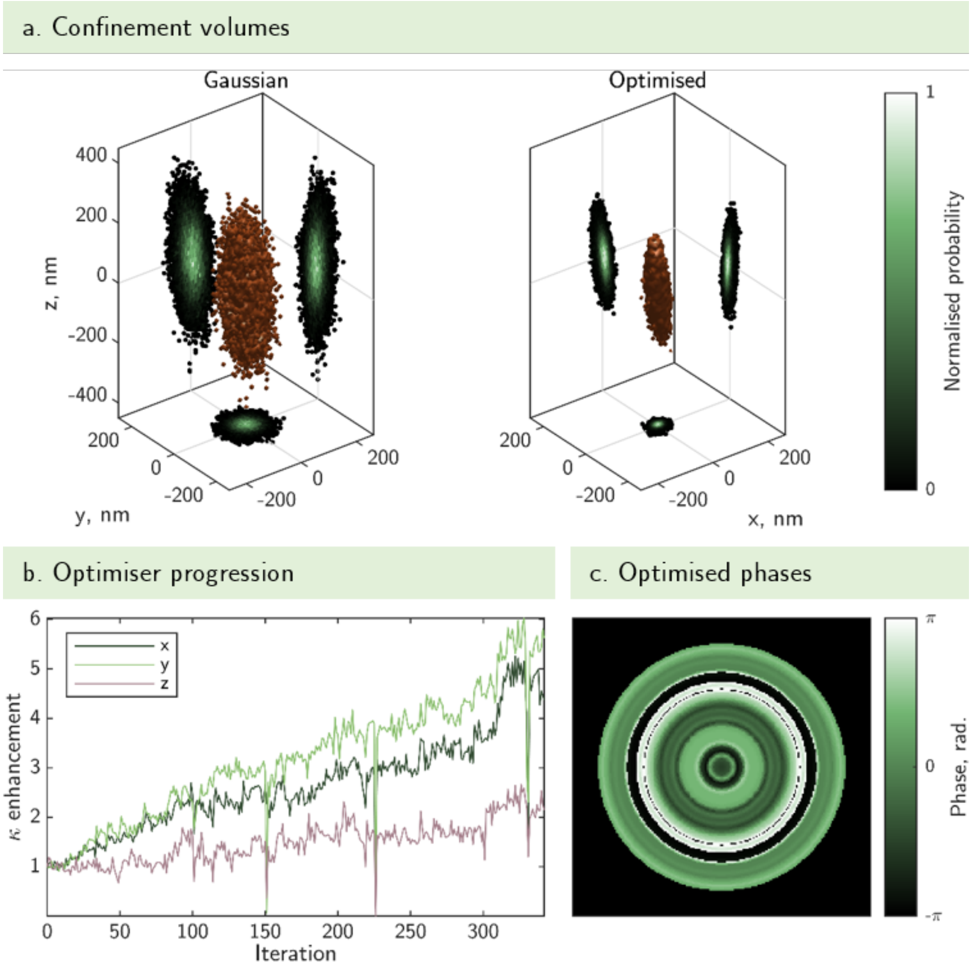

FIGURE D.1: Live optimiser results for a 2.59 µm radius silica micro-sphere. Integration time $\Delta t = 10$ s.

a. Confinement volumes

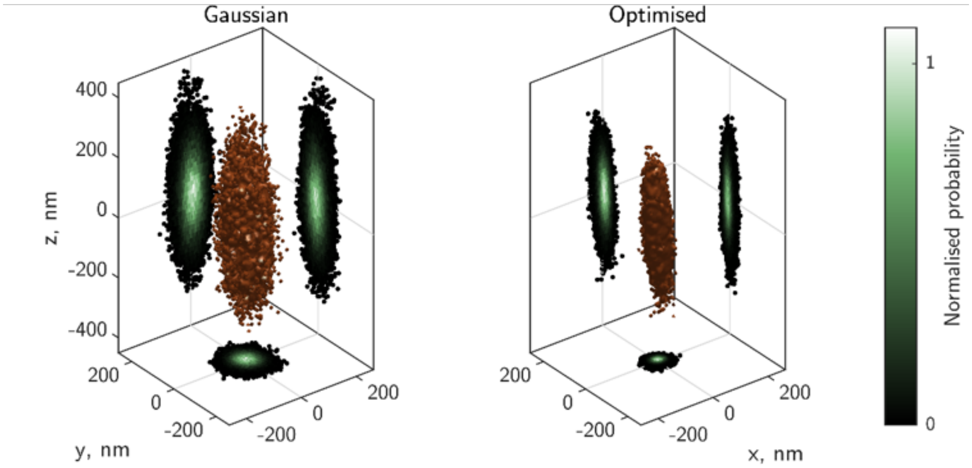

b. Optimiser progression

c. Optimised phases

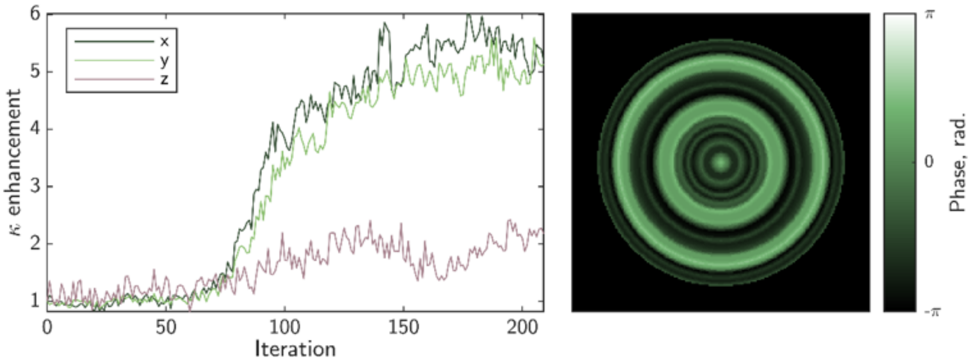

FIGURE D.2: Live optimiser results for a 2.59 µm radius silica micro-sphere. $\Delta t = 10$ s.

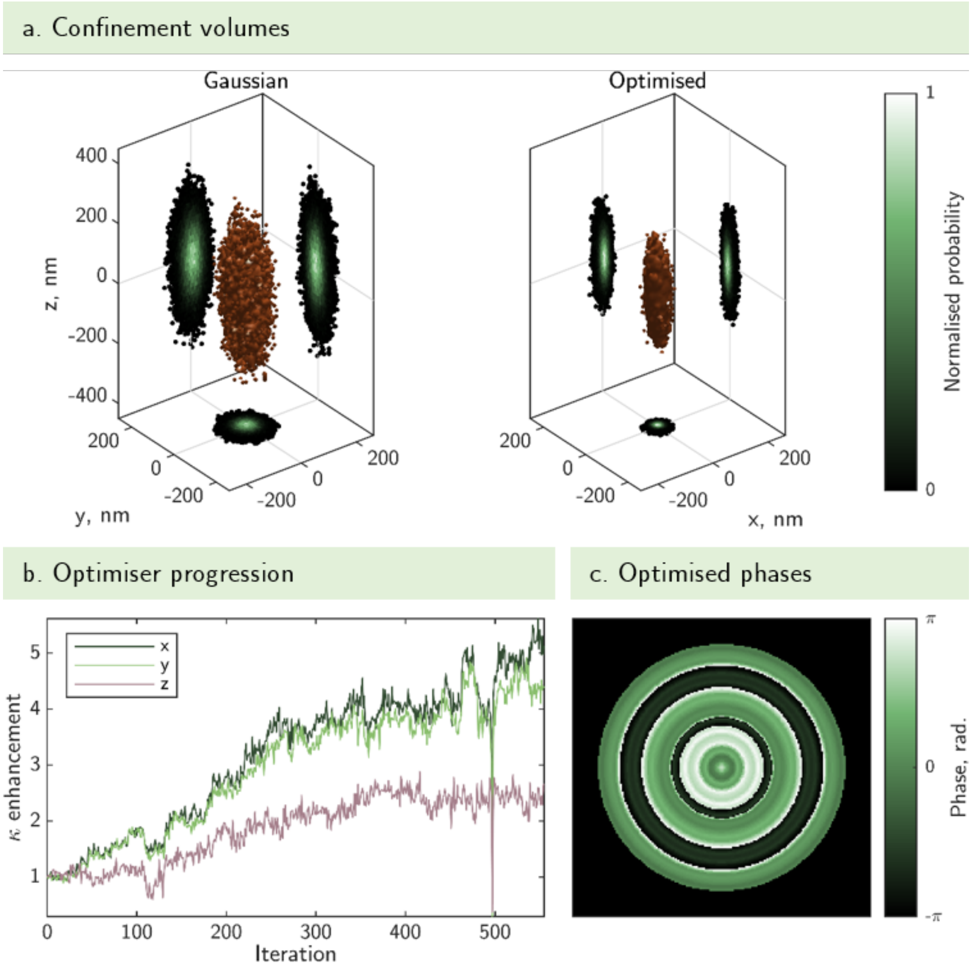

a. Confinement volumes

b. Optimiser progression

c. Optimised phases

FIGURE D.3: Live optimiser results for a 2.59 µm radius silica micro-sphere. $\Delta t = 10$ s.

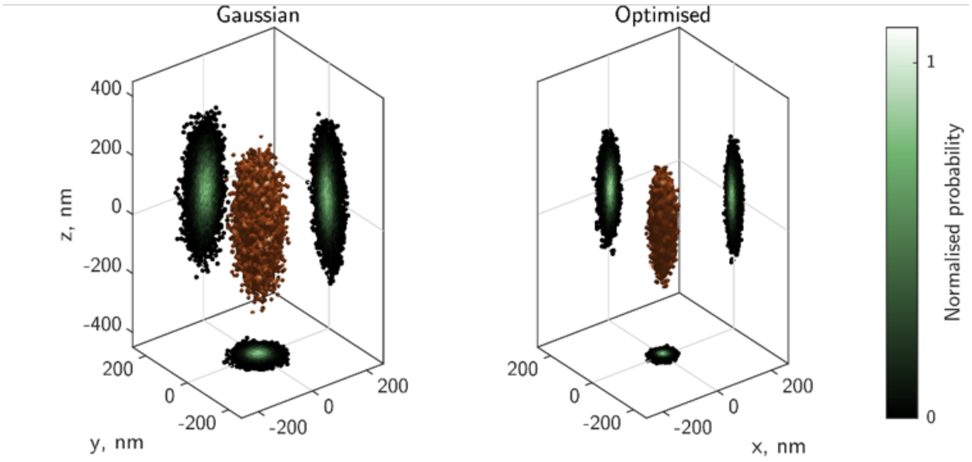

a. Confinement volumes

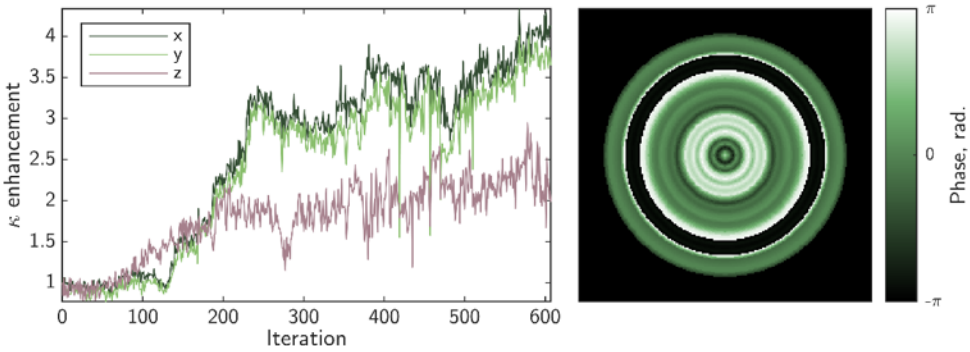

b. Optimiser progression

c. Optimised phases

FIGURE D.4: Live optimiser results for a 2.59 µm radius silica micro-sphere. $\Delta t = 10$ s.

a. Confinement volumes

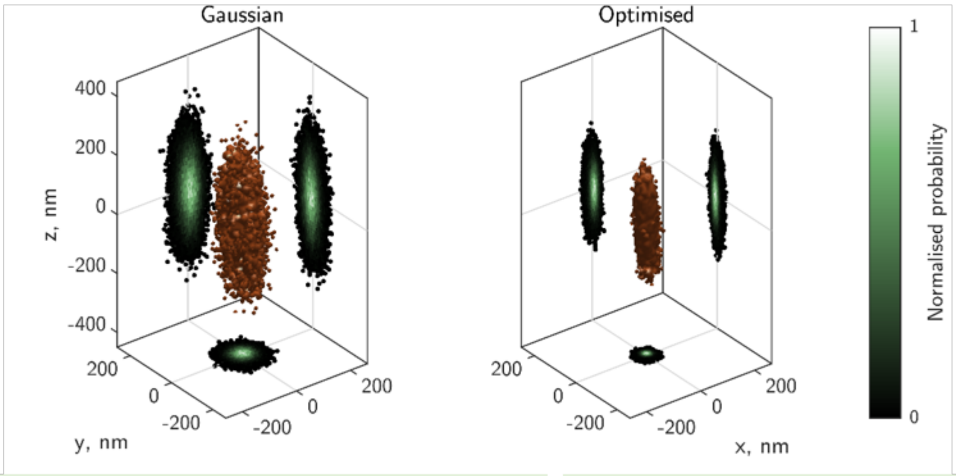

b. Optimiser progression

c. Optimised phases

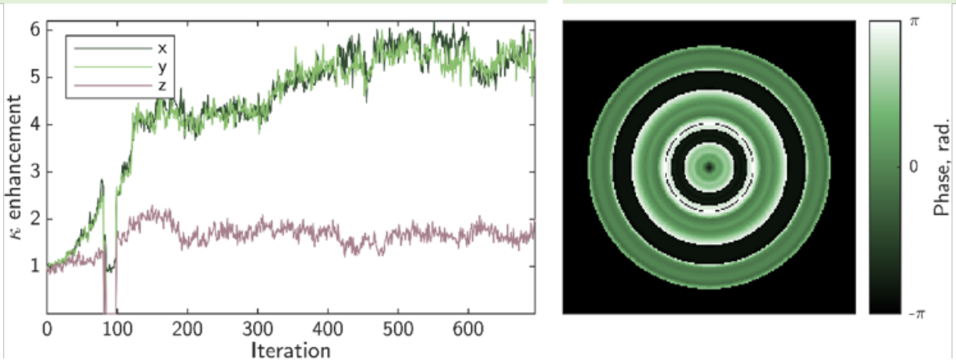

FIGURE D.5: Live optimiser results for a 2.59 µm radius silica micro-sphere. $\Delta t = 10$ s.

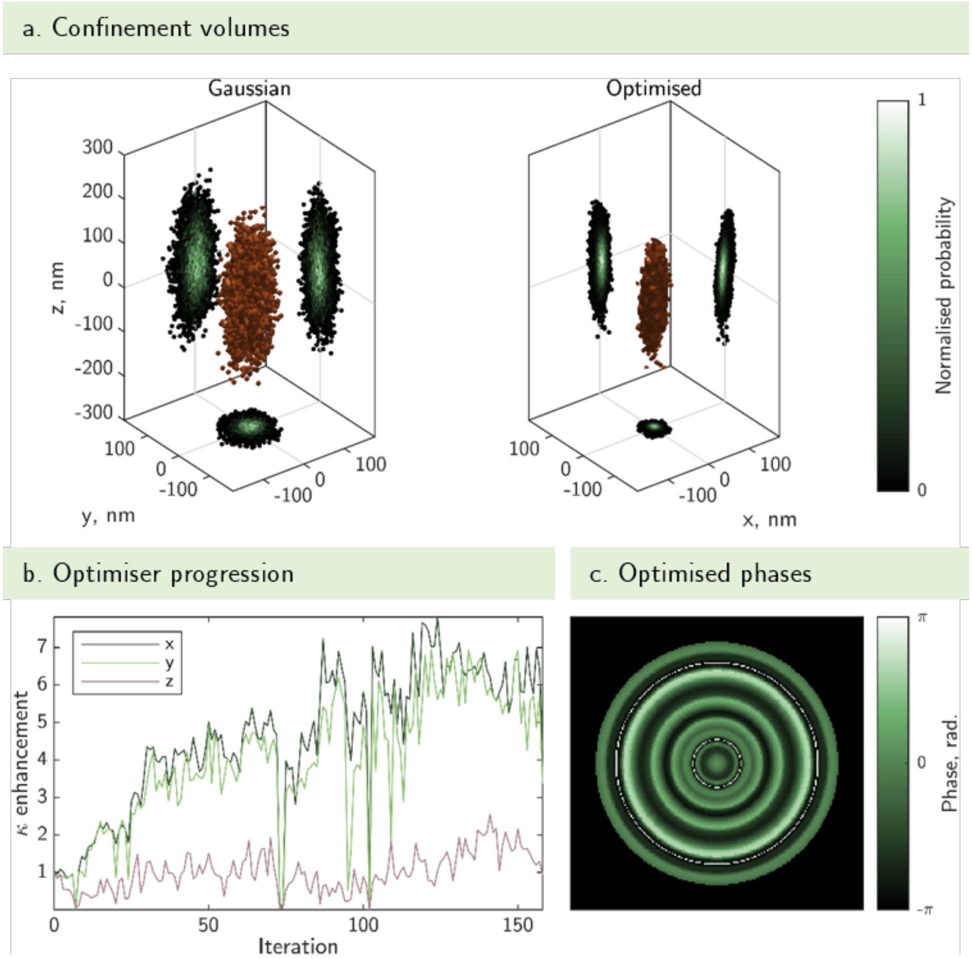

FIGURE D.6: Live optimiser results for a 4.01 µm radius silica micro-sphere. $\Delta t = 10$ s.

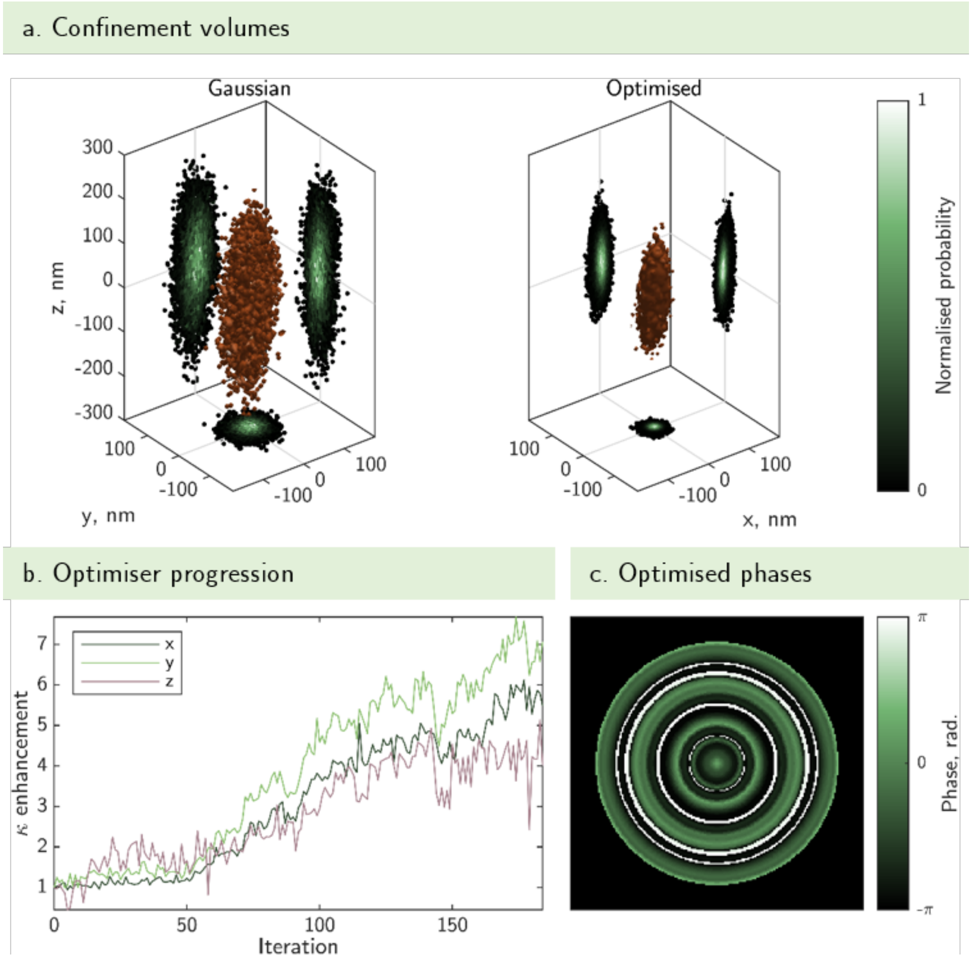

FIGURE D.7: Live optimiser results for a 4.55 µm radius silica micro-sphere. $\Delta t = 10$ s.

a. Confinement volumes

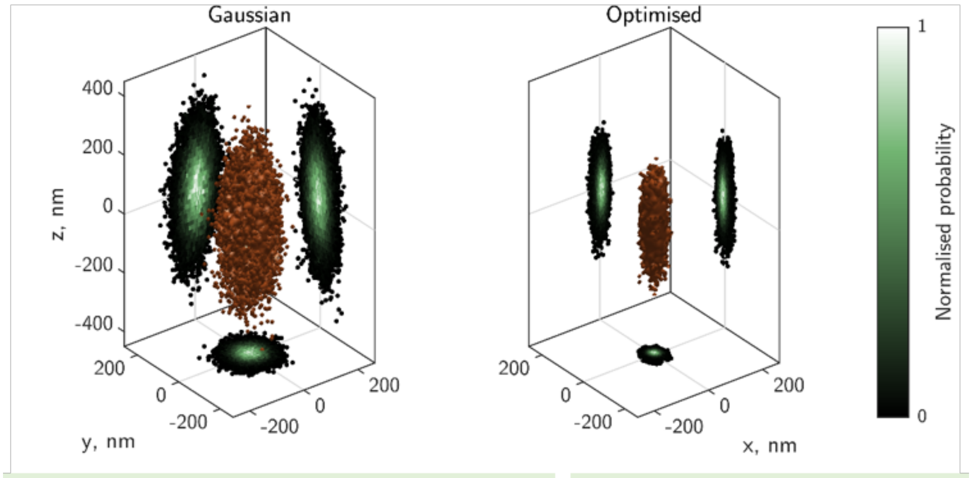

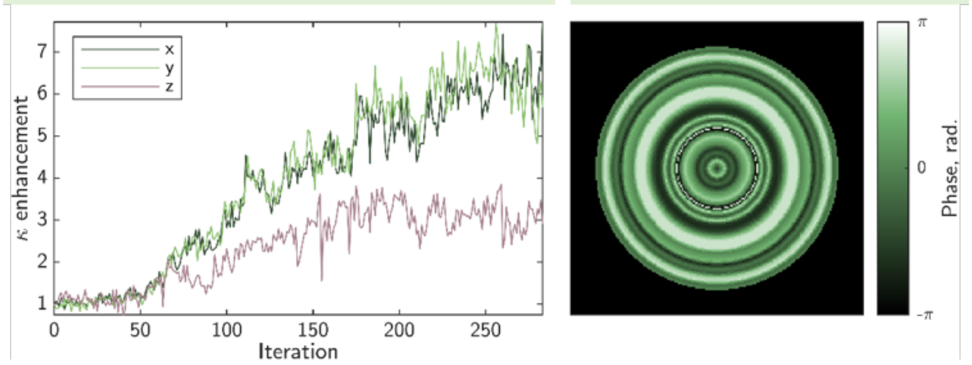
b. Optimiser progression

c. Optimised phases

FIGURE D.8: Live optimiser results for a 4.99 µm radius silica micro-sphere. $\Delta t = 5$ s.

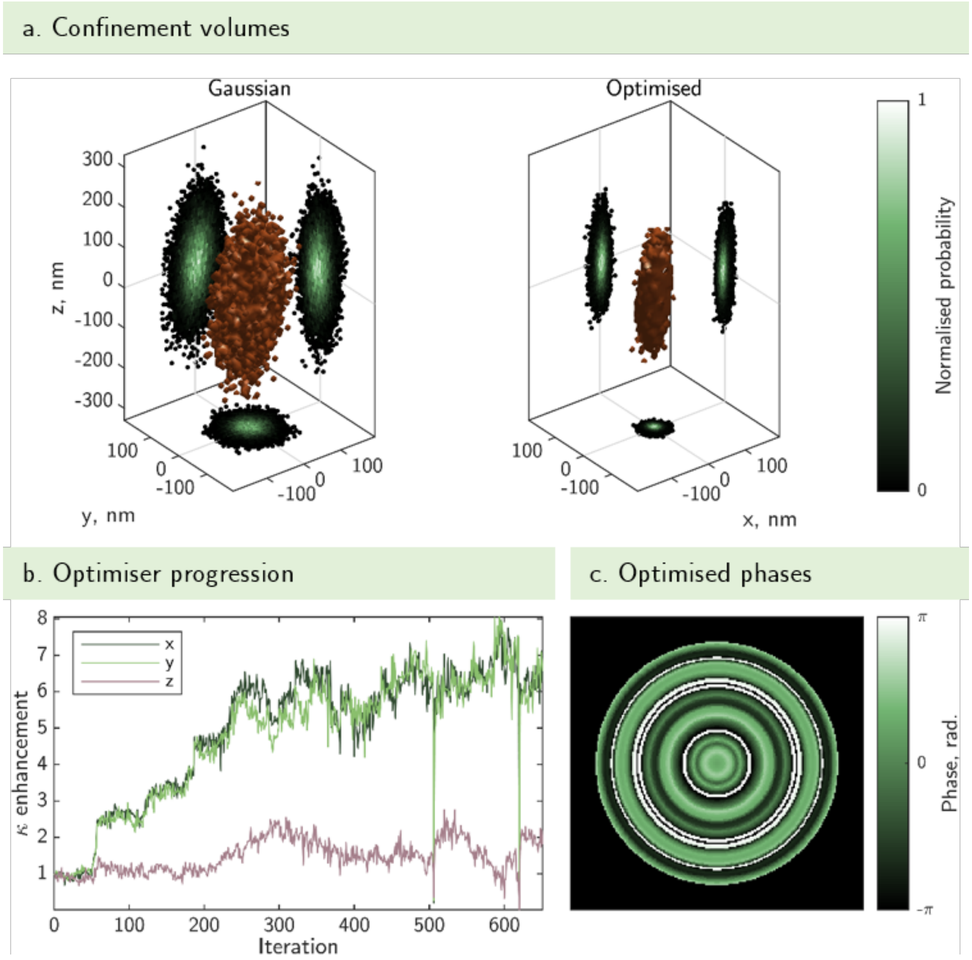

FIGURE D.9: Live optimiser results for a 4.99 µm radius silica micro-sphere. $\Delta t = 10$ s.

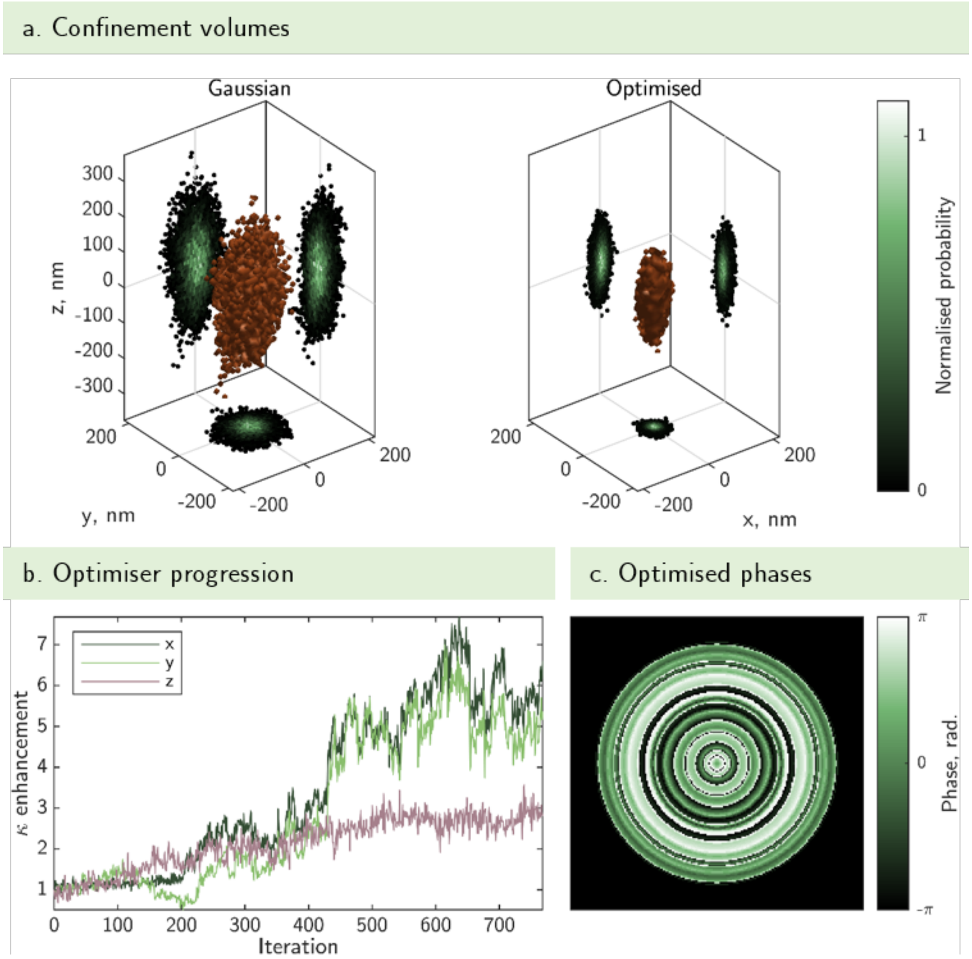

FIGURE D.10: Live optimiser results for a 4.99 µm radius silica micro-sphere. $\Delta t = 10$ s.

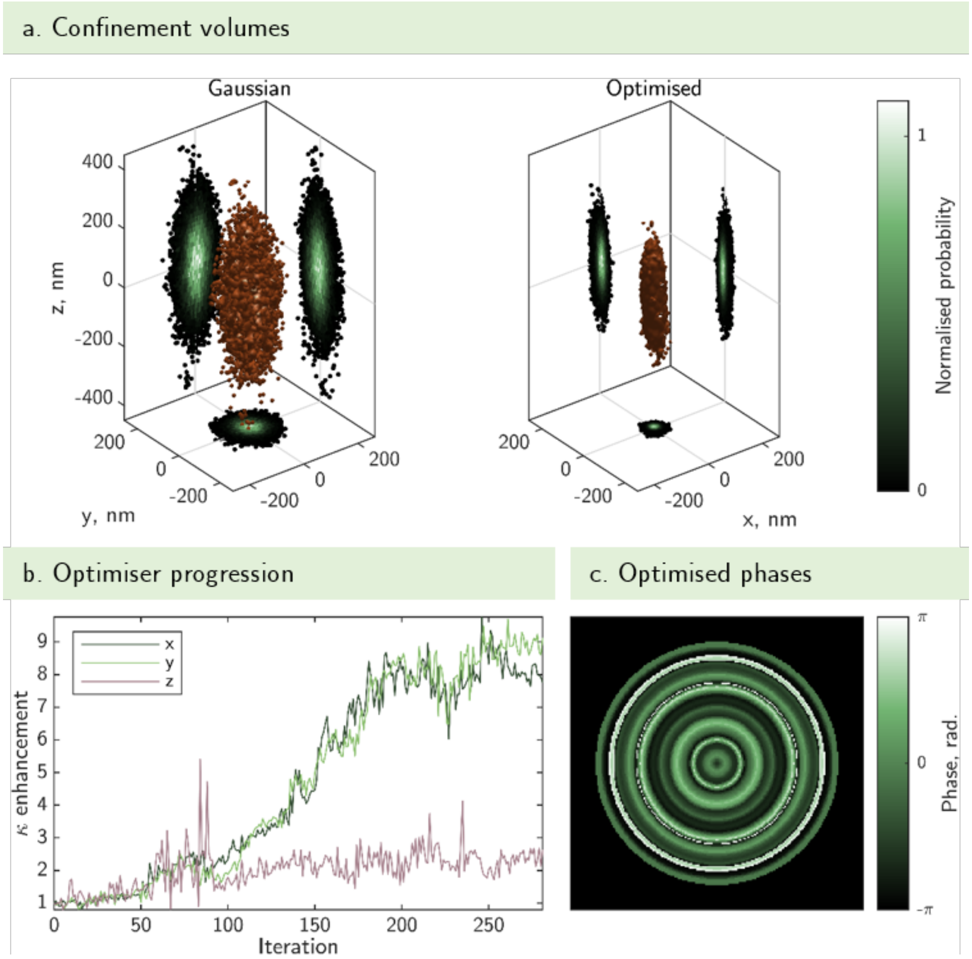
a. Confinement volumes

b. Optimiser progression

c. Optimised phases

FIGURE D.11: Live optimiser results for a 4.99 µm radius silica micro-sphere. $\Delta t = 6$ s.

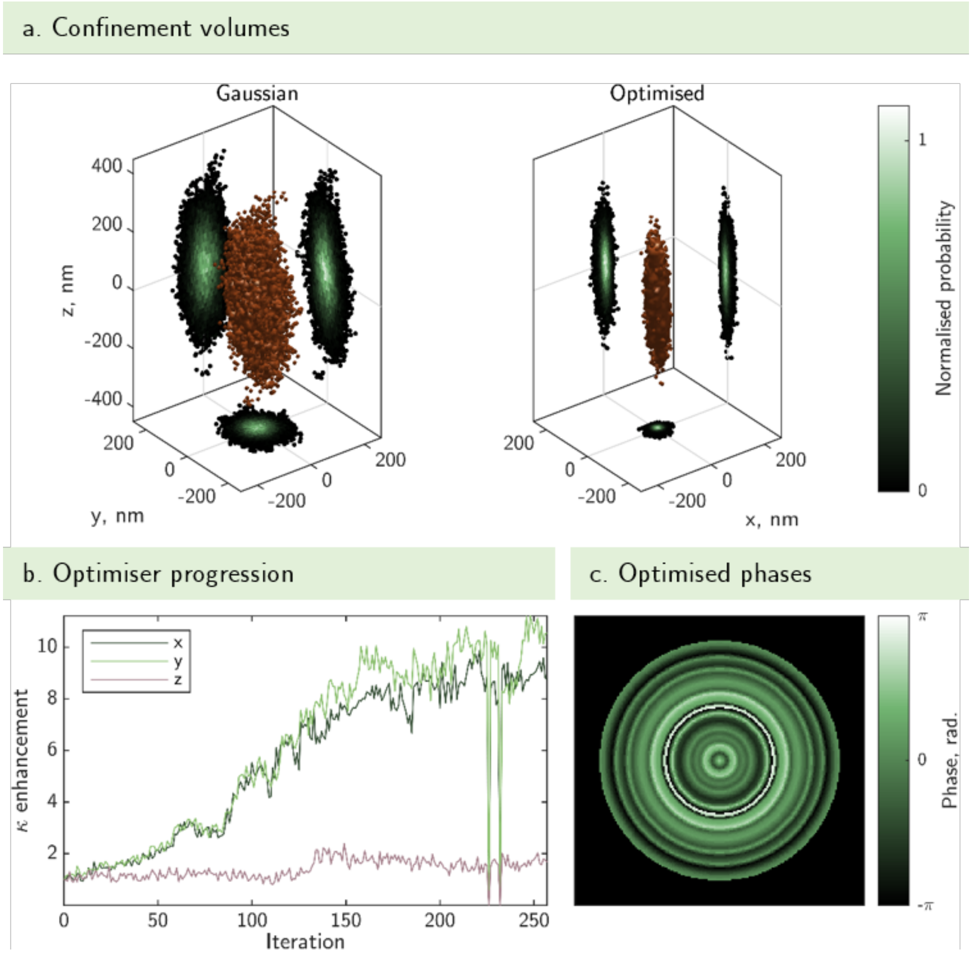

FIGURE D.12: Live optimiser results for a 4.99 µm radius silica micro-sphere. $\Delta t = 10$ s.

# Appendix E

# Controlling the holographic optical tweezers setup

The hardware and software in the holographic optical tweezers setup can be finicky. Here, a detailed description of the order in which everything should be turned on/initialised is presented to help any future researchers who may use this setup. For future researchers looking to use the same code, it is located on the computer next to the holographic optical tweezers system at *D:\Optical Tweezers\RedTweezers\red_stereotweezers \red_tweezers_3DstiffnessOptimiser.vi.*

Before any of the LabVIEW code is run, the user should ensure that the SLM and camera are turned on. The settings for each should be checked as described in the first two sections of this Appendix.

## E.1 Camera

The camera used in the work for this thesis is a Mikrotron, EoSens CL. Below are some steps that need to be taken before any LabVIEW programs can call the camera.

1. Before opening the LabView program to run the camera, open the software **MC ControlTool** and check that all of the settings are correct. Pay special attention to the Tap Mode (10 x 8), which annoyingly resets everytime the camera is rebooted, and the Baudrate (9600).

2. Once the settings are sorted, NI MAX can be used to test that the camera is working as expected. Once the software is open, navigate to My System > Devices and Interfaces > NI PCIe-1433 ”img0” > Channel 0: Mikrotron MC1310 and click ”Grab” to begin running the camera. If this works without errors or issues, CLOSE the program (this is important!!). If you leave NI MAX open and try to run the camera using a LabView program, it won’t work because the computer sees that the camera is already in use.

3. **Troubleshooting:**

(a) For some reason, the Channel 0: Mikrotron MC1310 has reset to a different camera on occasion. To change it back, right click on the Channel 0 line, and select Camera > Mikrotron > Mikrotron MC1310.

(b) If you ever need to load a new camera to NI MAX, right click as above, select Camera > Search ni.com. Search your camera and download the appropriate file. To load it into NI MAX, right click on Channel 0 again and select Open Camera. Navigate to the file you downloaded from ni.com and select to. Now this new camera can be found as described in 3.

The frame rate and exposure time are adjusted within the MC ControlTool software.

## E.2 LED Illuminators

The LED illuminators are powered externally using a custom piece of hardware, that needs to be connected to each of the LEDs used as well as a power socket. The illuminators are controlled using a custom LabVIEW code, shown in the screenshot in Fig. E.1, which allows the user to adjust the relative amount of intensity from each illuminator.

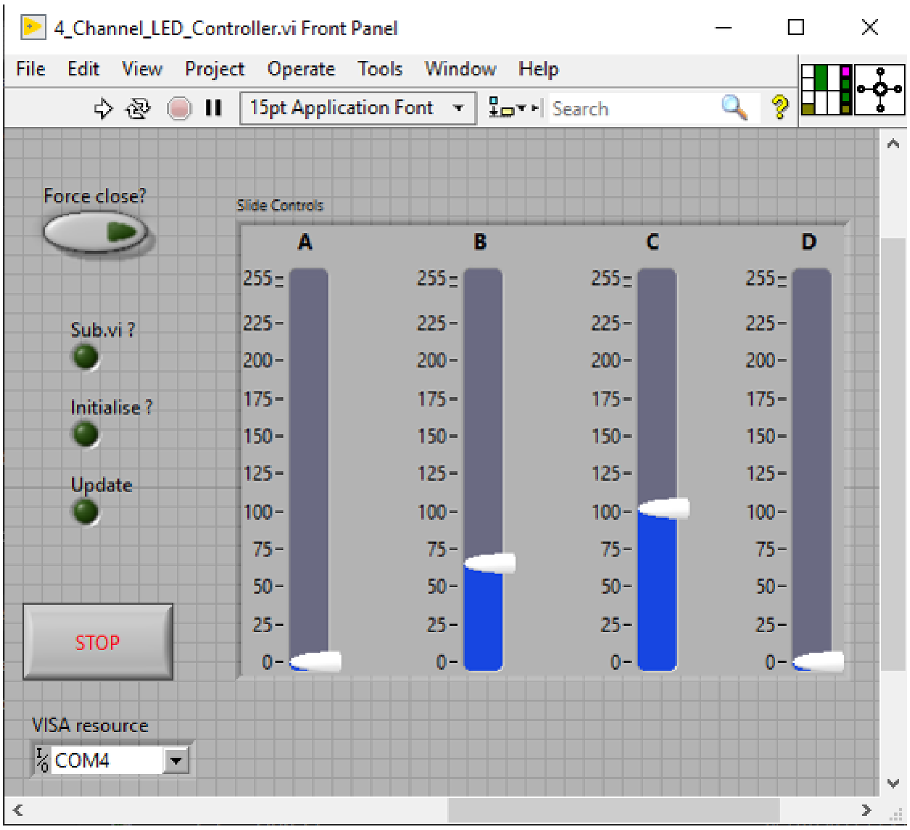

VISA resource: COM4

FIGURE E.1: Front panel of the LabVIEW program to control the LED illuminators in the optical tweezers setup.

This is run externally to the Red Tweezers software and can be opened and run at anytime. Once the run button is pressed, the 'Initialise?' Boolean will turn True for a few seconds. Once it has returned to off/False, the illuminator intensities can be adjusted at will. The 'VISA resource' needs to be set to the correct COM port, but this should default to the correct port. If it does not, check the computer's Device Manager to determine which COM port should be selected.

The relative intensities of the illuminators should be adjusted such that the images of the two eyes of the stereo-microscope have a similar contrast and intensity, after alignment.

## E.3 Spatial Light Modulator

The spatial light modulator (SLM) used in this work is a liquid crystal SLM (Boulder Nonlinear Systems: XY-series, 512 × 512 resolution). For the experiments presented here, the *Display on SLM* subVI written by supervisor Professor David Phillips is used. This program is used to display a desired U8 hologram on the SLM screen. The U8 hologram has values between 0 and 255, which are mapped from phases between 0 and $2\pi$ according to a blazing function shown in Fig. E.2. The blazing function can be manually adjusted if required, however the default one displayed in Fig. E.2 has been selected specifically for the SLM in the current holographic optical tweezers setup.

If another blazing table ever needs to be found, the cursors in the blazing function can be manually dragged and adjusted to different locations. The optimal configuration

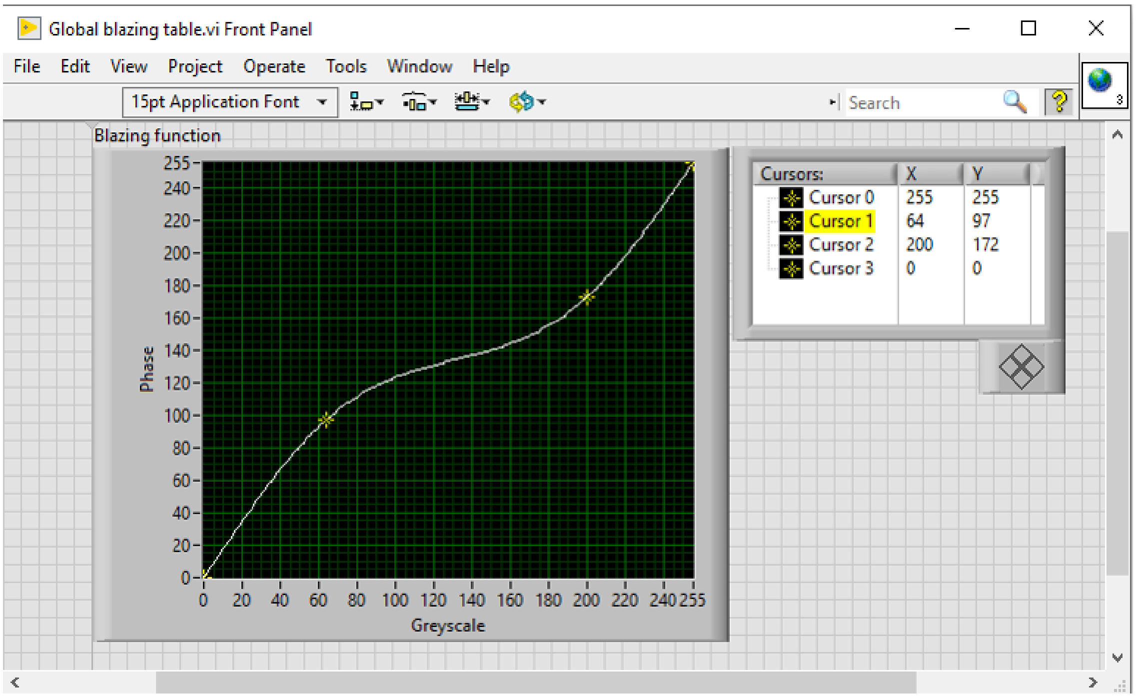

| Cursors: | X | Y |
|---|---|---|
| Cursor 0 | 255 | 255 |
| Cursor 1 | 64 | 97 |
| Cursor 2 | 200 | 172 |
| Cursor 3 | 0 | 0 |

FIGURE E.2: Blazing table VI showing the relation between U8 greyscale values and imparted phase delay.

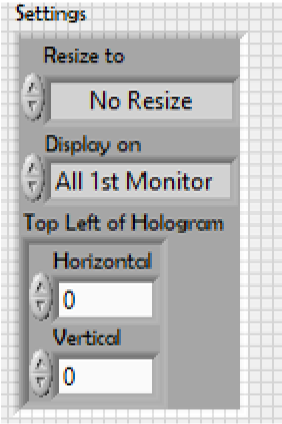

Settings

Resize to: No Resize

Display on: All 1st Monitor

Top Left of Hologram

Horizontal: 0

Vertical: 0

Figure E.3: Settings options for *Dislay on SLM* VI.

is determined by looking at the zero and first order intensities and optimising such that the first order contains as much and the zero as little power as possible. The shape of the curve should be similar to the S-shaped curve shown in Fig. E.2.

To ensure that this program functions as expected, the display settings of the computer need to be checked. If the SLM is properly connected with the USB cable, the computer will recognise it as an additional screen. In the display settings, determine which screen number is given to the SLM. The *Display on SLM* VI requires the user to input which screen the hologram should be displayed on using the 'Display on' control seen in Fig. E.3.

Before running a program that calls this VI, ensure that the front panel of *Display on SLM* is maximised (this is very important, otherwise the hologram isn't in the right place on the SLM), and the hologram is placed exactly at the top left corner of the screen, as in Fig. E.5. Fig. E.4 shows an example of an incorrectly aligned front panel.

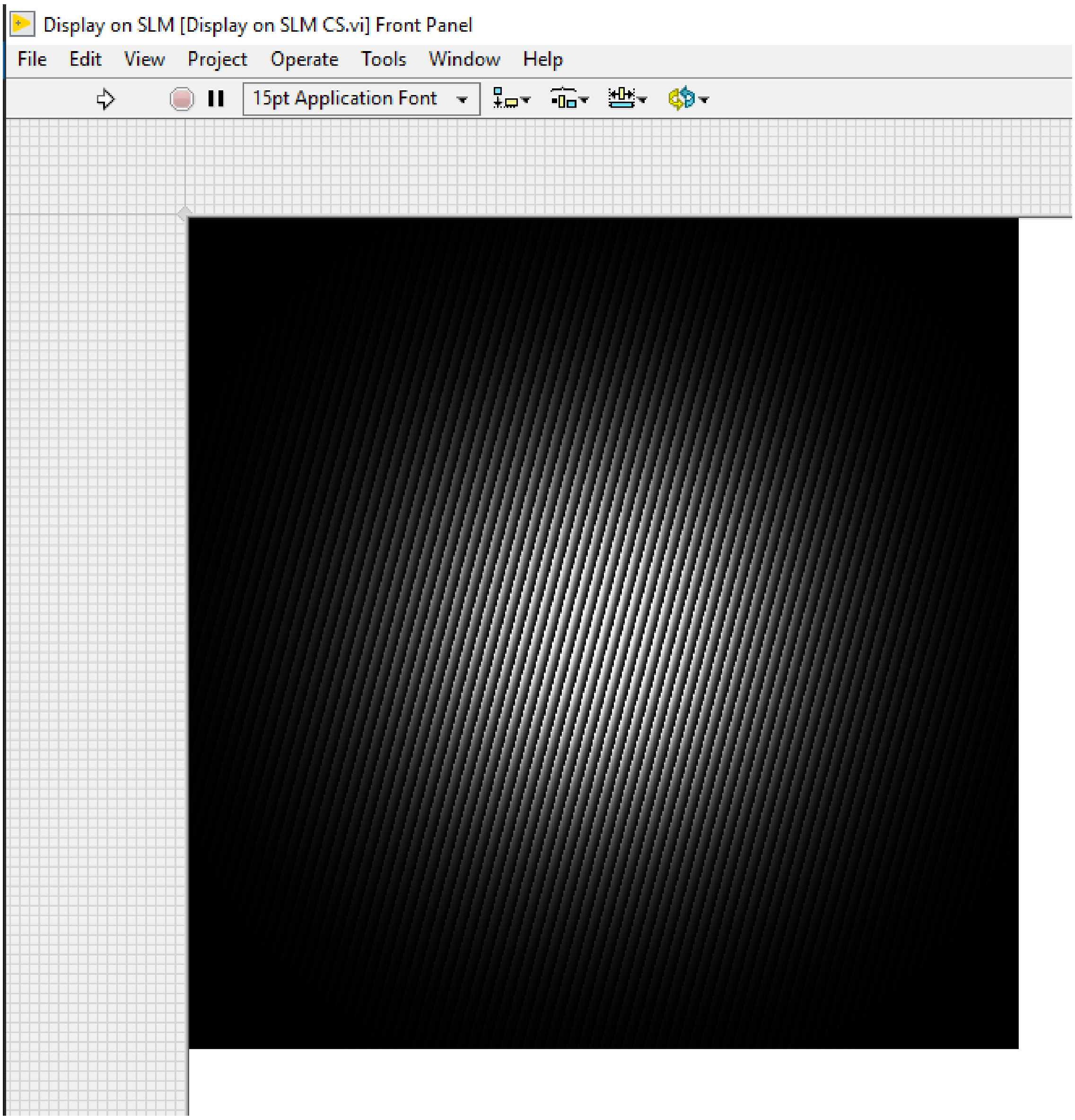

FIGURE E.4: Incorrect location of the hologram on the front panel of the *Display on SLM* VI.

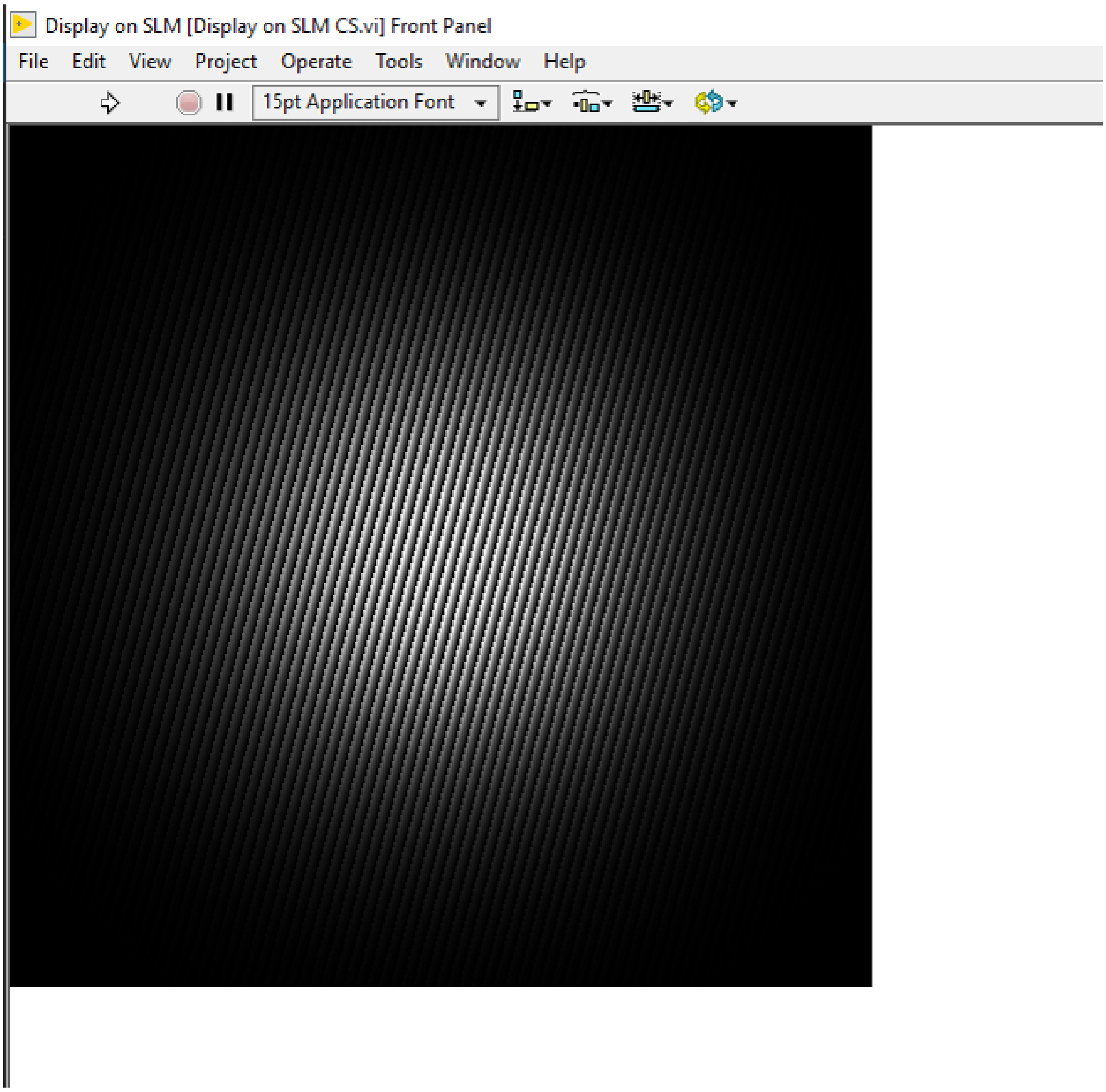

FIGURE E.5: Correct location of the hologram on the front panel of the *Display on SLM* VI.

## E.4 Modified Red Tweezers LabVIEW program

The software that was used to run the optical tweezers experiments was a modified version of Richard Bowman's *Red Tweezers* [119].

The front panel of the modified Red Tweezers LabVIEW software is shown in Fig. E.6. The left portion of the front panel contains tabs which contain the majority of the functionality, allowing one to e.g. create an optical trap at a given location or adjust tracking and ROI settings. There are many, many settings that one can adjust – here the author will detail the critical settings to being using the optical tweezers with stereo-vision live 3D tracking of a trapped micro-particle.

The back panel is shown in Fig. E.7. It is complicated, but can roughly be understood by splitting it into two sections - one that controls the optical traps, and one that performs the symmetry tracking and converts from two sets of 2D tracking data to one set of 3D tracking data. The camera frames, live tracking data, and optical trap information are placed in separate queues, allowing synchronisation across the three main for-loops of the program (one to control the traps, and two for tracking trapped micro-particles).

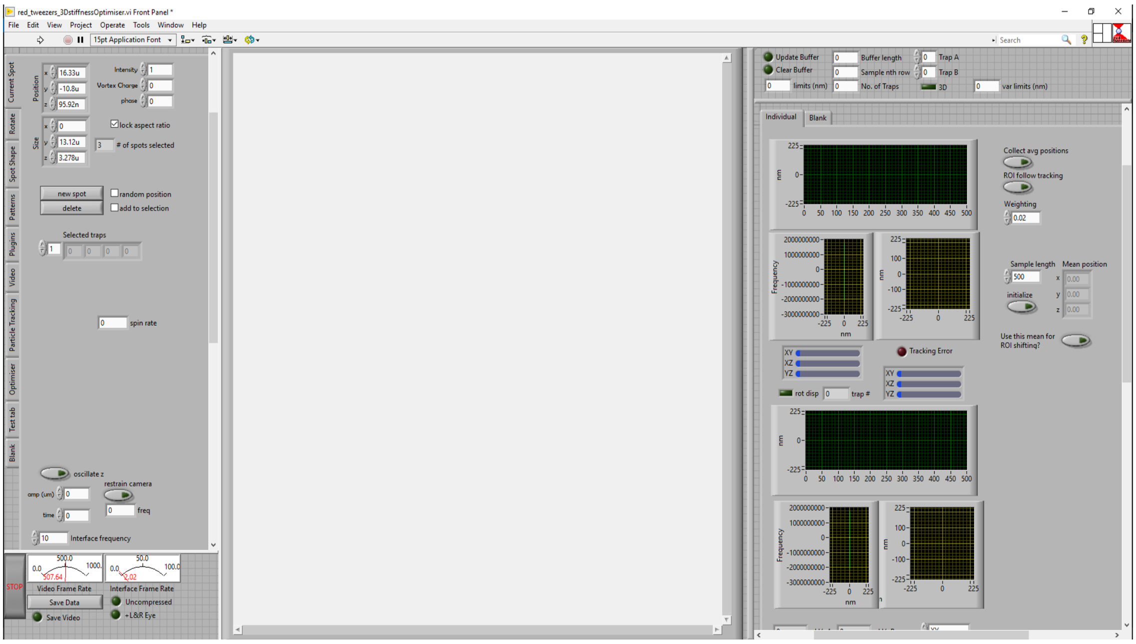

red_tweezers_3DstiffnessOptimiser.vi Front Panel *

15pt Application Font

Position x 16.33u
Position y -10.8u
Position z 95.92n
Intensity 1
Vortex Charge 0
phase 0
Size x 0
Size y 13.12u
Size z 3.278u
☑ lock aspect ratio
3 # of spots selected
☐ random position
☐ add to selection
Selected traps 1 0 0 0 0
0 spin rate
amp (um) 0
time 0
0 freq
10 Interface frequency
Video Frame Rate 507.64
Interface Frame Rate 2.02

0 Buffer length
0 Sample nth row
0 Trap A
0 Trap B
0 limits (nm)
0 No. of Traps
0 var limits (nm)
Weighting 0.02
Sample length 500
Mean position x 0.00
Mean position y 0.00
Mean position z 0.00
0 rot disp trap #

FIGURE E.6: Front panel of modified Red Tweezers LabVIEW program.

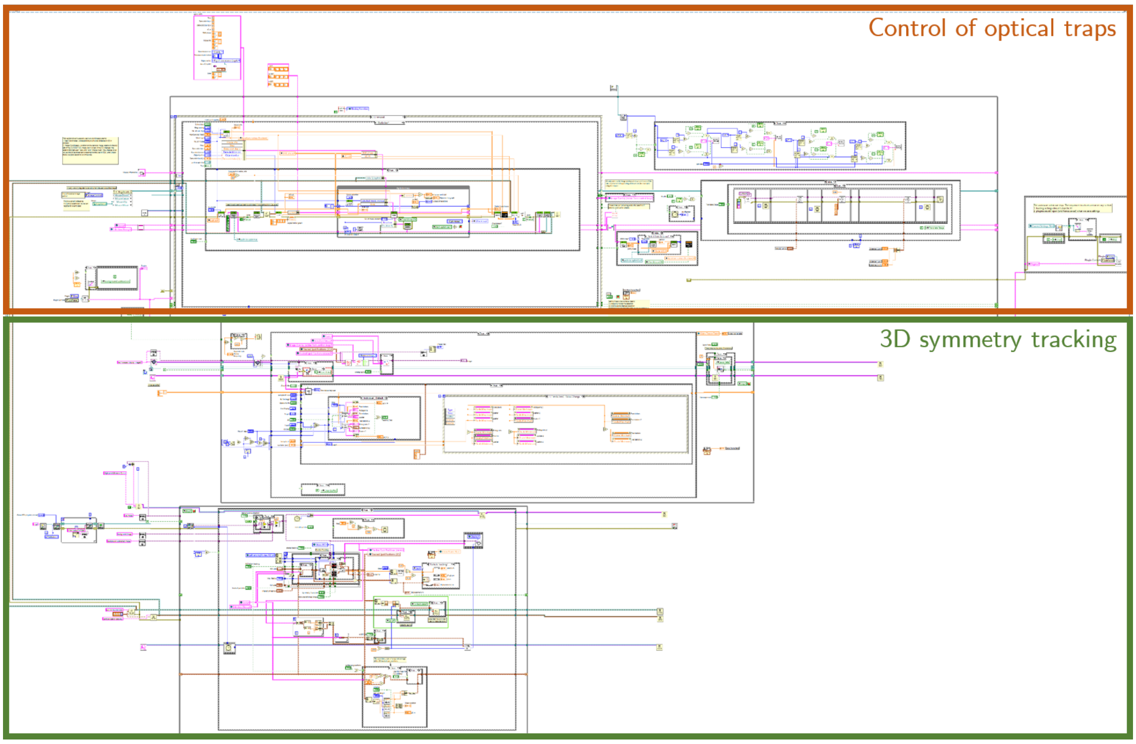

Figure E.7: Back panel of the modified Red Tweezers LabVIEW program. The orange box outlines the parts of the code that control the optical traps. The green box outlines the parts that perform the live 3D tracking.

### E.4.1 Enabling 3D tracking

The ability to 3D track a particle is introduced to the Red Tweezers code with a series of subVIs and added functionality first introduced by supervisor Professor David Phillips. Using parallax, the $z$ displacement can be calculated using only $x$ and $y$ displacements from a left and right eye image. The exact relation depends on the angle between the illuminators used in the stereomicroscope. This angle can be set in the Red Tweezers *red_tweezers_global_INTERNAL.vi* subVI with the ‘Separation half-angle’ control seen in Fig. E.9. The fastest and easiest way the author has found to open this (or any other) subVI used in the Red Tweezers program is to go to View > Browse Relationships > This VI’s SubVIs, as seen in Fig. E.8.

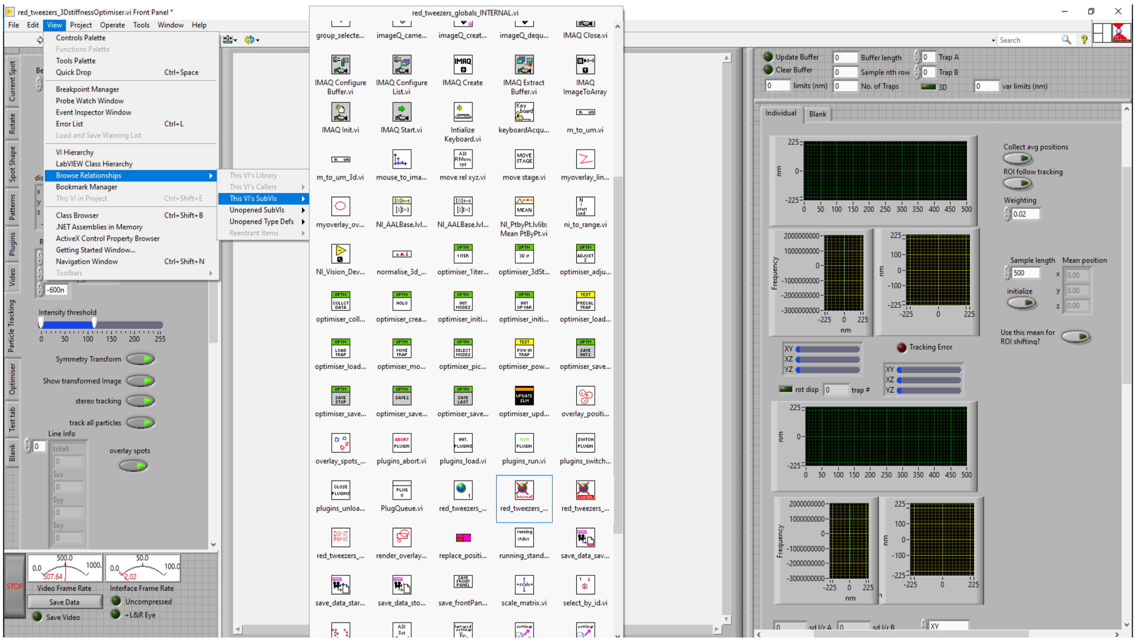

FIGURE E.8: A fast way to find and open any subVI used in a LabVIEW VI.

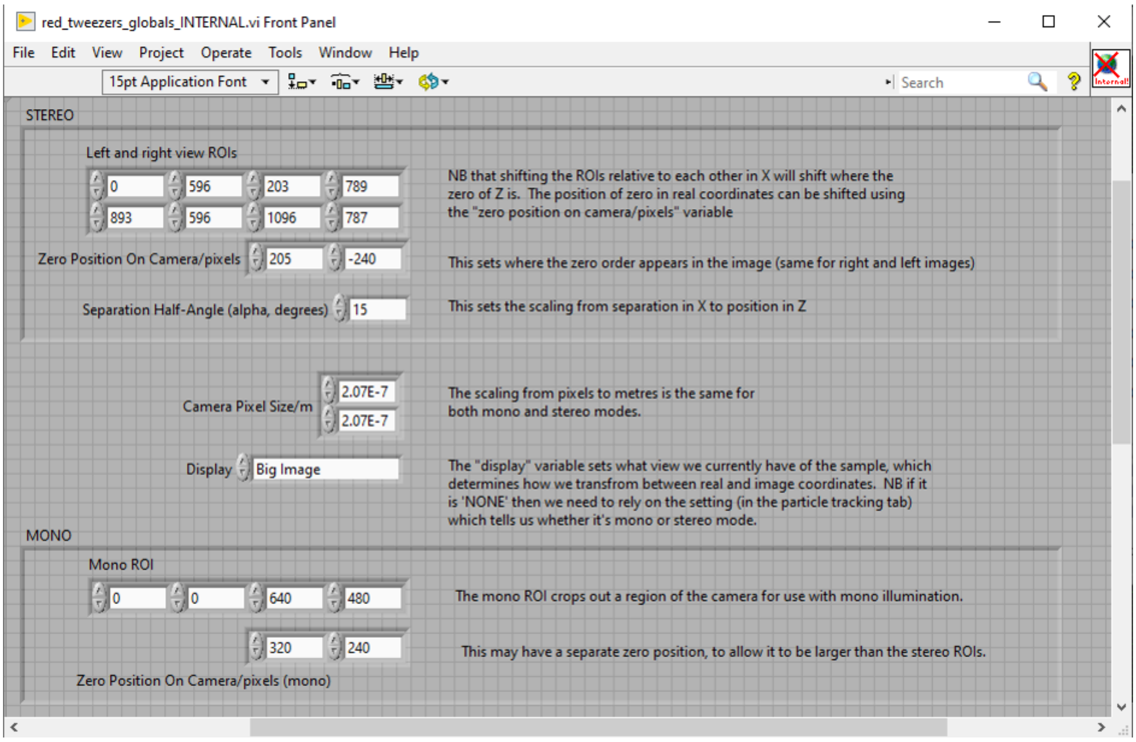
red_tweezers_globals_INTERNAL.vi Front Panel

STEREO

Left and right view ROIs

| 0 | 596 | 203 | 789 |
|---|---|---|---|
| 893 | 596 | 1096 | 787 |

NB that shifting the ROIs relative to each other in X will shift where the zero of Z is. The position of zero in real coordinates can be shifted using the "zero position on camera/pixels" variable

Zero Position On Camera/pixels 205 -240

This sets where the zero order appears in the image (same for right and left images)

Separation Half-Angle (alpha, degrees) 15

This sets the scaling from separation in X to position in Z

Camera Pixel Size/m 2.07E-7 2.07E-7

The scaling from pixels to metres is the same for both mono and stereo modes.

Display Big Image

The "display" variable sets what view we currently have of the sample, which determines how we transfrom between real and image coordinates. NB if it is 'NONE' then we need to rely on the setting (in the particle tracking tab) which tells us whether it's mono or stereo mode.

MONO

Mono ROI 0 0 640 480

The mono ROI crops out a region of the camera for use with mono illumination.

320 240

Zero Position On Camera/pixels (mono)

This may have a separate zero position, to allow it to be larger than the stereo ROIs.

FIGURE E.9: Front panel of modified *red_tweezers_global_INTERNAL.vi* for 3D tracking.

Adjusting the angle between the illuminators is discussed below. This subVI also contains controls that can be set to adjust the camera pixel size in metres. If the magnification of the imaging arm of the system is changed, this control will need to be adjusted in tandem. To do this, the physical size of the camera image on the front panel is measured in meters and divided by the number of pixels in the camera image.

Once these settings have been set, the main Red Tweezers code can be run in LabVIEW. Upon clicking run, after a few seconds of initialising all of the many subVIs, a live camera image should appear in the empty box in the middle of the front panel.

The ROIs referenced in this VI are also set within the main Red Tweezers software once it is running and the micro-particle to be tracked is found within a given sample. In the Video tab of the main Red Tweezers program (Fig. E.10), select ‘Set ROIs’ so that the Boolean is True. This allows one to manually select the left and right eyes as regions of interest (ROIs) on the live camera images. The ‘Constrain ROIs’ Boolean will make the two ROIs the same size, once they have been roughly placed and resized. The ‘Current ROI Tool’ control sometimes defaults to the Zoom Tool as seen in the screenshot in Fig. E.10. To adjust the ROIs, this needs to be changed to Rectangle Tool. The Global ROI control should be set to 1280, 1024 as in Fig. E.10, which is the full pixel resolution

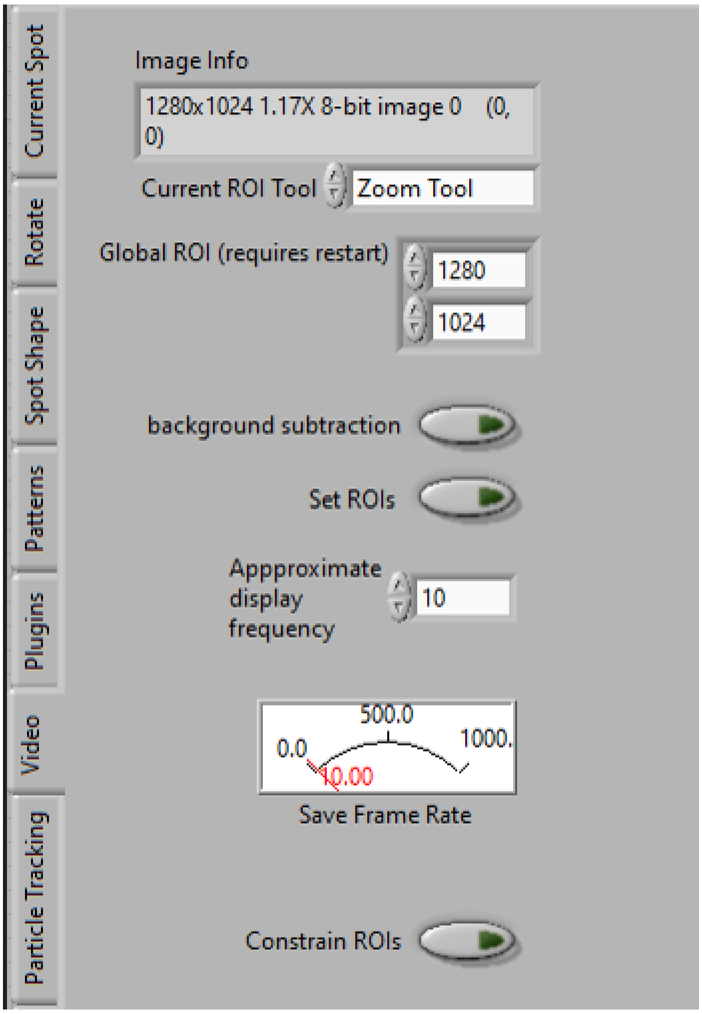

Image Info
1280x1024 1.17X 8-bit image 0 (0, 0)

Current ROI Tool: Zoom Tool

Global ROI (requires restart): 1280, 1024

Appproximate display frequency: 10

FIGURE E.10: Front panel of Red Tweezers showing the Video tab, where the ROI can be set.

of the camera.

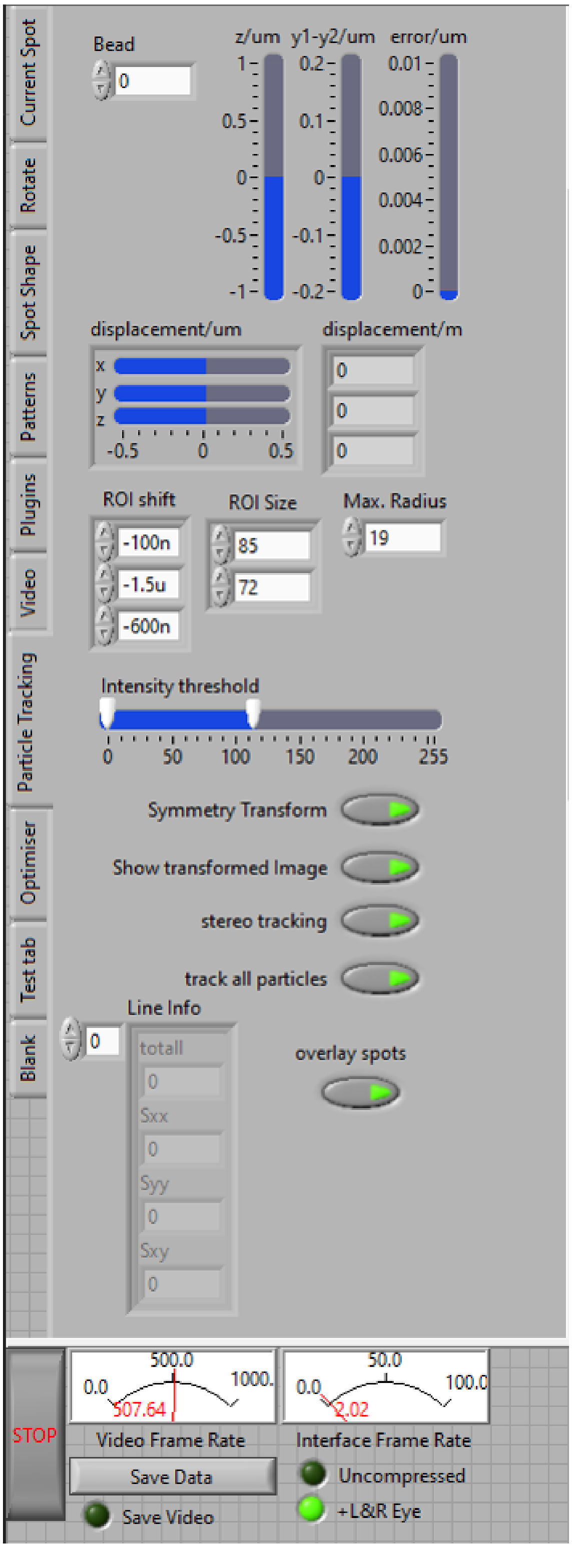

Bead 0

displacement/m 0 0 0

ROI shift -100n -1.5u -600n

ROI Size 85 72

Max. Radius 19

Line Info 0

totall 0

Sxx 0

Syy 0

Sxy 0

Video Frame Rate 507.64

Interface Frame Rate 2.02

FIGURE E.11: Front panel of Red Tweezers showing the Particle Tracking tab, where the ROI can be adjusted and symmetry tracking settings can be set.

Once the above settings and controls have been set, the next step to enabling 3D tracking with the modified Red Tweezers code is to adjust the mini-ROI around the optically trapped particle used for symmetry tracking. In the Particle Tracking tab of the main front panel, the Boolean controls named ‘Symmetry Transform’, ‘Show transformed Image’, ‘stereo tracking’, ‘track all particles’, ‘overlay spots’, and the Boolean control at the very bottom left hand side ‘+L&R Eye’ should all be set to True, as seen in the screenshot in Fig. E.11.

By default, the program should only create a trap at the zero order location. This can be changed manually after setup is complete. To create this initial trap, select ‘new spot’ on the Current Spot tab of the main front panel. The location of the optical trap should be properly set with the ‘Zero Position On Camera/pixels’ control seen in Fig. E.9, a magenta circle should appear, indicating the location where an optical trap will be formed once the laser has been turned on. If this location is incorrect, it can be tested by removing the laser filter from the imaging arm, turning the laser on (as described later), and adjusting the $x$ and $y$ locations of the zero position on the camera until the location of the magenta circle corresponds to the actual location of the zero order focus on the camera.

The translational stage should now be used to position the desired micro-particle so it is centred on the magenta circle/trap location. If the Booleans listed above are correctly configured, a small ROI should appear overlaying the image of the micro-particle. Disabling ‘Show transformed image’ will remove this overlay. With it enabled, go to the Particle Tracking tab and adjust the ROI shift, ROI Size, and Max. Radius controls to resize the mini-ROI that performs the symmetry transform for tracking. ROI shift will translate the region. ROI size adjusts the size of the region. Max. radius adjusts the number of pixels over which the symmetry is evaluated. Typically, the transformed image overlay should appear approximately the size of the micro-particle.

To reduce the error in the tracking, the micro-spheres should be slightly out of focus so that they appear as a bright circle surrounded by a darker ring, as in Fig. E.12.

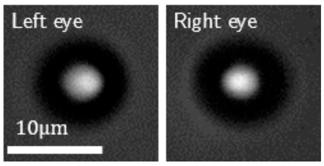

FIGURE E.12: Example of cropped left and right eye images showing slightly out of focus 4.99 µm radius silica micro-spheres.

The next step to initialising 3D tracking is to set a buffer length in the top right hand corner of the main front panel. This determines how many latest data points are displayed on the plots in the panel below showing the live tracking data in real time. Typically, the author used a buffer length between 500 - 1000. If the camera is running between 250 and 500 fps, this then corresponds to $\sim$ 2 s of live data. The ‘Clear buffer’ Boolean will clear the current live tracking data. The 'limits' control sets the displacement limits of the axes of the live tracking data plots.

Finally, to begin live 3D tracking, the 'Update buffer' and '3D' Booleans should be set to True, as seen in the screenshot in Fig. E.13. After this is done, the 3D tracking should begin and cross-hairs should appear over the centre-of-mass of the tracked micro-particle. At this point the author prefers to turn off the 'Show transformed image' Boolean, but this isn't necessary for the performance of the tracking. To ensure that the ROI can also follow the motion of the particle, first the 'Collect avg positions' Boolean should be enabled for a few seconds, and then the 'ROI follow tracking' Boolean should be enabed after that. This is useful e.g. when tracking an untrapped, freely diffusing micro-particle.

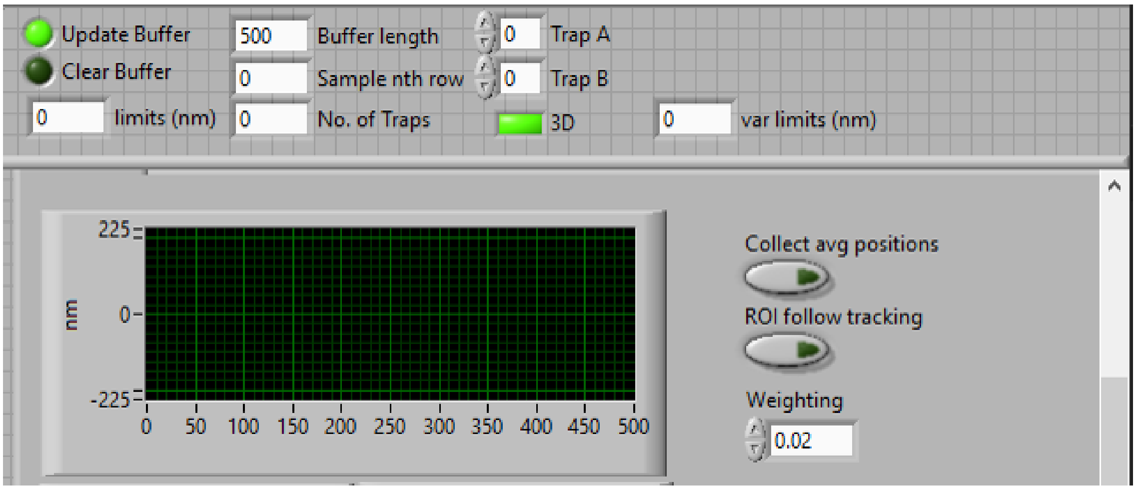
● Update Buffer
● Clear Buffer
0 limits (nm)
500 Buffer length
0 Sample nth row
0 No. of Traps
0 Trap A
0 Trap B
🟩 3D
0 var limits (nm)
Collect avg positions
ROI follow tracking
Weighting 0.02

FIGURE E.13: Screenshot showing the top right hand corner of the main front panel of the modified Red Tweezers.

The final step to initialising live 3D tracking is to adjust the 'Separation half-angle' control. To ensure that the control is set to the correct angle, the translational stage used to control $x$, $y$, and $z$ locations of the sample relative to the microscope objective is moved in $z$ some known amount. The author typically moved the microscope objective up and down 1 µm and ensured that the live 3D tracking on the right side of the front panel reflected that same displacement in $z$ (green lines). The buffer length and limits controls will need to be adjusted for this step. If the live tracking data for $z$ do not also change by e.g. 1 µm the 'Separation half-angle' is adjusted to correct this. This may require several iterations of adjusting the angle and testing the tracked $z$ displacement against the motion of the motorised stage a known amount.

To get the best performance possible, it is important that the images of the beads are not saturated on the camera. The 'Image max' indicator in the Particle Tracking tab tells the user the highest intensity pixel. This should stay under 255 to prevent saturation of the camera images. The 'Show transformed image' Boolean needs to be set to False for this! Otherwise the indicator will always show 255, because of the pixel values within the overlayed ROIs. If the images of the micro-particle are saturated, the frame rate or exposure time of the camera or the intensities of the LED illuminators need to be adjusted as described above.

### E.4.2 Optically trapping a particle

To protect users, the box around the system should be closed before the laser is turned on. The stages and SLM can be controlled from the outside of the box, so the only time the box should be opened is while the laser is off to replace samples or alignment work (to be performed only by experience researchers with knowledge of the system and the dangers of the laser). Details of and tips for alignment of the laser and imaging arms are discussed in Appendix C.

Once the 3D tracking is enabled, the laser can be turned on. For the current location, this requires turning the lab's interlock system on – a laser safety measure to prevent unauthorised users from entering the lab while this potentially dangerous laser is in use. Next, the laser itself must be turned on. It is located in the gantry above the setup. Once the laser controller has been powered up, the key needs to be inserted into it switched on. A button should begin blinking green, and once it is a stable green can be pressed to begin lasing. After a few seconds, the optical trap should be formed in the sample at the zero order location designated by the magenta circle in the Red Tweezers live camera image, if the above settings are correctly set.

Once the trap has formed, if the micro-particle is close enough to it, it should be sucked into the trap and held there. Now the trap can be moved to a desired location within the sample. This can be done in the Current Spot tab by adjusting the $x$, $y$, and $z$ Position or by clicking and dragging the magenta circle on the camera image to a desired location. This should be done in small, relatively slow steps so the tracking ROI can follow the bead to its new location.

When the position of the optical trap is changed, the queue containing this information synchronises the phase mask displayed on the SLM to reflect this change. The back panel for this part of the modified version of the Red Tweezers software is shown in Fig. E.14. The pink wire contains the queue of optical trap information; the Move Trap subVI converts this information into a phase mask which is output as a U8 hologram (blue wire) that is input to the Update SLM subVI, which displays the phase mask on the display monitor selected by the Display on SLM VI described previously.

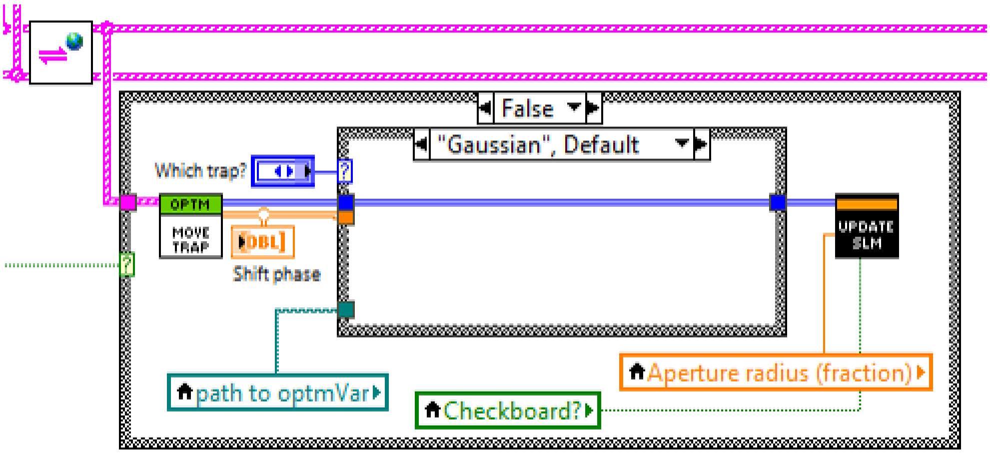

FIGURE E.14: Back panel of the modified Red Tweezers program, showing how the phase mask displayed on the SLM is changed using a queue.

The optical trap should be moved sufficiently far from the zero order so that the zero order does not also interact with the trapped micro-particle. For a 4.99 µm radius silica micro-sphere, for example, the author used a first order between 7 and 10 µm (calculated using the Pythagorean Theorem) away from the zero order. An example of the $x$ and $y$ locations of such a first order are (6 µm, 6 µm).

Next, the microscope objective is translated 25 µm from the bottom glass coverslip of the sample to ensure that the 3D motion of the trapped micro-particle is not restricted by the coverslip (i.e. so the microparticle doesn't continuously bounce into the glass). Because of radiation pressure, the optical trap will push the microparticle to a different $z$ position which can be adjusted by changing the $z$ location of the optical trap slowly. Typically changes between 0.1 and 0.25 µm in the $z$ position were sufficiently small to prevent the micro-particle from escaping the trap.

Adjusting the Position of the optical trap in the Current Spot tab adjusts the phase mask displayed on the SLM screen. Changes in $x$ and $y$ position correspond to a change in the phase grating, and changes in $z$ correspond to changes in the lens phase added to the phase mask.

After completing the steps detailed in this Appendix, it should now be possible to 3D track an optically trapped particle with nanometer precision. Further modifications can be made to the LabVIEW program to allow any desired phase mask to be displayed on the SLM screen. The Red Tweezers program has the built-in ability to save live tracking data and video. The 'Save Video' Boolean, which should be selected first if saved video is desired, enables saving video which is compressed by default but can be uncompressed using the associated Boolean. The 'Save Data' button begins the saving process and opens a pop-up allowing the user to name the saved data and place it in the desired file path.

## E.5 Shutting down the tweezers

To correctly turn everything off, first the LabVIEW program should be stopped. Next, the key in the laser controller should be switched to the off position. Finally, the power to all of the equipment can be cut and the lab's interlock disabled.

# Bibliography

[1] Rémi Carminati and John C Schotland. *Principles of Scattering and Transport of Light*. Cambridge University Press, 2021. DOI: `10.1017/9781316544693`.

[2] Jacopo Bertolotti and Ori Katz. “Imaging in complex media”. In: *Nature Physics* 18.9 (2022), pp. 1008–1017. DOI: `https://doi.org/10.1038/s41567-022-01723-8`.

[3] Sylvain Gigan et al. “Roadmap on wavefront shaping and deep imaging in complex media”. In: *Journal of Physics: Photonics* 4.4 (2022), p. 42501. DOI: `10.1088/2515-7647/ac76f9`.

[4] Allard P Mosk et al. “Controlling waves in space and time for imaging and focusing in complex media”. In: *Nature photonics* 6.5 (2012), pp. 283–292.

[5] Stefan Rotter and Sylvain Gigan. “Light fields in complex media: Mesoscopic scattering meets wave control”. In: *Reviews of Modern Physics* 89.1 (2017), p. 15005.

[6] David Huang et al. *Optical Coherence Tomography*. Tech. rep. 1991. URL: `https://www.science.org`.

[7] Fritjof Helmchen and Winfried Denk. “Deep tissue two-photon microscopy”. In: *Nature Methods* 2.12 (2005), pp. 932–940. ISSN: 1548-7105. DOI: `10.1038/nmeth818`. URL: `https://doi.org/10.1038/nmeth818`.

[8] Zhipeng Yu et al. “Wavefront shaping: A versatile tool to conquer multiple scattering in multidisciplinary fields”. In: *The Innovation* 3.5 (Sept. 2022), p. 100292. ISSN: 26666758. DOI: `10.1016/j.xinn.2022.100292`.

[9] Jacques M Beckers. “Adaptive Optics for Astronomy: Principles, Performance, and Applications”. In: *Annual Review of Astronomy and Astrophysics* 31.1 (1993), pp. 13–62. DOI: `10.1146/annurev.aa.31.090193.000305`. URL: `https://doi.org/10.1146/annurev.aa.31.090193.000305`.

[10] Richard Davies and Markus Kasper. “Adaptive Optics for Astronomy”. In: *Annual Review of Astronomy and Astrophysics* 50.1 (2012), pp. 305–351. DOI: `10.1146/annurev-astro-081811-125447`. URL: `https://doi.org/10.1146/annurev-astro-081811-125447`.

[11] Ioannis N Papadopoulos et al. “Scattering compensation by focus scanning holographic aberration probing (F-SHARP)”. In: *Nature Photonics* 11.2 (2017), pp. 116–123.

[12] Mooseok Jang et al. “Wavefront shaping with disorder-engineered metasurfaces”. In: *Nature Photonics* 12.2 (2018), pp. 84–90. ISSN: 1749-4893. DOI: `10.1038/s41566-017-0078-z`. URL: `https://doi.org/10.1038/s41566-017-0078-z`.

[13] I M Vellekoop and A P Mosk. “Universal Optimal Transmission of Light Through Disordered Materials”. In: *Phys. Rev. Lett.* 101.12 (Sept. 2008), p. 120601. DOI: `10.1103/PhysRevLett.101.120601`. URL: `https://link.aps.org/doi/10.1103/PhysRevLett.101.120601`.

[14] Ivo M Vellekoop and A P Mosk. “Focusing coherent light through opaque strongly scattering media”. In: *Optics Letters* 32.16 (2007), pp. 2309–2311. DOI: `10.1364/OL.32.002309`.

[15] Ivo Micha Vellekoop and A P Mosk. “Phase control algorithms for focusing light through turbid media”. In: *Optics Communications* 281.11 (2008), pp. 3071–3080.

[16] Donald B Conkey et al. *Genetic algorithm optimization for focusing through turbid media in noisy environments*. Tech. rep. 2012.

[17] Tomáš Čižmár, Michael Mazilu, and Kishan Dholakia. “In situ wavefront correction and its application to micromanipulation”. In: *Nature Photonics* 4.6 (2010), pp. 388–394.

[18] Bahareh Mastiani and Ivo M Vellekoop. “Noise-tolerant wavefront shaping in a Hadamard basis”. In: *Optics express* 29.11 (2021), pp. 17534–17541.

[19] Zahid Yaqoob et al. “Optical phase conjugation for turbidity suppression in biological samples”. In: *Nature Photonics* 2.2 (Feb. 2008), pp. 110–115. ISSN: 17494885. DOI: `10.1038/nphoton.2007.297`.

[20] KyeoReh Lee et al. “One-Wave Optical Phase Conjugation Mirror by Actively Coupling Arbitrary Light Fields into a Single-Mode Reflector”. In: *Phys. Rev. Lett.* 115.15 (Oct. 2015), p. 153902. DOI: `10.1103/PhysRevLett.115.153902`. URL: `https://link.aps.org/doi/10.1103/PhysRevLett.115.153902`.

[21] Daifa Wang et al. “Focusing through dynamic tissue with millisecond digital optical phase conjugation”. In: *Optica* 2.8 (2015), pp. 728–735.

[22] Edward Haojiang Zhou et al. “Focusing on moving targets through scattering samples”. In: *Optica* 1.4 (2014), pp. 227–232.

[23] Yan Liu et al. “Focusing light inside dynamic scattering media with millisecond digital optical phase conjugation”. In: *Optica* 4.2 (2017), pp. 280–288.

[24] Chaitanya K Mididoddi et al. “High-fidelity off-axis digital optical phase conjugation with transmission matrix assisted calibration”. In: *Optics Express* 28.23 (2020), pp. 34692–34705.

[25] S M Popoff et al. “Measuring the transmission matrix in optics: an approach to the study and control of light propagation in disordered media”. In: *Physical review letters* 104.10 (2010), p. 100601.

[26] Shuhui Li et al. “Compressively sampling the optical transmission matrix of a multimode fibre”. In: *Light: Science & Applications* 10.1 (2021), pp. 1–15. DOI: `10.1038/s41377-021-00514-9`. URL: `https://doi.org/10.1038/s41377-021-00514-9`.

[27] Sébastien Popoff et al. “Image transmission through an opaque material”. In: *Nature Communications* 1.1 (2010), p. 81. ISSN: 2041-1723. DOI: `10.1038/ncomms1078`. URL: `https://doi.org/10.1038/ncomms1078https://drive.google.com/open?id=1XhhruygSIOrJOYZUvYeaYNKED6F5oZOv`.

[28] Antoine Boniface, Jonathan Dong, and Sylvain Gigan. “Non-invasive focusing and imaging in scattering media with a fluorescence-based transmission matrix”. In: *Nature communications* 11.1 (2020), pp. 1–7.

[29] Antoine Boniface et al. “Transmission-matrix-based point-spread-function engineering through a complex medium”. In: *Optica* 4.1 (Jan. 2017), p. 54. ISSN: 23342536. DOI: `10.1364/optica.4.000054`.

[30] Claire Prad, Jean Louis Thomas, and Mathias Fink. “The iterative time reversal process: Analysis of the convergence”. In: *Journal of the Acoustical Society of America* 97.1 (1995), pp. 62–71. ISSN: NA. DOI: `10.1121/1.412285`.

[31] Emmett N Leith and Juris Upatnieks. “Holographic Imagery Through Diffusing Media”. In: *Journal of the Optical Society of America* 56.4 (1966), p. 523. DOI: `10.1364/JOSA.56.000523`. URL: `https://opg.optica.org/abstract.cfm?URI=josa-56-4-523`.

[32] Baptiste Blochet, Laurent Bourdieu, and Sylvain Gigan. “Focusing light through dynamical samples using fast continuous wavefront optimization”. In: *Optics letters* 42.23 (2017), pp. 4994–4997.

[33] Jiamiao Yang et al. “Fighting against fast speckle decorrelation for light focusing inside live tissue by photon frequency shifting”. In: *ACS photonics* 7.3 (2020), pp. 837–844.

[34] Molly A May et al. “Fast holographic scattering compensation for deep tissue biological imaging”. In: *Nature Communications* 12.1 (2021), pp. 1–8.

[35] Jiawei Luo et al. *High-speed single-exposure time-reversed ultrasonically encoded optical focusing against dynamic scattering.* Tech. rep. 2022. URL: `https://www.science.org`.

[36] Omer Tzang et al. “Wavefront shaping in complex media with a 350 KHz modulator via a 1D-to-2D transform”. In: *Nature Photonics* 13.11 (2019), pp. 788–793. ISSN: 1749-4893. URL: `https://drive.google.com/open?id=1EDoZsj8OYN-OVjDWi1EGCOsdNxJGZzmv`.

[37] Daniel Feldkhun et al. “Focusing and scanning through scattering media in microseconds”. In: *Optica* 6.1 (2019), pp. 72–75.

[38] Donald B Conkey, Antonio M Caravaca-Aguirre, and Rafael Piestun. *High-speed scattering medium characterization with application to focusing light through turbid media*. Tech. rep. 2012.

[39] Sergey Turtaev et al. “Comparison of nematic liquid-crystal and DMD based spatial light modulation in complex photonics”. In: *Optics express* 25.24 (2017), pp. 29874–29884.

[40] Cheng Peng et al. “Design of high-speed phase-only spatial light modulators with two-dimensional tunable microcavity arrays”. In: *Optics Express* 27.21 (Oct. 2019), p. 30669. ISSN: 10944087. DOI: 10.1364/oe.27.030669.

[41] Christopher L. Panuski et al. “A full degree-of-freedom spatiotemporal light modulator”. In: *Nature Photonics* 16.12 (Dec. 2022), pp. 834–842. ISSN: 17494893. DOI: 10.1038/s41566-022-01086-9.

[42] Jacopo Bertolotti et al. “Non-invasive imaging through opaque scattering layers”. In: *Nature* 491.7423 (2012), pp. 232–234.

[43] Benjamin Judkewitz et al. “Speckle-scale focusing in the diffusive regime with time reversal of variance-encoded light (TROVE)”. In: *Nature Photonics* 7.4 (Apr. 2013), pp. 300–305. ISSN: 17494885. DOI: 10.1038/nphoton.2013.31.

[44] Roarke Horstmeyer, Haowen Ruan, and Changhuei Yang. “Guidestar-assisted wavefront-shaping methods for focusing light into biological tissue”. In: *Nature Photonics* 9.9 (2015), pp. 563–571.

[45] Gerwin Osnabrugge et al. “Generalized optical memory effect”. In: *Optica* 4.8 (2017), pp. 886–892. DOI: 10.1364/OPTICA.4.000886. URL: https://doi.org/10.1364/OPTICA.4.000886.

[46] Amaury Badon et al. *Distortion matrix concept for deep optical imaging in scattering media*. Tech. rep. 2020, pp. 7170–7192. URL: https://www.science.org.

[47] Shuhui Li et al. “Memory effect assisted imaging through multimode optical fibres”. In: *Nature Communications* 12.1 (2021), pp. 1–13.

[48] Lorenzo Valzania and Sylvain Gigan. “Online learning of the transfer matrix of dynamic scattering media: wavefront shaping meets multidimensional time series”. In: (Oct. 2022). URL: http://arxiv.org/abs/2210.04033.

[49] Peter Lebedew. “Untersuchungen über die Druckkräfte des Lichtes”. In: *Annalen der Physik* 311.11 (1901), pp. 433–458. ISSN: 00033804. DOI: 10.1002/andp.19013111102.

[50] E. F. Nichols and G. F. Hull. “A Preliminary Communication on the Pressure of Heat and Light Radiation”. In: *Physical Review (Series I)* 13.5 (Nov. 1901), pp. 307–320. ISSN: 1536-6065. DOI: 10.1103/PhysRevSeriesI.13.307.

[51] Mo Li et al. “Harnessing optical forces in integrated photonic circuits”. In: *Nature* 456.7221 (Nov. 2008), pp. 480–484. ISSN: 0028-0836. DOI: 10.1038/nature07545.

[52] O. Arcizet et al. “Radiation-pressure cooling and optomechanical instability of a micromirror”. In: *Nature* 444.7115 (Nov. 2006), pp. 71–74. ISSN: 0028-0836. DOI: `10.1038/nature05244`.

[53] L. Rios-Reyes and D. J. Scheeres. “Solar-Sail Navigation: Estimation of Force, Moments, and Optical Parameters”. In: *Journal of Guidance, Control, and Dynamics* 30.3 (May 2007), pp. 660–668. ISSN: 0731-5090. DOI: `10.2514/1.24340`.

[54] David A. Spencer et al. “The LightSail 2 solar sailing technology demonstration”. In: *Advances in Space Research* 67.9 (May 2021), pp. 2878–2889. ISSN: 02731177. DOI: `10.1016/j.asr.2020.06.029`.

[55] Arthur Ashkin. “Acceleration and trapping of particles by radiation pressure”. In: *Physical review letters* 24.4 (1970), p. 156.

[56] Arthur Ashkin et al. “Observation of a single-beam gradient force optical trap for dielectric particles”. In: *Optics letters* 11.5 (1986), pp. 288–290.

[57] Arthur Ashkin and James M Dziedzic. “Optical trapping and manipulation of viruses and bacteria”. In: *Science* 235 (1987), pp. 1517–1521.

[58] C. Xie et al. “Identification of Single Bacterial Cells in Aqueous Solution Using Confocal Laser Tweezers Raman Spectroscopy”. In: *Analytical Chemistry* 77.14 (July 2005), pp. 4390–4397. ISSN: 0003-2700. DOI: `10.1021/ac0504971`.

[59] Min-Cheng Zhong et al. “Trapping red blood cells in living animals using optical tweezers”. In: *Nature Communications* 4.1 (Apr. 2013), p. 1768. ISSN: 2041-1723. DOI: `10.1038/ncomms2786`.

[60] Steven M Block, Lawrence S B Goldstein, and Bruce J Schnapp. “Bead movement by single kinesin molecules studied with optical tweezers”. In: *Nature* 348.6299 (1990), pp. 348–352.

[61] Iddo Heller et al. “Optical tweezers analysis of DNA–protein complexes”. In: *Chemical reviews* 114.6 (2014), pp. 3087–3119.

[62] David G Grier. “A revolution in optical manipulation”. In: *Nature* 424.6950 (2003), pp. 810–816. DOI: `10.1038/nature01935`.

[63] Unė G Būtaitė et al. “Indirect optical trapping using light driven micro-rotors for reconfigurable hydrodynamic manipulation”. In: *Nature communications* 10.1 (2019), p. 1215.

[64] Eric R. Dufresne and David G. Grier. “Optical tweezer arrays and optical substrates created with diffractive optics”. In: *Review of Scientific Instruments* 69.5 (May 1998), pp. 1974–1977. ISSN: 0034-6748. DOI: `10.1063/1.1148883`.

[65] O Brzobohat\‘y et al. “Experimental demonstration of optical transport, sorting and self-arrangement using a ‘tractor beam’”. In: *Nature Photonics* 7.2 (2013), pp. 123–127.

[66] Miles Padgett and Richard Bowman. “Tweezers with a twist”. In: *Nature photonics* 5.6 (2011), p. 343.

[67] D B Phillips et al. “Surface imaging using optically controlled microrods”. In: *Optical Trapping and Optical Micromanipulation VIII*. Vol. 8097. 2011, p. 809704.

[68] D B Phillips et al. “Surface imaging using holographic optical tweezers”. In: *Nanotechnology* 22.28 (2011), p. 285503.

[69] A. M. Kaufman, B. J. Lester, and C. A. Regal. “Cooling a Single Atom in an Optical Tweezer to Its Quantum Ground State”. In: *Physical Review X* 2.4 (Nov. 2012), p. 041014. ISSN: 2160-3308. DOI: `10.1103/PhysRevX.2.041014`.

[70] Felix Tebbenjohanns et al. “Quantum control of a nanoparticle optically levitated in cryogenic free space”. In: *Nature* 595.7867 (2021), pp. 378–382.

[71] Uroš Delić et al. “Cooling of a levitated nanoparticle to the motional quantum ground state”. In: *Science* 367.6480 (Feb. 2020), pp. 892–895. ISSN: 0036-8075. DOI: `10.1126/science.aba3993`.

[72] Erwin J G Peterman, Frederick Gittes, and Christoph F Schmidt. “Laser-induced heating in optical traps”. In: *Biophysical journal* 84.2 (2003), pp. 1308–1316.

[73] Alfonso Blázquez-Castro. “Optical tweezers: Phototoxicity and thermal stress in cells and biomolecules”. In: *Micromachines* 10.8 (2019), p. 507.

[74] M E J Friese et al. “Optical angular-momentum transfer to trapped absorbing particles”. In: *Physical Review A* 54.2 (1996), p. 1593.

[75] N B Simpson et al. “Optical tweezers with increased axial trapping efficiency”. In: *Journal of Modern Optics* 45.9 (1998), pp. 1943–1949.

[76] David B Phillips et al. “Optimizing the optical trapping stiffness of holographically trapped microrods using high-speed video tracking”. In: *Journal of Optics* 13.4 (2011), p. 44023.

[77] Niall McAlinden et al. “Accurate position tracking of optically trapped live cells”. In: *Biomedical optics express* 5.4 (2014), p. 1026.

[78] Brijesh K Singh et al. “Particle manipulation beyond the diffraction limit using structured super-oscillating light beams”. In: *Light: Science & Applications* 6.9 (Mar. 2017), e17050–e17050. ISSN: 2047-7538. DOI: `10.1038/lsa.2017.50`.

[79] Edward M Purcell and Carlton R Pennypacker. “Scattering and Absorption of Light by Nonspherical Dielectric Grains”. In: 186 (Dec. 1973), pp. 705–714. DOI: `10.1086/152538`.

[80] M. A. Yurkin and A. G. Hoekstra. “The discrete dipole approximation: An overview and recent developments”. In: *Journal of Quantitative Spectroscopy and Radiative Transfer* 106.1-3 (July 2007), pp. 558–589. ISSN: 0022-4073. DOI: `10.1016/J.JQSRT.2007.01.034`.

[81] J. M. Zhao and Z. M. Zhang. “Electromagnetic energy storage and power dissipation in nanostructures”. In: *Journal of Quantitative Spectroscopy and Radiative Transfer* 151 (Jan. 2015), pp. 49–57. ISSN: 0022-4073. DOI: `10.1016/J.JQSRT.2014.09.011`.

[82] Abhijit Sanjeev, Vismay Trivedi, and Zeev Zalevsky. “Optical reciprocity induced wavefront shaping for axial and lateral shifting of focus through a scattering medium”. In: *Scientific Reports* 12.1 (Apr. 2022), p. 6387. ISSN: 2045-2322. DOI: `10.1038/s41598-022-10378-7`.

[83] Mickael Mounaix et al. “Spatiotemporal Coherent Control of Light through a Multiple Scattering Medium with the Multispectral Transmission Matrix”. In: *Physical Review Letters* 116.25 (June 2016). ISSN: 10797114. DOI: `10.1103/PhysRevLett.116.253901`.

[84] Moonseok Kim et al. “Transmission matrix of a scattering medium and its applications in biophotonics”. In: *Optics Express* 23.10 (May 2015), p. 12648. ISSN: 1094-4087. DOI: `10.1364/OE.23.012648`.

[85] C W J Beenakker. “Random-matrix theory of quantum transport”. In: *Rev. Mod. Phys.* 69.3 (July 1997), pp. 731–808. DOI: `10.1103/RevModPhys.69.731`. URL: `https://link.aps.org/doi/10.1103/RevModPhys.69.731`.

[86] Michael Horodynski et al. “Optimal wave fields for micromanipulation in complex scattering environments”. In: *Nature Photonics* 14.3 (2020), pp. 149–153.

[87] Eugene P Wigner. “Lower limit for the energy derivative of the scattering phase shift”. In: *Physical Review* 98.1 (1955), p. 145.

[88] Felix T Smith. “Lifetime matrix in collision theory”. In: *Physical Review* 118.1 (1960), p. 349.

[89] Philipp Ambichl et al. “Focusing inside disordered media with the generalized Wigner-Smith operator”. In: *Physical review letters* 119.3 (2017), p. 33903.

[90] Nicholas Bender et al. “Depth-targeted energy delivery deep inside scattering media”. In: *Nature Physics* 18.3 (Mar. 2022), pp. 309–315. ISSN: 17452481. DOI: `10.1038/s41567-021-01475-x`.

[91] Chaitanya K Mididoddi et al. “Threading light through dynamic complex media”. In: *arXiv preprint arXiv:2301.04461* (2023).

[92] Marvin K Simon and Mohamed-Slim Alouini. “Digital communications over fading channels”. In: *IEEE Transactions on Information Theory* 54.7 (2008), pp. 3369–3370.

[93] Giorgio Taricco. “On the capacity of separately-correlated MIMO Rician fading channels”. In: *GLOBECOM - IEEE Global Telecommunications Conference.* 2006. ISBN: 142440357X. DOI: `10.1109/GLOCOM.2006.81`.

[94] D Hosli and Amos Lapidoth. "The capacity of a MIMO Ricean channel is monotonic in the singular values of the mean". In: *ITG FACHBERICHT* (2004), pp. 381–386.

[95] A Kolmogorov. "The Local Structure of Turbulence in Incompressible Viscous Fluid for Very Large Reynolds' Numbers". In: *Akademiia Nauk SSSR Doklady* 30 (Jan. 1941), pp. 301–305. ISSN: 0002-3264. URL: `https://ui.adsabs.harvard.edu/abs/1941DoSSR..30..301K`.

[96] Mitchell A. Cox et al. "Structured Light in Turbulence". In: *IEEE Journal of Selected Topics in Quantum Electronics* 27.2 (Sept. 2020), pp. 1–21. ISSN: 1077-260X. DOI: `10.1109/jstqe.2020.3023790`.

[97] David Bachmann et al. "Highly Transmitting Modes of Light in Dynamic Atmospheric Turbulence". In: *Physical Review Letters* 130.7 (Feb. 2023). ISSN: 10797114. DOI: `10.1103/PhysRevLett.130.073801`.

[98] Pauline Boucher et al. "Full characterization of the transmission properties of a multi-plane light converter". In: *Physical Review Research* 3.2 (June 2021), p. 23226. DOI: `10.1103/PhysRevResearch.3.023226`. URL: `https://link.aps.org/doi/10.1103/PhysRevResearch.3.023226`.

[99] Hlib Kupianskyi, Simon A R Horsley, and David B Phillips. "High-dimensional spatial mode sorting and optical circuit design using multi-plane light conversion". In: *APL Photonics* 8.2 (2023), p. 26101.

[100] Zdeněk Bouchal and Marek Olivík. "Non-diffractive Vector Bessel Beams". In: *Journal of Modern Optics* 42.8 (Aug. 1995), pp. 1555–1566. ISSN: 0950-0340. DOI: `10.1080/09500349514551361`.

[101] Bahareh Mastiani, Gerwin Osnabrugge, and Ivo M. Vellekoop. "Wavefront shaping for forward scattering". In: *Optics Express* 30.21 (Oct. 2022), p. 37436. ISSN: 1094-4087. DOI: `10.1364/OE.470194`.

[102] James Clerk Maxwell. "VIII. A dynamical theory of the electromagnetic field". In: *Philosophical Transactions of the Royal Society of London* 155 (Jan. 1997), pp. 459–512. DOI: `10.1098/rstl.1865.0008`. URL: `https://doi.org/10.1098/rstl.1865.0008`.

[103] Giovanni Volpe et al. "Roadmap for optical tweezers 2023 (Chapter 2)". In: *Journal of Physics: Photonics* (2023).

[104] A. Ashkin. "History of optical trapping and manipulation of small-neutral particle, atoms, and molecules". In: *IEEE Journal of Selected Topics in Quantum Electronics* 6.6 (Nov. 2000), pp. 841–856. ISSN: 1077-260X. DOI: `10.1109/2944.902132`.

[105] J Millen et al. "Nanoscale temperature measurements using non-equilibrium Brownian dynamics of a levitated nanosphere". In: *Nature nanotechnology* 9.6 (2014), pp. 425–429.

[106] Jeffrey E Melzer and Euan McLeod. "Assembly of multicomponent structures from hundreds of micron-scale building blocks using optical tweezers". In: *Microsystems & Nanoengineering* 7.1 (2021), p. 45.

[107] Philip H Jones, Onofrio M Maragò, and Giovanni Volpe. *Optical tweezers: Principles and applications*. Cambridge University Press, 2015.

[108] Timo A Nieminen et al. "Optical tweezers computational toolbox". In: *Journal of Optics A: Pure and Applied Optics* 9.8 (2007), S196.

[109] David B Phillips et al. "Force sensing with a shaped dielectric micro-tool". In: *EPL (Europhysics Letters)* 99.5 (2012), p. 58004.

[110] Jonathan M Taylor. *Optical Binding Phenomena: Observations and Mechanisms*. Springer Science & Business Media, 2011.

[111] Unė Gabrielė Būtaitė. "Enhanced optical tweezing: from hydrodynamic micromanipulation to optimised optical trapping". PhD thesis. University of Glasgow, 2020.

[112] Michael Mazilu et al. "Optical eigenmodes; exploiting the quadratic nature of the energy flux and of scattering interactions". In: *Optics express* 19.2 (2011), pp. 933–945.

[113] Michael A Taylor. "Optimizing phase to enhance optical trap stiffness". In: *Scientific Reports* 7.1 (2017), p. 555.

[114] B Agate et al. "Femtosecond optical tweezers for in-situ control of two-photon fluorescence". In: *Optics Express* 12.13 (2004), pp. 3011–3017.

[115] Unė G. Būtaitė et al. "Photon-efficient optical tweezers via wavefront shaping". In: (Apr. 2023).

[116] Michael A Taylor et al. "Enhanced optical trapping via structured scattering". In: *Nature Photonics* 9.10 (2015), p. 669.

[117] R F Hay et al. "Four-directional stereo-microscopy for 3D particle tracking with real-time error evaluation". In: *Optics express* 22.15 (2014), pp. 18662–18667.

[118] Hilding Faxén. "Der Widerstand gegen die Bewegung einer starren Kugel in einer zähen Flüssigkeit, die zwischen zwei parallelen ebenen Wänden eingeschlossen ist". In: *Annalen der Physik* 373.10 (1922), pp. 89–119.

[119] Richard W Bowman et al. "Red Tweezers: Fast, customisable hologram generation for optical tweezers". In: *Computer Physics Communications* 185.1 (2014), pp. 268–273.

[120] M C Müllenbroich, N McAlinden, and A J Wright. "Adaptive optics in an optical trapping system for enhanced lateral trap stiffness at depth". In: *Journal of Optics* 15.7 (July 2013), p. 075305. ISSN: 2040-8978. DOI: `10.1088/2040-8978/15/7/075305`.

[121] Kurt D. Wulff et al. “Aberration correction in holographic optical tweezers”. In: *Optics Express* 14.9 (2006), p. 4169. ISSN: 1094-4087. DOI: `10.1364/OE.14.004169`.

[122] Eirini Theofanidou et al. “Spherical aberration correction for optical tweezers”. In: *Optics Communications* 236.1-3 (June 2004), pp. 145–150. ISSN: 00304018. DOI: `10.1016/j.optcom.2004.03.009`.

[123] Richard W Bowman, Amanda J Wright, and Miles J Padgett. “An SLM-based Shack–Hartmann wavefront sensor for aberration correction in optical tweezers”. In: *Journal of Optics* 12.12 (Dec. 2010), p. 124004. ISSN: 2040-8978. DOI: `10.1088/2040-8978/12/12/124004`.

[124] N. B. Simpson, L. Allen, and M. J. Padgett. “Optical tweezers and optical spanners with Laguerre–Gaussian modes”. In: *Journal of Modern Optics* 43.12 (Dec. 1996), pp. 2485–2491. ISSN: 0950-0340. DOI: `10.1080/09500349608230675`.

[125] A Jesacher et al. “Wavefront correction of spatial light modulators using an optical vortex image”. In: *Opt. Express* 15.9 (Apr. 2007), pp. 5801–5808. DOI: `10.1364/OE.15.005801`. URL: `https://opg.optica.org/oe/abstract.cfm?URI=oe-15-9-5801`.

[126] R W Gerchberg. “Phase determination from image and diffraction plane pictures in the electron microscope”. In: *Optik* 34 (1971), pp. 275–284. URL: `https://cir.nii.ac.jp/crid/1571417124634973824`.

[127] R W Gerchberg. “Super-resolution through Error Energy Reduction”. In: *Optica Acta: International Journal of Optics* 21.9 (Sept. 1974), pp. 709–720. ISSN: 0030-3909. DOI: `10.1080/713818946`. URL: `https://doi.org/10.1080/713818946`.

[128] R W Gerchberg and W O Saxton. “Comment on ‘A method for the solution of the phase problem in electron microscopy’ ”. In: *Journal of Physics D: Applied Physics* 6.5 (1973), p. L31. ISSN: 0022-3727. DOI: `10.1088/0022-3727/6/5/101`. URL: `https://dx.doi.org/10.1088/0022-3727/6/5/101`.

[129] Guo-zhen Yang et al. “Gerchberg–Saxton and Yang–Gu algorithms for phase retrieval in a nonunitary transform system: a comparison”. In: *Applied Optics* 33.2 (Jan. 1994), p. 209. ISSN: 0003-6935. DOI: `10.1364/AO.33.000209`.

[130] M Hedley, H Yan, and D Rosenfeld. “A modified Gerchberg-Saxton algorithm for one-dimensional motion artifact correction in MRI”. In: *IEEE Transactions on Signal Processing* 39.6 (1991), pp. 1428–1433. ISSN: 1941-0476. DOI: `10.1109/78.136552`.

[131] D F McAlister et al. “Optical phase retrieval by phase-space tomography and fractional-order Fourier transforms”. In: *Optics Letters* 20.10 (1995), pp. 1181–1183. DOI: `10.1364/OL.20.001181`. URL: `https://opg.optica.org/ol/abstract.cfm?URI=ol-20-10-1181`.

[132] Eric Noel. “Optical implementation of a regularized Gerchberg iterative algorithm for super-resolution”. In: *Optical Engineering* 32.11 (1993), p. 2866. ISSN: 00913286. DOI: `10.1117/12.148125`.

[133] von F. Zernike. “Beugungstheorie des schneidenver-fahrens und seiner verbesserten form, der phasenkontrastmethode”. In: *Physica* 1.7-12 (May 1934), pp. 689–704. ISSN: 0031-8914. DOI: `10.1016/S0031-8914(34)80259-5`.

[134] P S Salter et al. “Exploring the depth range for three-dimensional laser machining with aberration correction”. In: *Opt. Express* 22.15 (July 2014), pp. 17644–17656. DOI: `10.1364/OE.22.017644`. URL: `https://opg.optica.org/oe/abstract.cfm?URI=oe-22-15-17644`.

[135] Daniel Iwaniuk, Pramod Rastogi, and Erwin Hack. “Correcting spherical aberrations induced by an unknown medium through determination of its refractive index and thickness”. In: *Optics Express* 19.20 (2011), pp. 19407–19414.

[136] Simon Moser, Monika Ritsch-Marte, and Gregor Thalhammer. “Model-based compensation of pixel crosstalk in liquid crystal spatial light modulators”. In: *Optics express* 27.18 (2019), pp. 25046–25063.

[137] Min Gu. “Effect of apodization on axial resolution with a high-aperture objective”. In: *Three-Dimensional Microscopy: Image Acquisition and Processing III*. Vol. 2655. 1996, pp. 53–61.

[138] Colin J R Sheppard. “Aberrations in high aperture conventional and confocal imaging systems”. In: *Applied Optics* 27.22 (1988), pp. 4782–4786. DOI: `10.1364/AO.27.004782`.

[139] Chao He, Jacopo Antonello, and Martin J Booth. “Vectorial adaptive optics”. In: *arXiv preprint arXiv:2110.02606* (2021).

[140] Richard Bowman et al. “Stereoscopic particle tracking for 3D touch, vision and closed-loop control in optical tweezers”. In: *Journal of optics* 13.4 (2011), p. 44003.

[141] M P Lee et al. “Optical shield: measuring viscosity of turbid fluids using optical tweezers”. In: *Optics Express* 20.11 (2012), pp. 12127–12132. DOI: `10.1364/OE.20.012127`. URL: `https://opg.optica.org/oe/abstract.cfm?URI=oe-20-11-12127`.

[142] David Benjamin Phillips. “Applications of closed-loop feedback control with holographic optical tweezers”. PhD thesis. University of Bristol, 2012.

[143] Daryl Preece et al. “Increasing trap stiffness with position clamping in holographic optical tweezers”. In: *Optics express* 17.25 (2009), pp. 22718–22725.

[144] Anders E Wallin et al. “Stiffer optical tweezers through real-time feedback control”. In: *Applied Physics Letters* 92.22 (2008), p. 224104.

[145] Mario Krenn. *Quantum experiments with spatial modes of photons in large real and Hilbert spaces*. 2017. URL: `https://permalink.obvsg.at/AC14507693`.